University of Southampton

Faculty of Engineering and Physical Sciences

School of Engineering

The bone microstructure of living and fossil birds: high-resolution 3D imaging for enhanced avian palaeobiology

by

Katherine Anne Williams

Thesis for the degree of Doctor of Philosophy

November 2018

University of Southampton

Abstract

Faculty of Engineering and Physical Sciences
School of Engineering

Doctor of Philosophy

The bone microstructure of living and fossil birds: high-resolution 3D imaging for enhanced avian palaeobiology

by Katherine Anne Williams

Accurately estimating developmental age and life history traits in fossils is crucial for identifying and classifying extinct species and understanding how biological attributes evolved. The evolution of life history traits such as growth pattern is far from clear in birds, and development has been studied in only a handful of modern species. The exceptionally rapid growth of modern birds means ageing methods based on annual incremental growth lines, used in other vertebrates, are inapplicable to birds and robust alternative methods remain to be established.

Analysis of avian intracortical bone microstructure, which varies both with age and tissue deposition rate, is a promising approach already used in palaeobiology. However, current thin section-based histological methods are destructive. Moreover, to date, most microstructural studies in avian bone are qualitative, 2D, and involve a limited range of extant species. The objective of this study was to investigate cortical bone microstructure and developmental age and life history traits in living birds, to identify phenotypes which can then be applied to examination of the fossil record, using minimally-destructive high-resolution 3D imaging.

First, the necessity of 3D measurement was tested: a combination of idealised, simulated datasets and real synchrotron-based computed tomography (SR CT) datasets were used to compare published methods for measuring key microstructural traits based on 2D sections and 3D volumes. Next, SR CT imaging and quantitative measurements were used to characterise age-related changes in bone microstructure in a range of extant bird species: growth series ducks and pheasants, and a smaller sample size in starlings, rock doves, partridges, and ostrich. The methods tested in modern material were applied to fossils as a proof-of concept.

It was found that 3D quantification methods are required for measuring vascular canal orientation and osteocyte lacunar shape and volume, though 2D sections could be used to measure traits such as bone volume fraction (BV/TV) and osteocyte lacunar volume. In all species studied, juvenile, subadult, and adult species could be distinguished by their values of BV/TV, and further information could be added using measured values of vascular canal diameter as well as qualitative assessment. Using a synchrotron-based CT system, high-resolution 3D datasets comparable to modern bone samples were obtained from fossils, and preliminary estimates of developmental age can be made.

Further work may reveal more changes within juvenile age stages, and better characterise the variation within extant birds, allowing more accurate interpretation of the fossil record. Therefore developmental studies in a greater number of extant bird species are required using larger sample sizes, to support and add to the results presented in this thesis.

Contents

List of Figures

List of Tables

UNIVERSITY OF Southampton

Research Thesis: Declaration of Authorship

Print name:	Katherine Anne Williams

Title of thesis:	The bone microstructure of living and fossil birds: high-resolution 3D imaging for enhanced avian paleobiology

I declare that this thesis and the work presented in it is my own and has been generated by me as the result of my own original research.

I confirm that:

1. This work was done wholly or mainly while in candidature for a research degree at this University;
2. Where any part of this thesis has previously been submitted for a degree or any other qualification at this University or any other institution, this has been clearly stated;
3. Where I have consulted the published work of others, this is always clearly attributed;
4. Where I have quoted from the work of others, the source is always given. With the exception of such quotations, this thesis is entirely my own work;
5. I have acknowledged all main sources of help;
6. Where the thesis is based on work done by myself jointly with others, I have made clear exactly what was done by others and what I have contributed myself;
7. Either none of this work has been published before submission, or parts of this work have been published as: [please list references below]:

Signature:		Date:	

Acknowledgements

This work is funded by a PhD studentship from the Institute for Life Sciences and the Faculty of Engineering and the Environment at the University of Southampton.

First and foremost, I would like to thank my supervisors for their support and guidance at every stage.

The SR CT experiments were performed at the TOMCAT beamline of the Swiss Light Source (SLS) at the Paul Scherrer Institut (PSI), Villigen, Switzerland, with support from beamline scientists Pablo Villaneuva and Goran Lovric, and at I13-2 beamline of Diamond Light Source at Harwell Science and Innovation Campus, UK, with support from beamline scientists Shashidhara Marathe, Andrew Bodey, and Silvia Cipiccia. These experimental sessions would not have been possible without the help of Elis Newham, Christian Laurent, Roeland de Kat, Richard Cook, Hannah Cheales, Aileen O'Brien, Colin Palmer, Juan Núñez, Patricia Goggin, Alisha Sharma, Erik Meilak, Madhu Bangalore Narasimha Murthy, Roxanna Ramnarine-Sanchez and Harry Rossides.

I would additionally like to thank μ-VIS Southampton, and in particular Katy Rankin, Mark Mavrogordato, and Rich Boardman for support with scanning, data processing, and storage, and Patricia Goggin and Stef Inglis for some very useful discussions and training respectively relating to bone histology, sample preparation and correlative imaging. Thanks to Joshua Steer for help and advice with simulating shapes in ScanIP.

Samples were kindly donated by Warawee Duck farm, Pollards Moors Road, Copythorne, Southampton, Hampshire, Blackmoor Game Farm, Hampshire, Matt MacGregor-Sharp, University of Southampton, Marc Jobling, Neil Gostling, and Dale Serjeantsen (Southampton Osteoarchaeology reference collection). Thank you to Dan Doran, University of Southampton, for assistance with preparing the fossil samples.

Special thanks go to my parents and my fiancé for their unwavering support, even when it looked like everything was impossible, and to Josh Steer and Tom Mabey for a lot of laughs and reminding me to keep my chin up.

Finally, I would like to thank Dr Ian Moore, for shaping the way I see and question the world, for introducing me to the world of research, and going above and beyond in supporting me through my early scientific career. You will be missed.

Chapter 1

Project Overview

1.1 Introduction

Accurate estimation of developmental age, growth rate and developmental mode (precocial or altricial) in fossils is crucial for understanding taxonomy and evolutionary patterns in extinct animals but, in birds, robust ageing remains to be established. Histological study provides a promising approach, since the microstructure of cortical bone is known to vary with both age and tissue deposition rate [2, 15], and can be preserved in fossils with high fidelity. However, to date, most histological studies have been qualitative, 2D, and tested in only a limited range of extant species. This has recently been shown to be problematic in terms of accuracy of estimation [16–18] and application beyond the study species [2, 15].

The aim of this project is to use high-resolution, minimally-destructive, three-dimensional imaging (synchrotron-based computed tomography) to improve current understanding of age-related changes in bone microstructure in birds, for the purpose of better understanding the biology and taxonomy of extinct birds.

The bone cortex is a mineralised tube of bone, containing two main sources of porosity: networks of vascular canals through which blood vessels run, and osteocyte lacunae, in which bone cells reside. The microstructure of pores within cortical bone varies according to the depositional history of the bone and can provide information about factors from age [19] and bone deposition rate [2, 19] to genome size [20], and bone loading [21]. However, bone microstructure in birds, how it changes with age, and how this is influenced by factors such as body mass and developmental pattern are not fully understood. In order to interpret developmental age, as well as understand the influences of life history and body mass on bone microstructure, it is necessary to collect systematic comparative datasets in extant species [22]. In addition, these datasets should be quantitative, to allow continuous rather than categoric assessment [6], and to allow direct and objective comparisons between different studies.

Current histological techniques largely focus on traditional 2D histological sections, produced by physically cutting a fossil and polishing the surface to study its microstructure under a microscope [22]. However, this process is destructive, a problem for irreplaceable fossils, and time consuming. It reduces the complex 3D structure to a 2D surface which may not be able to accurately portray the true 3D structure [23], and also limits the sample volume that can be

imaged. Therefore, destructive 2D histology is undesirable from the point of view of preservation of irreplaceable materials, but also may result in inaccurate measurements of histological characters, especially those that require 3D information such as orientation of vascular canals [18].

Instead, histological study is moving towards 3D approaches, using synchrotron-based X-ray computed tomography (SR-CT) [24, 25]. SR-CT uses X-rays to generate a series of 2D radiographs taken at angles all the way around the object, which can be used to generate a full 3D volume, differentiating between materials that absorb X-rays to different extents. These techniques can resolve details smaller than 1 micrometer in diameter and are therefore ideal for imaging histological-level detail in 3D. However, given most studies in the past have used 2D histology, it is important to be able to compare the results obtained using 2D and 3D histology. In addition, at this stage, where most studies still use conventional histology, but some use SR-CT, it is valuable to test the quantitative advantages to using 3D imaging, whether 3D measurements of, for example, canal orientation, are more accurate from 3D models, and whether there are cases where 2D histology could be used.

Therefore, the first part of this project compared published methods for measuring a variety of histological measurements which are commonly used to interpret fossils, including canal orientation, and osteocyte lacunar volume and aspect ratio, based on 2D sections and 3D volumes. First, an *in silico* approach was taken, using simulated cylinders to represent idealised vascular canals and ellipsoids to represent idealised osteocyte lacunae. These were used to test the theoretical applications and limitations of measurement methods based on a single virtual section or based on the whole volume. The same measurement methods were then compared in real CT datasets, using single CT slices to simulate histological sections, to test whether 2D and 3D methods would produce the same results as each other in real datasets.

The second part of this project aimed to address the currently limited quantification of bone microstructure through development in extant birds, and therefore provide information on which to base estimates of developmental age in unknown samples. Changes in bone microstructure through development in birds have received little attention. A small number of studies have described microstructural change, and especially looked at growth rates, in extant birds [2, 15, 19], but little work has been done to quantify changes, and few species have been studied. In order to extrapolate to fossils, a sound understanding of age-related changes in vascular canals and osteocyte lacunae is required. This is especially important given the change towards 3D techniques, which may produce different results to older 2D techniques [18].

Cortical bone in the midshaft of the tibiotarsus, femur, and humerus from a growth series of two extant species (domestic ducks, *Anas platyrhynchos* and pheasants, *Phasianus colchis*) was measured using SR-CT and quantified using the methods tested in Chapter 4, to test for age-related changes in various metrics of cortical bone microstructure. The two species were chosen because they have similar body masses, follow similar precocial developmental patterns (walk almost from hatching), but differ in the fact that in the duck, flight is delayed compared to in the pheasant, and that the duck grows faster than the pheasant [26]. Therefore, in the context of all extant birds, these two species are fairly similar. If the bone microstructure and its age related changes differed substantially between these two similar species, extrapolation to extinct species would be questionable. Therefore, two similar species were selected initially.

Although the duck and the pheasant provide two model species on which to base the beginnings

of a characterisation of bone microstructure in birds, further study is required to understand how these changes vary across the range of extant species, in order to accurately extrapolate to fossils. Therefore, in the third part of this project, a preliminary assessment of a wider range of extant bird species were studied using the same microstructural methods as the previous chapters. First, the question of life history was addressed: a further precocial species (partridge, *Alectoris rufa*), along with two altricial species (starling, *Sturnus vulgaris*, and rock dove *Columba livia*) was measured. Two to three age stages were studied for each species, depending on sample availability. Additionally, samples with differing body masses were measured: the pheasant was compared with the partridge, the starling with the rock dove, and finally ostrich *Struthio camelus* samples were measured, to test the extreme case of extant avian body mass. Information from these samples provides information about how bone microstructure varies in extant birds, which is a crucial step for extrapolating to fossils, where these traits are unknown.

Finally, given that the aim of this project is to add to current understanding of avian bone microstructure, for the purpose of interpreting fossils, it was necessary to test the same methods in fossils. Fossil bone can retain a great deal of structural information, down to the cellular level [27], but is chemically different from recent bone [28], and it is possible that features may appear different in fossils compared with recent bone.

Additionally, in CT scanning, the best scan resolutions are obtained from small samples, ideally fitting within the field of view, which for scans using voxel sizes of around 1 μm, this may only be 1-2 mm. However, fossil birds are often preserved in large slabs. Given that fossils are irreplaceable, the ideal situation would be for 3D imaging to be completely non-destructive. Additionally, although this project has focussed on SR CT, since it can be used to produce very high-contrast, high-resolution, rapid scans, it is less accessible to users than lab-based CT systems which are becoming increasingly common in universities and museums. Therefore, it is of interest to test the current state of lab-based CT systems and consider whether these could be used for histological-scale imaging of large, flattened, fossil samples.

As well as technological testing, a crucial part of this project was to test the quantification methods used in modern bone in fossils, and to try to estimate developmental age in some fossil birds.

Therefore, the final chapter of this thesis firstly applied the same imaging techniques used in modern birds in previous chapters to image the microstructure of ideal, cut-to-size fossil bone samples. Then, a much more awkward, larger, flat fossil was imaged at the best possible resolution for the object size and density in a lab-based system, to assess whether histological-scale imaging was possible. Finally, the microstructure of the fossil bird bone was quantified using the methods applied in previous chapters, and interpretations made about their developmental age.

1.2 Aims, objectives, and hypotheses

The aim of this project is to use high-resolution, minimally-destructive, three-dimensional imaging (synchrotron-based computed tomography) to improve current understanding of age-related changes in bone microstructure in birds, for the purpose of better understanding the biology and taxonomy of extinct birds.

Hypothesis: 3D imaging techniques, applied to growth series of a range of modern birds, can add to and improve current understanding of age-related changes in bone microstructure, enabling more accurate estimation of developmental age in extinct birds.

1. Quantifying intracortical bone porosity: an appraisal of 2D and 3D methodologies in the domestic duck (*Anas platyrhynchos*)
    - Hypothesis: Methods for quantifying bone histological features, namely vascular canal orientations and osteocyte lacunar aspect ratio and volume, based on 2D histological sections are less accurate than 3D alternatives using μ-CT datasets.
    - Objective: To test the relative accuracy of 2D and 3D quantitative histological methods using simulated and real test datasets. Specific aims:
        (a) To test the accuracy and precision of canal orientation measurement methods using 2D and 3D datasets when geometric assumptions are met
        (b) To test the sensitivity of 2D and 3D canal orientation measurement methods to deviations from the assumption that canals are perfectly cylindrical
        (c) To test the accuracy and precision of osteocyte lacunar aspect ratio and volume measurement methods using 2D and 3D methods
        (d) To test the sensitivity of osteocyte lacunar aspect ratio and volume measurement methods to different experimental conditions, namely different voxel sizes
        (e) To compare results obtained using 2D and 3D methods in real datasets, both for the canal orientation and osteocyte lacunar volume, and for measures that do not require modelling (BV/TV and osteocyte lacunar number density)
2. Testing how bone microstructure changes throughout development in two modern birds
    - Hypothesis: age-related changes in bone microstructure can be used to help estimate developmental age in birds.
    - Objective: Characterise bone microstructural changes throughout development in two modern bird species (duck and pheasant). Specific aims:
        (a) To investigate how porosity changes throughout development and differs between two modern bird species
        (b) To investigate how canal orientation changes throughout development and differs between two modern bird species
        (c) To investigate how osteocyte lacunae change throughout development and differs between two modern bird species
3. A preliminary investigation into interspecific variability in bone development across extant birds.

- Hypothesis: Variation in bone microstructure seen between pheasant and duck represents a small proportion of the variation across modern birds: species with different developmental patters and body masses will have substantial differences in bone organisation which may make age estimation *etc*. difficult to extrapolate
- Objective: To characterise bone microstructure in a range of modern birds with precocial and altricial developmental patterns, and with differing body masses. Specific aims:
  (a) To test the effects of developmental mode (precocial/altrical) on bone microstructure
  (b) To test the effects of body mass on bone microstructure

4. Application to extinct birds and future challenges

- Hypothesis: The imaging techniques applied to recent material in previous chapters can be applied to fossil specimens to interpret the biology of extinct birds
- Objectives: To apply the same imaging and analysis techniques developed in previous chapters to some extinct species (*Aepyornis*, *Mullerornis*, *Lithornis*, and an unidentified Pleistocene bird from Florida). Specific aims:
  (a) To apply high-resolution SR CT imaging techniques to small fossil samples
  (b) To test the limits of current lab-based CT techniques for imaging microstructural detail in a large, flat, fossil sample
  (c) To interpret the biology of a range of extinct birds

Chapter 2

Literature Review

2.1 Introduction

Despite an influx of new avian fossils over the last 15 years, including those from the Early Cretaceous Jehol Biota of north eastern China (e.g. [29, 30], the biology, taxonomy, and evolution of birds remains enigmatic [31]. It is widely accepted that modern birds (birds are here defined as the crown group including *Archaeopteryx*) are living dinosaurs, and that their evolutionary history has involved an increase in metabolic and growth rate, adaptations for flight, and a decrease in body size [32]. However, the order and timing of these innovations, together with their potential contributions to the survival of the avian lineage through the end-Cretaceous extinction, is unclear.

Bone histology, the microstructural study of bone tissue, has long been applied to understanding the functional biology of fossil animals [33, 34], as bone microstructure reflects its depositional history [15]. Recently, for example, histology has been used to infer that ornithurine and basal ornithuromorphs had microstructure and therefore metabolic and growth rates comparable to modern birds, while enantiornithes contemporaneous with basal ornithuromorphs are thought to have biologies that are similar to early diverging taxa such as *Archaeopteryx* [30]. However, the proportion of avian fossils that have been studied histologically remains relatively small (Figure 2.1 and Table 2.1): fossil material is irreplaceable and many avian fossils are preserved as just single specimens. While this is true to some extent across palaeontology, some taxa have been better studied than others. For example, in non-avian sauropod dinosaurs, a set of thirteen histological developmental stages were developed to estimate age [35] and later, to compare life histories across sauropods. These stages were developed from a large sample set (167 bones) taken from the growth series in eight different species in standardised anatomical positions, providing the most robust life history estimates for dinosaurs to date. Thus osteohistology has significantly contributed to the understanding of the biology and evolution of non-avian sauropod dinosaurs [36], although, no equivalent standard series exists for avian dinosaurs.

In addition, just a handful of longitudinal studies have been carried out in modern birds to test in a rigorous way how histology relates to functional biology and ontogeny and this shortcoming has limited the development of validated methodologies to infer the biology of

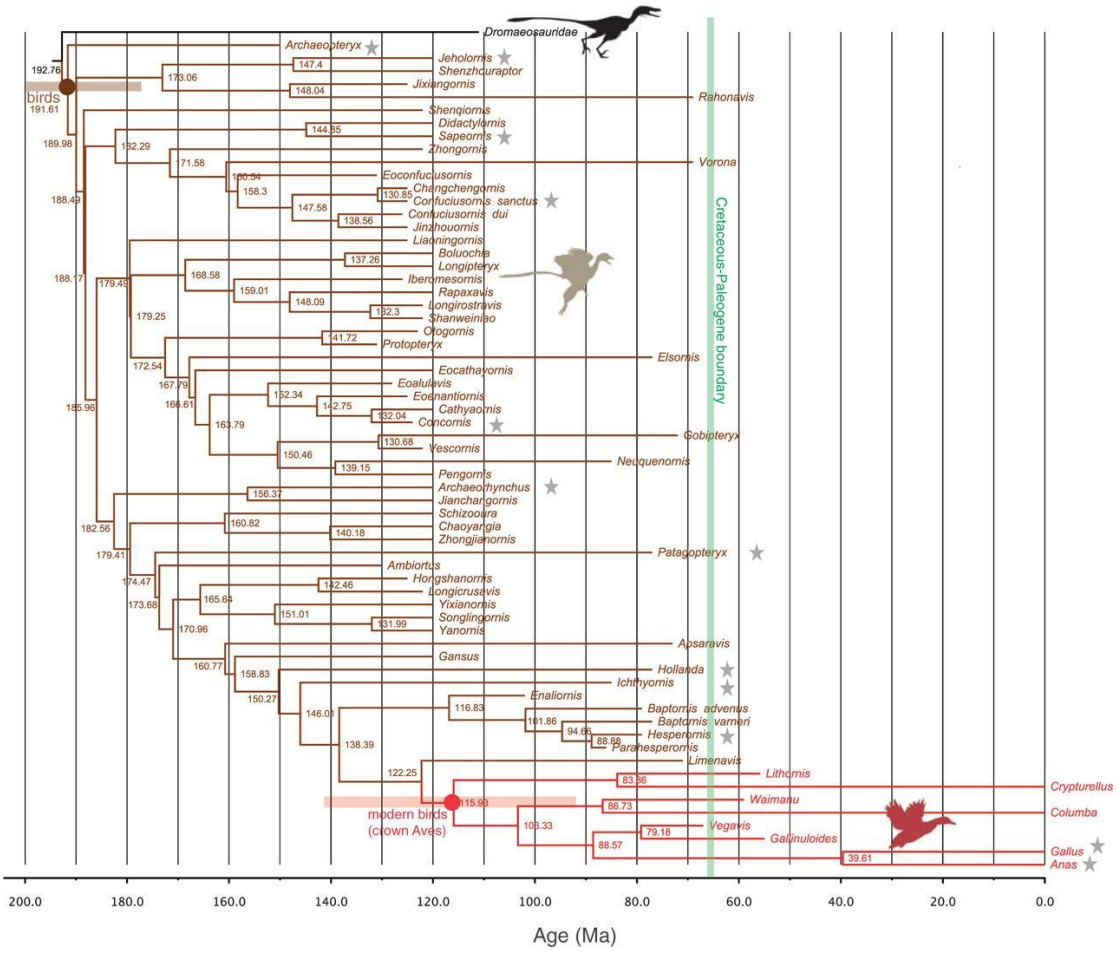

FIGURE 2.1: Phylogenetic tree of bird evolution. Stars represent fossils where histology of bone tissue has been described in literature, demonstrating the relatively small proportion that has been studied histologically (see Table 2.1). Figure based on [1].

fossil birds. Thus, the study of modern birds through the application and, critically, validation of less destructive imaging techniques offers an opportunity to examine and re-examine fossil specimens allowing more accurate conclusions to be drawn.

2.2 Open questions in avian palaeobiology and the importance of accurate histology

Modern birds differ from their non-avian theropod ancestors in several key ways. For the most part, modern birds are much smaller, they have extraordinarily high growth and metabolic rates, and they fly [37]. The interpretation of growth rate and metabolic rate from histology have been used to infer relationships between very early bird fossils, and to distinguish between the earliest birds and non-avian dinosaurs [38, 39], however, the relationships between these fossils remains much debated. Further histological study, including a better understanding of growth and metabolism in extant birds and reptiles, could help to clarify these relationships.

Histology may also tell us more about life histories because patterns of development, including variations in growth rate throughout the life course, vary between species with different life

histories [40]. Altricial birds, which are entirely reliant on parental care and do not bear weight until late in development, have different patterns of ossification in comparison to precocial birds, which use their lower limbs almost from hatching. These patterns of growth may be recorded in the bone microstructure [41], and identifying these patterns in living birds could aid in deciphering the life history of an extinct bird.

Bone histology can provide life history information about the individual, such as developmental stage, as well as the biology of different species. An accurate estimation of developmental stage is critical for understanding both the biology and taxonomy of a specimen. For example, knowing the developmental stage of an animal is necessary to interpret potential sexual dimorphism and the timing of sexual maturity. Within the Cretaceous bird *Confuciusornis sanctus*, where, an unusually large number of specimens have been collected, potential sexual dimorphism has been extensively debated [42–46]. Amongst the several hundred fossils, three size classes and two distinct morphological features (*i.e.*, the presence or absence of elongate tail feathers (retrices)) have been identified, although the presence or absence of these features is not correlated with body size classes. Peters and Peters [43, 45] suggested that the two larger body size classes represent sexual size dimorphism, while Chiappe [42, 44] and Chinsamy *et al*. [46] argued that retrices are sexually dimorphic while size is not. If the latter is true, sexual maturity is reached long before skeletal maturity as even small individuals with retrices could be inferred to be sexually mature. This observation would be in stark contrast to living birds which reach full body size rapidly, but do not reach sexual maturity until later in life. Critically, this would be an important finding for our understanding of the evolution of birds. However, true evidence of sexual maturity (in the form of medullary bone) has only been identified in a single individual (one without retrices) [46], while the skeletal developmental stage of most of the other specimens is unknown, and few have been studied histologically. Current understanding based on histology would allow distinction between rapidly-growing juveniles and fully mature adults, and some attempt has been made to estimate absolute age based on modern growth rates in ducks [47]. However, it is important to note the evidence is limited, given how few species have been used as a comparison. Furthermore, even if an accurate estimate of age could be established, examination of each fossil using destructive histological sampling is undesirable. This suggests that enhanced understanding of bone histology, together with the application of non-destructive techniques, could allow many more of these specimens to be examined histologically and the nature of sexual dimorphism and maturation in *Confuciusornis* elucidated.

Perhaps of greater fundamental relevance than our understanding of fossil biology, accurate age estimation is critical for correct taxonomy, upon which all evolutionary interpretations are based. Morphological changes that can occur through development can be similar to those used to differentiate between species, [48–50]. It is clear that phylogenies built on morphological characters raise issues if key taxonomic characters are in fact developmental. Histological analysis is already used to clarify taxonomy by identifying juvenile specimens; for example, histological study of the early Cretaceous bird *Sapeornis* suggested that one specimen was a sub-adult, leading to calls to reclassify the sapeornids [51]. However, for these studies to be of most value, further studies in modern species are required, and ideally non-destructive methods should be adopted, as histology may not be able to be applied to all fossils.

It follows from the above that the classification of juvenile specimens as new species is

problematic in the avian fossil record. Over 120 species of Mesozoic birds have now been described (see Figure 1 for a summary of avian phylogeny) but with a few notable exceptions, such as *Confuciusornis sanctus* [52], each species is represented by just a single specimen. This could be a result of incompleteness in the fossil record [31]. Equally, we may question whether it is likely that (almost) every new specimen found represents a new species. Perhaps instead, some of these separate species may in fact represent different juvenile stages of the same species. If this is the case, this has significant implications for taxonomy as well as for our interpretation of palaeobiology [53].

2.3 Bone development and the functional interpretation of histology

Bone histology is often published alongside descriptions of new fossils with biological interpretations, typically drawn from a small number of longitudinal studies carried out in living animals, together with biomedical studies of bone development. Bone development in humans and rodents has been extensively studied [50, 54–56], but less work has been carried out across a wider range of vertebrates, and particularly birds. Although birds have similarly rapid growth and metabolic rates to mammals, they evolved independently of each other so studies in mammals may not be applicable to birds.

In a histological description, the features usually described and interpreted are the number density and orientation of the vascular canals, the shape and number density of the osteocyte lacunae, and the orientation of the collagen fibres, as seen using polarised light [22]. Together, these form the basis of a set of bone types which have been associated with different growth rates [15]. The most rapidly deposited bone is known as woven bone. Woven bone, which is deposited first in fetal bones and also involved in fracture healing, is characterised by an open, porous structure with disordered, rounded osteocyte lacunae and a disordered collagen matrix. Although woven bone can be deposited very rapidly, it lacks mechanical strength and therefore very little woven bone is found in adult bone. The most slowly deposited bone type is parallel-fibred (including lamellar, following [57]) bone, which is deposited appositionally and may be almost avascular [15, 34, 58]. Much of the bone in birds is a mixture of these two types of bone, a structure known as fibrolamellar complex. This bone is deposited initally as a porous, foam-like structure of woven bone around blood vessels with large spaces and a large proportion of uncalcified osteoid. As the bone matures, the pores are infilled by appositional deposition, resulting in primary osteons which contain a vascular canal at their centre. Fibrolamellar complex is therefore made up of a woven bone matrix with primary osteons.

Within the life of an animal, growth rates can vary. Narrow, avascular layers with different collagen fibre orientation from their surroundings can form if growth slows or stops, for example, seasonally, leading to the appearance of incremental growth rings known as lines of arrested growth (LAGs), and annuli. In other taxa, LAGs are used to estimate the absolute age of an animal in years [59–62]. However, as LAGs are present in only some [63] (not all) birds, both Mesozoic and modern, their application to birds in general for ageing is limited. Increments formed at finer temporal scales than LAGs, such as bone lamellae, have also been considered potentially useful for skeletal ageing in birds, but these are typically much less

well-delineated than they are in mammals and reptiles, perhaps due to a rapid tissue deposition rate [64]. The number of incremental layers within the endosteal layer in modern birds has been used to estimate age with limited success [55, 65–67].

2.3.1 Bone microstructure: vascular canals

In fibrolamellar bone, the organisation of vascular canal networks provide the basis for much interpretation of bone microstructure. For example, there appears to be a relationship between the growth rate of bone and the presence and proportion of primary osteons [15, 58, 68], which are related to the initial porosity of bone on deposition.

In rapidly-growing bone, tissue is richly vascularised and highly porous with limited mineralisation. This allows the bone to grow quickly, though this bone may be limited in mechanical competence [19]. The diameter of vascular canals, and therefore primary osteons, may be associated with deposition rate, though final canal diameter may be related to erythrocyte size [56]. Bone with a large number of initial pores will eventually have a large number of primary osteons, with bone deposition rate predicted to influence the number of primary osteons. In slower-growing bone, vascularisation is reduced, sometimes to almost avascularity, such as in the outer circumferential layer (OCL), a layer of slowly deposited bone that forms temporally at the end of bone growth. In this case, bone is deposited in an appositional, circumferential manner, leading to the formation of lamellar bone which is not porous at first deposition and therefore lacks primary osteons. The initial differences in vascularisation, and therefore porosity, have been attributed to diffusion distances between blood vessels and osteocytes, which require oxygen and a route for removal of waste products [69]. However, there is also evidence of a phylogenetic signal in vascular number density [41, 70].

Osteonal number, however, is only one aspect of canal organisation. In king penguin chicks (*Aptenodytes patagonicus*) it was found that the tissue type, defined by both the presence and orientation of vascular canals, was strongly related to tissue deposition rate [2]. Canal orientations can be classified as reticular, longitudinal, and circumferential, with varying levels of connectivity. It is often stated in the literature that reticular, highly anastomosing networks of canals are related to fast tissue deposition, while longitudinal arrangements relate to slower deposition (Figure 2.2). This relationship has been supported in some studies [2, 18], but has not always been found to be significant [15]. In addition, vascular organisation is correlated with body mass [69] and appears to influence the mechanical properties of bone [21, 71]. It has been argued that a circumferential organisation of canals is an adaptation to increased torsional resistance, a hypothesis supported by the presence of this type of bone in the humerus, which in flight undergoes greater torsional loading than, for example, the tibiotarsus in walking [21]. However, a recent study looking at 31 bird species found that fewer laminar vascular canals were found in the humerus than the femur [18], suggesting the relationship may be more complex than sometimes stated.

Haversian systems, resulting from secondary remodelling of primary tissue, are understood to a lesser extent in terms of functional biology, although a recent study found that the diameter of secondary osteons scales with body mass in mammals, independent of phylogeny [72]. Other

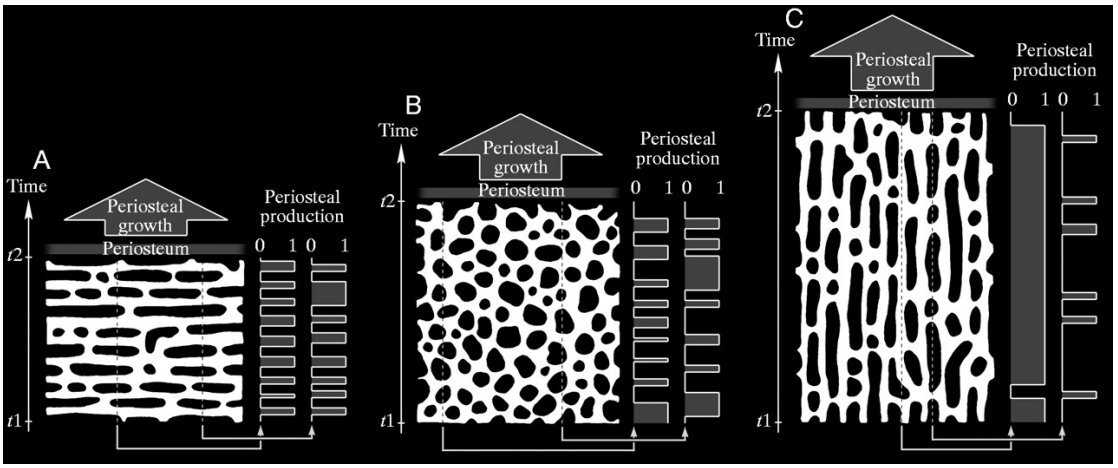

FIGURE 2.2: Putative relationship between canal orientation and growth rate. (A) Laminar organisation of vascular canals results in the slowest bone growth. (B) Longitudinal vascular canals produce an intermediate growth rate. (C) Rapid bone deposition where canals are radial. Figure reproduced from [2].

relationships remain less clear, poorly studied, and thus most interpretations are based on primary osteons.

2.3.2 Bone microstructure: osteocyte lacunae

As osteoblasts deposit osteoid they can become trapped in the tissue they are forming [3, 73] (Figure 2.3). In this case, the cells differentiate to become osteocytes, which reside in spaces (osteocyte lacunae) within calcified tissue (Figure 2.4), and play a pivotal role as bone mechanosensors in bone modelling and remodelling in response to mechanical stimuli [3, 74–77]. Osteocytes, until recently, have been poorly studied relative to other bone cell types given their inaccessibility deep within calcified tissue [3]. Isolation of osteocytes for studies in vitro have been limited [78], although there has been a recent increase in studies of osteocytes with the application of new imaging techniques [4, 13, 79–85].

In palaeohistological studies, tissue containing osteocytes that are described as plump and irregularly arranged in space is inferred to have been rapidly deposited [22, 63]. It has been suggested that this variation in osteocyte shape, size, and orientation is related to differences between two different types of bone formation, static and dynamic osteogenesis [17]. Osteocyte lacunar orientation is correlated with the orientation of the collagen fibres [86], which are more or less random in rapidly-growing woven bone and highly ordered in slow-growing bone [87]. Given these observations, a more regular organisation of osteocyte lacunae in slow-growing, adult bone compared with juvenile bone could be predicted. In terms of the actual orientation of osteocyte lacunae, collagen fibre orientation is important in bone remodelling according to the direction of mechanical strains [88], and therefore, the orientation of osteocytes and osteocyte lacunae may also be related to the mechanical strains imposed on a specific bone. The number density [89], volume [16], surface area [64], and shape [63] of osteocyte lacunae have all been linked with bone deposition rate by palaeohistologists or age in the biomedical field [74], though the shape and orientation are very difficult to assess from single-orientation thin sections [17, 90].

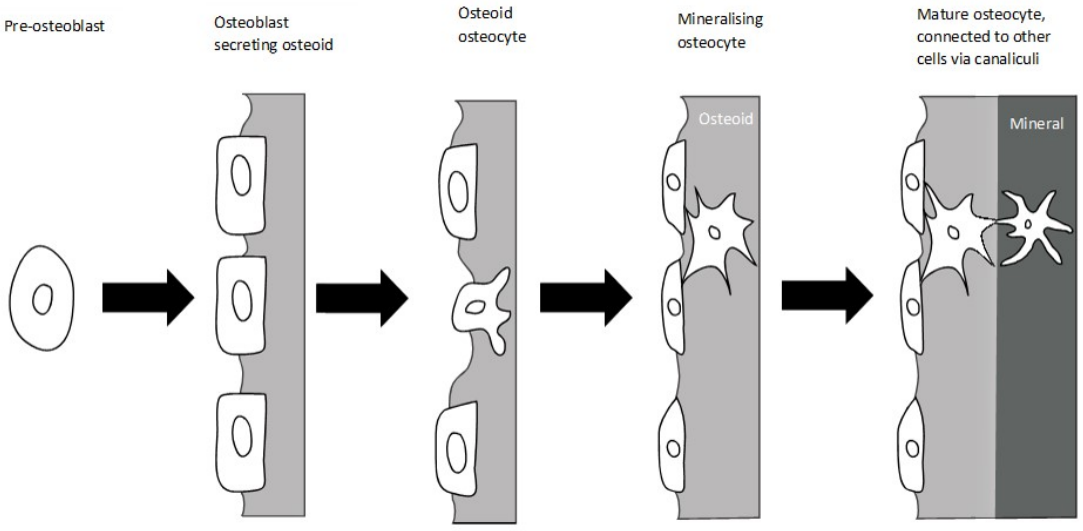

FIGURE 2.3: Bone deposition by osteoblasts and the differentiation of bone cells. Pre-osteoblasts differentiate into osteoblasts, which secrete osteoid (un-mineralised bone tissue). Some osteoblasts become trapped within the matrix and differentiate into osteocytes, around which the matrix becomes mineralised. Based on [3].

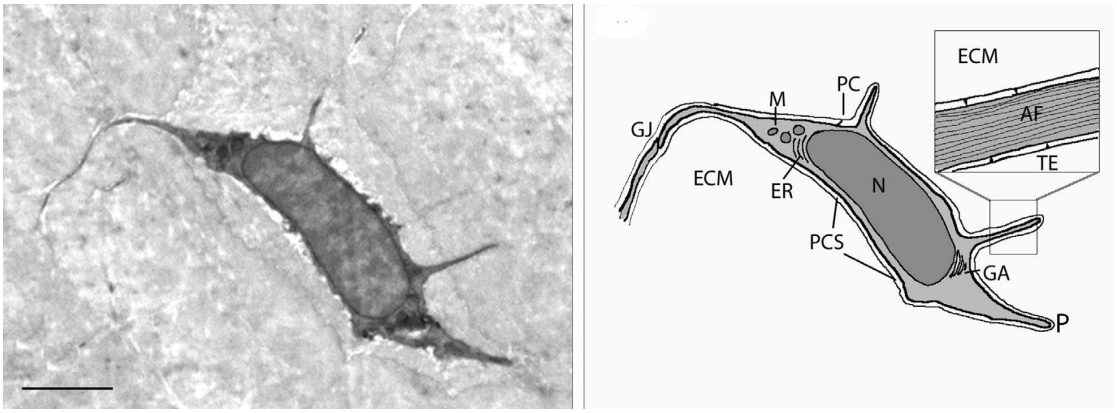

FIGURE 2.4: An osteocyte within an osteocyte lacuna. Left: Transmission electron microscopy (TEM) image of murine bone. Scale bar is 2 μm. Right: sketch showing osteocyte cell organelles and pericellular space. Abbreviations: actin filaments (AF), endoplasmic reticulum (ER), extracellular matrix (ECM), gap junction (GJ), Golgi apparatus (GA), mitochondria (M), nucleus (N), osteocyte cell process (P), primary cilium (PC), pericellular space (PCS), tethering elements (TE). Image reprinted from [4] with kind permission of eCM, AO Research Institute Davos.

On the endosteal surface, bone tissue is resorbed by cells known as osteoclasts [91], while osteoblasts deposit new bone tissue at the periosteal bone surface. This allows the thickness of the bone cortex to be regulated as the overall bone diameter increases [92]. Altered relative cortical thickness, such as cortical thickening, can be an adaptation to behaviours such as diving [93], and thus, determination of relative thickness is a useful measure. Nevertheless, bone remodelling also has implications for the ability of bone microstructure to inform about deposition history, given the earliest deposited bone is likely to be lost as a consequence of remodelling as the animal grows.

Recent studies have highlighted the importance of quantitative measurements, in 3D [17, 90], in large samples [70], and across different bones [85] and species, and the importance of

understanding the effects of phylogeny [70] and body mass [94] on bone microstructure. Rensberger *et al.* [64] attempted a quantification of canalicular networks across a wide range of species, with results indicating that birds have osteocyte lacunar networks with exceptionally high surface areas. However, the sample site was not uniformly chosen across species, which is problematic given that some properties of osteocyte lacunae, namely the number density, varies widely within an individual [85]. D'Emic *et al.* [16] measured the volumes of a large number of osteocyte lacunae in a range of avian and non-avian dinosaurs, using orthogonally-cut thin sections in acknowledgement of the limitations of single tissue orientations. Again, a large amount of intra-individual variation was observed, though much less at homologous skeletal sites between individuals of the same species, indicating a strong effect of skeletal site. The authors found a weak correlation between osteocyte lacunar volume and whole-body growth rate, in addition to scaling with body mass, metabolic rate, and genome size.

A final consideration in interpreting bone histology is that, within a species, growth rate can vary markedly as a consequence of environmental conditions or individual variation [92, 95]. Starck and Chinsamy [92] argued that this variability makes generalisations around age estimations highly questionable. Nevertheless, while individual variability will inevitably introduce error into age estimates, this does not mean that bone microstructure and generalisations cannot be informative. Indeed, bone microstructure will reflect individual growth rate, which may in some cases enable quantification of variation in growth rate in a population, where several individuals of similar body sizes are present. Clearly, further study is required to quantify the relationships between various bone microstructural features and age and growth rate across different taxa, and the biology underpinning these relationships.

In order to enhance our understanding of avian biology and evolution, it is clear that a quantitative method of estimating age and life history is required, which is fit for purpose and, critically, validated in terms of quantitative performance. While it is accepted that bone microstructure varies with age and deposition rate, an ideal method would be based on functional biology rather than observed correlations. However, the functional biology that might influence these features is far from clear (see Table 2.2).

TABLE 2.1: Examples of studies of avian palaeohistology and conclusions reached concerning developmental age in different Mesozoic bird taxa. Most Mesozoic avialans have not been studied histologically and those that have been are, for the most part, studied from just one or two thin sections. Lines of arrested growth (LAG), which suggest protracted growth compared with most modern birds, have been used to estimate developmental age, inner circumferential layer (ICL), and outer circumferential layer (OCL), which suggest that growth has more or less ceased and the animal is at full adult size. The presence of bone remodelling also suggests a relatively mature individual.

Fossil	**Age**	**Bones studied**	**Bone types present**	**Remodelling**	**LAG**	**OCL**	**Interpretation**
Archaeopteryx lithograhica [38] (Basal bird)	Jurassic	Femur, tibiotarsus	Parallel, nearly avascular	Not present	Y	N/A	Juvenile, relatively slow growth rate (compared with modern birds), taking several years to grow to full size
Archaeorhyncus spathula [29] (Earliest ornithuromorph)	Early Cretaceous	Humerus, tibiotarsus	Woven, parallel	2°osteons	Y	Y	Adult, slow, interrupted growth, similar to enantiornithes – slow growth rate in common ancestor of enantiornithes and ornithomorphs
Concornis lacustris [63] (Enantiornithine)	Early Cretaceous	Tibiotarsus, tarsometa-tarsus	Parallel, some osteonal	2°osteons	Y	Y	Adult, slow growth in late development although possibly more rapid in early development
Confuciusornis sanctus [96] (Confuciusornithiforme)	Early Cretaceous	All long bones	Woven/ fibrolamellar	2°osteons	Y	Y	Adult, interrupted growth but faster rates than e.g. Archaeorhynchus. One individual found to have medullary bone – egg-laying
Iteravis huchzermeyeri [97] (Ornithuromorph)	Early Cretaceous	Ulna, tibiotarsus	Fibrolamellar, some lamellar	Medullary expansion	N	N	Nearly adult, though lacking in LAGs suggests relatively rapid growth

Jeholornis sp. [98] (Basal bird)	Early Cretaceous	Ulna, femur	Woven, parallel	2°osteons	Y	Y	Adult, relatively slow growth rate (compared with modern birds), taking several years to grow to full size
Sapeornis sp. [51] Basal bird	Early Cretaceous	Tibia	Woven, parallel	2°osteons	Y	?	Sub-adult, LAGs and parallel-fibred bone indicate slow growth rate, taking several years to grow to full size
Chongmingia zhengi [29] (Non-ornithothorace)	Early Cretaceous	Humerus, femur	Fibrolamellar, parallel	2°osteons	N	?	Adult, more vascularised than Archaeopteryx and Jeholornis, grew to full adult size within a year
Parapengornis eurycaudatus [99] (Enantiornithine)	Early Cretaceous	Femur	Woven	Not present	N	N	Juvenile/sub-adult, flattened osteocyte lacunae in outer layers suggest growth has slowed but not stopped
Patagopteryx deferrariisi [100] (Ornithuromorph)	Late Cretaceous	Femur	Fibrolamellar, primary osteon	2°osteons, some resorption	Y	Y	Adult, interrupted growth over more than one year
Ichthyornis victor [93] (Ornithurine)	Late Cretaceous	Humerus	Fibrolamellar, some woven	Medullary expansion, no 2°osteons	N	?	Adult, relatively rapid growth within a year, relatively thin bone cortex suggests flight
Hesperornis [93] (Ornithurine)	Late Cretaceous	Femur (midshaft and distal)	Fibrolamellar, primary osteons	Medullary expansion, 2°osteons	N	Y	Adult, relatively rapid growth within a year, relatively thick bone cortex linked to diving behaviour
Hollanda luceria [101] (Ornithurine)	Late Cretaceous	Tibiotarsus	Fibrolamellar, parallel	Not present	Y	N	Sub-adult, interrupted growth over more than one year

TABLE 2.2: Hypothesised, or described, relationships between bone histological features and functional biology in vertebrates, with a review of the evidence for the relationship and potential confounding variables for each histological feature. Nomenclature of quantitative morphometric measures follows [13].

Bone histological feature	**Potential correlations with functional biology**
Osteocyte lacuna number density (N.Lc/Ct.TV)	-Positive correlation with growth rate - related to bone formation rate in a range of tetrapods [70] though this may not hold for all vertebrates [102] -Negative correlation with body mass [103] -Loss of mechanical loading reduces osteocyte lacuna number density in rats [80], while compressive loading increases number of viable osteocytes in vitro [104] -Does not appear to be related to ageing in humans ($<$ 50 years vs. $>$ 50 years old) [74] -Skeletal location – osteocyte lacuna number density varies more between bones in an individual than between average individual osteocyte lacuna number density [62]
Mean osteocyte lacuna volume (Lc.V = Lc.V/N.Lc)	-Weak negative correlation with growth rate in birds and other dinosaurs [16] -Reduction in mean osteocyte volume with ageing (30% larger volume in younger human bone ($<$ 50 years vs. $>$ 50 years old) [74, 83] -Loss of mechanical loading reduces mean osteocyte lacuna volume in rats [80] -Weak positive correlation with body mass [16] -Positive correlation with genome size [20, 105]
Osteocyte lacuna surface area	-Positive correlation with growth rate, evidence both within birds and in comparison with other vertebrates [15]
Osteocyte lacuna shape	-Plump in fast-growing, flattened in slow-growing animals [17, 63] -Mechanosensory function – round are more mechanosensitive than flattened osteocytes in vitro [84] -Flatter and less spherical in younger human bone ($<$ 50 years vs. $>$ 50 years old) [106] -Dependent on skeletal location and histological section orientation [107]
Vascular canal number density (N.Ca/Ct.TV)	-Vascular canal number density decreases throughout growth in monitor lizards [94] -Correlated with body mass, related to diffusion distances from vasculature to bone cells for oxygen and respiratory waste products [69]
Mean vascular canal orientation (Ca.θ)	-Random in fast-growing, longitudinal and sometimes reticular in slow-growing animals [17], with a significant correlation with growth rate across archosaurs [69], though does not appear to be correlated in monitor lizards [94] -Radial canals correlated with faster growth in broiler chickens [108] -Perhaps related to mechanical strength of bone [71]
Collagen fibre orientation	-Random in fast-growing, highly organised in slow-growing animals [6] - differs between different bone types: perhaps disordered fibres can be deposited more rapidly [87] -Mechanical strains – related to direction of loading [88]

2.4 Current methods in palaeohistology

To date, most measurements of microstructural features have used traditional methods, typically light microscopy analysis of a single transverse thin section from a long bone [22]. Some studies have focussed on natural bone fractures and examined the structures at the surfaces of the fractures [38]. Thin sections have permitted quantification of the number of osteocyte lacunae seen in a single plane, or several planes in a small volume, and subsequent extrapolation to estimate the numbers in a set volume [89], enabling estimations of volume, surface area, and shape [64].

However, quantitative estimates of 3D variables, such as osteocyte number, from two-dimensional (2D) slices is difficult, particularly in a structure as anisotropic as bone [89]. This may account for some of the variability in osteocyte number counts described in the literature, especially as sample volume is critically important in obtaining reliable counts [17]. Estimates of mean osteocyte or osteocyte lacuna volume are also likely to be inaccurate as their shape is modelled as spheres or ellipsoids but again is seldom isotropic [16]. Viewed in different planes, osteocytes and osteocyte lacunae can appear in different shapes [107]. Recently, different cutting planes have been used to capture more of the 3D shape of osteocyte lacunae [16], yet, it is important to note that these estimates still lack the accuracy (and precision) of a true 3D measurement. Similarly, while estimates have been attempted at number density and orientation of vascular canals [6, 109], canal orientation is difficult to distinguish from shape in individual sections [14, 18, 23]. Finally, connectivity is especially difficult to quantify [5], while assessment of collagen networks using cross-polarised light can be similarly challenging [17].

Serially ground sections through a sample can theoretically be reconstructed virtually to produce a 3D image, however, the destructive and time-consuming nature of such procedures have precluded widespread adoption [110]. Therefore, a non-destructive 3D imaging technique enabling bone microstructure analysis at the cellular level is important.

2.5 3D visualisation of bone microstructure using micro-computed tomography

Within the biomedical field a number of destructive and non-destructive 3D imaging techniques exist to study the microstructure and ultrastructure of bone [4, 111]. Although some of these techniques are restricted to soft or modern tissue (particularly techniques that rely on staining proteins in cells or translucency of the tissue), others can be applied successfully to fossil material. Micro-computed tomography (μ-CT) in particular exhibits significant potential for quantitative, 3D virtual histology in bone tissue [13, 71, 80, 82, 112]. Indeed, μ-CT is becoming more widespread in palaeobiology. μ-CT is typically applied at relatively low spatial resolutions to capture overall fossil morphology without excavation [113] or to capture the internal morphology of structures such as the braincase [114]. μ-CT uses X-rays to distinguish materials of different radio-densities in a series of radiographs, which are subsequently reconstructed in 3D [115], enabling 3D quantitative volumetric and structural assessment from segmented data (Figure 2.5).

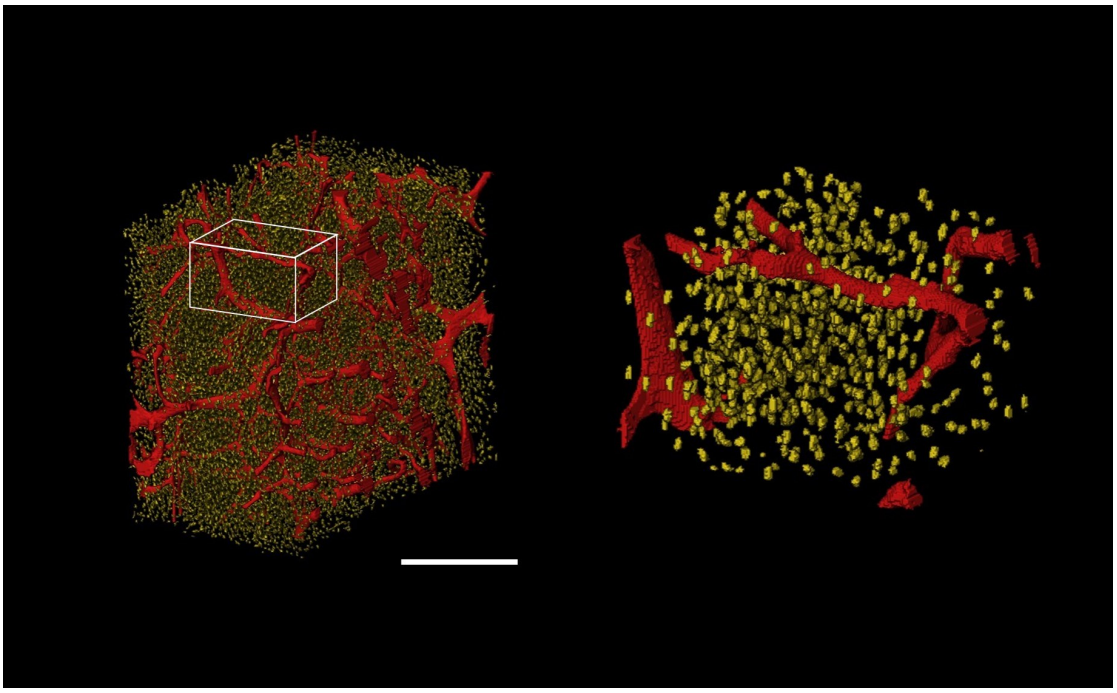

FIGURE 2.5: Duck (*Anas platyrhynchos*) tibiotarsus cortical bone sample imaged using synchrotron radiation-based CT. Duck was 3 months old at time of death. Segmented intracortical canals are shown in red and osteocyte lacunae in yellow. (A) Region of cortical bone (B) Highlighted region from (A) at higher magnification. Data collected at TOMCAT beamline of the Swiss Light Source (0.65 μm voxel size at an energy of 18.5 keV). Scale bar is 200 μm.

Medical CT scanners have been used in palaeobiology, although, their relatively low spatial resolution ($>$ 0.1 mm) preclude their use for imaging bone microstructures. In contrast, lab-based μ-CT systems are capable of producing 3D images at micrometre resolutions, ideal for studying the internal microstructure of fossil bone. Commercially available μ-CT systems are available that provide sub-micrometre voxel sizes and spatial resolutions around 1 μm, but they are limited by the time required for image acquisition. While typical μ-CT imaging systems reach the required spatial resolutions for histological study ($\approx$1-10 μm) the limited X-ray flux available from lab-based tube X-ray sources may not provide a sufficient signal-to-noise-ratio if prohibitively long scanning times of many hours up to a day and more are inacceptable, particularly in dense fossil material [110]. This issue can be addressed by using a synchrotron source as X-ray source. A synchrotron radiation source provides orders of magnitude greater X-ray flux (and coherence) compared to a conventional X-ray tube. Generally speaking, high-resolution images at very good signal-to-ratio levels are provided by synchrotron radiation source-based CT, even for fairly dense samples (see Figures 2.5 and 2.6) and, importantly, at a fraction of the time needed using lab-based μ-CT systems (a few minutes vs. hours up to a full day for scans around spatial resolutions in the μm range and below), facilitating high-throughput and thus allowing sufficient sample numbers for reliable quantitative analysis. For example one could image one hundred samples in 48 hours to be imaged, given the right experimental settings at a synchrotron, compared with single digit sample numbers using a lab-based system during the same time frame. One important consideration for high-resolution 3D imaging, though, is that the volume of data generated for even a single sample is substantial and the challenges in image processing and data management are significant. Nevertheless, the

advantages of 3D, non-destructive imaging mean an increasing number of palaeobiologists are turning to μ-CT [24, 25, 115].

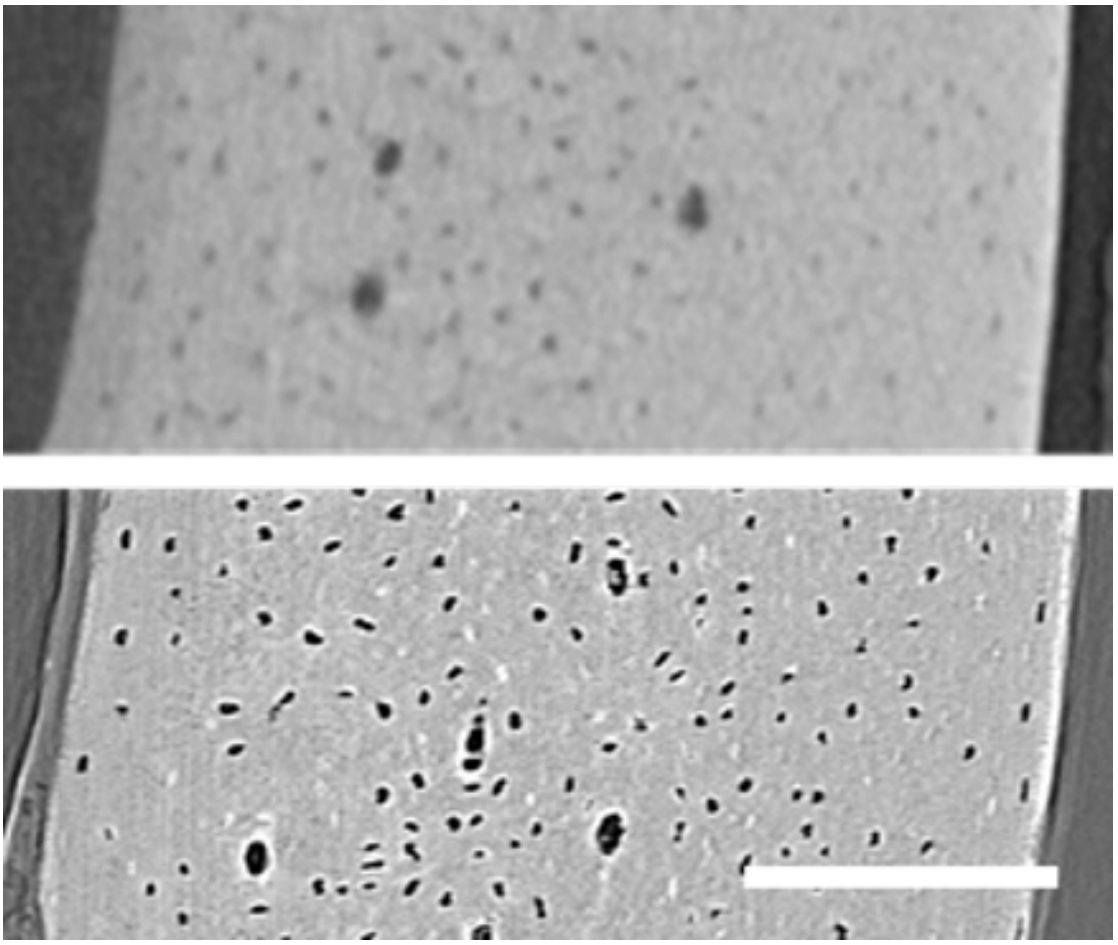

FIGURE 2.6: Midshaft section of pigeon (*Columba palumbus*) tibiotarsus imaged using high-resolution CT. (A) Data taken on a lab-based μ-CT system (Versa 510; Xradia/Zeiss) at 1.7 μm voxel size. osteocyte lacunae can be identified, but they are difficult to segment due to the limited spatial resolution and the rather low signal-to-noise ratio. (B): Data taken at TOMCAT beamline of the Swiss Light Source (0.65 μm voxel size at an energy of 18.5 keV). Osteocyte lacunae are clearly visible and can be segmented straightforwardly. Osteocyte lacunae (LC), vascular canals (VC). Scale bar 100 μm.

It is important to note that not all fossils will allow for high-quality CT data as the image contrast for this technique relies on the features present absorbing X-rays to a greater or lesser extent. Therefore, fossils forming from rock of similar X-ray radio density to the surrounding rock may not be suitable for CT imaging. Contrast can be enhanced using, for example, phase contrast imaging which uses differences in X-ray refraction rather than X-ray absorption [24], expanding the range of samples that can be imaged. Samples with high-density minerals can be problematic to image, due to full X-ray absorption or photon starvation, but are not impossible given sufficiently high X-ray energies, although increasing X-ray energy in order to penetrate the sample will lead to reduced image contrast.

In addition, the highest spatial resolutions below the micrometre range demand small sample sizes due to the inherent trade-off between spatial resolution and field of view. Although it is possible to perform local tomography of larger samples, where only a portion of the specimen is assessed, this introduces artefacts and detrimentally affects CT image quality. In the worst cases

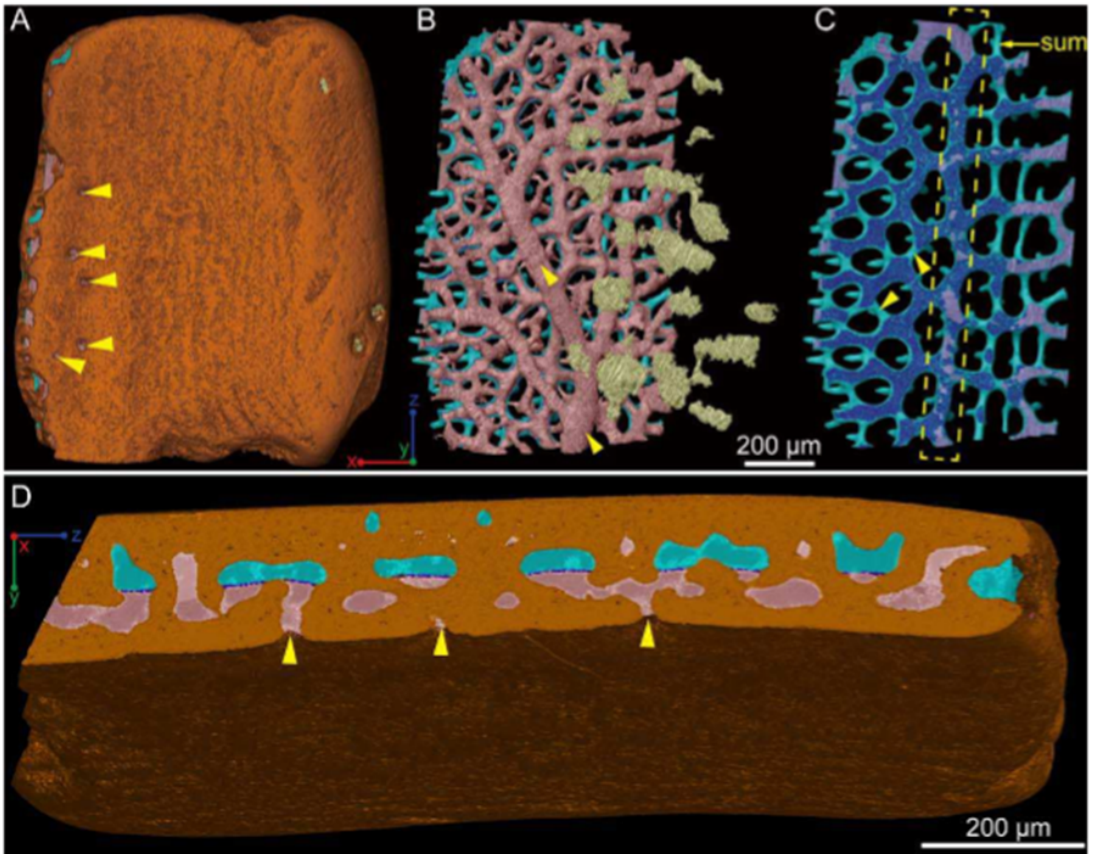

FIGURE 2.7: Synchrotron-based computed tomography for 3D virtual histology in fossil osteostracan scales. 3D visualisation of canal networks and their connectivity within scales led to reinterpretation of previously described morphologies, changing functional and developmental interpretations. Image from [5] with kind permission of Journal of Morphology, Wiley Periodicals Inc.

this can result in severe photon starvation or even complete X-ray absorption. This limitation acts on the longest, rather than the shortest, axis of a sample, making large flat fossils challenging to scan. Thus, the optimal sample for CT scanning is a small shard or bone core rather than an entire fossil specimen, at least for larger specimens. Nevertheless, new advances in laminographic techniques, which use a smaller range of rotation angles compared with conventional CT to capture 3D information particularly in large, flat samples, may improve imaging of awkward specimens [116], and both lab-based and synchrotron-based CT technologies are continually improving.

2.6 Multimodal approaches: combining old and new methods

Segmentation of CT data can be subjective. Thus, a dual approach combining histology and CT is ideal, where histology provides information on the soft tissues in modern material (including blood vessels and osteocytes) and regions of low X-ray contrast, which are difficult to discern in X-ray (absorption-based) CT, whereas CT provides bone tissue structure and architecture in 3D in a non-destructive manner. Therefore, even with high-resolution 3D imaging available, it may

still be worthwhile producing a small number of thin sections in order to compare with published literature and confirm that the structures appear as expected, particularly in samples where X-ray radio density is more homogeneous across the sample and image contrast in the reconstructed CT data is therefore reduced. However, the need for this type of validation may be reduced as non-destructive techniques are more widely adopted and further refined.

2.7 Conclusions

1. The microstructure of cortical bone has long been recognised as having the potential to be used to estimate age and growth rate, and to inform the understanding of metabolic rate and life history in birds.

2. Examination of developmental age, growth rate, metabolic rate, and life history is critically important for understanding the biology, evolution and classification of birds. For example, distinguishing between adult and juvenile specimens is key in clarifying classification and interpretations of palaeobiology.

3. A number of methods exist for estimating developmental age in fossils, from gross morphology and growth series to incremental growth lines and other microstructural features. However, while some of these methods are effective in other vertebrate taxa, no reliable method has yet been developed in birds.

4. Development of validated methods to assess age, growth rate, life history etc. in birds will rely on a better understanding of bone deposition and remodelling in modern birds. Our current understanding supports a correlation between, for example, the structure of bone vasculature and age/growth rate. The causes of variation in other features such as osteocyte lacuna number density and shape are currently poorly understood. Further study is required to fully understand the relationships between bone microstructure and biological, mechanical, and life history traits informative of avian palaeobiology.

5. Current methods in palaeohistology limit the number of fossils whose microstructure can be studied, as creating thin sections is destructive. In addition, basing microstructural interpretations of complex 3D tissues on 2D thin sections is inherently problematic and may cause a lack of precision and accuracy in estimations of, for example, age.

6. High-resolution CT (μ-CT and synchrotron radiation source-based CT) offers significant potential to inform our understanding of the relationship between bone growth, age, and microstructure in fossil birds in a non-destructive and reproducible 3D fashion. Thus, new vistas await to determine age and growth rate, clarifying hypothesised relationships which have not been possible to examine to date and, critically, relate these to findings from biomedical sciences [74, 80, 82–84]. It is worth noting that a high-throughput approach will enable large-scale studies to be undertaken, providing information, currently limited, not only on the life histories of extinct birds but also their population structures and ecology [117]. Furthermore, if similar studies were undertaken non-destructively, then a far greater number of fossil specimens (including rare specimens) could be studied histologically, the large assemblage of *Confuciusornis sanctus* to clarify the source of controversial size range (age-related, species-related or sexually

dimorphic) [45, 46, 118] for instance. These types of studies would allow us to study Mesozoic birds as living animals in an ecological setting.

In summary, advances in our understanding of avian evolution and the biology of Mesozoic birds will necessitate an interdisciplinary approach, harnessing knowledge and techniques from biomedical and engineering sciences to progress palaeobiology. For optimal use, it will be necessary to develop effective 3D imaging techniques, to validate such approaches using conventional 2D approaches, and to subsequently test hypotheses in longitudinal studies of modern birds where development is well-understood, before applying to fossil material. Nevertheless, such approaches directed at quantitative and 3D methods have exciting implications for understanding the palaeobiology of birds.

Chapter 3

Methods

3.1 Introduction

This project combines a number of different methods to interrogate the microstructure of avian bone in relation to developmental age, body mass, and life history, including CT scanning at high spatial resolutions, image processing and quantification, and traditional histological methods for validation of CT scans.

The region of interest for scanning was decided as the midshaft region of the long bones, as this is most commonly described in histological literature [22]. The bones selected were the tibiotarsus and femur (bones of the leg) and the humerus (a wing bone) (Figure 3.1), in order to compare the upper and lower limbs which carry out different biomechanical functions in birds.

Most of the data used in this project are synchrotron-based μ-CT scans, but validation has used other methods, including lower-resolution lab-based μ-CT and histological sectioning. Pilot CT experiments were carried out for optimisation of imaging techniques to allow 3D, non-destructive imaging of avian cortical bone and histology to validate the structures observed in scans.

This methods section provides a general introduction to the methods and samples used in the

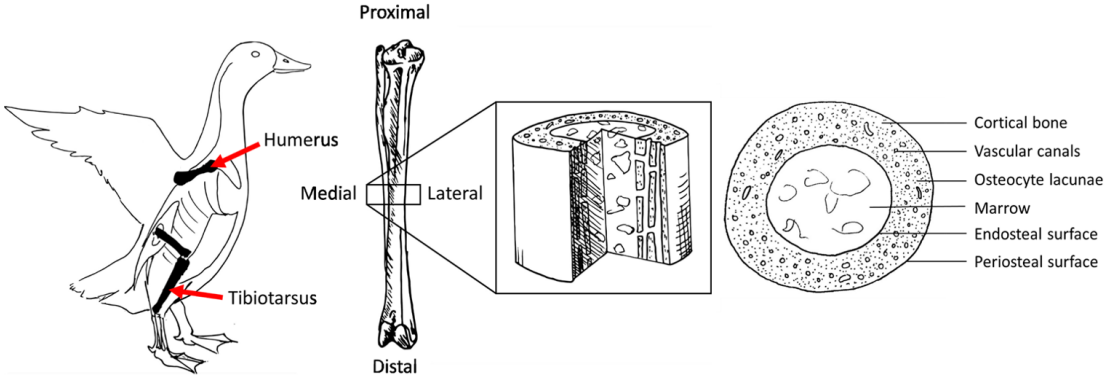

FIGURE 3.1: Region of interest for scans.

project, including samples used, sample preparation, sample mounting, imaging, image segmentation and analysis, and covers optimisation of these methods. Some more specific details may be repeated or only included in results sections where appropriate, for example settings for specific CT scans which may differ from the general methods.

3.2 Samples

Samples of modern avian bone were obtained from a number of sources. No birds were raised or killed specifically for this project.

For initial pilot experiments, fresh samples of wood pigeon (*Columba palumbus*) were purchased from a butcher (The Wild Meat Company, Suffolk, UK).

Naturally deceased fresh samples of domestic ducks, of the Cherry Valley variety (a Mallard x Peking cross of *Anas platyrhynchos* produced commercially for egg-laying) were donated by Warawee Duck Farm, Pollards Moors Road, Copythorne, Southampton, Hampshire. Samples included 21 ducks and ducklings across the entire developmental range from 1 day after hatching to two years old (Table 3.1). The exact ages of some samples were known (1 at 1 day old, 1 at 6 weeks old, 1 at 3 months old, and 3 at 2 years old) but the ages of the others were not and therefore their ages were estimated by extrapolating between the 1 day old individual and the 6 week old individual, assuming linear growth between the ages of 1 day and 6 weeks. For this study, it was important that the individuals are kept in similar conditions so that the influence of environment on growth rate is reduced. Therefore, animals were sourced from a single farm, and all ducks hatched on the same day.

TABLE 3.1: Duck samples used in growth series grouped into size/age classes

Age class	No. ducks	No. pheasants
1-7 days	7	0
8-14 days	1	3
15-21 days	5	1
22-28 days	2	0
29-35 days	1	3
36-42 days	1	3
43-49 days	3	0
Subadult	1	2
Adult (2 years)	3	0

Naturally deceased fresh samples of pheasant and partridge (*Phasianus colchis* and *Alectoris rufa*) were donated by Blackmoor Game Farm, Hampshire. Samples included 10 juvenile pheasants across the developmental range from 2 weeks after hatching to 6 weeks old (Table 3.1). The ages of the samples (in weeks) was recorded by the farm, and the body masses were measured.

Two adult pheasants and an adult red-legged partridge (*Alectoris rufa*) were kindly donated by Matt MacGregor-Sharp, University of Southampton, UK.

Fresh samples of ostrich (*Struthio camelus*) were purchased from a butcher (The Exotic Meat Company).

Dry bone samples from starling (*Sturnus vulgaris*) and rock dove (*Columba livia*) were loaned from the University of Southampton Osteoarchaeology Reference Collection.

Subfossil samples of the extinct elephant birds *Mullerornis* and *Aepyornis* were provided by James Hansford, thanks to the Natural History Museum, University of Oslo and the Museum National d'Histoire Naturelle, Paris.

A fossil specimen of *Lithornis*, a small, flighted, Eocene palaeognath from the London Clay in the Isle of Sheppey, UK, was kindly loaned from the private collection of Mark Jobling.

Am Ordovician fossil echinoderm (*Pleurocystites*), and an unidentified bird tarsometatarsus from Pleistocene deposits in Dixie County, Florida, was loaned from the private collection of Neil Gostling.

3.3 Sample preparation

On receipt, fresh bird samples were weighed and stored at -20°C then thawed overnight before dissection. Thawed bone samples (tibiotarsus, femur and, in most cases, humerus) were dissected out and cleaned of soft tissue. They were cut into pieces small enough to fit into the limited field of view for high-resolution scanning (approximately 2 mm) using a low-speed saw (Buehler Isomet, Essligen, Germany). Samples were fixed in 4% formaldehyde for at least 48 hours then then stored in 70% ethanol. Before scanning, samples were removed from ethanol.

Samples from the archeological reference collection were left undamaged.

For the *Lithornis* fossil, 4 mm sections were cut from the exposed ends of the humerus and tibiotarsus using a handheld rotary tool.

Matchstick shaped samples were cut from the elephant bird and ostrich samples using a low-speed saw (see Chapters 6 and 7). As the cortical thickness of these samples was greater than the field of view required for CT scanning, these matchsticks were cut across the cortex (periosteal to endosteal), allowing the whole cortex to be scanned by joining multiple scans.

3.4 Histology

In order to validate the 3D imaging methodologies used in this thesis, the images were compared to traditional histological sections taken from the same specimens and stained in order to visualise the different cells and tissues in the section.

Histological techniques are used to visualise tissues in 2D by cutting into thin tissue sections. Sectioned tissues can then be stained with various dyes and immunostains, allowing the locations of specific materials, such as nuclear material (stained by haematoxylin), to be visualised and structures identified.

Unlike CT scanning, which can be carried out non-destructively on whole samples, histological sectioning requires a great deal of sample preparation before good-quality sections can be produced. For paraffin histology, tissue must first be fixed, stabilising structures by, for example, cross-linking proteins using a fixative such as formaldehyde; otherwise soft structures tend to degrade.

After fixation, samples must be embedded in a solid medium to allow thin sections (typically 5-7 μm) to be cut. Paraffin will not infiltrate a hydrated sample as it is immiscible with water. Therefore samples must be dehydrated, removing any water gradually by replacement with alcohols in increasing concentrations, then the alcohol removed using a hydrophobic clearing agent before infiltration with molten paraffin. Then the sample can be embedded in moulds in additional paraffin wax, which provides a good base which can be cut using a microtome. For mineralised tissue such as bone, cutting with a standard microtome is not feasible. Mineralised bone can be cut using a heavy duty microtome if embedded in resin rather than paraffin [119], but more commonly is decalcified before processing, using either slow, gentle decalcifying agents such as Ethylenediaminetetraacetic acid (EDTA) or more rapid but harsher agents such as nitric acid. After cutting, sections are mounted onto glass slides and dried.

Then, stains can be applied: the most common general purpose histological stain is haematoxylin and eosin (H and E), but useful for distinguishing bone and cartilage is Alcian Blue and Sirius Red (A and S). Although histology only works in 2D and can be spatially distorted due to the cutting process, it can help to identify and separate structurally similar but functionally different structures. Here, histology is used to validate microstructural features in CT datasets, such as osteocyte lacunae and vascular canals, and to identify the soft tissue within bone porosity. For this, a combination of Weigert's haematoxylin, Alcian Blue and Sirius Red stains are used [120]. The nuclear stain (haemotoxylin) is used to identify cell nuclei and therefore whether pores are occupied by cells, and to study the distribution of cells within the bone and marrow. Bone tissue, or the mineralised tissue shown in CT scans, is stained using Sirius Red, which will stain for collagen. In the younger bone, it is useful to be able to distinguish this from cartilage. Cartilage is rich in proteoglycans, components of the extracellular matrix which provide structural and osmotic functions in cartilage [121], which are stained by Alcian Blue.

Additionally, H and E staining was used to examine structures and directly compare with CT data.

Here, the following protocols were followed.

3.4.1 Decalcification

Bone samples were decalcified in 5% EDTA in tris(hydroxymethyl)aminomethane (Tris) on a roller to maintain agitation. EDTA solution was removed weekly and replaced with fresh solution. X-ray was used to test for complete decalcification: if any mineral was still present this was visible as a point of X-ray density. Here this took 3 weeks to completely disappear from the thickest parts of the samples.

3.4.2 Embedding

Samples were dehydrated through a graded series of ethanol to remove water gradually, reducing tissue distortion, and the ethanol was then removed using the hydrophobic clearing agent Histo-clear (National Diagnostics), which also removes much of the fat present; this may otherwise act as a barrier to wax penetration. Samples were then placed into each of the following solutions for 40 minutes before being transferred to the next:

1. 90% ethanol in dH_2O
2. 100% ethanol
3. 100% ethanol
4. 50% ethanol/50% Histo-clear
5. Histo-clear
6. Histo-clear
7. Incubation for 1 hour in molten paraffin wax (Leica Biosystems)at 60°C

Infiltrated samples were mounted in larger wax blocks for histological sectioning.

3.4.3 Sectioning

Wax blocks were sectioned to 7μm sections using a microtome then the paraffin sections were mounted onto glass slides using a heated water bath. Slides were dried thoroughly and stored at 5°C.

3.4.4 Staining

Slides were rehydrated through Histo-clear and then a grades series of ethanol washes (100%, 90%, 50% in dH_2O). They were then stained with Weigert's Haematoxylin and Alcian Blue/Sirius Red, which indicate deposition of proteoglycans and collagen respectively.

Alternatively, slides were stained with haemotoxylin and eosin, for nuclear material and general tissue staining respectively.

Stained sections were dehydrated through graded ethanols and Histo-clear then mounted with the mounting medium DPX (distyrene plasticizer xylene) (Fisher Scientific, UK).

3.5 Lab-based μ-CT

3.5.1 Whole bone imaging

Whole bones were scanned using an *in vivo* micro-computed tomography (μCT) system (Skyscan 1176; Bruker μCT, Kontich). This lab-based CT system is designed to be used *in-vivo*, mostly for mice and rats. It is therefore optimised for imaging bone and soft tissue at the scales of small animals and is ideal for imaging the avian bone samples with comparable sizes to rodent bones. Inside the scanner, the sample is placed onto a carbon-fibre bed and remains stationary while the source and detector rotate around the sample to capture X-ray projections at different angles between 0°and 180°.

The X-ray source generates a polychromatic beam (X-rays generated at various wavelengths or energies), which can cause beam-hardening artefacts due to differential X-ray absorption at different wavelengths by the sample so that lower energy X-rays are absorbed to a higher

degree [122]. This can cause reconstructed regions away from the center of the sample to appear more X-ray opaque than they are, making density quantification inaccurate across a sample. To reduce beam-hardening artefacts, and other polychromaticity artefacts such as streaking around hard objects, the beam is 'pre-hardened' using a filter made out of metal, for instance. The thickness and material of the filter depends on the energy used, where the ideal X-ray for CT imaging depends on the density and size of the sample. A larger and highly X-ray opaque sample (for example a fully mineralised bone) will need a higher energy and a thicker filter than a small and more X-ray transparent sample (such as bone tissue that is only partially mineralised.

Samples were scanned at 18μm voxel size. This voxel size is sufficient to identify trabeculae and large intracortical canals and therefore can be used for measuring cortical thickness and other bone dimensions, and measure bone mineral content (BMC) though not the fine network of small intracortical canals or LC. Bones were scanned at 45kV and 552μA using a 0.25mm aluminium filter.

CT datasets were reconstructed using Bruker's NRecon software (v.1.6.4.6, Bruker μCT, Kontich) and visualised using their CTVol software (v.2.3.1.0, Bruker μCT, Kontich).

3.5.2 Imaging cortical microstructure

The smallest achievable voxel size using the Skyscan system is 9μm, which is too large to be able to identify osteocyte lacune (approx 7 μm across) and is unlikely to be able to capture the microvasculature within the bone cortex (approx 10 μm in diameter). Therefore, to image these structures in a lab-based system at sufficient spatial resolutions, a different μCT system is used (Versa 510; Zeiss/Xradia). Unlike the Skyscan system, which is optimised for *in vivo* scanning and therefore aims to minimise the X-ray radiation dose, the Versa system can be operated at higher energies and exposure times. It can achieve sub-micrometre resolutions, allowing cell spaces and intracortical canals to be visualised.

For scans undertaken on the Versa/Xradia lab-based CT system, samples were embedded in paraffin wax inside a plastic tube fixed to an aluminium SEM stub to prevent movement. This setup allowed all three samples to be mounted in one setup and the position of each recorded. A spatial resolution of 1.7 μm and energy of 20 KeV were chosen, with 360°rotation to increase the field of view. Each scan required approximately 24 hours.

3.6 Synchrotron-based μ-CT (SR CT)

Lab-based CT sources can reach sub-micrometre resolutions and can be used to penetrate even very dense materials such as rock or metals. However, as mentioned before, they can suffer from beam-hardening artefacts due to the polychromatic nature of X-ray sources and, in addition, can require very long scan times for achieving sub-micromentre resolutions at satisfactory SNR. These problems can be overcome by using a synchrotron X-ray source rather than a lab-based source. A synchrotron beam uses an electron accelerator to generate (typically monochromatic) X-rays of far higher flux and brilliance than a lab-based source [24], which

allows for quick scans (a few minutes) at sub-micrometre resolutions and SNR levels, which are sufficient to segment osteocyte lacunae and intracortical canals.

In this project, CT datasets have been collected at two different synchrotron sources: the TOMCAT beamline at the Swiss Light Source (SLS, Paul Scherrer Institut, Villigen, Switzerland) and I13-2 beamline at Diamond Light Source (DLS, Harwell), and sample mounting and imaging setup was optimised at each separately.

3.6.1 Sample mounting

For initial pilot scans, carried out at SLS, samples were dried for several days in air after fixation (see Sample preparation) in order to make mounting more straightforward. The samples were glued to (mostly X-ray transluscent) carbon rods which could be mounted directly into the sample holder at TOMCAT. The glue and carbon rod that ensure no movement is possible during scanning. However, samples dried in air cannot reasonably be used for histological sectioning later (used for validation) as the sample dries and soft tissue shrinks.

Therefore, it was necessary to mount the samples in the beam without them drying, so that the same samples could later be sectioned and stained for comparison between histology and CT imaging. The were samples onto the lids of 1.5ml tubes (Eppendorf) using a soft wax (beeswax) which, for hard samples, can be moulded by hand, and for more delicate samples the wax can be melted using a soldering iron or equivalent and then left to set. The lids with the samples attached were then mounted using the same wax onto aluminium stubs and the body of the tube placed over the lids to create a humidity chamber to reduce drying (Figure 3.2). This solution is rapid to implement and samples were mounted firmly preventing sample movement (Figure 3.3). Visually, drying appears to be minimal as pores throughout the sample remain filled with soft tissue or fluid and no shrinkage is seen away from the mineralised tissue, except perhaps in some pores around the edge where there the extra edge enhancement suggests greater X-ray contrast and therefore perhaps these pores are air-filled rather than ethanol-filled (Figure 3.3). Given that these apparently drying pores are few and near to the edges, it was concluded that drying was minimal, allowing later histology to be carried out (see Histology).

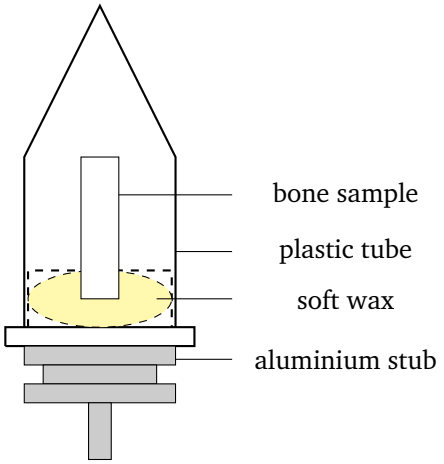

FIGURE 3.2: Humidity chamber setup.

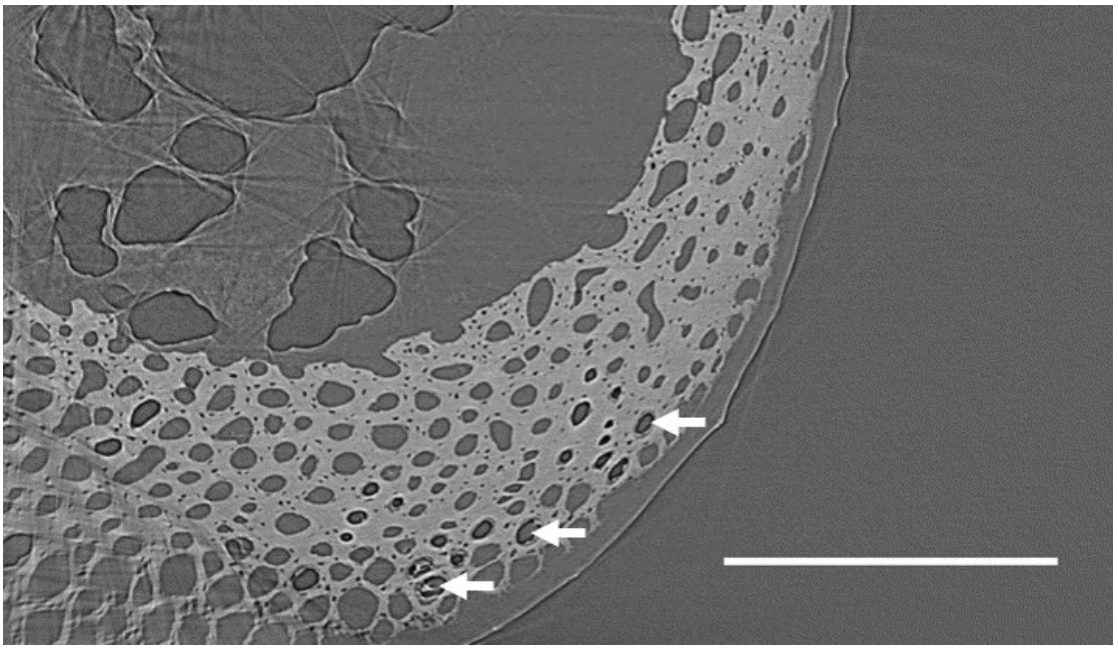

FIGURE 3.3: SR CT scans of duckling tibiotarsus midhsaft bone using humidity chamber setup shown in Figure 3.3. Arrows indicate potential drying within pores. Data taken at TOMCAT beamline, SLS. 0.65 μm voxel size. Scale bar = 200 μm

Material from the Osteoarchaology collection, on the other hand, is dry, and it was necessary to mount them in such a way that the samples were not damaged. Again, soft wax worked best for sample mounting as it could be moulded with only the warmth from hands and sets hard very rapidly. At hand-moulded temperatures, the wax did not mark the bone, therefore was non-damaging and could easily be removed.

3.6.2 Imaging optimisation

3.6.2.1 Optimisation at the Swiss Light Source

The Swiss Light Source (SLS) has a storage ring which operates at 2.4 GeV, which is used to power 14 different beamlines. Tomographic experiments are carried out at TOMCAT beamline and researchers from Southampton have been working at TOMCAT on bone and other mineralised tissue for some years now. Therefore, bone imaging optimisation taken place (by Juan Núñez, Elis Newham and coworkers) could be implemented and only minor optimisation was required. At TOMCAT a monochromator is used to filter X-rays to a single energy, removing beam hardening artefacts.

An energy of 18.5 KeV was used and pilot scans were carried out at 0.65 μm voxel size. Later scans used a voxel size of 1.6 μm in order to fit the samples within the field of view in a 180°scan.

Initial scans were carried out at 150 ms per projection exposure, but this did not exploit optimally the detector's dynamics so this was increased to 180 ms. 1500 projections were acquired, which was based on the sample width rather than the detector width as samples did not fully fill the field of view.

Some scans were also carried out at higher resolution (voxel size 0.33 μm), to allow more accurate measurement of osteocyte lacuna shape and volume in a smaller total bone volume.

3.6.2.2 Optimisation at Diamond Light Source

The Diamond Light Source (DLS) has a larger storage ring than SLS, and runs at 3GeV. In these experiments, tomography is carried out at the beamline I13-2.

The beam at I13-2 is not yet fully monochromatic: there is a multilayer monochromator which in theory can produce a monochromatic beam but this is still in testing phases and was found to be too unstable to produce high-quality images. Therefore the pink beam (nearly monochromatic) was used. This still produced far less beam-hardening than lab-based CT.

A parameter sweep was carried out to find the optimal image settings for identification of osteocyte lacunae and vascular canals while maintaining reasonable scan times. The settings chosen were a voxel size of 1.6 μm, 20KeV energy, 0.15s exposure time per projection, and a sample to detector distance of 20 mm.

However, it was later decided that the signal-to-noise-ratio (SNR) in the scans carried out in the first DLS beamtime could be improved and therefore for the second beamtime, initial voxel size was changes to 0.8 μm, and the voxel sizes were increased later to match the datasets from the first session by pixel averaging across the image, which also improved the SNR.

3.6.3 Reconstruction

Raw CT data is collected in the form of a series of radiographs. In order to reconstruct these images as a 3D volume, Fourier-based reconstruction algorithms are used to calculate a stack of slices perpendicular to the original radiographs. Ring artefact reduction was applied at the reconstruction stage at SLS.

3.6.4 Comparison with lab-based scans

Initial experiments were carried out to test the principle of using of μ-CT in virtual osteohistology. Avian bone has not previously been imaged at resolutions sufficient to carry out histology using CT and therefore optimisation was required. In addition, image quality from lab-based X-ray sources was compared with that of a synchrotron source. In theory, lab-based and synchrotron X-ray CT systems can reach similar sub-micron resolutions, a requisite for imaging features such as osteocyte lacunae which measure approximately 7 μm across. However, a lab-based X-ray source produces X-rays of far lower flux and brilliance than a synchrotron beam, which uses a particle accelerator to produce X-rays [116]. The difference in brilliance between the systems allows the X-rays produced by a synchrotron system to be filtered to a monochromatic beam. In contrast to the polychromatic light of a lab-based CT system, a monochromatic beam does not produce beam-hardening artefacts so a synchrotron source is able to produce images of higher quality and also signal to noise ratio. Furthermore, the scan times required for the highest resolutions are orders of magnitude greater using lab-based CT than synchrotron-based CT, making imaging robust sample sets less feasible.

However, lab-based sources are widely available and methods developed using these systems are available to a larger number of researchers.

Therefore, an investigation was carried out to test whether a lab-based system could produce images of sufficient quality to accurately segment osteocyte lacunae and within reasonable timescales, enabling measurement of a large number of samples, or whether a synchrotron source was required. To address this issue, a sample of modern adult avian tibiotarsus (wood pigeon *Columba palumbus*) was scanned using the Versa/Xradia system at μ-VIS Southampton and compared with scans taken at TOMCAT beamline, SLS.

It was found that the Versa/Xradia scans produced high-quality images at 1.7 μm spatial resolution, which showed all of the features of interest: osteocyte lacunae could be identified and vascular canals segmented. However, the spatial resolution and signal-to-noise ratio were too low to enable accurate segmentation of the osteocyte lacunae (Figure 3.4).

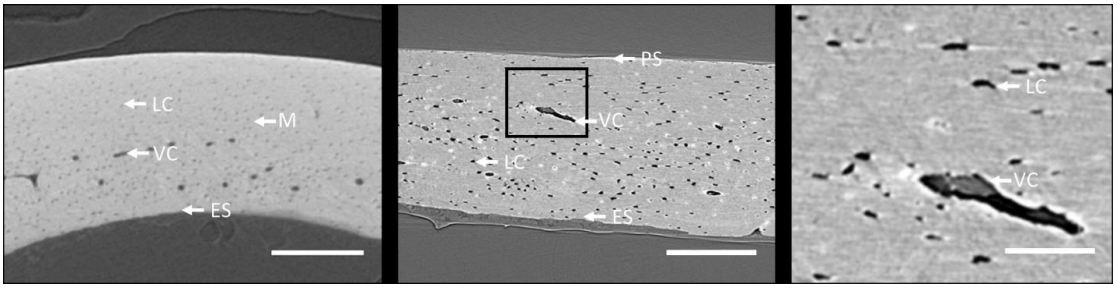

FIGURE 3.4: Midshaft section of pigeon (*Columba palumbus*) tibiotarsus imaged using high-resolution CT. (Left) Data taken on a lab-based μCT system (Versa 510; Xradia/Zeiss) at 1.7 μm voxel size. LC are identifiable but difficult to segment due to the limited spatial resolution and the low signal-to-noise ratio. (Middle and right) Data taken at TOMCAT beamline of the Swiss Light Source at 0.65 μm voxel size. (Right) Highlighted region at a higher magnification. LC are clearly visible and can be segmented straightforwardly. (Left and middle and right) (LC) osteocyte lacunae, (VC) vascular canals, (ES) endosteal surface, (PS) periosteal surface, (M) bone matrix. Scale bars are (left and middle) 200 μm and (right) 50 μm.

Images produced at TOMCAT beamline, SLS had a greater signal-to-noise ratio than the lab-based scans due to higher flux and the edges of both osteocyte lacunae and vessels are clear and sharply defined (Figure 3.4). Images could be segmented accurately and with relative ease and, crucially, each scan was completed in a short timeframe (minutes) in contrast to the lab-based scans that required close to a full day.

These initial studies indicate a synchrotron source is more appropriate than a lab-based source for analysis of avian cortical bone microstructure, given the improved image quality, enabling enhanced quantification and, crucially, enhanced throughput leading ultimately to a high-volume, robust and quantitative approach.

3.6.5 Validation of structures using histology

A selection of reconstructed scan data was compared with histological sections taken from the same sample. Where possible, the exact slice was matched. Some sections were stained with A/S (Figure 3.6), which highlights new bone deposition, and some with H/E (Figure 3.6), a more general tissue stain to study the overall structure and demonstrate the CT images are comparable to histological sections.

It was found that the CT images were highly comparable to histological sections, and the mineralised regions could reliably be identified as bone. In some scans, soft tissue was also visible, but would not be mistaken for bone given its very different grey values. It was therefore concluded that CT could provide an accurate structural representation of mineralised bone tissue.

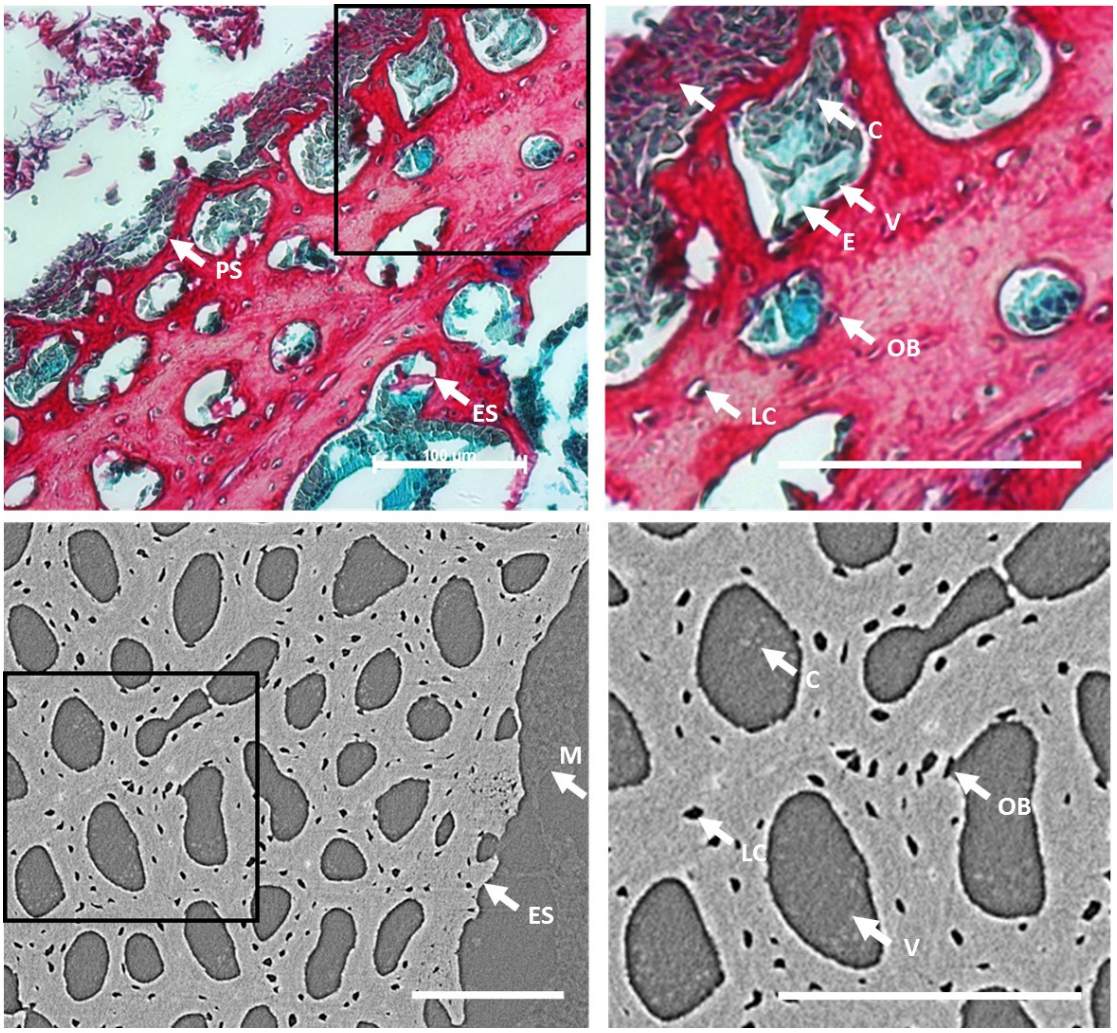

FIGURE 3.5: Comparison between conventional histological section and virtual histological section based on SR CT. (Top) Transverse histological section of cortical bone in a duckling tibiotarsus, stained with Alcian Blue and Sirius Red (A/S). 20x magnification. SR CT images of a duckling tibiotarsus midshaft at the same scales. Voxel size 0.33 μm. The virtual section is comparable in quality and resolution to conventional histological sections, but is not affected by distortion. PS Periosteal surface, ES endosteal surface, V blood vessel, C cells, M bone marrow, OB osteoblasts (some being trapped in bone matrix), E possible erythrocytes. Scale bars 100 μm.

3.6.6 Segmentation of pores

In order to quantify and visualise in 3D the cortical microvasculature and osteocyte lacunae, these pores were first defined as objects using the SR CT data. SR CT data from TOMCAT were processed in Fiji/ImageJ[123, 124], an open source free image processing software which works well for batch processing samples. Additional packages were also used from the BoneJ

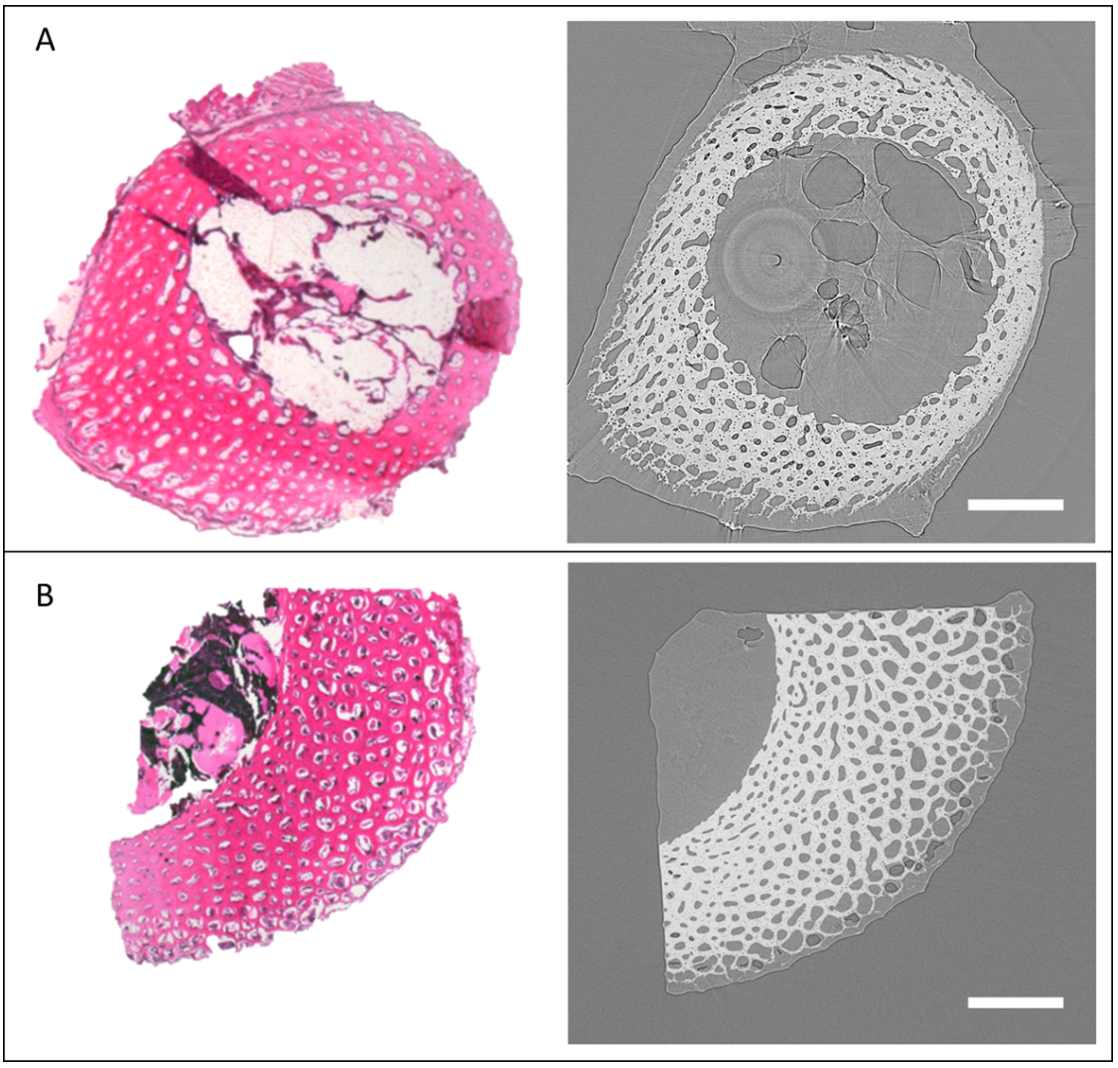

FIGURE 3.6: Matched conventional histological section and virtual histological section based on SR CT. (Left) Transverse histological sections of cortical bone in a duckling tibiotarsus, stained with H and E. 10x magnification. (Right) SR CT images of a duckling tibiotarsus midshaft at the same scales. (A) Sample from a 1 day old duckling (B) sample from a 3 week old duckling. Voxel size 1.6 μm. The virtual section is comparable in quality and resolution to conventional histological sections, but is not affected by distortion. Scale bars 500 μm.

plugin for ImageJ [125], a set of functions which is designed to facilitate quantitative analysis of 3D bone image data.

The first step in producing a segmented 3D model from CT data is to create a binary dataset from the greyscale CT dataset. This is done using, in this case, a fixed threshold value: voxels with grey values above the threshold value are 'on' and voxels below the threshold value are 'off'. The threshold is used to separate mineralised regions from air, liquid, or soft tissue as they have distinct X-ray absorption, defining the region classified as 'bone'.

For this project, the features of interest are not the bone itself but the pores and canals within the bone. These are defined, using the threshold value, as the same as background, so further steps must be taken to separate them from the background and define them as objects (summarised in Figures 3.7, 3.8, and 3.9). To do this, the cortical bone region is defined using a solid mask.

The solid cortical mask is created by applying a series of morphological operations the thresholded image. First, an opening operation is used to separate noise outside the bone region from the bone. Then, the objects in the binary image are labelled using component labelling and only the largest (the cortical bone) kept, removing external noise. At this point, the mask contains all of the pores within the bone, but to separate the pores inside of the cortex from the outside they must be filled in the mask. This will define intracortical pores by their spatial location. Therefore, pores within the cortex are filled by a series of closing operations which will leave the medullary cavity unfilled. A final small erosion step is performed to create a mask slightly smaller than the original bone volume, which removes noisy edges present in the binarised image. Finally, the mask is added to the inverted binarised image, so that only features which are both in the mask and the binarised image remain: thus the pores are segmented out. Once segmented, a 3D model can be built and analysed morphologically.

The segmentation workflow can be easily modified to take into account different parameters such as voxel size and contrast. Modifications to this workflow are specified in the appropriate chapters.

3.7 Quantitative analysis

To support qualitative descriptions of bone development and provide a quantitative basis for estimations of age and life history, various properties of the segmented pores should be quantified in an objective and consistent way, which can be automated throughout. The two main sources of porosity, osteocyte lacunae and canals, have both been suggested to be important indicators of age, growth rate and loading (Table 2.2) and so, in order to test these claims, both should be quantified. These measures will be used to quantify features across the developmental range and test the current palaeobiological assumptions of relationship with age and life history.

Intracortical pores have a number of properties which could be quantified, including volume, shape, orientation, and distribution. Some of these measures are straightforward to compute, particularly volume and number-based measures while others are more computationally intensive.

The first step in any analysis, however, is to define which pores are osteocyte lacunae and which are vascular canals. In fact, this is fairly trivial as their volumes differ by several orders of magnitude and therefore a volume-based threshold can be applied. In addition, the thresholded images contain many small 'pores' which are neither lacunae nor canals but are due to noise; these can also be removed by a volume-based threshold though their volumes are more difficult to distinguish from lacunae than those of canals. Based on published measures of lacunar volume in birds [16], a volume range of 50-500μm^3 was defined as lacunae and anything above this as canals. The Particle Analysis toolbox in BoneJ [125] was used to measure the volumes of segmented pores in each bone and these were then separated by volume to define the different pore types.

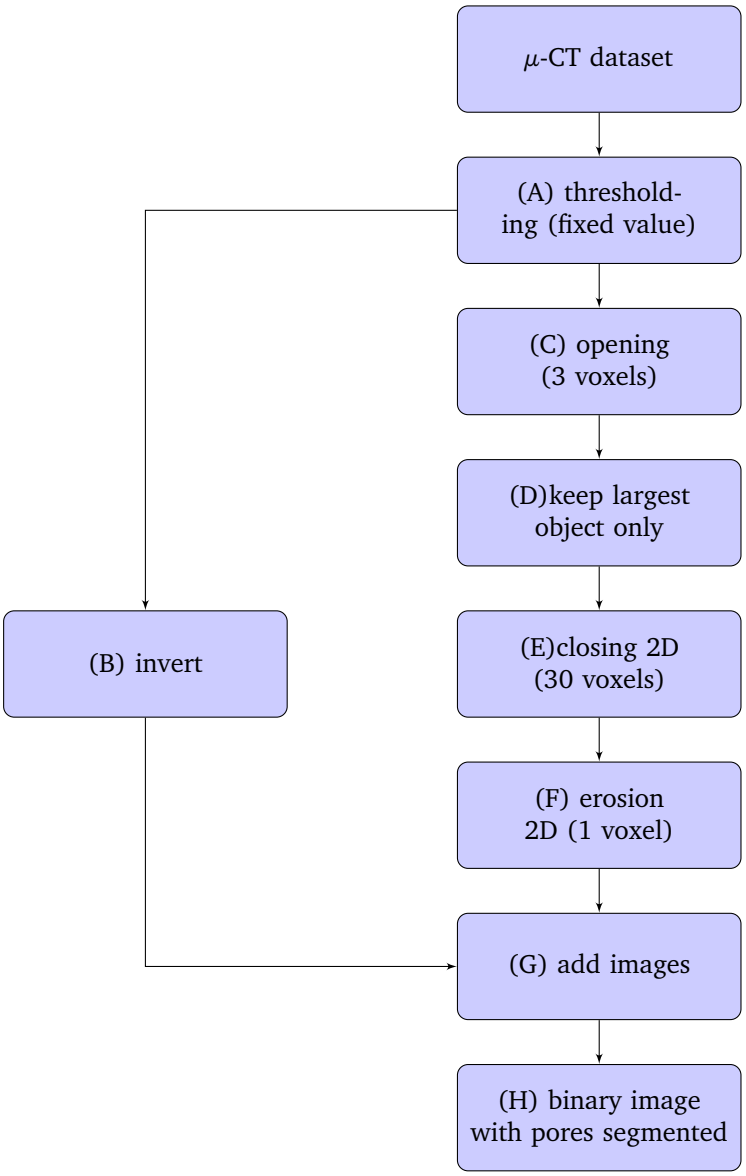

FIGURE 3.7: Image processing workflow for datasets collected at synchrotron sources. This produces a segmented image, with the osteocyte lacunae and vascular canals separated by volume. Steps are illustrated with correlating letters in Figure 3.8.

3.7.1 Vasculature

Overall cortical bone volume fraction (BV/TV), here defined as the proportion of mineralised bone tissue within a cortical mask, was measured in 3D volumes using the Analyse Particles toolbox in BoneJ and in single sections using the Particle Analysis toolbox standard in ImageJ.

Cortical thickness and canal diameter were measured using the Thickness function in the Analyse Particles toolbox.

Canal orientation was measured in 3D using an implementation of the method described by Pratt 2018 [108]. Segmented canal networks are skeletonised (thinned to single lines of pixels) using the Skeletonize 2D/3D tool within BoneJ, and analysed using the Analyze Skeleton tool. Orientation of canals, defined as lines between branch points, are measured, defined using a longitudinal and radial angle. These angles are used to calculate a radial, longitudinal, and

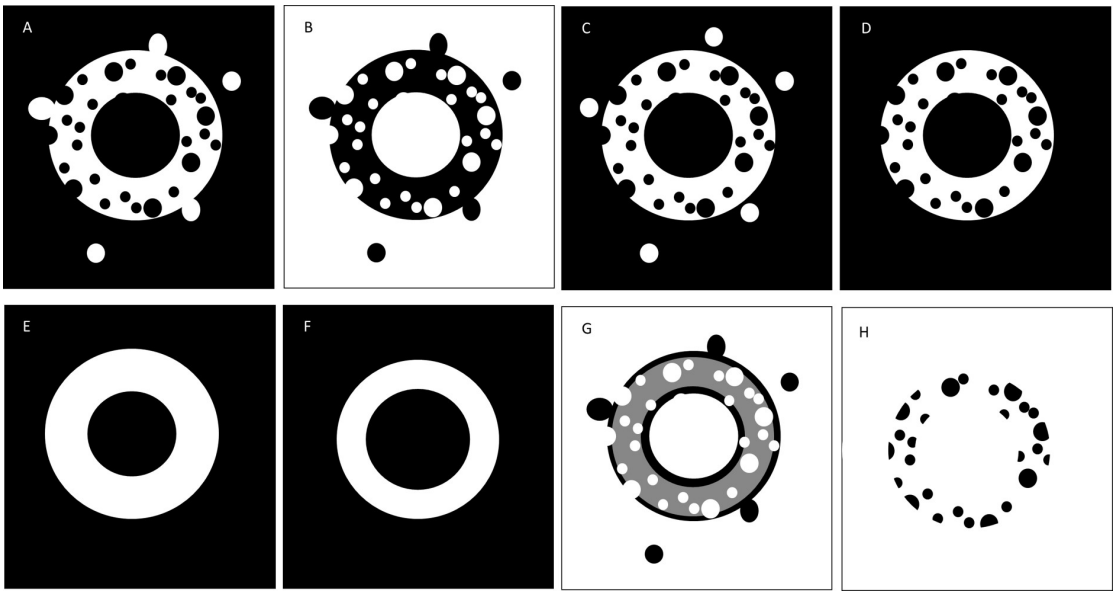

FIGURE 3.8: Image processing workflow schematic: letters correlate to steps in Figure 3.7. Image represents a cross-section through porous cortical bone, with external noise. (A) Thresholding, (B) Invert image, (C) Opening, (D) Keep largest object, (E) Closing, (F) Erosion, (G) Add images, (H) Binary image with segmented pores.

FIGURE 3.9: Simplified steps in segmenting pores from a bone volume (midshaft cortical region of duckling tibiotarsus, data collected at SLS TOMCAT, voxel size 1.3 μm). Left to Right: bone volume selected using greyscale threshold and largest object chosen to isolate bone, holes filled (shown here in colour for clarity, red = vascular canals, yellow = osteocyte lacunaein red and yellow) to create a mask to identify the whole cortical region, and pores extracted by adding bone volume and mask.

laminar index for each scan, showing the proportion of canals corresponding to each orientation. Full method is detailed in Chapter 4.

Orientation in 2D (based in single slices), was estimated by modelling the canals as cylinders, and estimating their orientation based on their cross-sectional aspect ratio and the angle of the longest axis of the cross section. Full method detailed in Chapter 4.

3.7.2 Osteocyte lacunae

Volume is straightforward to calculate based on the particle analysis already carried out, and works well when there are sufficient voxels within a pore to accurately define it. However, when voxel sizes are 1.6μm, and LC are only approximately 5-10μm across, each osteocytes lacuna is represented by only 3-7 voxels across. Therefore, a large proportion of the voxels within the lacuna are likely to be affected by partial volume effects (where one voxel contains

information from both bone and non-bone compartments), making segmentation problematic and volume and shape estimates inaccurate.

To reduce the problem of partial volume effects, a number of scans used a higher spatial resolution (voxel size 0.33 μm), which will allow more accurate measurement of lacuna shape and volume. However, the higher resolution necessitates a smaller field of view and therefore the volume visualised in these scans is very much smaller than in the lower resolution scans. In order to maximise the sample volume, as much analysis as possible will be carried out on the lower resolution scans (1.6 μm voxel size).

Even at 1.6 μm voxel size, locating and counting the osteocyte lacunae is feasible and robust, as is an estimate of osteocyte volume, as volume is less sensitive than shape to partial volume effects. It is only necessary to bear in mind that volume estimates may be inaccurate and therefore a larger difference in volume will be necessary to draw conclusions from.

Although volume estimates may not be fully accurate, the centre of mass of individual osteocyte lacunae this can still be used to locate them in a robust manner, while the number density should not change with spatial resolution assuming that osteocyte lacunae are bigger than the upper threshold for noise/lower threshold for osteocyte lacuna volume (50 μm^3.) Number density can be calculated straightforwardly from the segmented model, by defining the osteocyte lacunae as objects of a particular size (see workflow, Figure 3.7) and counting the number of objects within this size range. A count of the number of volumes falling within the lacunar size range gives an absolute count of lacunae, which can then be displayed as a number density per mm^3 bone volume.

Osteocyte lacunar shape was measured as the aspect ratio between the major and minor axis of an ellipsoid fitted to the shape.

3.8 Verifying methods and selecting a scan region

An important consideration for osteocyte lacunae is that osteocytes are thought to play a mechanosensory role in bone and therefore their volume and distribution may be linked to biomechanical stimulus and remodelling [68], leading to variation between bone regions under different mechanical stimuli. In a long bone, the different sides of the cortex can be under different mechanical stimuli (compressive and tension forces, bending) [129] and thus if lacunae are influenced by mechanical stimulus, their distribution is likely to be different in different regions of the cortex even within a bone. To test the hypothesis that lacunar properties are related to anatomical regions, the volume and number density of lacunae were measured in four different quadrants of bone (Figure 3.10) within the tibiotarsi of a single age class.

The mean lacunar number density and volume measured were similar to those reported in the literature and therefore the 3D measurements used appear to be appropriate. For example, Stein and Werner [8] measured 46000 lacunae per mm^3 in ostriches, so the measurements here of between 25000 and 60000 lacunae per mm^3 bone appear to be within the correct order of magnitude.

Interestingly, there is a difference in the number density between the different quadrants (ANOVA $F=26.4$ $p<0.01$), particularly opposite quadrants which would be expected to be under quite different mechanical loading (Figure 3.10).

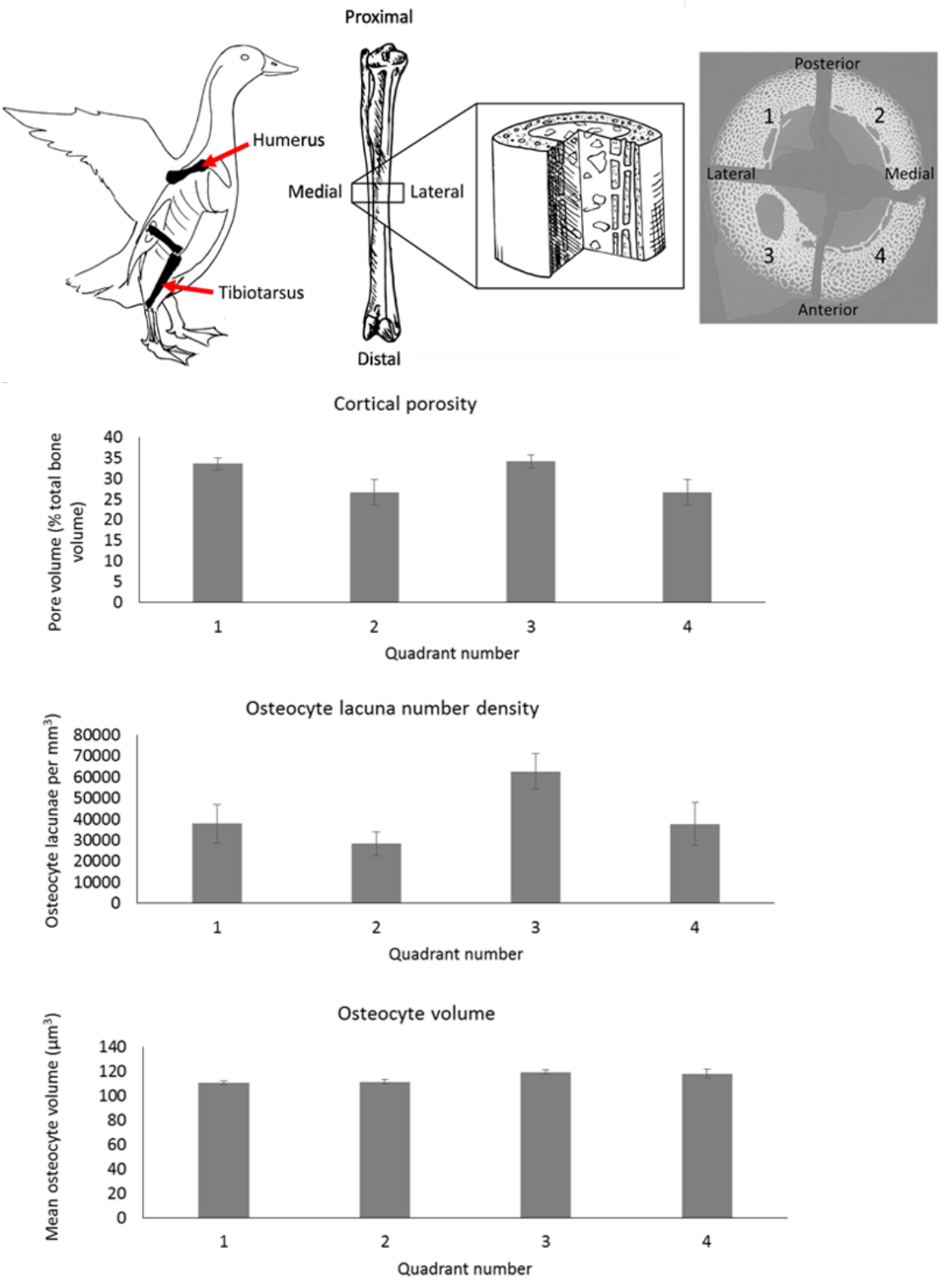

FIGURE 3.10: Measures of porosity at different anatomical regions within a bone and across individuals. (Top) All scans were performed on bone sections from the midshaft of the right tibiotarsus. (Right) Quadrants 1-4 represent posterio-lateral, posterio-medial, anterio-lateral and anterio-medial quadrants respectively, scanned independently using SR CT (1.2 μm voxel size). Graphs show comparisons of measurements from scans of the four quadrants across the tibiotarsi of 3 juvenile ducks with body masses of approximately 500g. Variation between quadrants is not significantly greater than variation within quadrants at p=0.05 (ANOVA, F= 2.56, 3.60, 1.17, P=0.128, 0.066, 0.380).

When considering osteocytes, it is crucial to fully account for anatomical position. As expected if osteocytes play a mechanosensory role, these cells appear to be unevenly distributed in the bone even at a single height. The distribution is most different between opposite sides of the bone cortex. These results indicate lacunar measurements from different quadrants cannot be considered interchangeable, with anatomical position a key consideration to review.

3.9 Simulated datasets

Shapes were generated as surface models in ScanIP 2016.09-SP1 (Synopsis, Inc.), a piece of commercial image processing and model generation software. The surface models were converted to pixel images, which were then thresholded to produce a binary image comparable to segmented CT datasets. For full details of simulated datasets see Chapter 4.

Chapter 4

Quantifying intracortical bone porosity: an appraisal of 2D and 3D methodologies in the domestic duck (*Anas platyrhynchos*)

4.1 Introduction

Studying bone histology to discover correlations between intracortical bone microstructure and wide ranging biological traits from growth rate to lifestyle has greatly enhanced our understanding of extinct animals [22, 36, 38, 126]. In particular, the arrangement of microvasculature within the bone cortex, or vascular canals, and the spaces where bone cells reside, the osteocyte lacunae, can provide information about the age [83, 106], the growth rate of the bone being studied [2, 15, 68], and how the bone may have been loaded in life [21, 80, 84]. Additionally, bone microstructure is influenced by body mass [69], metabolic constraints [69], and phylogeny [70]. The study of bone histology in extant and extinct animals has led to substantial shifts in the way we view, for example, dinosaurs: their bone histology reveals that, rather than being the slow-growing, slow-moving reptiles of Victorian illustration, they were more bird-like in their growth [36] and their metabolism was likely endothermic [127] or mesothermic [128].

However, much remains to be learned from bone histological study. Although loose correlations have been identified between bone porosity and age [129], vascular density and growth rate [2, 15], vascular orientation and growth rate [2, 108] and loading [21], and the shape and size of osteocyte lacunae and growth rate/tissue type [57], results have not been consistent across studies for some factors, including correlations between growth rate and canal orientations [2, 15, 18, 21], and functional study has been limited. As standard, histological descriptions of new fossils are qualitative, placing observed tissues into a set of bone types [130] and relating these to 'rapid growth', or even sometimes specific growth rates [15]. These interpretations are based on a relatively small number of studies in extant species, and the categories used to

define bone types do not fully capture the continuous nature of variation in bone microstructure [6].

While most histological descriptions remain entirely qualitative, using descriptive definitions of bone types [2], quantitative approaches are crucial to standardisation and robust testing of hypotheses. Some studies have taken such a quantitative approach, testing how metrics such as the orientation and density of vascular canals and the volume, shape, or density of osteocyte lacunae, relate to biological traits. For example, canal orientation has been correlated with bone deposition rate [2, 15, 131], and biomechanics [21, 132, 133], vascular density is commonly related to growth rate [69, 94]. Osteocyte lacunar shape and volume have been linked with body mass [16], growth rate [16], and genome size [16, 20, 105], and lacunar density linked inversely with body mass [89]. Understanding the correlations between morphology and biological origins of those morphologies can help us to understand the biology of living organisms, but also to make interpretations of the biology of extinct organisms from fossilised bone.

The correlations identified by such histological studies highlight the potential that histological approaches hold, if the different factors influencing these relationships can be fully disentangled. However, further elucidation of relationships between form and function or developmental origin is contingent on accurate and reproducible histological measurements, and not all observations have been reliably reproduced across different studies in different species [2, 15, 108]. The variation in results between studies is likely to be in part due to real differences in biology between species, and as yet undefined variables determining structure. However, it is also possible that methodological problems are reducing the accuracy and reliability of results.

The use of 2D histological methodologies, based on a single or small number of thin sections for each sample, is a potential source of inaccuracy of measurement. Firstly, the small sample volume included in a histological section may not be representative of the bone as a whole, leading to an overestimation of the variation between samples, when similar variation could potentially be present within a single bone. Using traditional histological methods, this would only be apparent if a number of sections were taken from each bone, and this is not the standard approach. Secondly, doubt has been cast on the suitability of traditional 2D approaches for estimating 3D traits such as shape and orientation of canals [23], which cannot be easily disentangled, volumes calculated by modelling shapes in 3D using information gained from 2D sections [16], and connectivity of pores and other structures [5], both within [14, 17, 134] and outside palaeobiology [13]. Similarly, outside the bone field entirely, other fields are noting the importance of understanding 3D structures fully, from the structure of bubbles in cake batter [135] to complex branching plant root systems [136].

In this study, the structures of interest are the microscopic pores within the cortex of long bones. These pores are divided into vascular canals, which are more-or-less cylindrical structures that run at different angles through the cortex [130], and osteocyte lacunae, which are described as scalene ellipsoids [90]. In histological descriptions, the main orientations of the vascular canals are commonly described, and related to bone growth rate, or loading. For example, in the cortex of the humerus in birds, the canals are said to have a more laminar, or circumferentially oriented canal network, compared to the tibiotarsus where canals run more longitudinally [21]. Histological descriptions also frequently include an assessment of the

overall porosity of the bone, and the density of the canal network, relating these to age and growth rate. For the osteocyte lacunae, a standard histological description includes their size (whether they are large or small, based on subjective assessment), and whether they are 'rounded' or 'flattened', as well as their number density within the tissue, in order to assess bone type, maturity, and growth rate.

As standard, histological descriptions are based on single transverse thin sections from a bone. Therefore, estimation of the orientation of canals, and the shape and volume of the osteocyte lacunae are based on their shapes in cross-section. In general, these assessments are descriptive, but some quantitative methods have been developed to quantify histological characteristics to capture continuous variation and improve comparability between samples and studies. In these methods, the structures of interest have been modelled as idealised 3D shapes, extrapolated from their cross-sectional properties.

De Boef and Larsson's 2007 method [6] for estimating vascular canal orientation from a 2D section involves modelling the canal as a perfect cylinder. From a 2D section, this cylinder can be characterised as having two different rotational angles: a radial angle (the angle of the main axis of the canal relative to a tangent to the bone surface)(Figure 4.1 A) and a longitudinal angle (the angle the canal makes with the long axis of the bone (Figure 4.1 C). Each uses the properties of the elliptical cross-section of the canal. The radial angle is measured using the orientation of the major axis of the ellipse (Figure 4.1A). The longitudinal angle is estimated using the relative lengths of the major and minor axes of an ellipse fitted to the cross section (Figure 4.1C). Then, the two angles are used to calculate three indices: a longitudinal index, a radial index, and a laminar index, showing the proportion of canals with each respective orientation.

Quantitative measurements of the osteocyte lacunae either characterise the area of the lacunar cross section [64], or the volume of the whole lacuna. Otherwise, the volume is estimated by modelling the lacuna as an ellipsoid, based on the 2D cross-sectional ellipse.

Two methods for estimating the mean osteocyte lacunar volume based on 2D sections have been published. The most straightforward requires a single transverse section and uses the major and minor axes of a fitted ellipse to calculate the volume of the 3D ellipsoid using the formula:

$Volume = \frac{4}{3}\pi r_1 r_2^2$

where r_1 is the long axis of the ellipse, and r_2 is the short axis of the ellipse.

Only the largest cells are chosen, as these are thought to be the ones where the cross section is taken closest to the middle of the cells and therefore the axes measurement is more accurate [64].

An alternative method has been published to take into account the fact that osteocyte lacunae are better modelled as scalene ellipsoids [16, 90], and therefore require three different axis lengths. This is not possible from a single section, therefore d'Emic and Benson (2013) [16] proposed that two sections should be taken: a transverse and a longitudinal section. While this will not section the same cells, it is assumed that there is some consistency within the osteocyte lacunar population and therefore average values taken from both sections can be used to estimate mean lacunar volume using the average major, intermediate, and minor axes, using the formula:

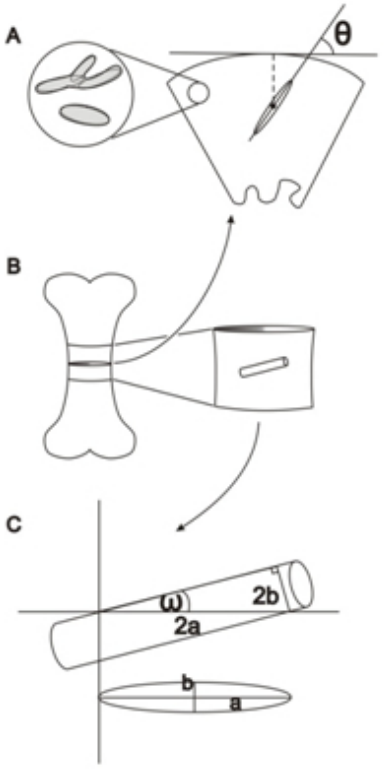

FIGURE 4.1: Method for measuring the orientation of vascular canals in terms of a radial and a longitudinal angle, based on a 2D transverse histological section. (A) The radial angle is measured as the angle the long axis of an ellipsoid fitted to the cross-section of the canal makes with a tangent to the bone surface. (B) Vascular canals have a 3D orientation within the bone cortex. (C) Longitudinal angle is calculated by modelling the canal as a cylinder based on its cross sectional aspect ratio. Image reprinted from de Boef and Larsson (2007)[6]

$Volume = \frac{4}{3}\pi r_1 r_2 r_3$

where r_1, r_2, and r_3 are the major, intermediate, and minor axes of the ellipsoid.

This method is based on the important assumption that most osteocyte lacunae are oriented with the long axis of the bone, and therefore a longitudinal section will more or less capture the long axis of the ellipsoid, while a transverse section will underestimate lacunar volume as the two shorter axes are visible in that orientation [16].

Estimation of the orientation of vascular canals from 2D sections, or the shape and volume of osteocyte lacunae, are heavily dependent on strict assumptions including perfect cylindricality for canals [6], and 'improved' methods of measuring osteocyte lacunae rely on particular alignments for osteocyte lacunae [89], which are difficult to test when the only data available are 2D sections. Strict geometric assumptions are seldom met in biological systems. For example, osteons traditionally described as cylindrical are in fact more elliptical in cross section, and cylindricality can even change with age [134]. Osteocyte lacunae, though perhaps having a preferential longitudinal orientation, also align with collagen fibres [86] which, where osteons are present, run circumferentially around the osteon as well as longitudinally, and osteocyte lacunae in woven bone have a random orientation [89].

Even if all the required geometric assumptions were met, there is still no guarantee that a 2D section will produce accurate results. This would depend upon perfectly perpendicular

sectioning which, although possible, is very difficult to achieve in practice. Additionally, 2D sections cannot provide information on traits such as connectivity of canal networks, their tortuosity, or spatial variation within a sample, and therefore limit our understanding of the 3D structure of the bone.

Despite these criticisms, 2D approaches have some advantages over 3D approaches. 2D properties of bone histology are already well characterised, histology does not require expensive equipment such as synchrotron radiation sources for the highest resolutions, and higher resolutions can be reached [4], allowing canaliculi [64] and cement lines [137] to be identified. Histological approaches may also be faster, especially as histology is already a standard technique [89]. Additionally, collagen fibre orientation can be studied using polarising light microscopy [17]. These advantages have meant that most palaeohistology is still carried out using 2D sections. However, traditional histology also have some major disadvantages: sectioning fossils is destructive, the 2D sectioning produces a small sample volume which does not necessarily capture variation within the specimen, and a great deal of information is lost in losing the third dimension.

3D approaches may be able to solve some of the problems involved in 2D histology. A number of methods exist which could be used to study bone in 3D [4]. In fossil bone, some attempt has been made using different focal planes and simple light microscopy [138] and confocal laser scanning microscopy [103], which provide some depth information, though the depth resolution and volume imaged is limited by the transparency of sample. High-resolution micro-computed tomography (μ-CT) allows a truly 3D approach, is minimally destructive, and can generate images with sub-micron spatial resolution. For the highest resolutions and best signal-to-noise ratio (SNR), a synchrotron source is required, but lab-based CT systems can also reach required resolutions with longer scan times. Although CT has limitations, progress is continuing to be made allowing resolutions and signal-to-noise-ratios to be constantly improved, even in traditionally difficult samples (large size, unequal aspect ratio, areas of high density), including histology from whole bird fossils [25]. In addition, new approaches are allowing structures to be visualised for the first time in 3D, for example, phase retrieval can be used to identify cement lines and therefore primary and secondary osteons [134]. They can also add information impossible to gain through 2D approaches alone, such as connectivity [5] and tortuosity. For quantifying intracortical porosity, μ-CT could be the ideal solution. It can be used to image cortical bone in true 3D, at sub-micron resolutions, enabling later segmentation and quantification of intracortical pores [13, 14, 108, 134].

3D CT-based techniques can be used to measure the true 3D orientations, shapes, and volumes of structures. Using 3D synchrotron-based CT datasets, Pratt et al. [14] published a method for measuring the canal orientation within bone. The method aims to reduce bias present in 2D estimates, and accurately quantify the orientations or the canal networks in true 3D. First, the canal network is skeletonised, or thinned to a single line of pixels. It is then simplified and broken into branches which can be measured as line sections. The orientation of the line sections is measured, producing a longitudinal and radial angle in the same way as the 2D method discussed above. Then, like the 2D method, a set of indices are calculated to demonstrate the predominant orientation of canals within the bone. It was found using this method that 2D measurements significantly underestimated the longitudinal index [18], and the 3D indices were able to distinguish between different bones [14]. However, the comparison

between 2D and 3D measurements was limited since in real biological datasets the ground truth cannot be known and the two methods can only be compared to each other.

Measuring the volume and aspect ratios of osteocyte lacunae using 3D datasets can be carried out by counting the pixels included within a segmented ellipsoid, or by fitting an ellipsoid to the shape and calculating its volume using the formula:

$Volume = \frac{4}{3}\pi r_1 r_2 r_3$

The latter is necessary for measuring the aspect ratio and, if desired, the orientation of the major axis. However, it is important to note that osteocyte lacunae are very small structures, only a few micrometers across, and therefore accurately measuring their volume, shape, and orientation requires high resolutions. For example, Mader [139] found that in order to measure the orientation of osteocyte lacunae, at least 100 voxels are required. Sampling at this high resolution limits the sample volume that can be measured, and is towards the limit of lab-based systems.

Across palaeobiology, there is increasing adoption of CT and μ-CT [24, 25, 115, 140], but to date little work has focussed on quantification and validation, especially at the microstructural level. In particular, the accuracy of 2D and 3D approaches have been minimally addressed, despite findings that, for example, shape and orientation cannot be distinguished based on 2D sections [18, 23].

At this stage, when quantitative 3D approaches are beginning to be taken, but traditional 2D approaches retain some advantages, it is important to appraise their relative merits and carry out a thorough test of the accuracy of each. Some 2D methods require fewer assumptions to be made (for example measuring bone porosity only requires that the section taken is representative of the bone in general, rather than requiring a geometric model to be made), and may be more robust than others. It is important to understand which can be used robustly, what assumptions must be met in order for these to be used, and which require a different approach. Relevant 3D measurements are assessed and discuss where these too have limitations.

In this study, the theoretical application of 2D and 3D methods for measuring canal orientation, and osteocyte lacunar shape and volume, were tested using simulated idealised datasets. The simulated datasets were manipulated to represent possible biological and experimental scenarios, including cylinders with non-circular cross-sections, osteocyte lacunae in different orientations, and different voxel sizes in order to test the limitations of the different measurement methods.

In addition to the simulated datasets, the same methods were tested in real datasets to compare the results obtained using 2D and 3D measurements. Real datasets are more complex than individual simulated cylinders and ellipsoids, and therefore it was important to be able to compare the methods in a more realistic scenario, and confirm that any limitations identified were relevant to real data. Additionally, further standard histologial methods (bone volume fraction (BV/TV) and osteocyte lacunar number density) were tested to investigate which, if any, measurements can be made reliably using 2D sections.

- Hypothesis: Methods for quantifying bone histological features, namely vascular canal orientations and osteocyte lacunar aspect ratio and volume, based on 2D histological sections are less accurate than 3D alternatives using μ-CT datasets.

- Objective: To test the relative accuracy of 2D and 3D quantitative histological methods using simulated and real test datasets. Specific aims:
    1. To test the accuracy and precision of canal orientation measurement methods using 2D and 3D datasets when geometric assumptions are met
    2. To test the sensitivity of 2D and 3D canal orientation measurement methods to deviations from the assumption that canals are perfectly cylindrical
    3. To test the accuracy and precision of osteocyte lacunar aspect ratio and volume measurement methods using 2D and 3D methods
    4. To test the sensitivity of osteocyte lacunar aspect ratio and volume measurement methods to different experimental conditions, namely different voxel sizes
    5. To compare results obtained using 2D and 3D methods in real datasets, both for the canal orientation and osteocyte lacunar volume, and for measures that do not require modelling (BV/TV and osteocyte lacunar number density)

4.2 Methods

The methods used in this chapter combine *in silico* tests of 2D and 3D methods for measuring cylinder (vascular canal) orientation, and ellipsoid (osteocyte lacunar) shape and volume, with comparisons of the same methods, as well as bone volume fraction (BV/TV) and osteocyte lacunar number density, in real datasets.

Simulated datasets were used to test the efficacy of the different methods in an idealised theoretical context, then datasets were manipulated to investigate theoretical limitations to methods. Real datasets were used to compare 2D and 3D methods in a more realistic context, and also to determine whether these, or a selection of other histological measurements could be made reliably from 2D sections.

Simulated datasets aimed to test methods in a 'best case scenario' initially. Therefore, for each experiment, 100 cylinders or ellipsoids were generated and analysed individually. For 2D methods, the transverse midslice was used to simulate a perfectly 2D section. For a pseudo-3D measurement of the ellipsoids, a second, perpendicular slice was also used. Unlike in real datasets, the two sections are taken from single ellipsoids, which should in theory be more accurate than possible in real datasets using mean values from two sections.

4.2.1 Simulated datasets:

Shapes were generated as surface models in ScanIP 2016.09-SP1 (Synopsis, Inc.), a piece of commercial image processing and model generation software. The surface models were converted to pixel images, which were then thresholded to produce a binary image comparable to segmented CT datasets.

4.2.1.1 Vascular canals

Vascular canals are described as being roughly cylindrical in shape [6] and therefore idealised canals were simulated as cylinders and elliptic cylinders.

100 initial cylinders were generated with a diameter of 10 voxels, which is within the range of canal diameters found in real bone in preliminary studies here when visualised at 1.6 μm voxel size. A random value between 0 and 90°was generated for rotation in x, y, and z around the centre of the object (Figure 4.2).

Although described as roughly cylindrical [6], vascular canals are unlikely to always be perfectly cylindrical [23]. However, a cylindrical shape is a key assumption of the 2D orientation measurement method used [6]. Therefore, the sensitivity of the methods to deviations from this assumption were tested.

Elliptic cylinders were generated with cross-sectional aspect ratios of 1:1.25, 1:1.5, or 1:3 (Figure 4.2), representing perfectly cylindrical vascular canals, slightly elliptic vascular canals, moderately elliptic vascular canals, and extremely elliptic vascular canals. 100 elliptic cylinders were generated for each aspect ratio and each was rotated randomly using the method described above.

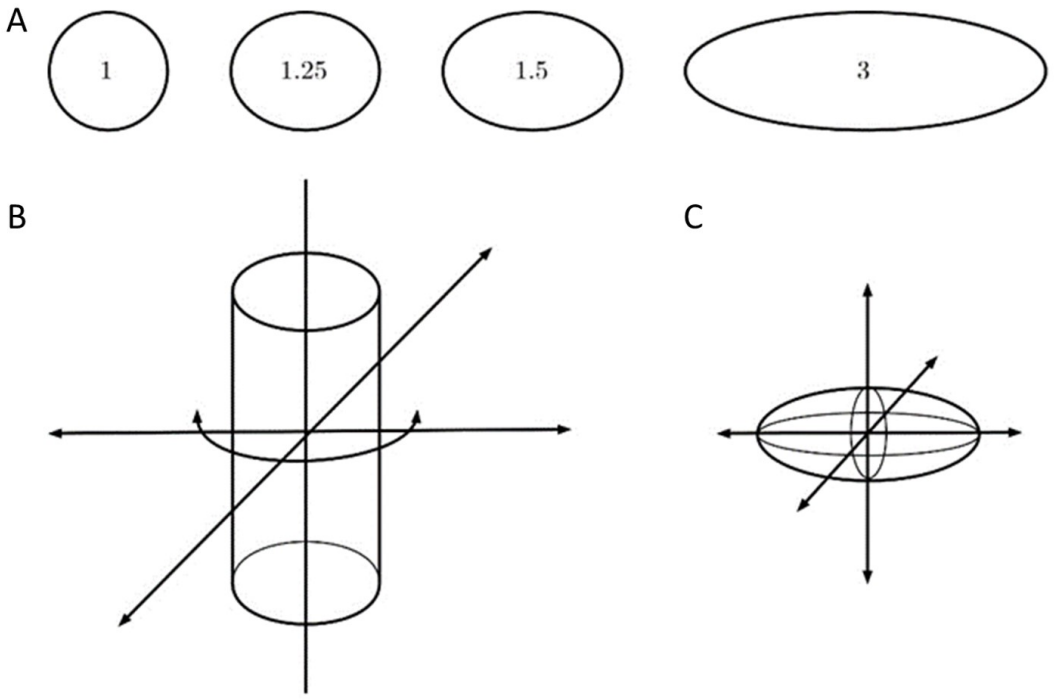

FIGURE 4.2: Generation of simulated datasets. (A) Cylinders were generated with cross-sectional aspect ratios of 1:1, 1:1.25, 1:1.5, or 1:3. (B) They were rotated around x, y, and z axes placed at the centre of the cylinder. (C) Ellipsoids were generated with a fixed aspect ratio (3:1:1) and rotated using the same method as the cylinders.

4.2.1.2 Osteocyte lacunae

Ellipsoids were generated to simulate measuring osteocyte lacunae using different voxel sizes, and orientations comparable to those found in parallel-fibred bone and woven bone, in order to test how sensitive the measurement methods are to the different conditions that may be found in real experiments.

Osteocyte lacunae are described as scalene ellipsoids, with an aspect ratio of approximately 3:2:1 [90] and a volume of between approximately 100-500 μm^3 in most birds, and more than 1000 μ^3 in the ostrich [16]. Here, the case was simplified to an aspect ratio of 3:1:1. Simulated ellipsoids measured 15x5x5μm^3, giving a volume of 196.25μm^3, within the range of lacunar volumes for birds. For each case, 100 ellipsoids were generated.

In order to simulate the randomly oriented osteocyte lacunae found in woven bone, each ellipsoid in one set of ellipsoids was given a random value between 0 and 90°for rotation in x, y, and z around the centre of the object (Figures 4.2 and 4.3).

To simulate parallel-fibred bone, each ellipsoid in another set of ellipsoids was given a random value between 0 and 22.5°for rotation in x, y, and z around the centre of the object (Figure 4.3).

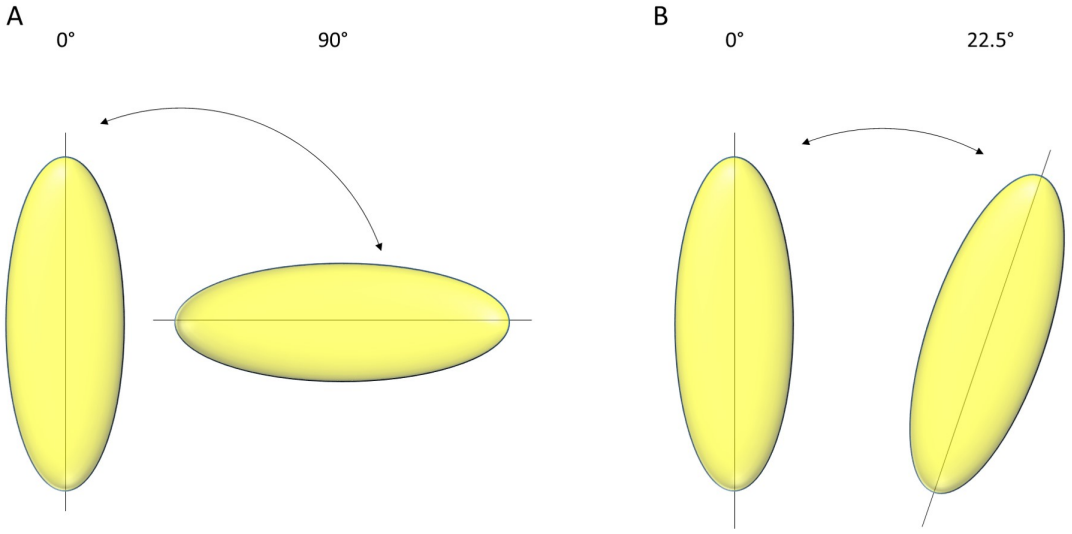

FIGURE 4.3: Simulation of osteocyte lacunae in different bone types, (A) with random orientation of osteocyte lacunae (rotation between 0 and 90°), representing woven bone, and (B) longitudinally aligned osteocyte lacunae (rotation between 0 and 22.5°), representing parallel-fibred bone.

Ellipsoids were also tested over three different simulated spatial resolutions to represent different CT scan settings: 1.6 μm voxel size, as achievable on a lab-based scanner and in reasonably large samples, and 0.8 and 0.33 μm voxel size, as best achieved in a synchrotron setting, and pushing the limits of a standard μ-CT scan. The different voxel sizes produce ellipsoid models with different numbers of voxels representing their shape (Figure 4.4). Previous work has shown that number of voxels are important for e.g. orientation [139].

4.2.2 Real datasets

4.2.2.1 Samples and preparation

3 individual commercially-reared and slaughtered domestic ducks were purchased frozen (Iceland Supermarket). The commercial slaughter age for ducks within the UK is approximately 7 weeks [141]. At this age, the ducks are not adult, but have reached adult body mass [26]. The right tibiotarsus and humerus of each duck were dissected out, and 2 mm x 10 mm matchsticks of cortical bone cut from the same location of the midshaft of each using a

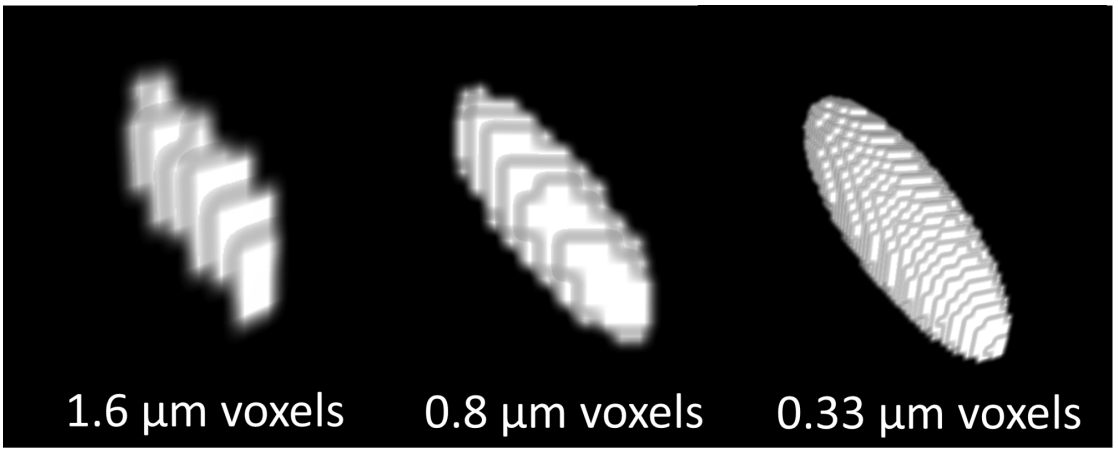

FIGURE 4.4: Simulating an osteocyte lacuna measuring 15 x 5 x 5 μm, imaged using different voxel sizes. At 1.6 μm voxel size, few voxels are present and the shape is not well-represented. At 0.8 μm voxel size, the shape is better represented but a high proportion of edge voxels makes the shape vulnerable to differences in threshold. At 0.33 μm voxel size, the shape is well-represented. Visualisation generated in ImageJ's 3D viewer.

slow-speed saw (Buehler Isomet, Essligen, Germany), to allow the sample to appear mostly within the field of view during scanning (See Methods chapter). The samples were fixed in 4% PFA for at least 24 hrs and stored in 70 % ethanol at 4°C.

4.2.2.2 Scan setup

Ethanol was removed immediately before scanning, and samples covered with a plastic tube to reduce drying (See Methods Chapter). Samples were scanned at 113-2 beamline at Diamond Light Source (Harwell Innovation Campus, UK), using pink beam with an average energy of 20 keV. Initial voxel size was 0.8 μm; this was binned to 1.6 μm by averaging after acquisition to improve signal-to-noise-ratio (SNR) and increase computational speed. 100 ms exposure was allowed per projection over 4001 projections. Propagation distance was set to 20 mm, so that most data collected was due to absorption rather than phase. Scans were reconstructed using a filtered back projection algorithm.

4.2.2.3 Image processing

3D datasets used the volume reconstructed from the CT scan (1280 x 1284 x 1000 voxels). 2D datasets were generated using the midslice from the scan as a 'virtual section'.

Intracortical pores were segmented out using a custom segmentation workflow in the FIJI distribution of ImageJ, a free, open-source image processing package[123].

First, a 3D Gaussian filter with a standard deviation of 1 was applied to reduce noise. Images were thresholded using the Li thresholding algorithm [142] implemented in ImageJ. The bone volume was separated from noise outside by a single pixel erosion and dilation, followed by a labelling process to remove all except the largest object. Holes in the bone cortex were filled by dilation and erosion to create a cortical mask. This mask was used to define the edges of the canal network and segment out the pores (intracortical canals and osteocyte lacunae) by

applying an AND function with the thresholded image. See Methods Chapter for full details of segmentation workflow.

Osteocyte lacunae and vascular canals were separated by volume. Osteocyte lacunae were defined as 50-500 μm^3[16], and vascular canals as $>$1000 μm^3. Objects between 500 and 1000 μm^3 were excluded as these were larger than the majority of published estimates for avian osteocyte lacunae, and in datasets used in the present chapter, it was found that these objects often represented several osteocytes very close together which could not be easily separated, or other ambiguous objects which should not be included in analysis of osteocyte lacunae.

4.2.3 Data analysis

Each simulated ellipsoid and cylinder was measured using 2D and 3D methods, with the aim of retrieving the values of aspect ratio and volume, or rotation angle, input while creating the models.

The orientation of canals was defined by two angles: a longitudinal angle and a radial angle [6]. The longitudinal angle is the angle the canal makes with a line perpendicular to the major axis of the bone (90°is perfectly longitudinal), and the radial angle is a measure of whether the canal runs radially (like spokes on a bike wheel, 90°) or circumferentially (like the rim of a wheel, 0°).

Canal orientation was measured in 2D by fitting best fit ellipses to the canal cross section using the Analyze Particles tool in ImageJ [6, 70] (Figure 4.1 and 4.5A-C). This method assumes that canals are circular in cross-section.

The longitudinal angle was estimated using the major and minor axes of the best fit ellipsoid to model the canal as a cylinder (Figures 4.1 and 4.6C), using the formula $sin^{-1}\frac{b}{a}$ where a is the major axis of the fitted ellipse and b is the minor axis.

For simulated datasets, the radial angle was estimated by calculating the angle between the major axis of the ellipse and x axis of the image. For real datasets, where canal orientation was measured relative to the bone surface, the radial angle was estimated by calculating the angle between the major axis of the ellipse and tangent to the edge of the bone nearest to the centroid of the ellipse (Figure 4.6D).

In 3D, the same two angles were measured using a skeletonisation process based on Pratt et al. 2017 [14, 18] and implemented using BoneJ, a plugin for ImageJ [125]. A custom ImageJ macro was written to automate the process. First, the segmented canal was skeletonized using the Skeletonize 2D/3D tool (Figure 4.5D). Then, the skeleton was analysed using the Analyse Skeleton tool, producing the coordinates of the end points of each branch in the skeleton (Figure 4.5E). Each canal was defined as the line between nodes in the skeleton. In Pratt's original method, each branch is broken into smaller segments to measure the orientations all the way along the branch, following any twists and turns. Here, a simpler skeleton is used and each branch is defined as a straight line. While this does reduce the accuracy of measurements of very curved canals, it provides a measurement of the overall direction of the canal. Simplifying the case in this way also reduces computational time, which can be significant in complex networks within large CT datasets.

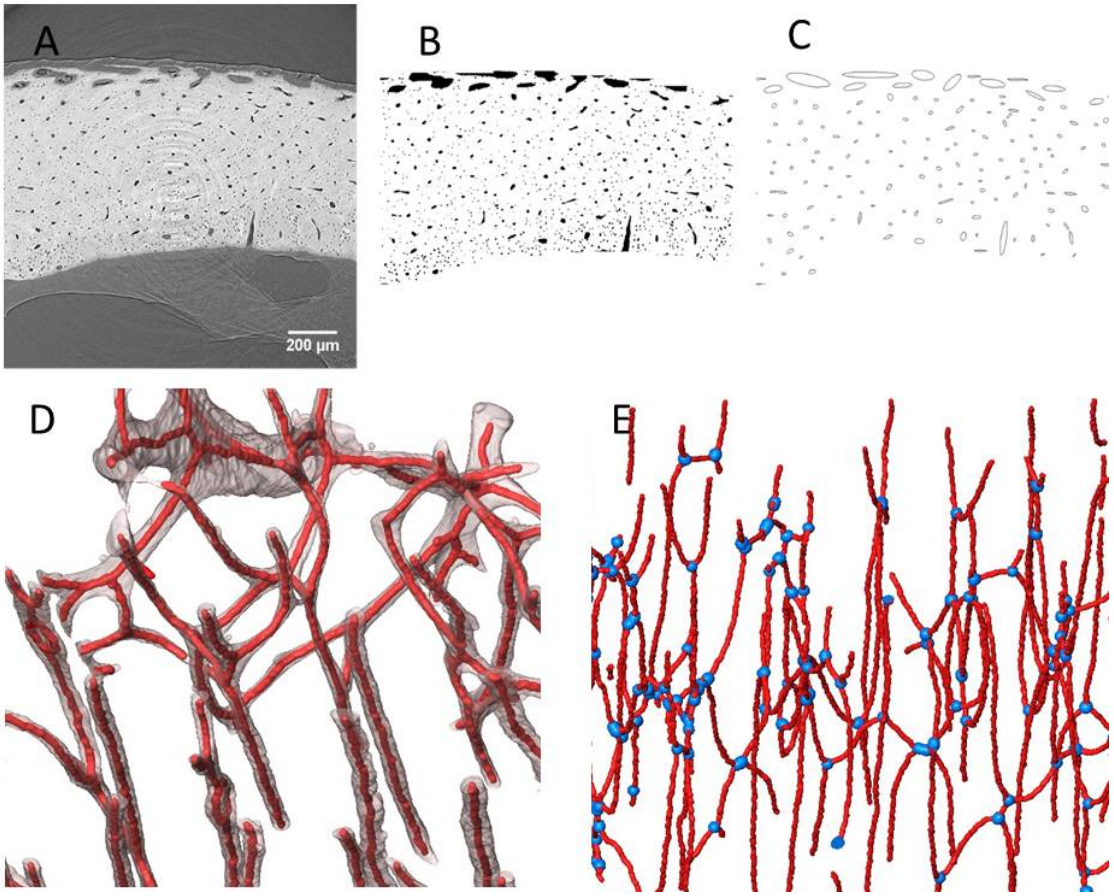

FIGURE 4.5: (A-C) Ellipse fitting to virtual sections 'cut' from CT volume. (A) CT slice. (B) Segmented CT slice showing both vascular canals and osteocyte lacunae. These are separated by area before further analyses. (C) Best fit ellipses are generated for the vascular canal cross-sections and used to estimate 3D orientation of each canal. (D-E) 3D measurement of canal network: skeletonisation process. (D) Skeletonisation: original segmented canals (transparent) are thinned to a single line of voxels (red, dilated for visualisation purposes). (E) Analysing the skeleton: locations of branch points (blue), length of branch, and Euclidian distance between nodes are recorded. Visualisation in Avizo.

The orientation of the main axis of the bone was defined by fitting a circle to 5 manually selected points on the surface of the bone in the first slice, and using a circle of the same diameter to fit the bone surface as closely as possible in the last slice. The bone axis was defined as the line between the midpoints of those two circles.

The radial angle was measured by calculating the angle of the skeleton in x and y (in the transverse plane) relative to the nearest tangent to the outside of the bone at the z slice level with the midpoint of the canal.

The longitudinal angle was measured by calculating the angle between the skeleton and the long axis of the bone. The original method was adapted to measure the longitudinal angle relative to the bone axes rather than the axes of the scan, allowing it to take into account imperfectly aligned scans.

Each canal measured using both the 2D and 3D method was categorised as longitudinal (having a longitudinal angle of more than 67.5°), radial (having a longitudinal angle of less than 67.5°and a radial angle of more than 67.5°), or laminar (having a longitudinal angle of

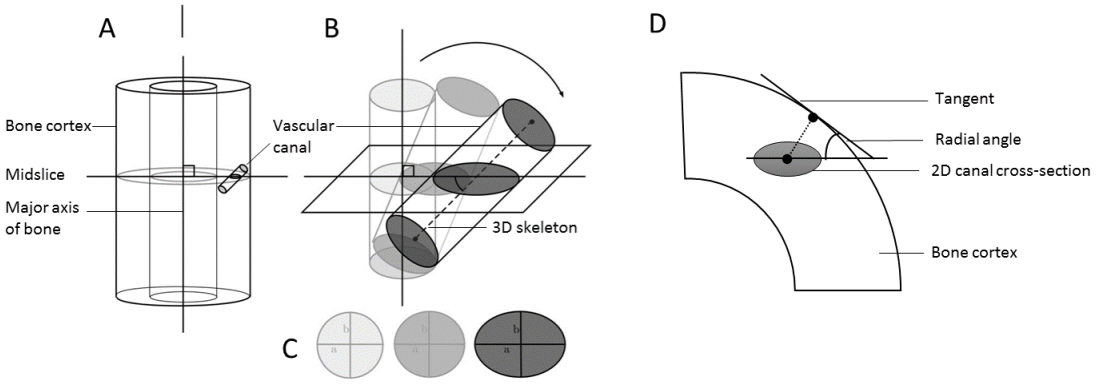

FIGURE 4.6: 2D and 3D methods for measuring canal orientation, defining a radial and a longitudinal angle. (A) Sketch showing a vascular canal within the bone cortex. (B-C) Sketch showing vascular canals at three different longitudinal orientations (Lightest to darkest: 90°, 22.5°, 45°). Midslice cross-sectional aspect ratio is related to longitudinal angle. A reduced longitudinal angle gives a greater value of a (the major axis of the ellipse). In 3D, this angle is measured using the skeleton of the object (dashed line). (D) The radial angle is measured in 2D using the angle of the major axis of the ellipse and a tangent to the surface of the bone.

less than 67.5°and a radial angle of less than 22.5°), (Table 4.1) following de Boef and Larsson (2007)[6]. These categories were used to calculate a longitudinal, radial, and laminar index showing the proportion of canals with each major orientation. For the 3D method, this index was weighted by length of canal to reduce the undue influence of short canals and give a more accurate representation of the whole network. Some canals do not fall into any of these categories as they have a more oblique orientation, therefore the indices are not expected to add to 1.

TABLE 4.1: Categorisation of canal orientations based on longitudinal and radial angles, following de Boef and Larsson (2007) [6]

Orientation category	Radial angle (degrees)	Longitudinal angle (degrees)
Longitudinal	0-90	67.5-90
Radial	67.5-90	0-67.5
Laminar	0-22.5	0-67.5

Osteocyte lacunae were measured in 2D by fitting best fit ellipses to the segmented cross-sections using Analyse Particles in ImageJ. Volume was calculated by modelling the 2D shapes as prolate ellipsoids using the formula $volume = \frac{4}{3}\pi r_1 r_2^2$, where r_1 and r_2 are the major and minor axes of the fitted ellipse. Additionally, a second estimate was made based on [16], using axes from two perpendicular sections to try to capture the 3D shape more accurately by estimating three different axes. The intermediate and minor axes were measured from the transverse section, and the major axis from the major axis of an ellipse fitted to a perpendicular section. The 3D volume was calculated by modelling the shapes as scalene ellipsoids using the formula $volume = \frac{4}{3}\pi r_1 r_2 r_3$, where r_1, r_2, and r_3 are the major, intermediate, and minor axes of the ellipsoid. Aspect ratio (shape) was measured as a ratio between the major and minor axes.

In 3D, the volumes of the osteocyte lacunae were measured using two methods: counting the voxels in the segmented object, and fitting best-fit ellipsoids. Both methods were carried out using the Particle Analysis toolbox in the BoneJ plugin for ImageJ [125]. Voxel counting has the advantage in larger datasets of being computationally faster, and more reliable, in that, in the author's experience, ellipsoids are not always successfully fitted, particularly to small objects

with few voxels. Ellipsoid fits were also used to calculate the aspect ratio (major:minor axis) of each lacuna.

In order to compare the geometric measurements of vascular canals and osteocyte lacunae with more straightforward histological methods, and therefore test which methods are most appropriately carried out in 2D and which in 3D, bone volume/tissue volume (BV/TV) and osteocyte lacunar number density were also measured. This was carried out using the Analyze Particles toolbar in ImageJ for 2D measurements, and the Particle Analysis toolbar in BoneJ for 3D measurements.

4.2.4 Statistics

Statistical tests were carried out in Microsoft Excel 2013.

Pearson's correlation coefficient was used to characterise correlations between input and measured values for simulated datasets.

A one-sample, two-tailed, Student's t-test was used to test for differences between predicted values and measured values in simulated datasets.

A two-sample, two-tailed, Student's t-test was used to test for differences between two population means (2D and 3D results from real datasets).

4.2.5 Visualisation

Visualisations were generated in Avizo 9.3.0, a commercial software package for segmentation, analysis, and visualisation of 3D datasets, or in ImageJ's 3D viewer.

4.3 Results

4.3.1 Measurement of orientation of individual simulated vascular canals based on 2D sections and 3D volumes

4.3.1.1 Testing theoretical application and limitations of 2D and 3D canal orientation methods using simulated cylinder datasets

First, simulated datasets were used to test the theoretical efficacy of measurement methods based on 2D sections and 3D volumes, when geometric assumptions were met, and when datasets deviated from these assumptions.

100 randomly rotated cylinders were measured, with the aim of retrieving the rotation angles input when creating the models. First, de Boef's 2007 [6] method for estimating canal orientation from a 2D section was applied to the midslice of each dataset. When simulated canals were perfectly cylindrical (aspect ratio 1:1), 2D estimates of canal orientation using ellipse fitting to single cross-sections correlated almost perfectly with input values of both longitudinal and radial angles (r^2=0.968 and 0.995, see Figure 4.7 and Table 4.2).

In real biological datasets, canals may not be perfect cylinders. Therefore, elliptic cylinders were generated with cross-sectional aspect ratios of 1:1.25, 1:1.5, and 1:3 (100 cylinders for each), to test the sensitivity of the different methods to deviation from the assumption of cylindricality.

Even the smallest skew in aspect ratio (1:1.25) reduced the correlation between input value and 2D measurement of both radial and longitudinal angles (r^2=0.613 and 0.905), and more substantial skews further reduced the correlation further (Table 4.2).

Aspect ratio was found to be very important for accurately measuring the radial angle. At a skew of 1:1.5, the correlation was 0.376, which is almost no correlation. As the skew in aspect ratio increased, the measured radial angle was increasingly influenced by the random rotation of the skewed canal axis around the long axis of the canal rather than its radial orientation. However, the measured radial angle did not show a systematic bias (the average difference between the input and measured value was not consistently smaller or greater than zero (Table 4.2)).

The reduction in correlation coefficient with increasingly skewed aspect ratio for the longitudinal angle was smaller than for the radial angle. For a small skew (1:1.25), the correlation coefficient was still above 0.9, and above 0.8 at an aspect ratio of 1:1.5, at which point the r^2 for the radial angle was 0.376. Even when the aspect ratio was 1:3, the correlation coefficient was 0.634. However, a systematic bias was observed in the measured values: measured values of longitudinal angle were consistently underestimated, by between 6 and 14°using the aspect ratios included here (Table 4.2)).

When canal orientations are reported in histological publications, a set of indices are calculated to present the proportion of canals with largely radial, largely circumferential, and largely longitudinal orientations, following de Boef and Larsson (2007) [6]. Given a completely random orientation, approximately 25% of the canals should be characterised as mostly longitudinal (having a longitudinal angle that is greater than 67.5°. However, even with a small skew of 1:1.25 no measured value exceeded the threshold value of 67.5°used to classify canals

as longitudinal. Therefore these canals would all be misclassified, leading to highly inaccurate results.

Secondly, an implementation of Pratt's 2017 [14] method was used to measure the orientation of each cylinder in true 3D. 3D estimates of canal orientation using this skeletonisation method provided near perfect correlations between predicted and measured values for all aspect ratios (Table 4.2) and showed no systematic bias.

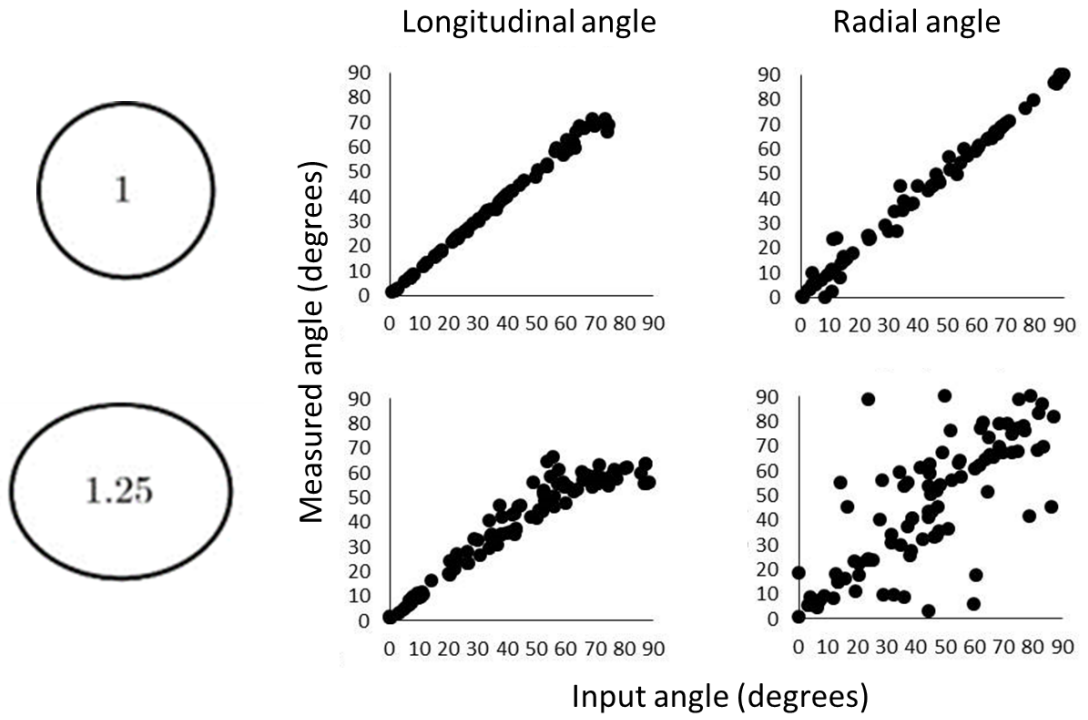

FIGURE 4.7: Sensitivity of 2D measurement of canal orientation to cylinder aspect ratio. Relationships between angles input during cylinder generation and angle measured from the transverse midslice, using simulated cylinders with aspect ratios of 1:1 and 1:1.25, n=100 for each case.

TABLE 4.2: Sensitivity of measurement of canal orientation 2D and 3D measurement to cylinder cross-sectional aspect ratio. 'True' (input) value for the radial and longitudinal angle of each cylinder is compared to the value measured by fitting an ellipse to the transverse midslice [6], and by skeletonising the whole shape[14].

	Aspect ratio of modelled cylinders	r^2 measured angle based on 2D ellipse fitting	Mean difference between true and measured value using 2D method	r^2 measured angle based on 3D skeletonisation
Radial	1:1	0.986	0.425	1.000
	1:1.25	0.613	0.088	0.999
	1:1.5	0.376	-1.930	0.998
	1:3	0.253	7.415	0.978
Longitudinal	1:1	0.995	-0.290	1.000
	1:1.25	0.905	-6.117	1.000
	1:1.5	0.819	-10.281	1.000
	1:3	0.634	-14.157	1.000

4.3.1.2 Comparing 2D and 3D methods for measuring vascular canals in real CT datasets

Following the simulated results, real datasets were used to test whether the geometric assumptions detailed above are met and therefore whether 2D estimations correlate with 3D estimations in real CT datasets, assuming 3D measurements are accurate.

No correlation was found between the indices calculated using 2D ellipse fits and those calculated using 3D skeletonisation for the radial index, longitudinal index, and laminar index of canal orientation (Figure 4.8). The laminar index was correlated (r^2=0.772), but the absolute values were significantly different (Student's t-test $p<0.05$). As predicted by the simulated datasets, almost no canals were categorised as longitudinal using a threshold angle of 67°.

As a comparison with a further standard measure, which does not rely on geometric modelling, the proportion of tissue that is mineralised (BV/TV) was measured using area in a 2D section and volume in a 3D volume. Unlike for the canal orientation, the result was strongly correlated between 2D and 3D estimates (r^2=0.8995).

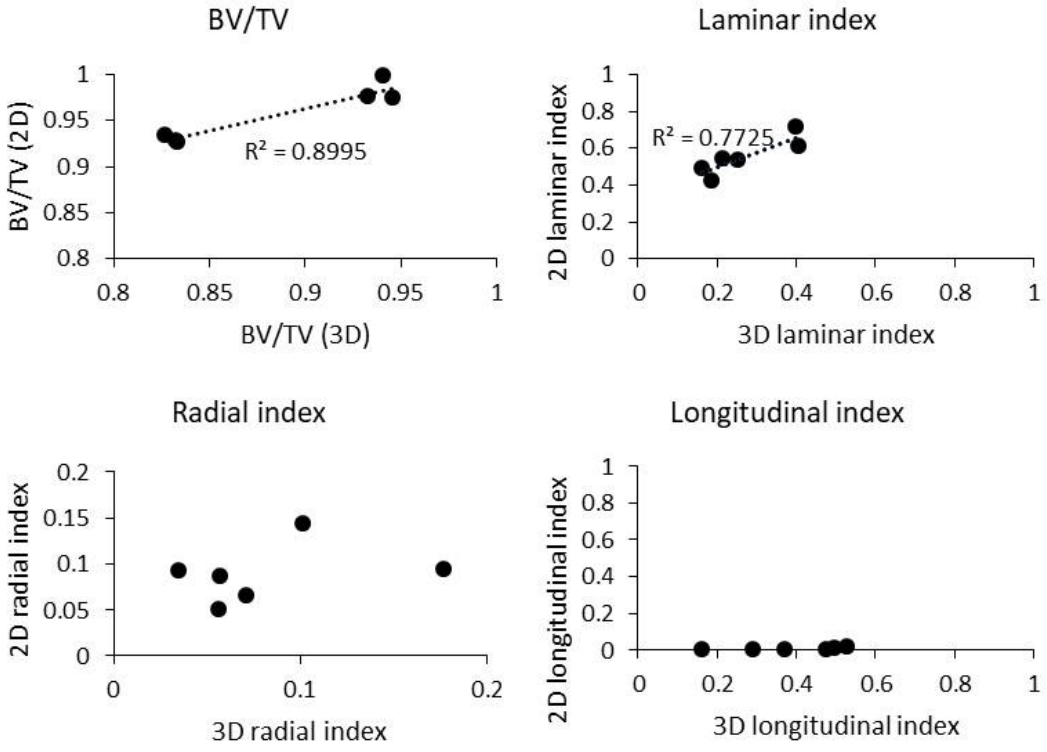

FIGURE 4.8: Do 2D measurements correctly predict 3D measurements in real datasets? Measurements based on 3D CT datasets from 5 duck bones. 2D measurements are based on the midslice of each dataset. Laminar and longitudinal indices have significant positive correlations (Pearson's correlation coefficient t= 3.685 and 2.866 respectively. $P<0.05$ for both). However, 2D measurements estimate almost no longitudinal canals, whereas 3D measures between 20 and 60 longitudinal. Laminar index does correlate significantly, actual values not the same: paired t test shows values are significantly different (two tailed Student's t-test, $p<0.05$).

4.3.2 Measurement of aspect ratio and volume of osteocyte lacunae based on 2D sections and 3D volumes

4.3.2.1 Simulated datasets

Shape and volume measurements were carried out using different methods for simulated ellipsoids, using three different simulated voxel sizes (0.33 μm, 0.8 μm, and 1.6 μm voxel size) and two different spatial arrangements (randomly oriented between 0 and 90°longitudinally, between 0 and 22.5°), to simulate different types of bone.

The first 2D method tested for measuring volume was based on modelling each ellipsoid from the major and minor axes of its transverse midslice. Using this method, the volume was underestimated in every case, except at 1.6 μm voxel size (Tables 4.3 and 4.4). The standard deviation of these estimates was also high, representing about 30% of the volume measurement. The volume was underestimated to a greater extent when the ellipsoids were aligned longitudinally, but standard deviation was much reduced. Therefore the results were more consistent, but less accurate when ellipsoids were aligned longitudinally, as in parallel-fibred bone.

The alternative 'pseudo-3D' method used two perpendicular midsections to better capture the full shape of the ellipsoid. When ellipsoids were randomly oriented, this measure slightly overestimated the volume of the shape, but standard deviation was even higher than that using the first method ($>$ 40% of the volume at the highest resolution). When ellipsoids were longitudinally aligned, the volume estimate was more accurate, and the standard deviation was lower, but the result was still statistically different from the true value (one sample T-test $p<0.01$), even at the highest resolution.

Finally, the ellipsoids were measured in 3D, either by counting the voxels contained within them or fitting an ellipsoid. The two methods produced very similar results. At the highest resolution, both methods produced results that were very close to the true value, with low variation between measurements. When compared across both the random rotation and limited rotation cases, very little distinguished the two methods.

The results found in this study are quite sensitive to voxel size. Although the highest resolution, 3D measurements were very accurate, the same methods used when voxel size was 0.8 μm produced results with a standard deviation several times larger. Nonetheless, at this voxel size, the mean value was close to the true value. However, at 1.6 μm voxel size, the measured volume was approximately 30% larger than the true value, and standard deviation was approximately 15% of the measured volume. Similar relationships between voxel size and measured volume were also present for the estimates based on 2D measurements.

An additional note is that at 1.6 μm voxel size, too few voxels were present for reliable ellipsoid fitting, and therefore not all datasets had ellipsoids fitted successfully.

The most accurate and precise estimation method of estimating both shape and volume was 3D ellipsoid fitting with high-resolution datasets, providing near perfect estimation whether the ellipsoids were aligned with the long axis or not (Tables 4.3 and 4.4).

For shape estimation, 3D methods were consistent regardless of the orientation of the ellipsoids. At high resolution, estimates were accurate and precise, but at low resolution, the

TABLE 4.3: Measurements of shape (aspect ratio) and volume of simulated longitudinally aligned (0-22.5°) oriented ellipsoid datasets using a 2D method based on the transverse midslice, a 2D method based on a transverse midslice and a second perpendicular slice, and 3D methods based on voxel numbers and ellipsoid fitting. n=100 for each case. Ellipsoids simulated as osteocyte lacunae imaged at three different voxel sizes (1.6 μm, 0.8 μm, 0.3 μm).

		True value	1.6 μm		0.8 μm		0.3 μm	
			Mean	SD	Mean	SD	Mean	SD
2D	Volume (xy)	196.25	203.60	75.46	134.70	33.60	129.89	41.56
	Volume (xy, xz)	196.25	340.11	106.38	209.10	73.00	227.49	95.59
	Shape	0.33	0.61	0.15	0.69	0.20	0.62	0.21
3D	Volume (ellipsoid)	196.25	310.86	49.01	201.48	17.87	195.29	5.51
	Volume (voxels)	196.25	343.65	53.79	203.13	14.05	192.05	2.25
	Shape	0.33	0.40	0.05	0.33	0.03	0.32	0.01

TABLE 4.4: Measurements of shape (aspect ratio) and volume of simulated longitudinally aligned (0-22.5°) oriented ellipsoid datasets using a 2D method based on the transverse midslice, a 2D method based on a transverse midslice and a second perpendicular slice, and 3D methods based on voxel numbers and ellipsoid fitting. n=100 for each case. Ellipsoids simulated as osteocyte lacunae imaged at three different voxel sizes (1.6 μm, 0.8 μm, 0.3 μm).

		True Value	1.6 μm		0.8 μm		0.3 μm	
			Mean	SD	Mean	SD	Mean	SD
2D	Volume (xy)	196.25	114.09	46.66	82.90	7.77	67.39	2.51
	Volume (xy, xz)	196.25	259.01	68.56	200.70	25.20	173.62	19.00
	Shape	0.33	0.43	0.06	0.42	0.04	0.39	0.05
3D	Volume (ellipsoid)	196.25	307.22	62.74	230.90	17.60	204.22	2.74
	Volume (voxels)	196.25	299.42	62.98	217.50	14.30	192.74	2.28
	Shape	0.33	0.47	0.07	0.39	0.02	0.35	0.00

aspect ratio was underestimated. For the 2D estimates, a single slice was incapable of capturing shape whether or not the ellipsoids were aligned, and two sections only improved estimation if the ellipsoids were aligned (Table 4.4). However, if ellipsoids are aligned then a 2-slice pseudo-3D estimate was able to measure shape with reasonable accuracy, though less accurately than the 3D measurement.

4.3.3 Real datasets

4.3.4 Measurement of mean shape and volume of populations of osteocyte lacunae in real datasets

3D measurements of osteocyte lacunae volume and number density were compared with the 2D two-section method tested above. Shape was not tested since the voxel size used was demonstrated in the previous section to be insufficient to accurately measure aspect ratio in osteocyte lacunae. Mean osteocyte volume was not correlated between 2D and 3D estimates.

However, osteocyte lacunar number density was strongly correlated between the 2D and 3D count (r^2=0.892). It is important to note that the absolute values are different due to measurement methods: in 2D, cells were counted per unit area, while in 3D they were counted per unit volume. With real thin sections, a number per unit volume could be estimated as the section has thickness.

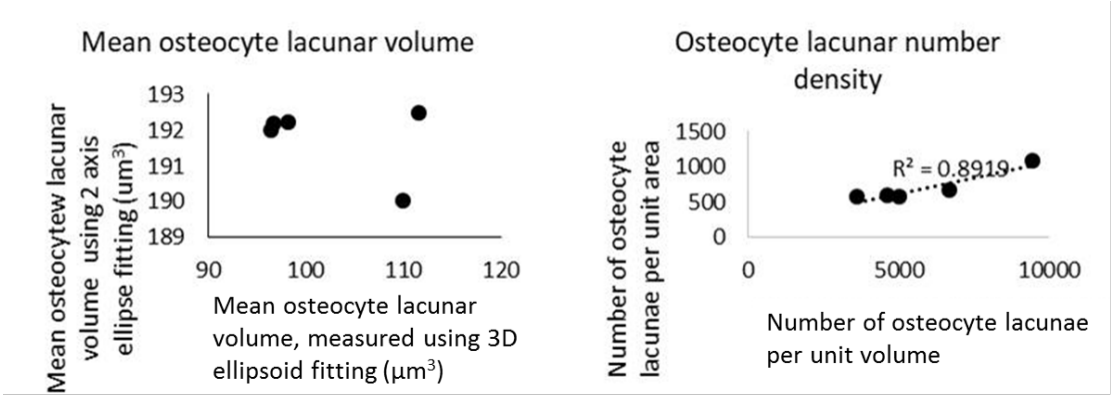

FIGURE 4.9: Do 2D measurements correctly predict 3D measurements in real datasets? Measurements based on 3D CT datasets from 5 duck bones. 2D measurements are based on the midslice of each dataset. Lacunar volume estimated by fitting 3D ellipsoids to segmented objects, and by measuring mean axis lengths from two perpendicular sections. Osteocyte lacunar number density measured per unit volume from 3D volume, and per unit area from 2D transverse section.

4.4 Discussion

4.4.1 Vascular canal orientation

The results of this study showed that, the 2D estimation method for measuring canal orientation published by de Boef and Larsson (2007) [6] is effective only as long as canals are perfectly cylindrical. In the simulated, idealised canals used in this study, a small skew in the cross-sectional aspect ratio of the canal was sufficient to reduce the precision of the radial angle measurement, and the accuracy and precision of the longitudinal angle measurement.

The radial angle was found to be highly sensitive to changes in aspect ratio, an important finding for application to histological sections. From a single section, it is not possible to tell whether a canal is elliptic or not, since that apparent shape may relate to its longitudinal orientation. Therefore, it is not possible to test whether the assumption of cylindricality has been met and whether the method can be considered at all reliable. Even with more-or-less cylindrical canals (aspect ratio 1:1.25), the estimation of radial angle could be quite inaccurate and therefore reduce the validity of any studies using radial orientations to estimate, for example, growth rates [70, 109, 143] or bone loading [21]. The results of any studies applying these methods should therefore be taken with caution.

Additionally, the longitudinal angle was consistently underestimated using the 2D method, as found in a previous study [108]. Here, this underestimation was shown to lead to a high proportion of canals being miscategorised. This methodological issue would have a large effect on the results of any study implementing it.

The degree to which the longitudinal angle is underestimated depended on the aspect ratio of the cylinder. If the aspect ratio of each canal could be identified, then perhaps a correction could be applied to reduce the underestimation of radial angle. Unfortunately, it is not possible to disentangle aspect ratio from longitudinal orientation from a single 2D section. Therefore it would not be sufficient to apply a correction value to the measurement without knowing the aspect ratio, which, in 2D, cannot be disentangled from orientation [23]. If multiple sections were taken, it may be possible to identify the true orientation of canals, but this would require serial sectioning, which is both time consuming and destructive[144].

The 3D method published by Pratt et al., (2017) [14], on the other hand, was not sensitive to changes in cylinder cross-sectional aspect ratio, even when aspect ratio was 1:3. 3D visualisations of skeletonisation demonstrated that skeletons and branch points were accurately identified by the method applied (Figure 4.5), so 3D measurements of orientations in real datasets are expected to be accurate. This method is therefore more robust to variation in canal shape and is a more accurate method for measuring the canal orientations within bone.

In real biological datasets, shapes are seldom perfectly symmetrical or perfectly cylindrical. In the real datasets used in this study, 3D visualisation suggests that canals are not perfectly circular in cross section (Figure 4.5). This result supports the result found by Pratt et al., [14], and is similar to results found in osteons [23] which have also been traditionally described as cylindrical[6], but in fact are elliptic cylinders [23].

Real CT datasets from young duck bone were used to compare the results produced using the 2D and 3D method. This aimed to test whether, despite the theoretical limitations of 2D measurement methods, there were any correlations between the 3D measurements (interpreted as closer to the true value following simulated results and visual verification of skeletons) and those estimated based on a 2D section. If so, it is possible that the assumptions of the 2D measurement method were met more closely than was apparent. However, no correlations were found between the results from the 2D and 3D methods of measuring canal orientation in the same samples. The lack of correlation between 2D and 3D estimates of orientation indices suggests that appropriate assumptions for 2D estimation have not been met. Worst was the estimate of longitudinal canals, of which almost none are measured in 2D despite their presence being apparent from visualisations and 3D measurement. These findings supports previous work which has also demonstrated underestimation of longitudinal canals, as well as overestimation of laminar canals [18], which was also observed here.

In addition to the geometric arguments already made, further considerations apply in comparing 2D and 3D visualisation methods. Firstly, in a 2D physical section, the appearance of that section will depend on the angle at which it was cut from the bone. Although sections are described as ‘transverse’, the chance of that section actually being exactly transverse is highly unlikely given manual sectioning protocols relying on subjective and often awkward cutting of samples. For canals, the observed angle will clearly be different if the section is cut at a different angle.

For canal orientations, it seems clear that 3D analysis is necessary for accurate quantification.

It is possible that differences in vascular orientation between different limb bones in previous studies are reflecting some aspect of the organisation of bone microstructure, but from individual sections it is impossible to say whether this is truly reflecting orientation or whether

shape is also important. While distinguishing the two may not be necessary for simply recognising bone types [130], if the functional relationships between bone loading and microstructure, and bone deposition and microstructure are to be understood, the difference is important, as the two different explanations may produce functionally different materials.

Although canal orientation could not be accurately measured using 2D histological sections, the proportion of mineralised tissue present (BV/TV) was found to be accurately estimated from a single section. BV/TV is a straightforward calculation of volume or area fraction, and its only assumption in terms of extrapolating from 2D to 3D is that the tissue is homogeneous throughout the bone. This may not be the case across an entire bone, but within the small sample regions studied here, the tissue was clearly fairly homogeneous in its BV/TV value. The measurement is not reliant on modelling shape or orientation from limited information and is therefore more accurate. It may be argued that this measurement, therefore, could be carried out with some confidence even if a single 2D section is used, and therefore some characterisation of the cortical bone can be carried out quantitatively even if 3D imaging methods are not available. However, the measurement would be more accurate if several sections were taken to account for intrasample variation.

4.4.2 Osteocyte lacunar shape and volume

Measurements of osteocyte lacunar size have been used in studies estimating genome sizes [20, 105], growth rates, and body mass between different species. Osteocyte lacunar shape is used to distinguish different bone types and therefore growth rates and age of an animal. Therefore it is important to be able to accurately measure both shape and volume of osteocyte lacunae to compare between species.

As standard, a single transverse histological section is described from a bone. In some studies, a more straightforward measurement of cross-sectional area has been used [64], but this fails to capture the 3D nature of the cell spaces. Therefore, the first method tested used only the transverse midslice to characterise the cell, fit an ellipse to the cross section, and use this to model the cell as an ellipsoid. This method underestimated lacunar volume in all cases except for the 1.6 μm voxel size. It very substantially underestimated lacunar volume when the lacunae were aligned longitudinally, since the transverse cross-section cuts through the smallest axes of the shape. This result highlights the importance of being able to distinguish shape or size from orientation, as these cells would appear much smaller if a transverse section was used compared with a longitudinal section. Additionally, very high standard deviations mean that it would be difficult to identify differences in mean lacunar volume between samples based on this method.

Given the importance of orientation of ellipsoids in measuring their shape, and based on the observation that osteocyte lacunae tend to orient parallel to the long axis of the bone[16], a second published method was tested to try to better characterise the scalene ellipsoid shape of osteocyte lacunae. This second method uses two perpendicular sections to model the ellipsoid. Using this method, it was found that measurements were closer to the true value, but that standard deviation was higher compared with using only one section. When ellipsoids were longitudinally oriented (between 0 and 22.5°), the standard deviation was reduced and it could

be argued that this method, under these conditions, provides a reasonable measure of lacunar volume in the absence of a true 3D measurement.

However, this method must be applied with some caution. In real bone, not all cells are likely to align with the long axis of the bone since they align with collagen orientation [86] which, in osteonal bone, runs circumferentially around osteons, and in woven bone is random, resulting in randomly oriented osteocyte lacunae. Therefore, this method can only be reliably applied to osteocyte lacunae in parallel-fibred bone and not applied more broadly.

In addition, in real samples, results for osteocyte shape and volume would be less accurate than those seen here because two sections could not capture the same osteocyte lacunae and therefore only average measurements could be used.

On the other hand, 3D measurements of osteocyte lacunar shape and volume were independent of orientation of cell, and are therefore more robust to differences in bone type and cell orientation. 3D measurement is therefore a more accurate method of measuring osteocyte lacunar shape and volume, whether ellipsoids are fitted of the number of voxels contained within the shape simply counted.

Measurements of osteocyte lacunar volume differed between different simulated voxel sizes, whether 2D or 3D methods are used. Osteocyte lacunae fall near the resolution limit for shape and volume estimation in CT scans. Although they can be resolved even with slightly lower resolution scans and in lab-based systems, the small number of voxels present make these estimates inaccurate. Firstly, the number of voxels within the shape is simply insufficient to accurately describe the shape and identify major axes. Secondly, accuracy is decreased due to partial volume effects leading to errors in discretisation. Partial volume effects occur where pixels at the edge of the ellipsoid cover both object and background, and therefore have an intermediate grey value, but must be classified as one or the other during thresholding. Where few pixels are present, partial volume effects are stronger as edge pixels make up a greater proportion of the total object. Partial volume effects also mean that slight changes in threshold values can have large effects on the measured volume and shape of an osteocyte lacuna, even if not their number. Therefore, when comparing such structures, thresholding and image processing must be consistent between different datasets. At higher resolutions (more voxels), the result will be more robust to differences in threshold, again highlighting the importance of using a sufficiently high resolution.

The effect of changing voxel size on accuracy of measurement highlights the importance of selecting the appropriate spatial resolution for the feature of interest, especially for shape and volume. If osteocyte lacunae are measured using CT datasets with inappropriately large voxel sizes, volume estimates are likely to be highly inaccurate and variation large making it impossible to compare accurately between samples. Spatial resolutions are equally important for measuring vascular canals accurately, as larger voxel sizes may be sufficient to resolve the structures but not measure them accurately. At the voxel sizes used here, the problem should be minimal, but at larger voxel sizes, such as 5-15μm, image quality and canal resolution has been found to degrade [145],

Although shape and volume estimates are inaccurate at lower spatial resolutions, it may still be possible to resolve and segment the structures of interest. Even in scans carried out at 1.6 μm voxel size, osteocyte lacunae were still segmented successfully, and a volume estimate was

successfully produced for every simulated lacuna at this voxel size. Therefore, although the measurements were not accurate, the counts of osteocyte lacunar number and therefore osteocyte lacunar number density are expected to be accurate. Additionally, because number density does not rely on geometric assumptions, it is possible to estimate this from 2D sections. In the real datasets measured here, osteocyte lacunar number density scaled very closely between 2D and 3D counts, suggesting that density is consistent within the volumes measured.

Therefore, in order to accurately measure osteocyte lacunar shape and volume, 3D datasets should be used, at the highest resolution possible, and at least 0.8μm voxel size. However, counts can be carried out at slightly lower resolutions, making osteocyte number density counts possible in lab-based scanners. If 3D imaging is unavailable, counts could also be estimated based on 2D sections.

4.5 Limitations and future work

The simulations used here were highly simplified models of vascular canals and osteocyte lacunae, using idealised geometric shapes, and therefore although the limitations of the measurement methods have been tested under conditions of idealised geometry, they have not been tested fully under more realistic conditions. For example, the canals generated were straight sections with no branch points, while real datasets have curved canals and branch points. This limitation was addressed to an extent through the use of real datasets and visual verification that segmentation and skeletonisation accurately reflected the vascular networks present, and branch points were correctly identified.

In addition, the real datasets used in this study used a voxel size of 1.6 μm. While this is sufficient for visualising the vascular canals and for identifying the osteocyte lacunae, it is not sufficient to characterise the shape and volume of the osteocyte lacunae. In order to fully test the methods, it would be necessary to compare results obtained from the same datasets at different scan resolutions, either using different scan settings, or by simulating this through post-scan binning of higher-resolution datasets.

More broadly, μ-CT does have some limitations which mean that in some cases and for certain questions, other approaches might be more desirable. For example, the resolutions required to accurately measure osteocyte lacuna shape and volume are not easy to achieve using a lab-based CT scanner, and, if achieved, require very long scan times. For the highest resolutions, smaller samples are optimal, and therefore, currently, in a lab-based system, samples may still need to be cut. In synchrotron systems, the highest spatial resolutions and better signal to noise ratios can be achieved due to brilliance which is orders of magnitude greater. However, access to these facilities is limited, restricting their use as a standard tool. Yet these systems are necessary if the shape and volume of osteocyte lacunae are to be measured accurately.

In addition, traditional histology can provide certain information impossible to gain using CT, namely the orientation of the collagen fibres, important for understanding the deposition of the bone and its mechanical properties. However, this could be addressed using the orientations of the osteocyte lacunae since they tend to align with the collagen network. In the past, resolution of cement lines and therefore osteons was a problem, but phase contrast approaches now allow 3D visualisation of osteonal structures [134].

4.6 Conclusions

The findings of this study have important implications for the quantitative study of cortical bone microstructure. There is a clear need for 3D imaging for accurate measurement of canal orientation, and osteocyte lacunar shape and volume. Given the inaccuracies identified even using idealised and best-case-scenario datasets in this study, applying the 2D methods studied here to real datasets will result in inaccurate results and likely incorrect conclusions.

Estimations of 3D measurements using 2D sections rely heavily on strict geometric assumptions. If these are met, then these estimates can be accurate, but even slight deviations from these assumptions can lead to inaccurate and imprecise results.

3D measurement of cylindrical and ellipsoidal objects, relevant to studying bone histology, and many other fields from engineering to plant sciences, requires a truly 3D approach. Estimates based on 2D sections rely on strict geometric assumptions seldom met in biological samples, and therefore measuring shape and orientation is often impossible from 2D. Although here the focus is on intracortical porosity in bone, the same shapes and problems are present in a wide range of structures, making the results here applicable far beyond bone.

Canal (cylinder) orientation cannot be estimated from 2D sections unless the assumption of perfect cylindricality can be shown to have been met, which is impossible from 2D sections alone, and sections are cut perfectly perpendicularly to the bone axis. Therefore, any study aiming to include measurements of canal orientation would be unwise to use estimates based on 2D ellipse fitting and should prioritise 3D measurements based on high-resolution CT scans.

Other measurements vary in their accuracy in 2D and 3D, and this must be taken into account when quantitative studies are carried out. Osteocyte lacunar (ellipsoid) shape and volume can be accurately measured using CT imaging if sufficient resolution is achieved but this is not always achievable in lab-based systems, therefore scan setup and resolutions are critical in achieving accurate results.

While some measurements are impossible from 2D sections, others can be estimated reasonably accurately, including BV/TV and possibly estimates of osteocyte number density, though both would be improved by larger sample volumes, or a larger number of sections. However, if we are to fully understand how bone microstructure and biological traits are correlated, including metrics that describe shapes, volumes, and orientations, as well as connectivity, tortuosity, heterogeneity, it is crucial to carry out studies using true 3D metrics. Currently, our understanding of these structures and how they relate to biology is being held back by imprecise and inaccurate measurements which may be hiding truly informative correlations.

Chapter 5

Testing how bone microstructure changes throughout development in two modern birds

5.1 Introduction

Estimating developmental age in animals is important for answering biological questions, in both extant and extinct species. For a modern population of wild animals, being able to estimate the developmental ages of individuals allows interpretation of age-related behaviour [146, 147], and population structure [148]: key for understanding, for example, how a population will respond to environmental change. For fossil animals, interpreting developmental age allows us a better understanding of traits such as growth rate (and therefore how long an animal takes to reach a particular size). This can in turn provide information about the ecological role of the animal. For example, prey animals have been thought to compete with their predators in some cases by outgrowing them [149]. Age and relative maturity at a particular size or age helps us to understand life history in extinct animals. These are important for understanding the biology of an extinct animal, and are particularly important in understanding the evolution of birds, as the origins of their rapid growth and metabolism are still debated [36, 127, 128].

Developmental age of specimens is also crucial for accurate taxonomy and for understanding evolution of particular traits. If key characters used in taxonomy are in fact related to juvenile traits rather than species-specific traits, this can cause inaccuracies in building phylogenies and therefore understanding evolutionary change. Additionally, it is important to be able to distinguish between a new species, and a juvenile specimen of an already-described species [150]. In birds, this is a salient issue: more than 120 species of Mesozoic birds have been described, but with a few significant exceptions [46], most are represented by only a single specimen. It is possible, and perhaps likely, that some of these specimens are in fact juvenile representatives of other species. In several dinosaur species, the validity of certain species have been strongly debated for this very reason [151, 152], and recent identification of a subadult Early Cretaceous bird has led to reidentification of other specimens [51].

Estimating developmental age in fossil species is not straightforward, as each specimen is present only at a single age stage and development cannot be studied directly. Instead, development and age-related changes can be studied in extant species, and extrapolated to extinct species, assuming that the traits studied are conserved through evolutionary time, or that changes can be extrapolated.

In many extant species, particularly reptiles [146, 147] and amphibians [153], developmental age is estimated using skeletochronology, where the number of years of life are measured by counting incremental growth rings in the bone cortex, in the same way as counting the rings in a tree. In temperate climates, the rate of bone deposition decreases at particular times of year, related to changes in temperature, or availability of food or water, or dependent on photoperiod [59] and results in distinct annual bands called Lines of Arrested Growth (LAGs). LAGs are present in the cortical bone of a wide variety of vertebrates, and have been used to estimate age in taxa from turtles [146, 147] to mouse lemurs [59], though their accuracy is variable [154, 155]. LAGs are also present in the bones of some modern birds, such as kiwis [156] and the parrot *Amazona amazonica*[157]. However, the presence of LAGs is dependent on skeletal growth occurring over more than one year [156]. In extant birds, growth is exceptionally rapid, and most species reach full adult size within a single season (in the scale of weeks rather than years).

Despite the lack of LAGs, estimating developmental age in fossil birds from bones is already possible to an extent. Estimates of age use observations of thin sections through bones, and qualitative descriptions of the patterns observed in the density and arrangement of vascular canals and size and shape of osteocyte lacunae (spaces in the bone where bone cells reside). In very young bone, most of the bone tissue is of the woven type, with irregular arrangement of collagen fibres, a porous structure, and large, globular osteocyte lacunae [89, 158]. This bone type is quickly laid down but weak, and is gradually infilled or replaced as the bone ages [89]. Initial bone deposition rapidly fills space and enables a high degree of plasticity and also nutrition for the growing bone [129]. However, the foam structure produced initially lacks much mechanical stiffness, and therefore is not appropriate when the animal begins to walk [129]. In fibrolamellar bone, the large spaces in the initially deposited bone, containing vascular canals, are infilled by concentric layers of bone, forming primary osteons. In adult bone, very little woven bone is present [89]. Infilling is important because the strength of cortical bone tissue is strongly inversely related to its porosity [159], so less porous bone tissue will be substantially stronger and more resistant to fracture.

In more slowly deposited bone, tissue may be deposited at the periosteal surface of the bone in thin layers, forming lamellar bone [22]. In some vertebrates, this type of bone makes up the majority of the bone present [22], but in birds it is usually only found at the very outer surface of the bone, in a region called the Outer Circumferential Layer (OCL) [160]. This layer forms in birds after they reach their adult body size and represents a small amount of slow residual growth.

In addition to these bone types, there may also be subtler clues relating to bone maturity. As an animal grows, its growth rate changes, slowing as full size is approached [26]. Bone deposited at different rates is described as having different microstructural properties [2, 108], and therefore more slowly deposited bone towards the periosteal surface may appear different to bone deposited earlier in life when growth was faster [19]. The density, size, and orientation of

vascular canals has been related to growth rate [19, 108]. For example, radially oriented canals (like the spokes of a bike wheel) have been correlated with more rapid tissue deposition [108], while longitudinal and laminar canals have been correlated with slower deposition, although evidence for this relationship is mixed [15, 108].

Alternatively (or additionally), a laminar canal orientation of canals has been linked to resisting torsional resistance [15], most important in the wing bones of flighted birds, though recent 3D quantitative study has found that in birds the humerus does not necessarily contain more laminar canals than the femur [18]. Previous studies relied on 2D methods [21, 161], which may explain the differences between this and previous studies, based on the findings from Chapter 4 of this thesis. Therefore the relationship between torsional loading and laminarity in birds is not yet fully understood.

In addition to bone deposition, the microstructure of bone is also influenced by remodelling. As cortical bone expands laterally, material is also resorbed from the endosteal surface. Later in life, bone may be remodelled to form secondary osteons: in humans secondary Haversian systems are formed early in life, though in other animals such as bovids (cattle), secondary remodelling occurs to a lesser extent [162] and in small birds remodelling may hardly occur at all [163]. Therefore, although bone microstructure reflects its depositional history, this can be altered by secondary remodelling, especially for early-deposited, endosteal regions of bone [22], though to a greater or lesser extent depending on species.

Therefore, very young bone can be identified by its relatively porous structure, random orientation of collagen fibres, and large, round osteocyte lacunae. Adult bone can be identified by the presence of an OCL, and potentially secondary remodelling. Growing bone can be identified as somewhere in between, with vascular arrangement providing information on growth rate, which changes with age and may also provide clues to bone maturity.

The different factors described above have been used to define a set of bone types [130], which are often used to interpret the biology of a fossil specimen. Although these observations have been used to interpret bone microstructure and make inferences about age, growth rate, and taxonomy, this approach has several problems. Traditional histological techniques based on thin sections are destructive, meaning that sections often cannot, or would not, if not completely necessary, be made. Secondly, this categorisation aims to place into neat boxes what is in fact a continuous set of variables which may, if measured quantitatively, provide more information than the reductive bone types [6].

Only recently has any work been carried out to characterise age-related changes in bone microstructure using quantitative, and also 3D approaches [108]. Histological study of fossil bone is becoming increasingly led by 3D approaches [24, 115], mostly using synchrotron-based micro computed tomography to non-destructively image the internal microstructure of fossil samples and, in some cases, quantify the results. These approaches have the potential to allow a wider range of specimens to be studied in greater detail and provide additional information unavailable using 2D methods alone. The results of these new studies have provided insight into bone structure not previously possible [5], and, in some cases, have thrown into question results of previous 2D studies [18]. Given findings in Chapter 4 that 2D and 3D quantification methods can provide completely different results, and that 2D methods can have significant systematic biases, it is critical at this point in the 3D study of bone to reassess what we know about bone microstructure in birds and how it changes with development. If we are to

accurately assess the microstructure of fossil bones, a systematic comparative dataset studying age-related changes in 3D bone microstructure in extant birds is required.

To test the hypothesis that age-related changes in cortical bone microstructure can be used to help estimate developmental age and better understand bone development in birds, 3D data on macrostructure and diaphyseal microstructure of avian bones was collected throughout development in a growth series of the domestic duck (*Anas platyrhynchos*) and ring-necked pheasant (*Phasianus colchis*) using using synchrotron-based computed tomography.

These two species were selected because they are both precocial and use their legs from day 1 after hatching and both have similar body masses, resulting in similar loading patterns at least in the lower limb. However, the two species differ in two important ways.

Firstly, their relative growth rates. Commercially reared ducks have very rapid growth rates, reaching approximately fully adult body mass (approx 2 kg) in 7 weeks [26, 141]. Pheasants have been less selected for rapid growth, and reach full body mass (up to 1.3 kg) in closer to 18 weeks [26].

Secondly, the two species differ in the age at which they first fly, and therefore the development of their wings. In the duck, the femur and tibiotarsus experience loading from day 1 as ducklings are precocial and begin to walk from hatching. However, ducklings cannot fly until 56 days of age [26] so the humerus is minimally loaded until this point [164]. In the pheasant, the lower limb bones experience early loading in the same way as the duck, but in contrast to the duck the wings develop much earlier, with flight appearing when the birds are only 11 days old and are far from reaching full body mass [26]. Therefore, the pattern of loading in the wings is distinct between the two species. In the pheasant, both upper and lower limbs could be described as following a precocial developmental pattern, while in the duck the upper limbs follow a more altricial developmental pattern [164, 165].

In precocial development, limbs grow more slowly but must be functional from very early in development [164, 166]. In altricial development, growth is more rapid and there are minimal loading-related requirements, and in fact in altricially developing species if bones are loaded too early this can lead to problems with bone development [167]. Therefore, age-related changes in development might be expected to differ between species or even limbs with different growth patterns and the ability to extrapolate to fossils depends on accurate characterisation of these differences.

The domestic duck samples used ranged from 1 day post-hatch to 2 years of age (Table 3.1), covering the full development and, to some extent, ageing of ducks [22]. The pheasant samples used ranged between 2 weeks and 6 weeks of age, with additional samples known to be adults but exact age unknown. Samples of the tibiotarsus, femur and humerus were compared as these bones are under distinct loading conditions to each other both in adulthood and at different developmental stages.

- Hypothesis: age-related changes in bone microstructure can be used to help estimate developmental age in birds.
- Objective: Characterise bone microstructural changes throughout development in two modern bird species (duck and pheasant). Specific aims:

1. To investigate how porosity changes throughout development and differs between two modern bird species
2. To investigate how canal orientation changes throughout development and differs between two modern bird species
3. To investigate how osteocyte lacunae change throughout development and differs between two modern bird species

5.2 Methods

5.2.1 Sample preparation

Samples of *Anas platyrhynchos* (commercially produced strains of a Mallard/Pekin cross known as Cherry Valley) were kindly donated by Warawee duck farm. Samples of *Phasianus colchis* were kindly donated by Blackmore Game Farm, and two additional adult pheasant samples were donated by Matt Sharp (University of Southampton). The samples donated by the farms were individuals that were naturally deceased throughout development. No animals were killed for this study. For most age classes, several individuals are available but as mortality rates decrease with maturity, only a single individual was available for the young full size individuals (Table 5.1). Therefore, in addition to these samples, a further 3 ducks were purchased from Iceland supermarket, as few samples were available at a subadult stage (here defined as near full size but not yet fully adult). These ducks fitted into the subadult stage as ducks in the UK are slaughtered for meat at approximately 7 weeks of age [141], when they are close to full body mass but not fully mature [26].

For the pheasant samples, ages to the nearest week were provided by the farm. For the ducks, the ages were provided for an individual at 1 day old, one at 6 weeks old, one at 3 months old, and three at 2 years old. To estimate the ages of samples between 1 day and 6 weeks old, linear growth was assumed between these ages, and body mass was used to provide an approximate age. For most analyses, only development up to 7 weeks of age was studied, as this includes the development process, but not ageing. However, in some cases, these have been compared to older adults (only available in the duck).

The long bones (humerus, tibiotarsus and femur) were harvested, their maximum length and minimum diaphyseal diameter measured using callipers, and fixed using 4% paraformaldehyde (PFA) for at least 48 hours and then transferred to 70% ethanol.

Birds for this study fall into the age classes shown in Table 5.1.

5.2.2 Scan setup

Samples were prepared to ensure the whole width fitted into the field of view (therefore samples were less than approximately 2 mm across), in order to prevent artefacts that may occur if the object was larger than the field of view, which could make images unusable. For smaller bones, the cortex was left intact lengthways, but older samples were cut lengthways to produce the sections shown in Figure 3.10. The anatomical position of each quadrant was consistent and recorded, and could be matched with the anatomical position of the whole bone.

TABLE 5.1: Duck samples used in growth series grouped into size/age classes

Age class	No. ducks	No. pheasants
1-7 days	7	0
8-14 days	1	3
15-21 days	5	1
22-28 days	2	0
29-35 days	1	3
36-42 days	1	3
43-49 days	3	0
Subadult	1	2
Adult (2 years)	3	0

Synchrotron scans were carried out at SLS TOMCAT on prepared individual bones, mounted as shown in Figure 3.3, using 18.5 KeV energy, and 180°rotation. Each scan took approximately 6 minutes. Pheasant and additional duck sample scans were carried out at DLS I13-2, using 180°rotation, and a voxel size of 0.8 μm, increased after scanning to 1.6 μm by averaging across values to improve signal-to-noise-ratio, and match the voxel size of datasets collected at SLS.

5.2.3 Image segmentation

Images were segmented following the segmentation workflow detailed in the Methods chapter. For DLS datasets, contrast was better than SLS datasets, but scans were slightly noisier, so a Gaussian blur (1 pixel kernel size) was applied before thresholding. Ideally, the same image processing would be applied to both sets of scans, but given the differences in scan quality, it was not possible to find a workflow which was optimised for both.

For the adult femur samples, medullary bone, a transitory bone type associated with egg-laying in birds [168], was present on the endosteal surfaces. Given in this study cortical bone is being studied, the cortical masks were manually edited to remove medullary bone and include the cortical bone only.

5.2.4 Data analysis

Segmented scans were analysed using methods discussed in Chapter 4. Bone volume fraction (BV/TV), defined as the proportion of mineralized tissue compared with the whole cortical bone region, canal diameter, osteocyte lacunar volume, and osteocyte lacunar number density were measured using the Particle Analysis tools in BoneJ [125], a plugin for ImageJ designed for measuring bone. The Fiji distribution of ImageJ was used [123].

Cortical thickness was measured using Particle Analysis tool in BoneJ. A cortical mask was produced by filling pores within the cortical bone and the thickness of the mask was measured. Relative thickness was defined as the thickness of the cortex as a proportion of the diameter of the bone.

Canal orientation was measured using the implementation of Pratt's 2017 method [14] detailed in Chapter 4. Segmented canal networks were thinned to single pixel lines (skeletonised) using the Skeletonize 2D/3D tool within BoneJ, and the network analysed using the Analyze Skeleton tool within the same plugin. The branch points of the skeleton were used to define individual

canals as straight segments and the orientation of each segment calculated as a radial angle and a longitudinal angle using a custom Python script. These two angles were then used to calculate a radial index, a laminar index, and a longitudinal index, describing the proportion of canals in the network with those specific orientations. The indices were weighted by canal length to reduce the undue influence of short canal segments.

3D visualisations were generated in Avizo 9 (Thermo Scientific), commercial 3D visualisation and analysis software.

For visualisations of osteocyte lacunar distributions, lacunae were assigned a colour based on their volume, ranging between dark blue (smallest) and red (largest).

5.2.5 Statistics

Statistical analyses were carried out in Microsoft Excel or in Graphpad Prism 7 (Graphpad Software, La Jolla, USA).

Pearson's correlation coefficient was used to characterise correlations.

ANOVA was used to test for differences between means, and Tukey's multiple comparison test was used to test for pairwise differences.

5.3 Results

5.3.1 Macrostructure: duck and pheasant long bones grow anisometrically, to different extents

First, macrostructural measurements (bone length and cortical thickness) were used to assess growth patterns in the two different species, and to compare growth in the humerus, tibiotarsus, and femur for each species. These measurements were important for contextualising the microstructural patterns observed in the following sections and understanding the differences between the two different species.

In both species, the tibiotarsus was consistently the longest bone (Figure 5.1).

In the duck, the lower limb bones grew more rapidly at early stages of development than the upper limb. The femur and tibiotarsus scaled isometrically with each other, but growth of the humerus was relatively delayed (Figure 5.1). As a result, its rate of growth was faster, but later, than the lower limb bones, following a more altricial growth pattern.

In the pheasant, all three bones scaled with each other: growth of the humerus was earlier than in the duck.

In the duck, the relative thickness of the cortex in the lower limb bones increased at first, then decreased, reaching a peak relative thickness at approximately 10 days for the femur and 21 days for the tibiotarsus (Figure 5.2). For the humerus, the relative thickness of the cortex remained more consistent throughout growth.

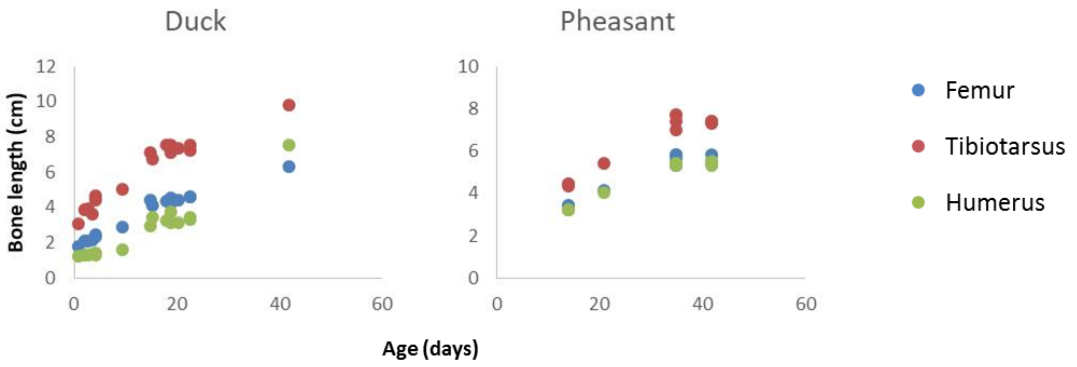

FIGURE 5.1: Growth curves (bone length in cm) for the humerus, femur, and tibiotarsus in the duck (*Anas platyrhynchos*) and pheasant (*Phasianus colchis*).

In the pheasant, the relative cortical thickness increased at first, then decreased, reaching a peak relative thickness at approximately 21 days for all three bones. All three bones had similar relative cortical thicknesses to each other at all ages studied.

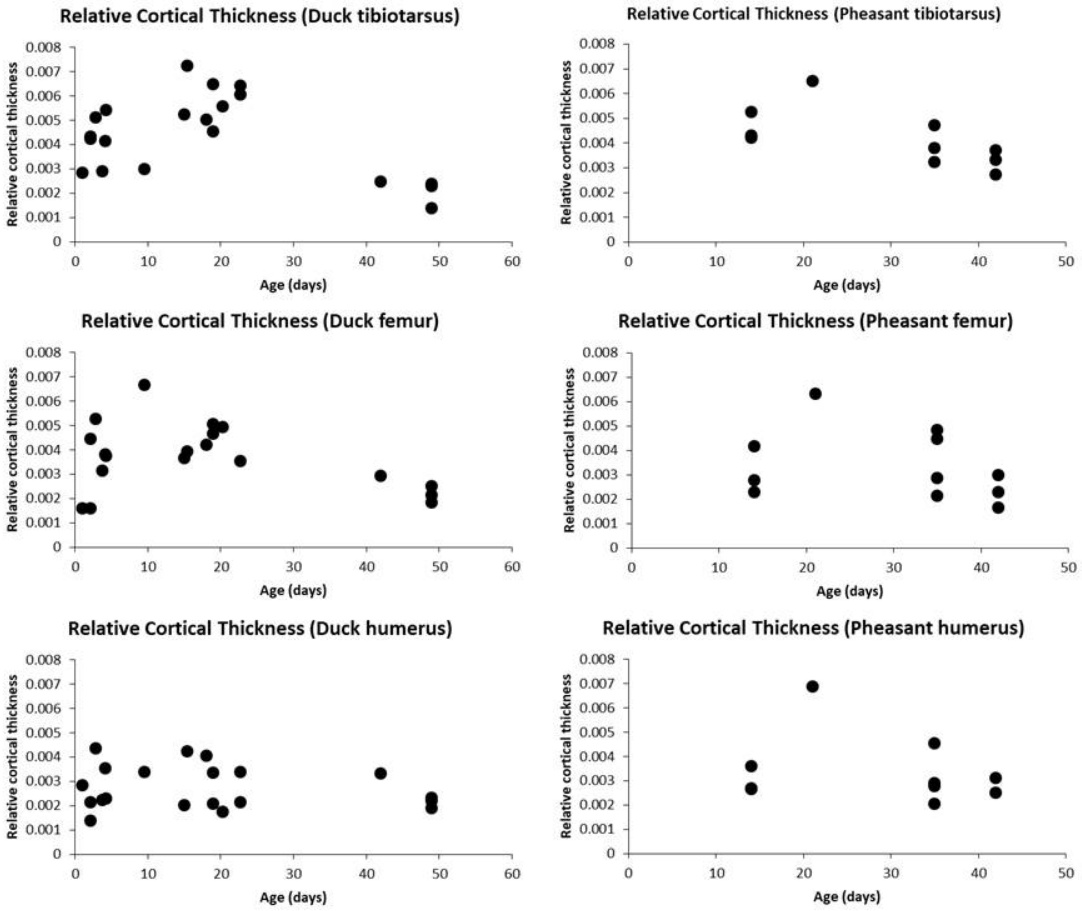

FIGURE 5.2: Relative cortical thickness (cortical thickness relative to bone diameter) at different ages for the humerus, femur, and tibiotarsus in the duck (*Anas platyrhynchos*) and pheasant (*Phasianus colchis*)

To summarize, the three bones measured in the pheasant scaled isometrically, and followed the same pattern of a slight increase then decreased in cortical thickness. In the duck, the

tibiotarsus and femur follow a similar growth pattern to the bones in the pheasant, but growth of the humerus was delayed and cortical thickness remained relatively constant.

5.3.2 Microstructure

5.3.2.1 Porosity

The percentage of cortical bone filled with mineralized tissue increases with bone maturity [129], so quantifying the change in bone volume fraction (BV/TV) within the bone cortex with age is likely to be valuable in estimating age in an unknown sample.

Duck

In the duck, at Day 1 post-hatch, bone was assumed to have developed largely before hatching. Therefore, bone resembling the structures seen at this stage, and at the appropriate scale, is here described as 'pre-hatching' bone. This age stage was not present for the pheasant and therefore pre-hatching bone has not been identified.

Qualitative and quantitative changes in porosity were observed throughout development and between the humerus, femur, and tibiotarsus within an individual in both species.

At Day 1, the bone cortices for all three bones were porous, but canals were quite narrow (Figure 5.3), resulting in a relatively high BV/TV (humerus 0.637, femur 0.685, tibiotarsus 0.777) compared with slightly older animals, especially in the tibiotarsus (Figure 5.4).

At two weeks of age, fine trabeculae of mineralised tissue were present at the periosteal surface (Figure 5.3). In the tibiotarsus and femur, the endosteal region appeared very similar to the structure seen in the Day 1 sample, so it was assumed that the periosteal trabeculae were deposited onto the surface of the pre-hatch bone while the pre-hatch bone remained relatively unchanged. This resulted in a thickening of the bone cortex. Therefore, at this stage, two distinct bands of porosity were present: an endosteal region with relatively narrow canals and a thicker periosteal region with much wider canals (Figure 5.3). In the humerus, the bone interpreted as pre-hatching is thinner than at Day 1, interpreted as endosteal resorption, and the thickness of periosteal growth is thinner than in the other two bones. New bone formed at this stage was most porous in the femur (Figure 5.4), followed by the tibiotarsus.

At 3 weeks of age, the tibiotarsus still retained the layer of pre-hatching bone while continuing to deposit bone periosteally. A gradient in canal diameter was observed from the endosteal to the periosteal surface (Figure 5.3). In the femur and humerus, prehatching bone had been resorbed by this stage. In the femur, overall porosity was reduced and the very porous periosteal region was no longer present. At this stage, the tibiotarsus was the most porous and the femur the least (Figure 5.4).

At 6 weeks, the ducks approached full adult body mass, though ducks do not reach full maturity until 6 months. This immaturity was evidenced by the bone microstructure, as although the pores were narrower in the tibiotarsus and femur than they were in the same bones in younger duckings, they remained wider than in fully adult bone. The endosteal and periosteal regions retained some wider pores. In the humerus, the bone was exceptionally porous, with some canals having a very large diameter compared with even the most porous stages of the other two bones studied. However, the periosteal edge was less porous than the rest of the bone.

At two years of age, all three bones were densely mineralised leaving only very narrow canals (narrower still than at 6 weeks).

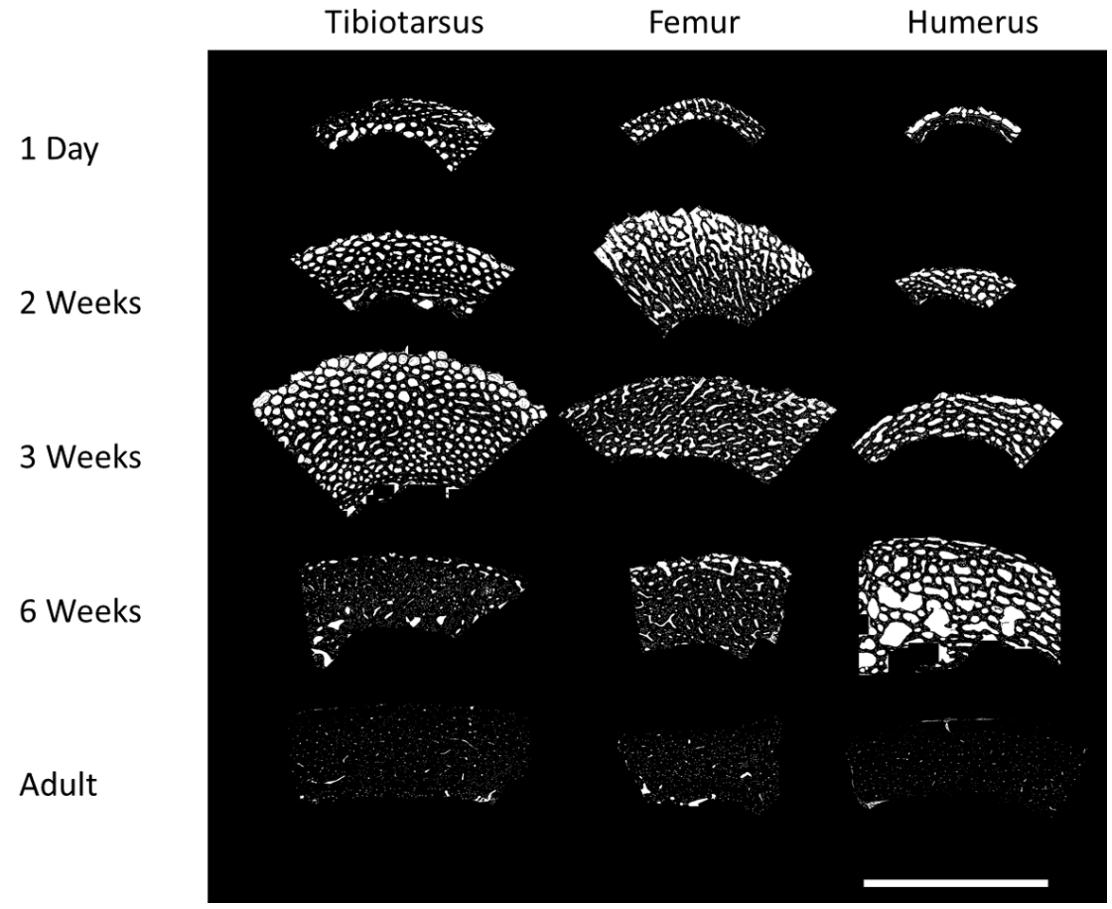

FIGURE 5.3: Cortical development in the long bones of the duck: Segmented midshaft section duck (*Anas platyrhynchos*) tibiotarsus, femur, and humerus at different ages, imaged using high-resolution CT. White regions are pores. The microstructure cortex changes through development: in very young bone, the pores are very wide, forming an open foam-like structure, and in adults the pores almost entirely close. Differences in structure and growth rate can also be seen between the different limb bones. Data taken TOMCAT beamline of the Swiss Light Source (1.6 μm voxel size at 18.5 keV). Scale bar 500μm.

In summary, in the duck, the three different bones studied had differences in their microstructural development, even between the tibiotarsus and femur, which scale isometrically. In all three bones, BV/TV initially decreased, then increased towards an adult BV/TV of more than 0.9. However, the tibiotarsus and the femur reached a near adult BV/TV earlier than the humerus. In terms of canal diameter, the three bones were quite different. In the tibiotarsus, canal diameter increases rapidly at first then dropped to near-adult thicknesses. In the femur, there was a fairly consistent decline in canal diameter. In the humerus, there was a great deal of variation in canal diameter, making it difficult to discern a pattern.

The changes in BV/TV in all three bones shows potential for distinguishing between age classes. In the duck, juvenile bone had significantly lower BV/TV than either adult or subadult in the femur and tibiotarsus (Figure 5.6). Although BV/TV appears lower in the subadult than adult, this was not significant for the tibiotarsus or femur. For the humerus, there was no significant

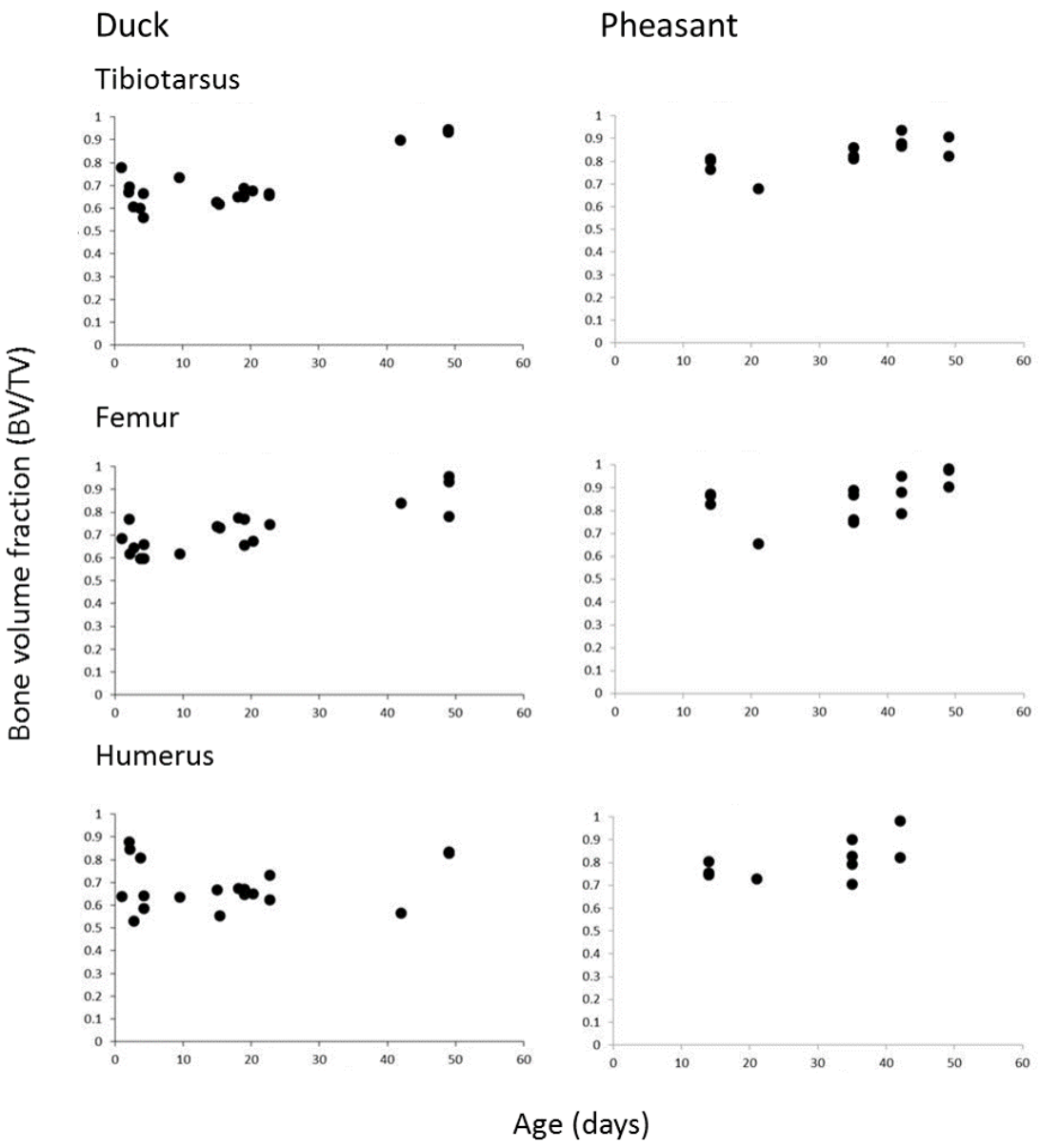

FIGURE 5.4: Bone volume fraction (BV/TV) in the midshaft of the tibiotarsus, humerus, and femur at different ages in the duck *Anas platyrhynchos* and the pheasant *Phasianus colchis*.

difference between juvenile and subadult, but there was between subadult and adult ($p<0.0001$).

Pheasant

In the pheasant (Figure 5.7), similar patterns were observed to the duck for the femur and tibiotarsus. However, the minimum BV/TV was higher in the pheasant than the duck. In the upper limb, the observed microstructure was similar in porosity to the lower limb bones, unlike in the duck. BV/TV in the pheasants initially increased then decreased again in all three long bones (Figure 5.4), and correspondingly the mean canal diameter initially decreased then increased. In the 6 week old samples, the canals had already become quite narrow (Figure 5.5).

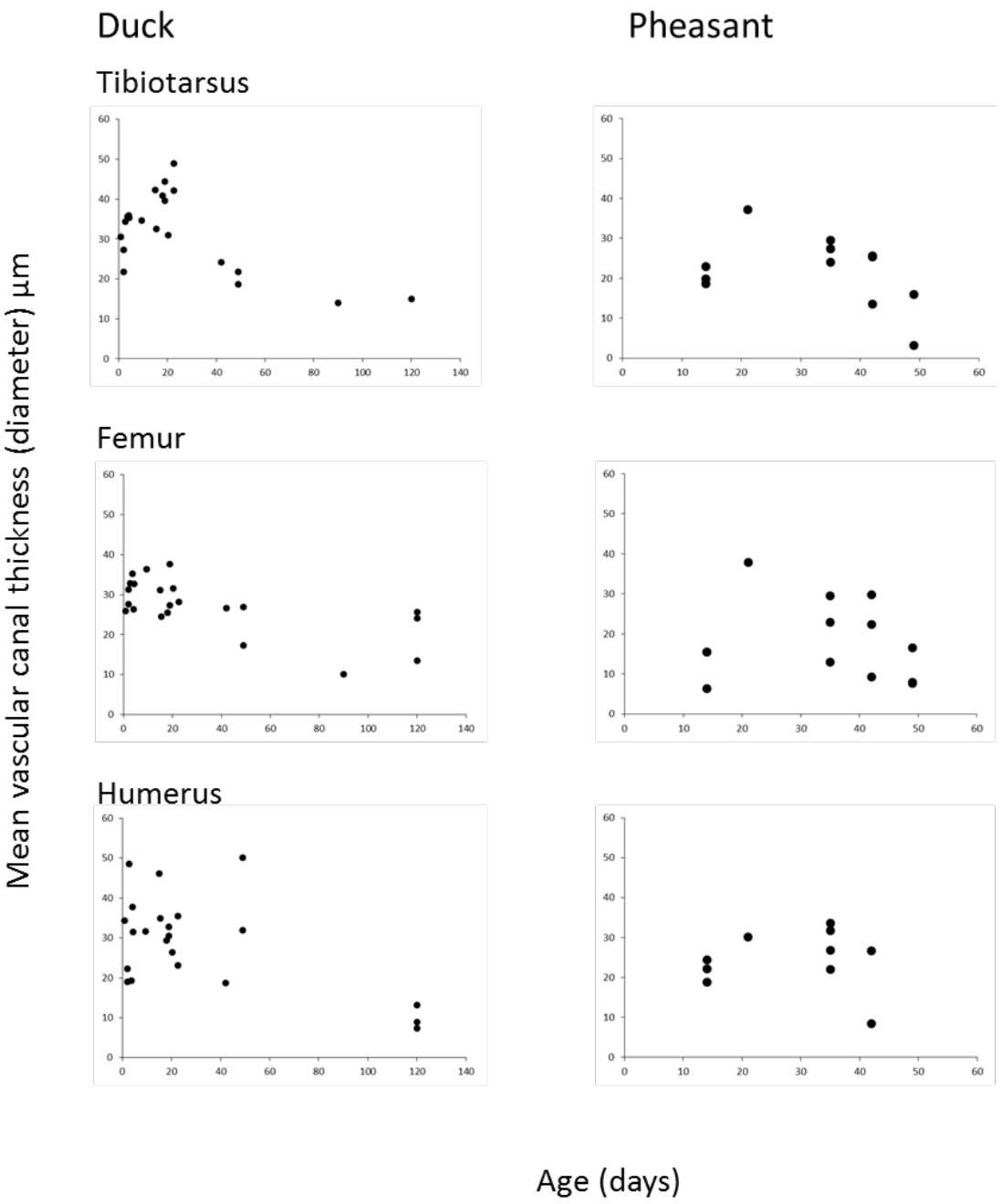

FIGURE 5.5: Vascular canal diameter (mean diameter) in the midshaft of the tibiotarsus, humerus, and femur at different ages in the duck *Anas platyrhynchos* and the pheasant *Phasianus colchis*.

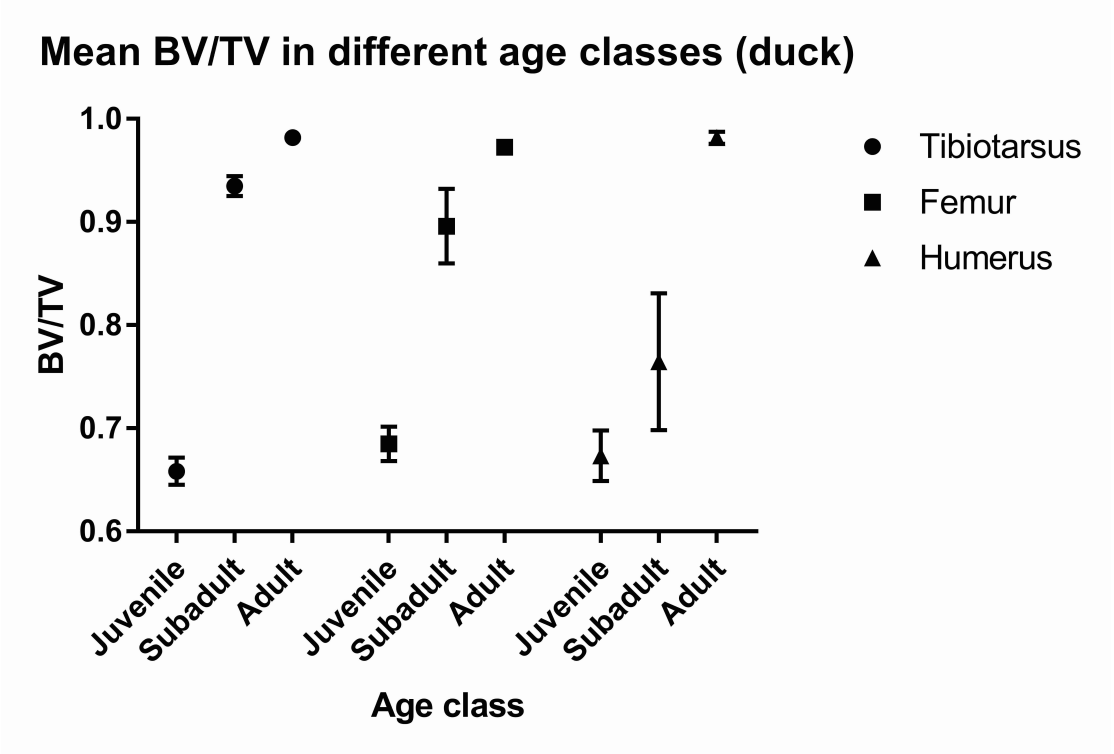

FIGURE 5.6: Mean bone volume fraction (BV/TV) for a region from the midshaft of the tibiotarsus, humerus, and femur in juvenile, subadult, and adult ducks (*Anas platyrhynchos*). Juvenile n = 15, subadult n = 5, adult femur and humerus n = 3, adult tibiotarsus n = 1. Error bars show standard deviation.

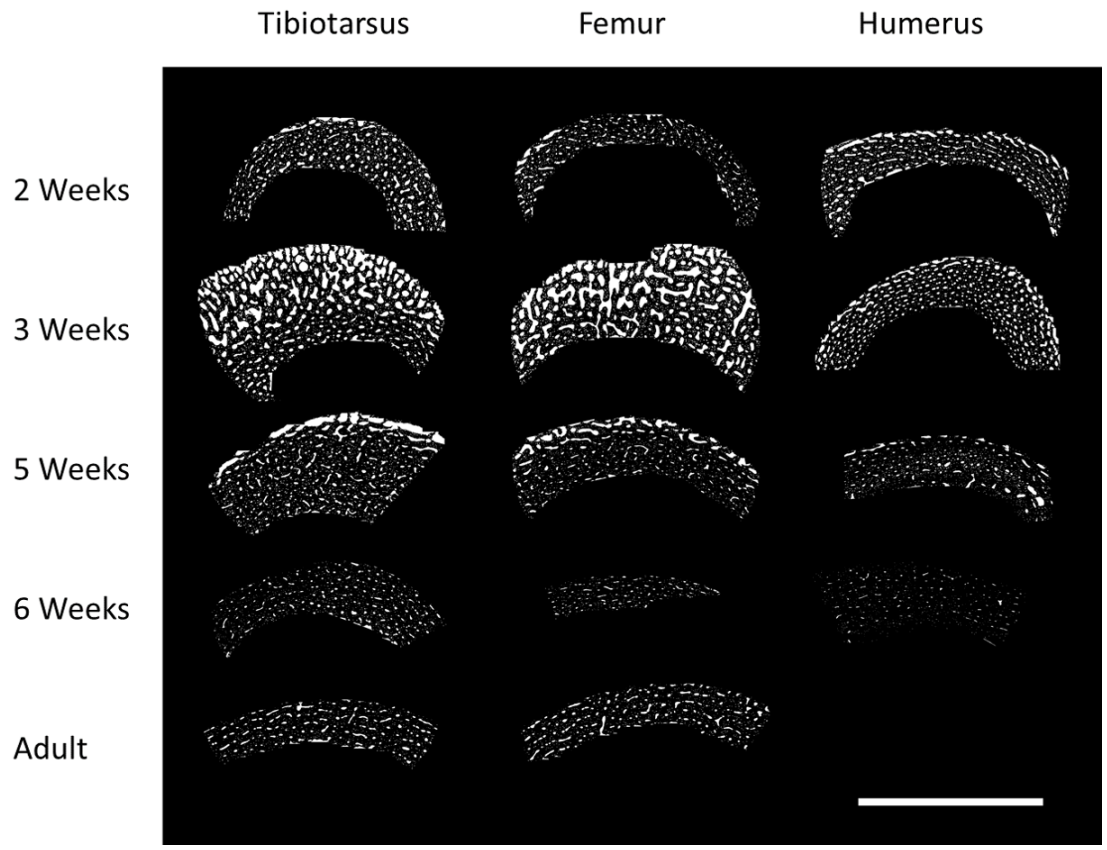

FIGURE 5.7: Cortical development in the long bones of the pheasant: Segmented midshaft section pheasant (*Phasianus colchis*) tibiotarsus, femur, and humerus at different ages, imaged using high-resolution CT. White regions are pores. For the adult sample, the humerus was unavailable. The microstructure cortex changes through development: in very young bone, the pores are very wide, forming an open foam-like structure, and in adults the pores almost entirely close. Differences in structure and growth rate can also be seen between the different limb bones. Data taken TOMCAT beamline of the Swiss Light Source (1.6 μm voxel size at 18.5 keV). Scale bar 500μm.

5.3.2.2 Canal orientation

The orientation of vascular canals within cortical bone has been linked to main direction of bone loading [21], and growth rate of bone [108]. Growth rate changes with age, following a sigmoidal curve, and therefore bone deposited at different stage in life may contain canals at different orientations [19]. Additionally, bone loading changes with growth and changes in bone use (e.g. beginning to walk or fly)[129] and therefore age-related changes in loading may also be reflected in canal orientation. Therefore characterising canal orientation and how it changes through growth may provide an indication of growth, slowing of growth, as well as bone use, which may be an indicator of stage of maturity.

Canal orientation is described both qualitatively, using 2D cross-sections, to relate observations found here with existing literature, and quantitatively, based on [14] and the analysis described in Chapter 4.

At all ages, in the duck tibiotarsus, almost all vessels appeared to run longitudinally along the bone, displaying a distinct round morphology in cross-section. In the femur, on the other hand, the canals in the juvenile bone were more flattened than circular in appearance in cross-section, suggesting a more oblique or radial orientation. In the humerus, the pores in the juvenile were noted to be rounded though less regularly compared to the tibiotarsus. In the adult, the majority of the canals appeared to run circumferentially.

In the pheasant, the shape of the cross sections of the canals in the three bones appeared to follow a similar pattern to that in the duck, with more longitudinal canals in the tibiotarsus, more laminar in the humerus, and more oblique in the femur, but these patterns were less distinct in the pheasant. The three bones appeared more similar to each other at all ages than the duck bones did.

In both species, no relationship was observed between age and either longitudinal index or radial index. In the duck, a positive correlation between age and laminar index was observed in juveniles (Figure 5.8, $r^2=0.6534$). No correlation was observed between the laminar index and age in the pheasant.

The canal orientations differed significantly between different bones within a species ($p<0.05$). In the duck, the tibiotarsus had a significantly different longitudinal index to both the femur and the humerus ($p<0.0001$). In the pheasant, the tibiotarsus was significantly different from the humerus ($p<0.05$) but not the femur. No significant differences were identified between the homologous bones of the two species (i.e. the tibiotarsus in the duck was not significantly different from the tibiotarsus in the pheasant).

For the laminar index, the duck tibiotarsus was significantly different from the duck femur ($p<0.01$) and duck humerus ($p<0.0001$), and also different from the pheasant tibiotarsus ($p<0.01$), but no significant differences were found between the different bones in the pheasant.

For the radial index, the duck tibiotarsus was significantly different from the duck femur ($p<0.0001$).

To summarise, canal orientation was consistent throughout development in most cases, except for the laminar index in the duck humerus, which increased with age. However, the different bones in both species had different canal orientations: the tibiotarsus had more longitudinal canals, the femur in the duck had more radial canals, and the femur and humerus in the duck

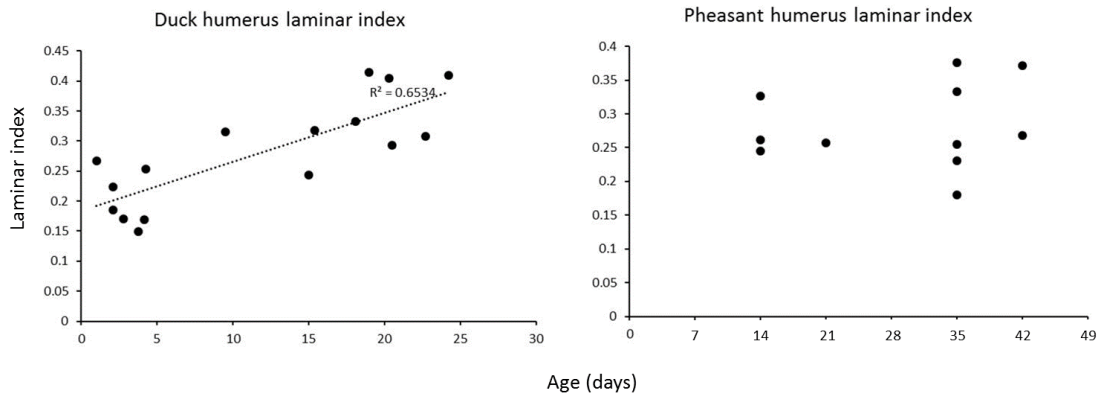

FIGURE 5.8: Laminar index (proportion of canals running parallel with the long axis of the bone) at different ages in the humerus midshaft of juvenile ducks and pheasants. Correlation between age and laminar index in the ducks is significant ($t=4.54$, $p<0.05$).

had more laminar canals. The canal orientations were more consistent between the different bones in the pheasant compared with the duck.

5.3.2.3 Osteocyte lacunae

The number density and size of osteocyte lacunae have been related to bone deposition [17] and age, so characterising how they change with age may help to estimate age in unknown samples.

Osteocyte lacunar density initially increased with age then decreased in the duck femur and tibiotarsus, and decreased consistently with age in the duck humerus (Figure 5.10). Similar patterns were observed in the pheasant, except that in the humerus the osteocyte lacunar number density remained higher later into development.

Size distribution patterns within samples were visualised by assigning a colour to each lacuna based on its volume (dark blue are smallest, red are largest) to show the positions of larger and smaller lacunae (Figure 5.11 and 5.12). For both species, the largest osteocyte lacunae were generally found near the periosteal surface. Additionally, a size gradient was observed with larger osteocyte lacunae furthest from the canals. This pattern was observed at all ages in the duck samples. A further band of larger osteocyte lacunae was observed in the adult duck endosteal surface in the tibiotarsus.

Similar patterns were observed in the pheasant (Figure 5.12), with the additional observation that larger osteocyte lacunae appeared in the thicker parts of the cortex in juvenile bone. In addition, a band of larger cells was present in the humerus in the pheasant.

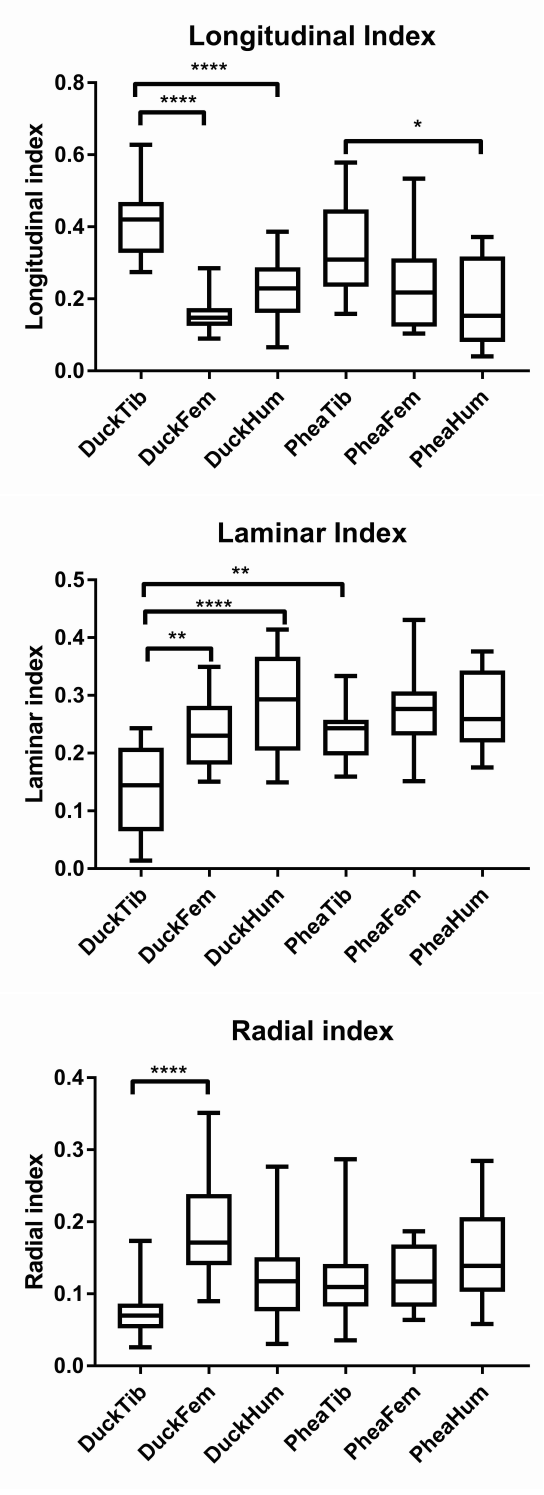

FIGURE 5.9: Comparisons of longitudinal, laminar, and radial vascular canal indices, measured at a midshaft region from the tibiotarsus, femur, and humerus of ducks (*Anas platyrhynchos*) and pheasants (*Phasianus colchis*), covering a range of ages between 1 day old and 2 years old. Duck tibiotarsus n = 21, duck femur n = 22, duck humerus n = 23, pheasant tibiotarsus n = 12, pheasant femur n = 14, pheasant humerus n = 10. Box plots show median values and interquartile range, whiskers show max and min values, asterisks indicate significance levels of differences (Tukey's multiple comparison test, ** $p < 0.01$, **** $p < 0.0001$)

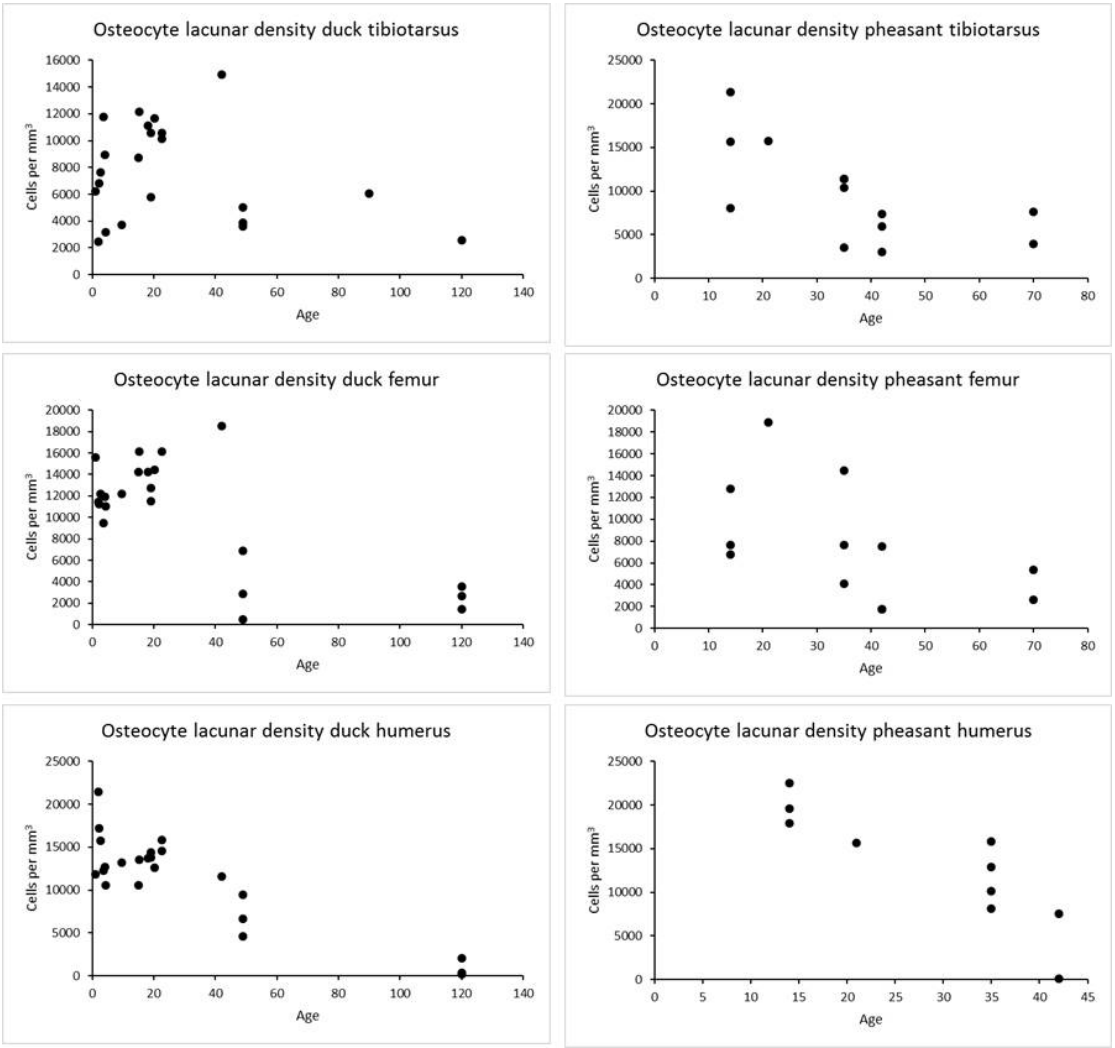

FIGURE 5.10: Osteocyte lacunar density at different ages in the midshaft of the tibiotarsus, femur, and humerus of ducks and pheasants.

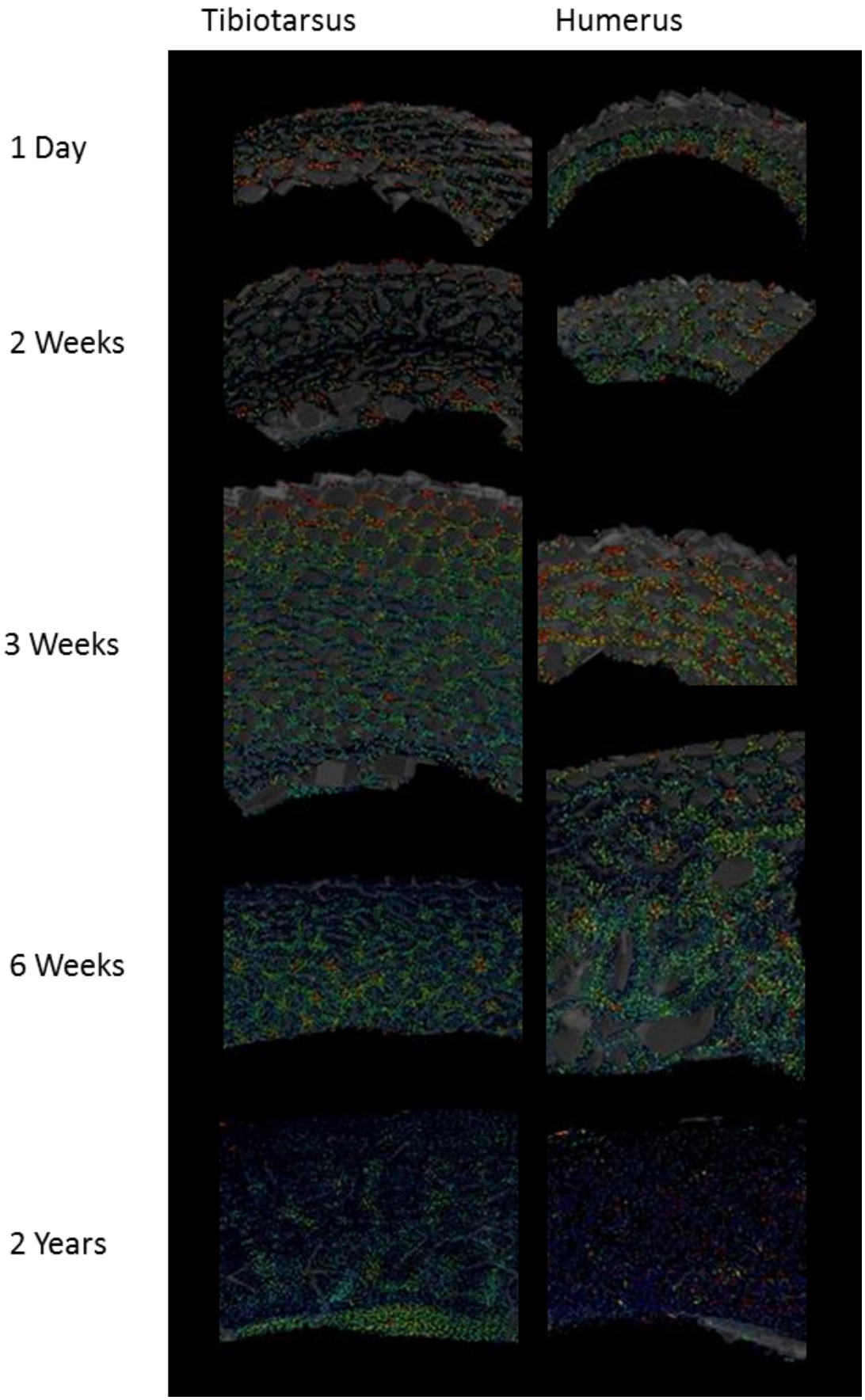

FIGURE 5.11: Distribution of osteocyte lacunae within cortical bone from the midshaft of the humerus and tibiotarsus from a growth series of domestic ducks (*Anas platyrhynchos*). Transparent grey = vascular canals, osteocyte lacunae coloured according to volume: dark blue are smallest, red are largest. For each section, the top edge is the periosteal surface and the lower edge is the endosteal surface.

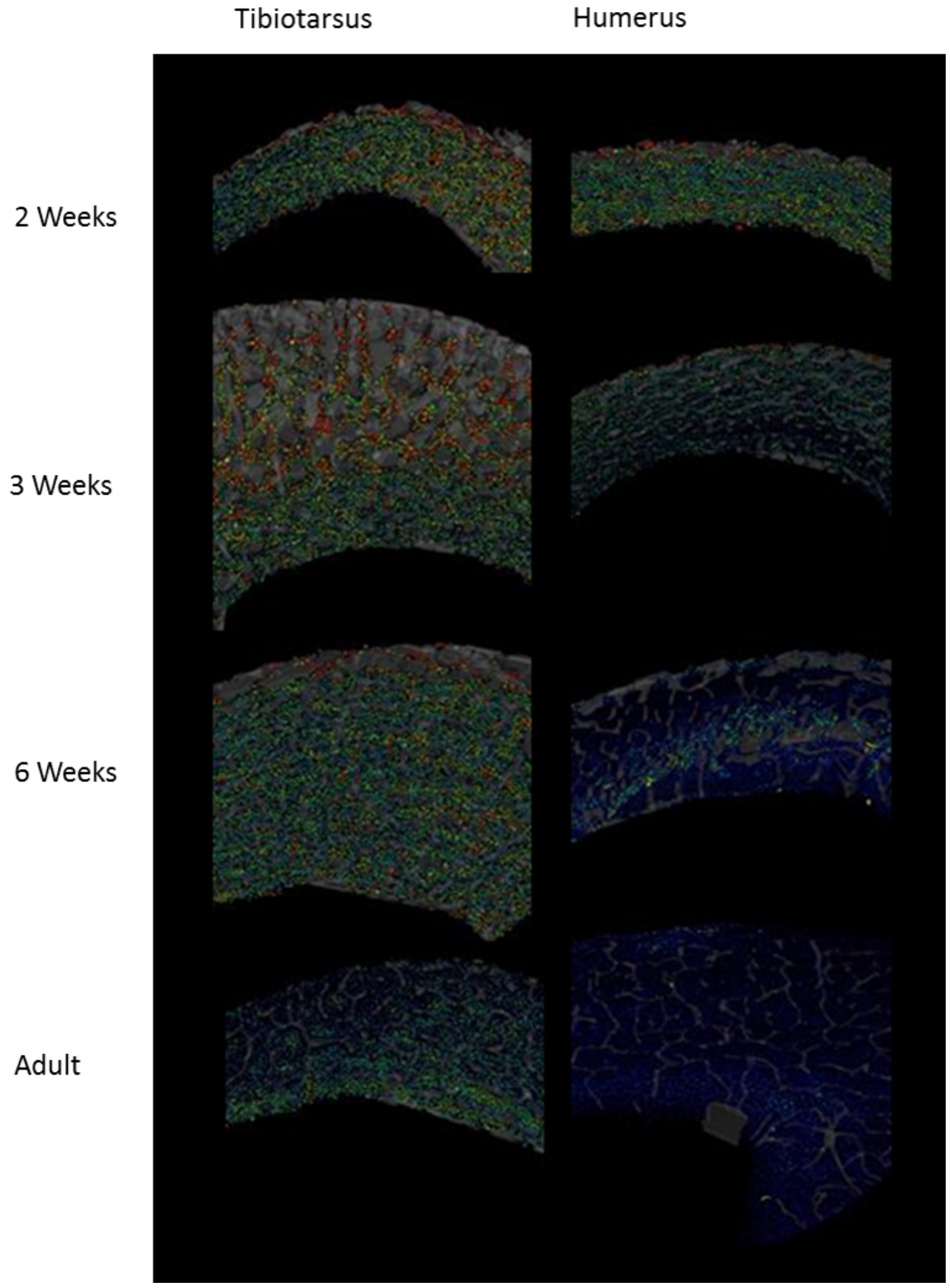

FIGURE 5.12: Distribution of osteocyte lacunae within cortical bone from the midshaft of the humerus and tibiotarsus from a growth series of pheasants (*Phasianus colchis*). Transparent grey = vascular canals, osteocyte lacunae coloured according to volume: dark blue are smallest, red are largest. For each section, the top edge is the periosteal surface and the lower edge is the endosteal surface.

5.4 Discussion

The work included in this chapter demonstrates that cortical bone microstructure in the duck and pheasant changes with age, and may be useful in determining maturity or developmental age in an unknown sample.

5.4.1 Macrostructure and porosity

Bone present at 1 day post-hatch is assumed to be largely that formed during pre-hatching development, where loading is minimal [169]. However, this bone tissue is loaded as soon as the duckling hatches.

In all bones studied, there was a general pattern of an initial decrease followed by increase in BV/TV with age. The changes in BV/TV generally corresponded to changes in vascular canal diameter: when BV/TV decreased, mean canal diameter increased, and *vice versa*. This suggests that the changes in BV/TV were largely due to changes in canal diameter rather than canal density i.e. fine trabeculae resulting in a porous structure initially, which is then infilled as observed in mice [129]. These changes show promise for quantitatively assessing developmental age, supported by the significant differences in BV/TV between juvenile, subadult, and adult bone in the duck. Given the two species show similar patterns of microstructural change, there may be a consistent pattern which can be applied more broadly and to fossils. However, this result must be interpreted with caution because in addition to the similarities between species and bones, there were also important differences.

Although the duck and pheasant both followed the same patterns of growth, and pore changes, the timings and absolute values differed. For example, in the tibiotarsus, which is expected to be under similar usage in both species at similar ages (both walk from soon after hatching), in the duck, the initial decrease in BV/TV occurred in the first week of growth, whereas in the pheasant it was delayed to between weeks 2-3. Additionally, the lowest value of BV/TV in the duck tibiotarsus was 0.559, whereas in the pheasant it was never measured as less than 0.6. Similarly, the maximum mean canal diameter was higher in the duck than in the pheasant. The differences in absolute values of porosity are likely to reflect the different growth rates of the species, since bone porosity has been previously shown to be higher in more rapidly growing animals [19]. The finding that, even within a species, nutritional intake can influence growth rates and bone porosity [19] might explain the variability seen in the porosity measurements in the juvenile bone of the same age. The differences in timing and absolute values of BV/TV and canal diameter relate to the differences in timings of growth in the two species. In the duck, very rapid growth has been selected for and therefore within the first 7 weeks their body masses increase by an order of magnitude. Pheasants grow and reach maturity more slowly [26].

In the pheasant, all three bones followed similar patterns to each other, while in the duck the three bones appeared different from each other even at the same developmental age. The differences are likely to be related to the different growth patterns in the upper and lower limb bones in the duck. For the pheasant, all three bones follow a precocial developmental pattern [164]. However, in the duck, the wings are not used until later [26] and follow a more altricial developmental pattern [164, 165]. This means that in the duck the growth of the wings is delayed but more rapid than the legs, and occurs during a time that the bones are not in use,

unlike the leg bones. This difference reflects the differing growth patterns of the two species and the age of flight: in the pheasant the wings are loaded from 11 days, compared with 56 days in the duck [26].

In the precocially developing bones, the relative cortical thickness was high at first and then decreases, opposite to the BV/TV. The inverse relationship between bone volume fraction and relative cortical thickness likely reflects the relative strength of rapidly developing bone and indicates a trade-off between rapid growth and loading. Growing in this manner allows a rapid increase in bone dimensions while maintaining strength and functionality by thickening the cortex, which is later remodelled to give a thinner, more densely mineralised cortex. This has previously been observed in the California gull, where hindlimb cortical thickness compensated for relatively weak bone tissue to maintain a constant breaking force for the bone, relative to body mass [166]. In the humerus, in the duck, like in the California gull [166], this trade-off is less important as the rapidly growing bone does not need the same strength that is required by the lower limb bones [164]. Therefore the bone can grow rapidly without the requirement for particular strength, and then becomes stronger (3 to 4 times stronger in the California gull [166]) only when the limb is required for flight. In the pheasant, however, the humerus is under biomechanical constraints at the same time as the lower limb bones [164] and therefore the cortex is thickened while bone tissue is weak to ensure overall bone strength [166].

In the duck, it is possible to use the BV/TV values to distinguish between adult, subadult, and juvenile, based on the femur or tibiotarsus, but the result from the humerus may differ. Therefore, it is important to combine the results from several bones. In the pheasant, older adults were not available, but there was a clear difference in BV/TV between the youngest and oldest individuals. Therefore, BV/TV could be used to identify broad developmental stage in these species. Comparing juvenile bone in the wings and legs provides information about whether the animal was yet flying, an important indication of lifestyle and how this changes with age.

Additionally, the presence of distinctly different pre-hatching bone could be used to distinguish very early growth from later growth.

5.4.2 Canal orientation

The only measure of canal orientation that changed with age was the measurement of laminar index in the duck. Given the limited number of young pheasants, it was not possible to confirm whether this same pattern was present in the pheasant. In the duck, however, measuring the proportion of radial canals in the humerus could provide some indication of the early developmental age of the bird.

In order to extrapolate beyond the duck, it is important to understand, however, the cause of the altered canal orientation within this bone. Canal orientation has been correlated with tissue deposition rate [68, 108], and with bone loading [21], with laminar canals hypothesised to be particularly important for resisting torsional resistance. Although it is not possible to test either of these hypotheses explicitly using these datasets, it is possible to consider which is most consistent with the data shown here.

Usually, radial canals are associated with increased growth rate, and laminar canals with a decreased growth rate [68, 108]. Therefore, given the growth of the humerus is delayed

relative to the lower limb bones, it is predicted that there will be a greater proportion of radial canals later in the development of the humerus, as at this stage the bone grows rapidly to catch up with the lower limb bones. Instead, the proportion of laminar canals increased, contrary to a growth-rate-based prediction. Interestingly, a previous study investigating the relationship between canal orientation and bone deposition rate in the duck found no relationship [15], contrary to studies in other species [2, 108]. It has been suggested that the result in the duck was due to the study design, where measurements were pooled between all the bones: substantial differences are known to occur in canal orientation between different limb bones [22]. However, the results here cautiously support the previous study in ducks [15] (the result cannot be compared directly since growth rates were not measured in this study).

Compared to the femur, the humerus in the duck had few radial canals, despite growing more rapidly. In addition, the faster-growing duck had no more radial canals than the pheasant in any bones. Therefore, in this study, the age-related change in canal orientation did not appear to be clearly related to changes in bone growth rate.

Instead, canal orientation may be more closely related to bone loading. Again, this cannot be tested explicitly here, but results can be compared to hypothesised results based on loading. A key hypothesis linking canal orientation with bone loading is that laminar canals are helpful for resisting torsional loading [21], which is experienced most in the wing bones in flighted birds [21, 161, 170]. In contrast, the tibiotarsus is under more compressive loading. Given ducks do not fly until 8 weeks of age [26], it is predicted that the torsional load in the wings will be low until near the point where flight occurs [164, 166], and therefore it may not be necessary to have particularly strong bone in torsion early in development. Therefore, the proportion of laminar canals within the bone might increase through development.

An increase in laminar canals through development of the humerus is indeed what was measured in the duck samples, supporting the hypothesis that increased loading through development results in or is at least related to canal orientation. Further supporting the argument that canal orientation relates to bone loading, the mean laminar index in the humerus in the duck was higher than in the tibiotarsus, as predicted due to the differences in loading between these bones [21].

However, this is not the full story. It was not possible to confirm or refute the hypothesis that laminar canal index increased with age in the pheasant due to limited sample numbers, especially individuals less than 2 weeks of age. However, the mean laminar index in the pheasant humerus was no higher than the other two bones studied in the pheasant. This makes the explanation of the relationship between canal orientation and bone loading less clear, since, in the pheasant too, it is expected that the humerus would be under greater torsional loads than the tibiotarsus.

Overall, the relationships between developmental age and canal orientation seem somewhat unclear. Without a better understanding of the functional reasons for changes in orientation in the duck, it would seem unwise to apply the findings here more broadly. However, the fact that laminar index did increase in the duck humerus suggests that this is an area that would benefit from further study.

5.4.3 Osteocyte lacunae

Several studies have found a relationship between the number density of osteocyte lacunae and age [106], and it is standard to describe the osteocyte lacunae in young, woven bone as large and plump, and in mature, parallel-fibred bone as smaller and flattened [89]. Therefore, the number density of osteocyte lacunae was measured in each sample, and the distribution of different osteocyte lacunar volumes visualised. The results in Chapter 4 demonstrated that the absolute volume measurements of lacunae at this spatial resolution are not to be trusted, so instead the comparative size distributions within samples were mapped to test whether differences could be observed both between bones and between different regions of a bone, and whether these related to developmental age.

The reduction in osteocyte lacunar number density with age in both species shows potential for ageing bone tissue, although this has not necessarily been found in previous studies (it does not appear to be the case in mice [129]. Care must be taken with this interpretation given the voxel sizes used in this experiment: if osteocyte lacunae reduce in size with age, then fewer voxels will be present in the osteocyte lacunae of older bone and therefore these cells may be less likely to be identified correctly, therefore leading to a reduction in the measured number density even if the actual number density stays the same.

Based on the colour-coded volume distribution maps, osteocyte lacunae appeared to decrease in volume with age of animal, being smallest in the oldest individuals. In addition, again based on these visualisations, the osteocyte lacunae were larger further from deposition surfaces. Even in subadult individuals, the largest osteocyte lacunae were in the regions furthest from the canals, which may indicate the presence of primary woven bone in these regions [89]. Additionally, bone within the endosteal laminar layers of adult bone contained relatively large osteocyte lacunae.

Studying osteocyte lacunar size distributions in this way has the potential to identify woven and lamellar bone, and potentially areas of remodelling, and can therefore be used to help in assessment of developmental age. However, resolution is limiting in this case since it has been demonstrated in previous chapters that measurements of osteocyte lacunar volume will not be accurate when voxel sizes of 1.6 μm are used. However, in these studies, the voxel size was chosen to enable a greater sample volume to be analysed.

If higher resolutions were used, it would also be possible to look at orientations of osteocyte lacunae [81], which could be used to identify collagen fibre orientations and therefore understand the growth are remodelling processes further.

5.4.4 Limitations and future work

This study provided a preliminary assessment of the changes that occur in 3D bone microstructure with age in two extant species, but further work will be required before the observations made in this chapter can be applied to fossils.

The first limitation is a technical limitation related to the voxel size chosen for these experiments. Although the voxel size chosen should be small enough to measure vascular canals, the measurement of osteocyte lacunae, and particularly lacunar volume, is likely to be unreliable, based on results from Chapter 4. Given that the volume of the lacunae appear to

decrease with age, it is possible that fewer lacunae are correctly segmented in older samples, resulting in an apparent reduction in lacunar number density. Before applying to fossils, this should be tested using higher resolution scans, sufficient to accurately characterise the osteocyte lacunae. However, this is a limitation of using osteocyte lacunae in these analyses: increasing the resolution decreases the field of view available and therefore may decrease the reliability of other measurements.

Due to the opportunistic nature of sampling, some ages in both species were represented by more specimens than others, so ideally more samples would be included, particularly subadult ducks and very young pheasants. Additionally, the birds used in this study are for the most part individuals that died of unknown causes which may have affected the results and reduced the applicability to healthy individuals. Therefore, a more comprehensive study could be carried out to assess bone microstructure are more regular and selected age stages, in healthy individuals, and using more replicates. Ideally, the individuals should also be weighed regularly throughout development, which would allow body mass growth rates at different times in development to be assessed, and tissue deposition rate could potentially be assessed using injection of fluorescent dyes [2, 15]. However, those studies were outside the scope of this project.

The ducks used in this study were all female, since they came from a farm specialising in egg production. This removed a potential source of variation within the datasets, but ideally male ducks should also be studied, as males and females can have quite different growth rates and final body masses [171].

In addition to the two species studied, it is also necessary to study a wider range of extant species before applying the findings to fossils. Even between these two fairly similar species, differences have been found in the development of their wings and their different growth rates, which have led to differences in their bone microstructures. It will be important to understand how microstructure differs between species where body mass is substantially different, to be able to apply the findings to a range of fossil birds. In addition, species should be studied that have more substantially different developmental patterns, such as following a fully altricial growth pattern (remaining in the nest throughout most of growth). This will help to test whether bone microstructural development changes similarly in these very different species, or whether limitations must be put into place when trying to estimate developmental age based on microstructure.

Finally, intraskeletal variation should be investigated further, both between different bones and between different regions of the same bone, since vascular organisation has been shown to differ between different regions of the same bone in mice [172], and canal orientations may differ in different regions [2].

5.5 Conclusions

This study provides the beginnings of a systematic comparative dataset, characterising 3D bone microstructure through development in two extant avian species. It was found that in both the duck and the pheasant, developing cortical bone first decreased, then increased in BV/TV, and first increased, then decreased in mean canal diameter, with different values of BV/TV for

juveniles, subadults, and adults. It was also observed that in the duck, the humerus appeared less mature at a later stage, and grew more rapidly to catch up with the other bones later. Therefore, it was concluded that the lower limb bones are a more reliable measure of age than the upper limb bones, but that comparing the two may provide insight into patterns of growth and time of first flight in an unknown species.

Canal orientation was not shown to change with age in either species, except in the case of the laminar index in the duck humerus, which increased with age in the juvenile birds. However, this same pattern was not seen in the pheasant and therefore further study is required to understand how canal orientation changes with age, and how this is influenced by growth rate and loading.

Osteocyte lacunar number density appeared to decline with age, but further study using higher resolutions is required before this finding is applied to fossils. The pattern of osteocyte lacunae with different volumes has the potential to distinguish different bone types and make interpretations about bone growth and remodelling, which help to determine age.

A combination of the BV/TV, canal diameter, and observations of the patterns of osteocyte lacunar volume within cortical bone can add to current qualitative method to support the identification of developmental age in unknown specimens including fossils. However, further study is required in order to fully understand the relationships between bone microstructure and age, as well as body mass, life history, and growth rate, in order to extrapolate reliably to fossils.

Chapter 6

A preliminary investigation into interspecific variability in bone development across extant birds.

6.1 Introduction

The previous chapter in this thesis aimed to characterise age-related changes in bone microstructure in three dimensions, and using quantitative, non-destructive methods not previously applied to this question. In Chapter 5, developmental datasets were generated for two extant bird species, the domestic duck (*Anas platyrhynchos*) and the ring-necked pheasant (*Phasianus colchis*). It was found that the two species examined followed different developmental trajectories, and that some of this was reflected in their bone microstructure, both through development and in adulthood. It was demonstrated that the bone volume fraction of the cortical bones changed with age, mostly explained by narrowing of vascular canals, and osteocyte lacunae varied in size according to the type of bone they are embedded within. Additionally, it was found that canal orientations tended to be longitudinal in the tibiotarsus in both species, but the femur and humerus had more circumferential canals. However, this was less consistent between the two species and may have been related to the altricial wing development in the duck [165].

If the observations made in extant species are to be extrapolated to fossils, then a wider range of extant birds must be studied, in order to characterise how 3D bone microstructure and age-related changes in microstructure, are affected by factors such as body mass and life history. Given that differences were observed even between the two similar species studied in Chapter 5, it would be predicted that much larger differences would be present between more different species, and it would therefore be naive to extrapolate to fossils based on just these two species.

Characterising the full spectrum of developmental differences across extant birds is a huge undertaking, and not within the scope of this project. However, it was important to carry out some preliminary studies in a wider range of extant species, to test how different modern birds can be in their microstructures, and whether any predictable patterns could be observed that

would allow interpretations to be made of fossil birds. Although the sample sizes involved here are small, this study provides the beginnings of a wider understanding of how 3D microstructure interacts with numerous biological factors.

Both species studied in Chapter 5 follow a precocial developmental pattern: they can walk and are semi-independent from hatching [173]. It is likely that many extinct birds were precocial, but it is uncertain whether precociality or altriciality is the ancestral state for modern birds [174]. The duck's 'altricial' wing development [165] already suggested depositional differences according to developmental pattern, supporting other recent work [164]. However, a significant proportion of extant birds develop in a fully altricial pattern [174, 175], (Figure 6.1). Altricial species hatch with less functionality, they are confined to the nest until they are fully grown and are fully dependent on parental care until, and a little after, fledging.

FIGURE 6.1: Precocial (A and B) and altricial (C and D) chicks. (A) Domestic duckling, day old (*Anas playrhynchos*), (B) red-legged partridge (*Alectoris rufa*), (C) Common starling (*Sturnus vulgaris)*, (D) Rock dove (*Columba livia*). Precocial chicks hatch with downy feathers and can run from soon after hatching. Altricial chicks have little down and are fully dependent on parental care until fledging.

Precocial birds like ducks and pheasants have very rapid growth rates, but they are slow in comparison to altricial species [40, 175]. Confined to a nest and protected from predators, altricial chicks are helpless for much of their somatic growth but reach full body mass in an exceptionally short period of time, approximately three to four times faster than precocial birds of the same body size [40, 175]. If there are differences in bone microstructure caused by differing growth rates, as found by several studies [2, 15, 108] it is therefore predicted that these differences will occur between the bones of altricial and precocial species.

The bones of altricial species are placed under entirely different loading conditions while growing compared to precocial species, where the birds are walking and in some cases even flying from very early in life. Altricial species, on the other hand, are free to grow rapidly with fewer biomechanical constraints on their bones; their bones are weaker than those of precocial species[176]. A starling, for example, cannot lift itself off its tarsi before day 10 of development, though can hop by approximately 15 days [40]. If an altricial chick is removed from the nest and forced to exercise before fledging, bone deformation can occur [167], highlighting the need for stronger bones in active chicks. For comparison, a duck or pheasant can run from day 1 after hatching [26], and some superprecocial species (Megapodes) can even fly at day 1 after hatching [177]. If growth rate and loading requirements are reflected in bone microstructure [2, 21, 108], then it is expected that the bone microstructure of precocial and altricial species will be different, at least during primary bone deposition.

In altricial chicks, the bone-to-cartilage ratio is small compared with precocial species [176], which reduces bone strength but may also allow more rapid growth. It is also known that bone strength decreases with porosity [178], so a very porous juvenile bone will be weak [129]. However, dense bone is slow to lay down, resulting in tradeoffs between bone strength in different loading scenarios and growth rate [129, 166]. In species where bones must be used even while growth is occurring, the inherent weakness of porous, rapidly growing tissue can be offset by the addition of extra material, giving a greater cortical thickness and therefore greater resistance to fracture [166].

In addition to overall bone porosity, bone microstructure is adapted for loading in particular directions. For example, laminar bone is known to be fairly strong in tension, while more longitudinally oriented Haversian systems are more resistant to compressive forces [178]. It is often argued that a laminar arrangement of vasculature and collagen fibres in wing bones is an adaptation for resisting torsional loads in flight, as composite materials are most resistant to tensile stresses aligned with the main direction of their fibres [21].

Bone remodelling in response to changing load can be very rapid in birds, enabling extra material to be added to bones where it is required mechanically [179]. In addition to extra material being added, bone tissue can remodel endosteally, removing depositional history, or throughout the tissue creating Haversian systems [163]. Secondary remodelling is not always observed in avian tissue [162], though large ratites, such as elephant birds, have been observed to have a high degree of Haversian remodelling, similar to humans [180]. It is therefore important to distinguish between primary bone, displaying the developmental history of the bone, and secondary remodelling, which may be indicative of present loading conditions.

Another key factor in understanding how bone microstructure varies between species is understanding how it scales with body mass and therefore bone size. Both duck and pheasant occupy a similar region of the body mass spectrum, while the range of extant bird species reaches from approximately 2g in the bee hummingbird to more than 100kg in ostriches [181]. Recently extinct elephant birds weighed several times more than an ostrich [11, 182]. Understanding how bone organisation changes with scale is important in extrapolating to fossil species, and for understanding evolution. For example, are the vascular organisations in very large birds fundamentally different from those in smaller birds or is there a repeating unit which can be scaled to any bone size? This question is important, because if there is a scalable repeating unit, then every bird has the genetic potential to develop bone structures seen in

much larger bones, providing flexibility in the evolution of body mass. If different, this suggests evolutionary innovations which have permitted extremes of body mass, and may represent an evolutionary constraint on size.

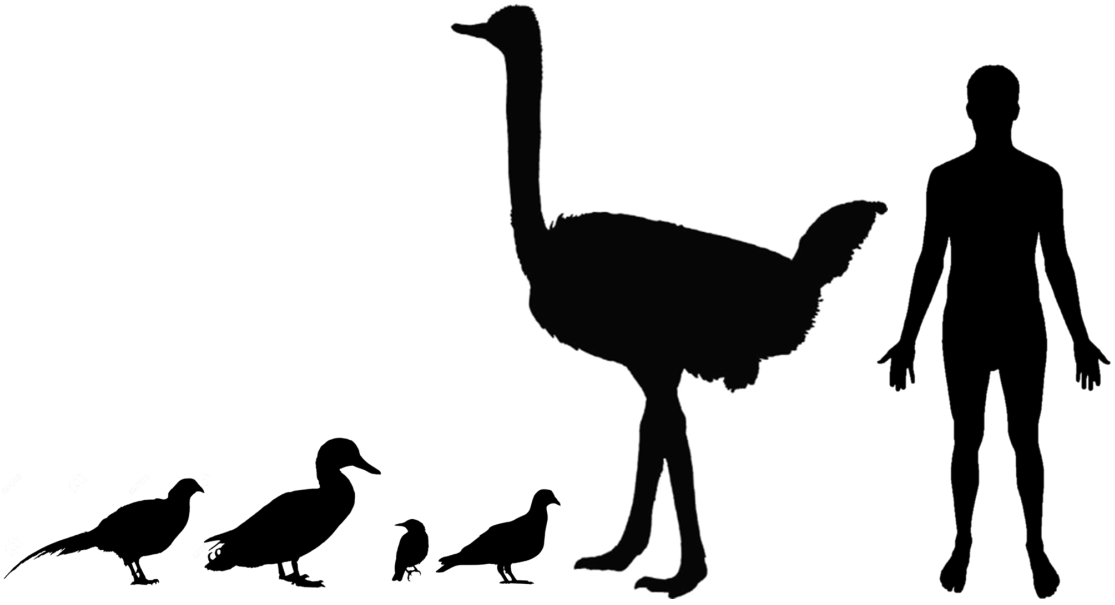

FIGURE 6.2: Bird species used in this study, shown to scale to demonstrate their different sizes. (Left to right) Ring-necked pheasant (*Phasianus colchis*), domestic duck *(*Anas platyrhynchos), starling (*Sturnus vulgaris*), rock dove (*Columba livia*), and a human for scale.

The microstructure of bone is contrained by the need to perform certain functions. For the vascular canals, that is supplying nutrients and oxygen to the bone cells [3]. The growth of primary osteons, and the distance between canals, is limited by oxygen diffusion to the cells furthest from the vessels [183], placing a physiological limit on the size of osteons and therefore the structure of primary bone. The existence of this physiological limit is supported by a very consistent maximum distance from blood vessels to osteocytes, in both mammals and birds [184]. Further from the blood vessels, cells become starved of oxygen, which would kill the cells, but may also trigger bone remodelling by vascular invasion. In very small birds, the whole cortex may be avascular [69], presumably because diffusion distances are small enough that oxygen can reach all bone cells from periosteal vessels. In larger birds, fibrolamellar bone forms, creating repeating units of vascular layers with interconnections, providing oxygen to all parts of the bone [163].

It has also been observed that bone vascular density is positively related to bone cross-sectional area, so larger animals tend to have higher vascular density in their cortical bone [69]. The positive relationship between cross-sectional area and vascular density is likely due to the smaller relative effectiveness of vascular supply, which depends on periosteal area. In a larger bone, the surface area to volume ratio is decreased and therefore the relative effectiveness of the periosteal vascular supply is also reduced.

In order to fully understand the relationships between bone microstructure, development, loading, and body mass, it is necessary to examine a wider range of extant species in a developmental context. In this chapter, the aim was to study some extant species with varying body masses and life histories, in order to start to understand the variation that exists in extant birds. Study species chosen were two altricial species with differing body masses, the common

starling (*Sturnus vulgaris*), the rock dove (*Columba livia*), and two precocial species, one smaller than the pheasant, the red-legged partridge (*Alectoris rufa*), and one at the extreme large end of avian body masses, the ostrich (*Struthio camelus*). Where possible, two different developmental stages have been studied, but this is a preliminary study containing small sample sizes, and serves to highlight the potential for studying development in an evolutionary and functional context within modern birds, in order to better understand fossil birds.

Red-legged partridges are in the family Phasianidae, the same family as pheasants (within the order Galliformes (Figure 6.3)). They are therefore closely related to pheasants, and follow a similar developmental path. They are precocial, and can both walk and fly early in development. Although otherwise similar to pheasants, they weigh between 400-550g, around half the mass of pheasants.

Starlings are mid-sized Passeriformes (Figure 6.3), weighing approximately 58-101g. They hatch with only a few tufts of down, can hop by day 10 of age, fly by day 15 [40], fledge at approximately three weeks of age, at which point they have reached adult body mass [40, 185] and continue to be fed by parents for a week or two after that. Starlings are strong fliers, a factor which differs from both the pheasant and the partridge.

Rock doves follow a similar altricial developmental path to starlings, though take slightly longer to fledge (approximately four weeks). They are larger than starlings, with body masses recorded between 238 and 380g in wild birds. They are not passerines; instead they fall within the Columbaves (Figure 6.3). However, they move by walking on the ground and are relatively strong fliers.

At the extreme end of extant avian body masses, ostriches are precocial but take much longer to reach maturity than their smaller counterparts. Adults can weigh more than 100kg [186], but sexual maturity is not reached until 2-4 years of age. Commercial slaughter occurs at approximately 1 year of age [187], when the birds may approach full body mass, but are still relatively immature. The samples used in this study were byproduct from the commercial meat industry and therefore the individuals the bones were from were subadult, at approximately 1 year of age. Ostriches are phylogenetically distinct from the other birds in this study: ratites are the earliest branching of the living bird groups (Figure 6.3). They are flightless but have long legs and can run quickly.

- Hypothesis: Variation in bone microstructure seen between pheasant and duck represents a small proportion of the variation across modern birds: species with different developmental patters and body masses will have substantial differences in bone organisation which may make age estimation *etc*. difficult to extrapolate
- Objective: To characterise bone microstructure in a range of modern birds with precocial and altricial developmental patterns, and with differing body masses. Specific aims:
    1. To test the effects of developmental mode (precocial/altrical) on bone microstructure
    2. To test the effects of body mass on bone microstructure

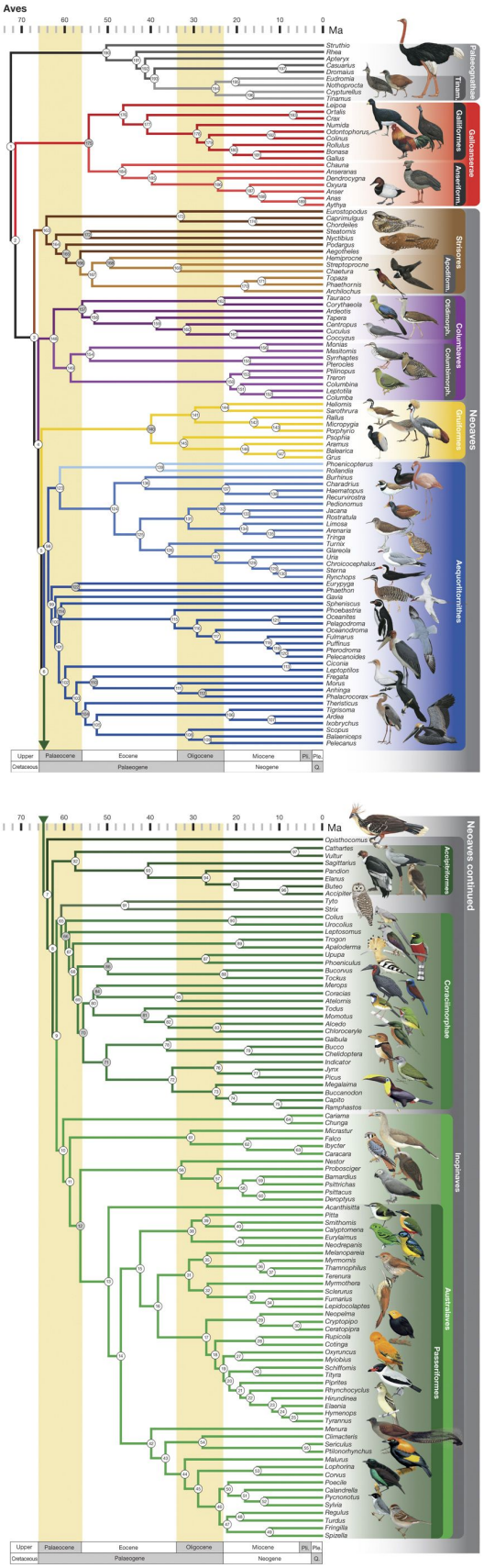

FIGURE 6.3: Phylogeny of extant birds. Species included in this study are Galliformes (pheasant, partridge), Anseriformes (duck), Palaeognaths (ostrich), Columbaves (rock dove), and Passeriformes (starling). Figure reproduced from [7]

6.2 Methods

6.2.1 Materials

Samples of rock dove *Columba livia* and starling *Sturnus vulgaris* were loaned from the Osteoarchaeology reference collection, University of Southampton (Figure 6.4). The loaned samples comprised three nestling starlings (from a single nest), one subadult starling (recorded as first year plumage), and two adult starlings, as well as one nestling rock dove and three adult rock doves.

Where possible, the right tibiotarsus, humerus, and femur, were scanned for all starlings; the femur and tibiotarsi were scanned where possible for the rock doves.

Ostrich *Struthio camelus* bone samples were purchased from the Exotic Meat Company, Leicester. Animals were reported to be approximately 1 year of age, and the femur and tibiotarsus from two different animals were supplied.

Juvenile partridge *Alectoris rufa* samples were kindly donated by Blackmoor Game Farm, Hampshire, and an additional adult tibiotarsus sample by Matt Sharp, University of Southampton.

FIGURE 6.4: Dry starling bones from Southampton Zooarchaeology reference collection. (Left) immature bones. (Right) Mature bones.

6.2.2 Sample preparation

Ostrich and partridge limb bones were cut into matchstick-shaped samples measuring approximately 3 mm (Figure 6.5) (to fit within the field of view while scanning) using a slow-speed saw and fixed using 4% PFA, then transferred to 70% ethanol.

Reference collection samples were imaged without damaging the specimens and were therefore not processed.

6.2.3 Sample mounting

Samples were mounted using a soft wax. The partridge and ostrich samples were stored in ethanol, therefore the ethanol was removed before scanning and the sample covered with a

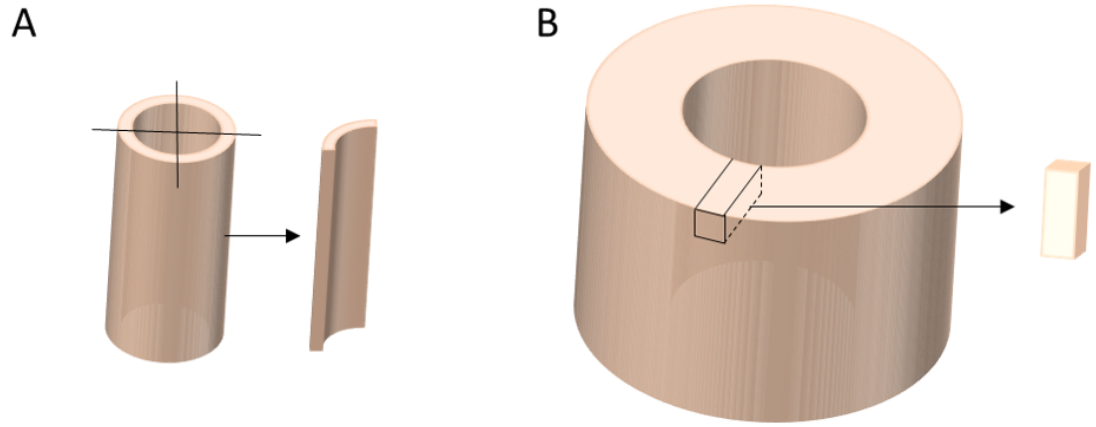

FIGURE 6.5: Sectioning samples. (A) Smaller samples e.g. partridge bones were either left as complete cortical sections (left) if smaller than 2mm, and if larger were cut lengthways into quadrants (right). (B) Ostrich tibiotarsus had a very thick cortex and therefore the sample was cut across the cortex and imaged in several scans which were then merged for analysis.

plastic tube to reduce evaporation (see Methods chapter). Starling and rock dove samples were mounted dry.

6.2.4 Scan setup

All samples were imaged at I13-2 beamline at Diamond Light Source, Harwell Science and Innovation Campus, Harwell, UK, over two beamtime sessions.

The rock dove and starling samples were imaged using pink beam, average energy 20 keV, using 4100 projections over 180 °rotation. Each radiograph was exposed for 0.15 s. The sample-to-detector distance was 20 mm. The voxel size was 1.6 μm.

The partridge and ostrich samples were imaged at a later beamtime, during the same session as the pheasant samples from the previous chapter of this thesis. In this session, the scan setup was optimised further to improve signal-to-noise-ratio, which was relatively poor in the initial session. The samples were imaged using pink beam, average energy 20 keV, using 4001 projections over 180 °rotation. Each radiograph was exposed for 0.1 s. The sample-to-detector distance was 20 mm. The voxel size at the detector was 0.8 μm, this was later reduced to 1.6 μm by averaging pixels, in order to generate datasets of comparable voxel sizes in both sessions, and to improve signal-to-noise-ratio.

6.3 Results

6.3.1 Bone growth and porosity

6.3.1.1 Precocial species

Partridge

At 1 week of age, the femur had the thickest cortex, and the humerus the thinnest. At 7 weeks of age, this order was reversed: the humerus had the thickest cortex (Figure 6.6).

Microstructurally, at 1 week old, the partridge bone appeared similar to the 1 day old duck bone. In the tibiotarsus, the bone tissue was fairly dense for juvenile bone and vascular canals were fairly narrow. In the femur and humerus, fine trabeculae could be seen at the periosteal surface, indicating bone growth. At this stage, it is likely that the endosteal bone retained some material deposited during pre-hatch development, but clear signs of resorption were present on the endosteal surfaces (concave 'cookie cutter' shapes at endosteal surface indicative of osteoclast activity).

At 7 weeks, the bone microstructure was less porous. The bone still appeared to be growing given the trabecular structures on the periosteal surface, and the bone was being resorbed from the endosteal surface. Canals had the largest diameter at the periosteal surface, suggesting they had not yet been fully infilled. At this stage, no inner or outer circumferential layers were present and no sign of reduction in vascularisation was visible towards the bone surface.

In the adult, only a tibiotarsus was available. In the tibiotarsus, the adult bone contained narrower canals than the tibiotarsus from 7 week old individuals and therefore was less porous. The cortical thickness was similar, but the inner and outer regions of the bones appeared close to avascular, indicating cessation of growth. The inner circumferential layer was clearly defined by darker greyscale values, suggesting less dense mineralisation, possibly due to remodelling and rapid deposition.

TABLE 6.1: Quantification of intracortical pore microstructure based on segmented SR CT scans of a midshaft region of cortical bone in the long bones of partridges (*Alectoris rufa*) at different age stages.

Bone	Age	Cortical thickness (μm)	BV/TV	Canal diameter (μm)
Tibiotarsus	Adult	124.5	0.986	9.15
Femur	Subadult	116.6	0.954	10.9
Tibiotarsus	Subadult	140.6	0.93	11.3
Humerus	Subadult	146.6	0.936	12.7
Femur	Juvenile	136.5	0.838	26.0
Tibiotarsus	Juvenile	147.4	0.823	16.7
Humerus	Juvenile	85.5	0.732	21.4

Ostrich

The cortices of the ostrich bones were very thick, much thicker in the tibiotarsus than the femur (Figure 6.7).

In the tibiotarsus, the cortex was densely mineralised throughout. (The darker region is a scanning artefact). At the periosteal surface, the bone was rough in texture, indicating immaturity, and densely organised primary osteons occurred right to the bone surface. Vascularisation in the periosteal half of the bone was evenly distributed and most canals appeared approximately the same thickness.

In the endosteal region, vascularisation was similarly dense, but appeared more disordered. A mixture of small and much larger canals were present, and around seemingly randomly distributed canals greyscale values were darker, indicating less dense mineralisation. This may be indicative of secondary remodelling, and the larger canals may be Haversian systems that have not yet fully infilled.

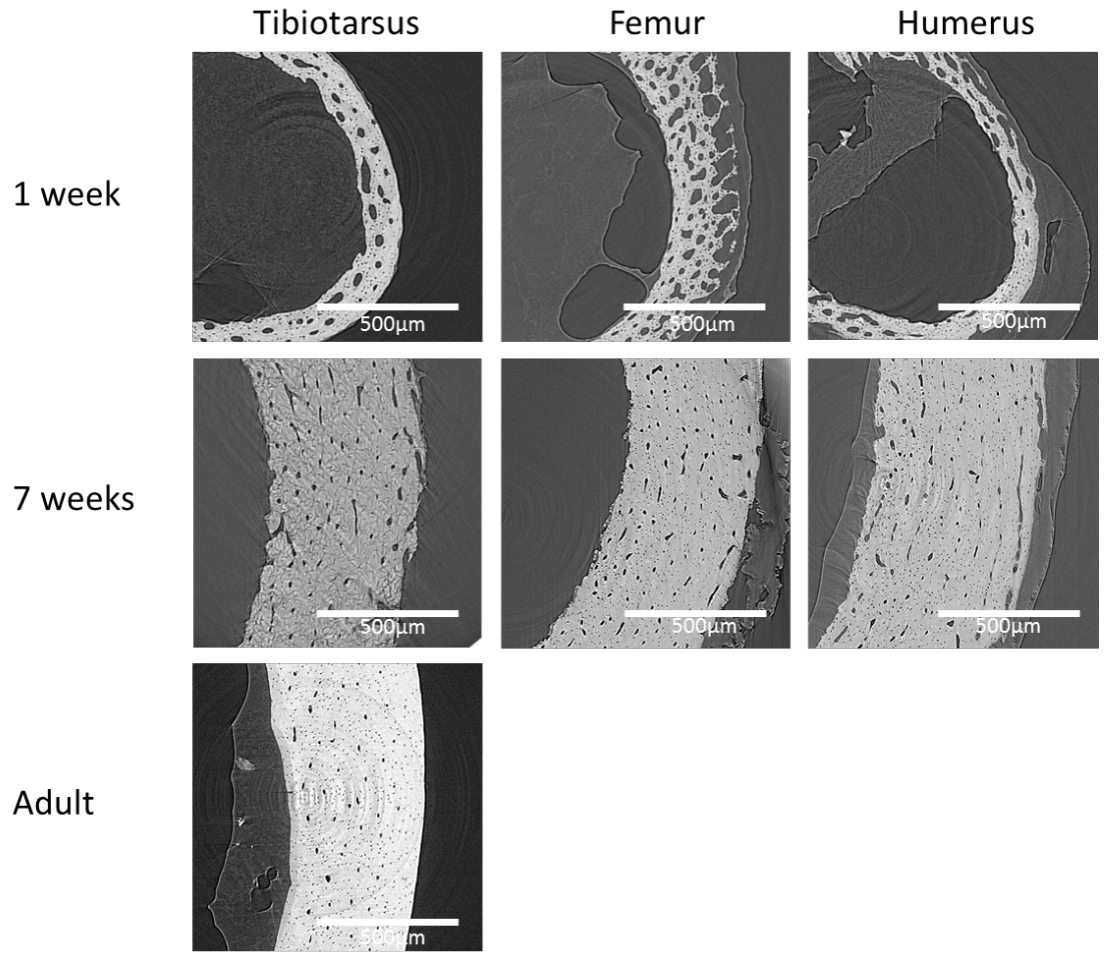

FIGURE 6.6: Transverse cross-sections from the midshaft of long bones in a growth series in the partridge (*Alectoris rufa*). Data collected at I13-2 beamline of Diamond Light Source, Harwell, UK. Voxel size 1.6 μm. For the adult, only the tibiotarsus was available.

In the femur, the cortex was much thinner, and, based on observation from a single SR CT slice, the two regions are less distinct, if at all visible. The outer region was similarly ordered, as in the tibiotarsus, but the inner region also appeared well-organised, lacking the enlarged canals present in the tibiotarsus. Grey values also appeared more even across the cortex.

For the tibiotarsus, the BV/TV was 0.964, and for the femur 0.981. The mean canal diameter were 30.8 μm and 7.66 μm respectively (Table 6.2).

TABLE 6.2: Quantification of intracortical pore microstructure based on segmented SR CT scans of a midshaft region of cortical bone in the long bones of a 1-year-old ostrich (*Struthio camelus*).

Bone	Age	BV/TV	Canal diameter (μm)
Femur	Subadult	0.981	7.66
Tibiotarsus	Subadult	0.964	30.8

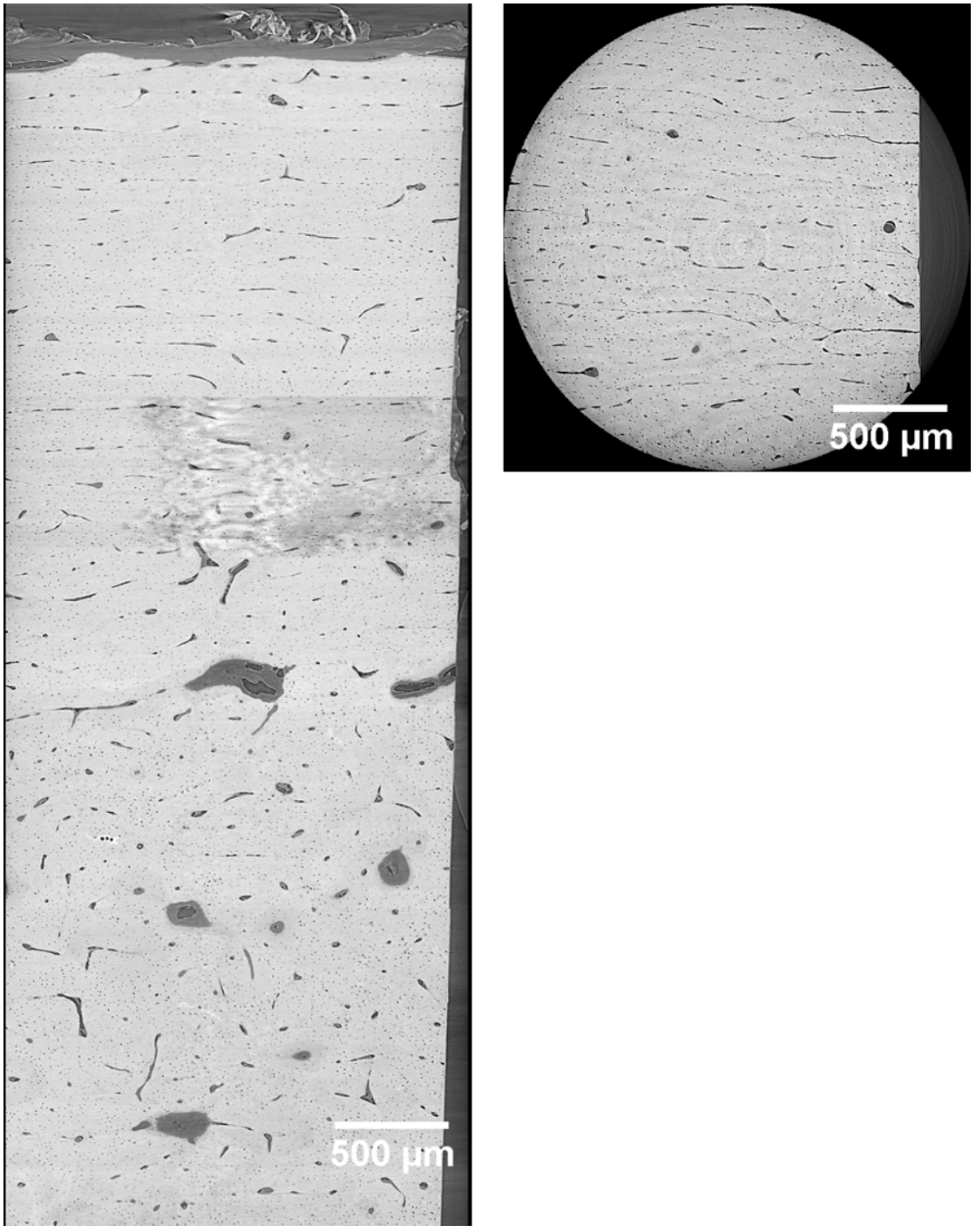

FIGURE 6.7: Transverse cross-sections from the midshaft of long bones in a year-old ostrich (*Struthio camelus*). Data collected at I13-2 beamline of Diamond Light Source, Harwell, UK. Voxel size 1.6 μm.(Left) tibiotarsus, (Right) femur.

6.3.1.2 Altricial species

Starling

In the starling, although the juvenile bones were almost the same dimensions as the adult bones (Figure 6.8), the articular ends of the bones were poorly formed and the surface texture was porous, confirming the fact that the bone was immature. Low-resolution CT showed that the mineralisation was lower in all three bones all the way along the bone, though more mineralisation is present in the midshaft of each bone (Figure 6.8). The cross-sections of the bones appeared less distinctly formed, with less well-defined muscle attachments in the juvenile.

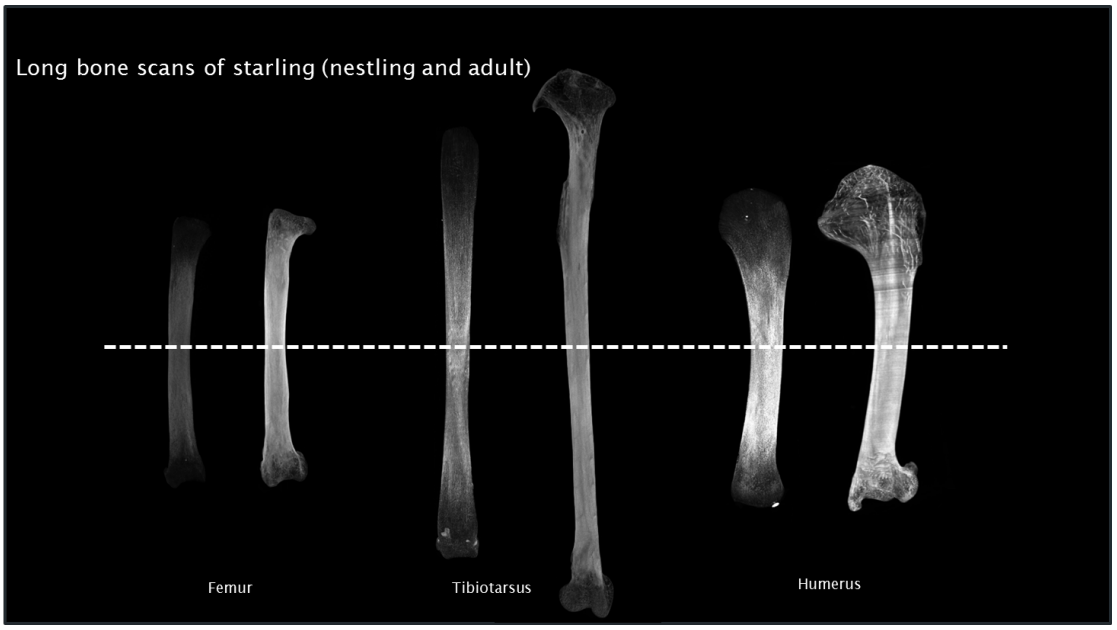

FIGURE 6.8: μCT scans of dry starling bones from Southampton Zooarchaeology reference collection. (Left) immature bones. (Right) Mature bones. Data collected using a Skyscan *in vivo* CT system (Bruker), with a voxel size of 9 μm.

TABLE 6.3: Quantification of intracortical pore microstructure based on segmented SR CT scans of a midshaft region of cortical bone in the long bones of starlings (*Sturnus vulgaris*) at different age stages.

Bone	Age	Cortical thickness (μm)	BV/TV	Canal diameter (μm)
Femur	Adult	52	0.994	7.5
Tibiotarsus	Adult	75.0	0.995	6.66
Humerus	Adult	78.1	0.998	9.05
Femur	Subadult	50.3	0.987	6.7
Tibiotarsus	Subadult	64.9	0.978	5.00
Humerus	Subadult	85	0.984	9.68
Femur	Juvenile	43	0.867	17.8
Tibiotarsus	Juvenile	48.6	0.752	15.9
Humerus	Juvenile	49.8	0.765	27.4

Unlike the precocial species, the relative cortical thickness in the juvenile starling bone was lower than in the adult(Table 6.3). Even in the subadult, where articular ends were fully formed and, externally, the bone appeared adult, the cortex remained a similar thickness to the

juvenile. The cortical thickness differed between the different limb bones: it was thinnest in the femur at all age stages, and thickest in the humerus. The tibiotarsus cortical thickness was similar, though slightly lower, than that of the humerus. Cortical thickness for all three bones increased with age.

Microstructurally, the three different age stages showed clear differences (Figure 6.9A). The cortical bone in the nestling had a mean BV/TV value of 0.87 in the femur and 0.75 in the tibiotarsus in the juvenile, which was much more porous than either the subadult or the adult. BV/TV was also slightly lower in the subadult than the adult (where BV/TV exceeded 0.99), but insufficient samples were present at any stage to carry out statistical analysis.

The difference in BV/TV was mirrored by differences in mean canal diameter, to an extent. Some of the difference in porosity can be attributed to the development of the avascular outer circumferential layer (OCL) in the adult. Both the subadult and adult had a region of reduced vascularisation near the periosteal surface, though the avascular region appeared thicker in the adult than the subadult, demonstrating that this region continues to develop after most somatic growth has occurred. In the humerus (Figure 6.9B), fewer canals were visible, and the outer avascular region appeared thicker.

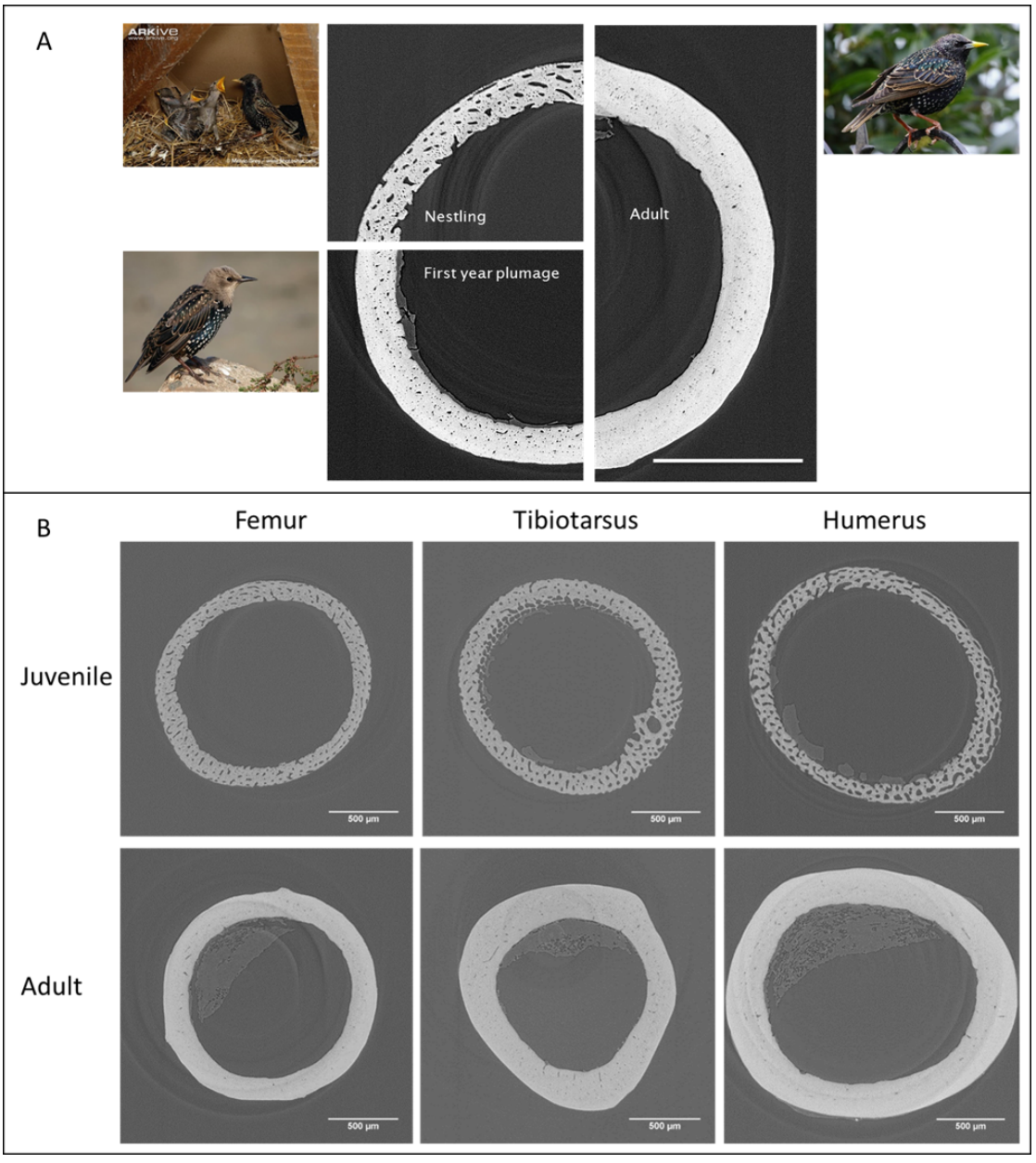

FIGURE 6.9: (A) Midshaft region of starling *Sturnus vulgaris* femur, juvenile (top left), subadult (lower left), and adult (right), demonstrating microstructural differences between all three age stages and the external appearances of the birds at these stages. All three images are to the same scale, scale bar 500 μm. (B) Comparison between the transverse midsections in the tibiotarsus, femur, and humerus in a juvenile and adult starling. Data collected at I13-2 beamline of Diamond Light Source, Harwell, UK. Voxel size 1.6 μm.

Rock dove

In the rock dove, only two age stages were available: nestling and adult. In addition, the humerus was not scanned as it was very thick and the imaging setup used in the relevant data collection session did not allow for imaging such thick samples.

The bone dimensions were similar between the juvenile and adult birds, both with well-formed articular surfaces. The cortical thickness was similar between the adult and juvenile bones, though slightly narrower in the juvenile (femur 72 μm and tibiotarsus 73 μm, compared with 78 μm and 91 μm respectively for the adult), similar to observed in the starling.

The juvenile bones were slightly more porous than the adult, though the mean canal diameter was higher in the adult femur than the juvenile femur (Table 6.4). In the juvenile, the periosteal surface appears rough due to a lack of avascular OCL. The endosteal surface showed convex 'cookie cutter' regions: evidence of resorption. In this individual, vascular canals were present, and densely so, right to the periosteal surface, indicating growth is still continuing. Both femur and tibiotarsus had similar vascular density and canal diameter.

In the adult bones, the periosteal region was less well-vascularised than the rest of the cortex, creating an OCL. However, the endosteal surface showed signs of remodelling. Given the relatively thin OCL, this bird may have been a young adult. This is supported by the structure of the cortical bone in the tibiotarsus of a wood pigeon (*Columba palumbus*, closely related to a rock dove) imaged in a pilot experiment, where a much thicker OCL is present, along with narrower canals (Figure **??**).

TABLE 6.4: Quantification of intracortical pore microstructure based on segmented SR CT scans of a midshaft region of cortical bone in the long bones of rock doves (*Columba livia*) at different age stages.

Bone	Age	Cortical thickness (μm)	BV/TV	Canal diameter (μm)
Femur	Adult	78	0.97	9.6
Tibiotarsus	Adult	91	0.99	8.4
Femur	Juvenile	72	0.95	7.4
Tibiotarsus	Juvenile	73	0.98	13.0

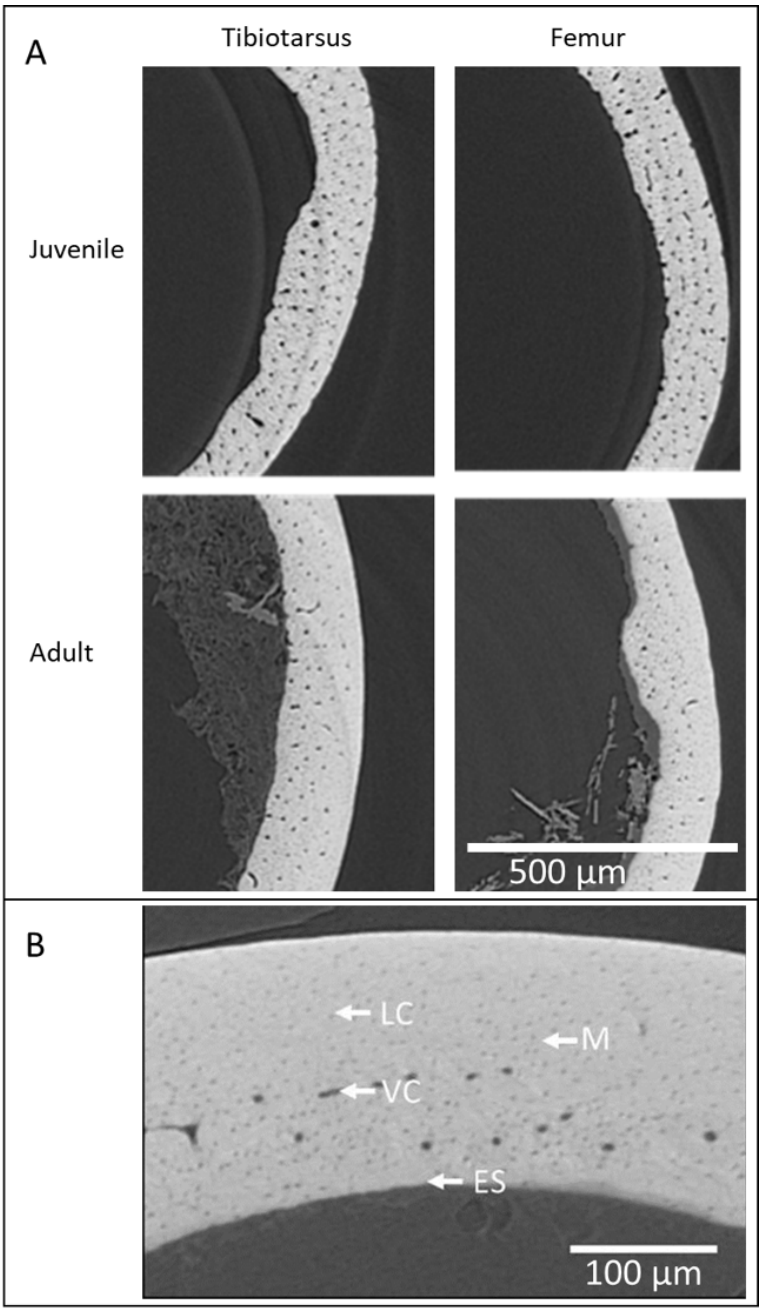

FIGURE 6.10: (A) Juvenile and adult cortical bone in the midshaft region of the femur and tibiotarsus in the rock dove (*Columba livia*). Juvenile is a fairly old nestling, adult appears quite young based on comparison with other species. Data collected at I13-2 beamline of Diamond Light Source, Harwell, UK. Voxel size 1.6 μm. (B) Transverse midshaft section of cortical bone from an adult wood pigeon tibiotarsus, showing thick avascular outer circumferential layer. LC osteocyte lacunae, M bone matrix, VC vascular canal, ES endosteal surface.

6.3.2 Vascular organisation and canal orientation

6.3.2.1 Precocial species

Partridge

Based on single SR CT slices, it appeared that in the 1 week old partridge, the canals run mostly longitudinally in the tibiotarsus, radial-oblique in the femur, and highly variable in the humerus. To some extent, this was supported by the 3D visualisations, which showed a network of canals running fairly longitudinally in the tibiotarsus, and more obliquely in the humerus. However, it was also clear from the 3D visualisation (Figure 6.11 that the cross-sectional shape of the canals was different between the different bones. In the tibiotarsus, the canals were very rounded, while in the humerus, they were radially flattened, enhancing the appearance of laminar canals in cross section. In the femur, the canals were intermediate in shape: more flattened than in the tibiotarsus but more rounded than in the humerus.

In the 7 week old partridge, these patterns persisted. From 2D sections, it appeared that the tibiotarsus had the most longitudinal canals, while the humerus had more laminar canals. In 3D, though the tibiotarsus did have more of a bias towards longitudinal canals, all three bones had highly anastomosing networks with canals running in different orientations. However, in the humerus the canals were more radially flattened in the humerus, and most rounded in the tibiotarsus.

Only the tibiotarsus was available for the adult. In this bone, the canals were predominantly longitudinal, with some connecting radial canals.

TABLE 6.5: Quantification of vascular canal orientation based on segmented SR CT scans of a midshaft region of cortical bone in the long bones of partridges (*Alectoris rufa*) at different age stages.

Bone	Age	Longitudinal index	Laminar index	Radial index
Tibiotarsus	Adult	0.681	0.172	0.0221
Femur	Subadult	0.252	0.227	0.130
Tibiotarsus	Subadult	0.142	0.353	0.110
Humerus	Subadult	0.285	0.336	0.0788
Femur	Juvenile	0.202	0.245	0.167
Tibiotarsus	Juvenile	0.353	0.255	0.117
Humerus	Juvenile	0.326	0.239	0.109

FIGURE 6.11: 3D visualisation of segmented vascular canals from a midshaft region of cortical bone from long bones in juvenile, subadult and adult partridges (*Alectoris rufa*). For each visualisation, (Left to right) transverse view, view through the cut edge of the cortex, and view from the periosteal surface. For the adult, only the tibiotarsus was available.

Ostrich

In the tibiotarsus, the thick cortex was divided into two distinct layers (Figures 6.7 and 6.12). In the outer region, from the 2D section, it appeared that the canals were organised into evenly spaced laminar primary osteons. In the endosteal region, canals appeared more disordered and orientations were less consistent. More canals appeared to run longitudinally and few ran circumferentially. In 3D (Figure 6.12) it was clear that the structures were more complex than appeared from the 2D section. In the periosteal region, canals were formed in distinct laminar layers of highly networked canals, interconnected by a smaller number of radial canals. The canals in the laminar networks were flattened, making them appear narrower in transverse cross-sections. In the inner region, canals did not form distinct layers and a small number of much larger canals ran through the network. All canals appeared more rounded in cross-section than those in the outer region. This layer is interpreted as secondary remodelling, and the larger canals as Haversian systems that have not yet been fully infilled.

In the femur, the two distinct layers were not clear in a 2D section (Figure 6.7), but were apparent in a 3D rendering (Figure 6.12). Similar to the tibiotarsus, evenly distributed layers of flattened networks formed the periosteal region, while a less ordered network filled the endosteal region. No very large vessels were present in this sample.

Although the cortical thicknesses were very different for the two bones, the canal orientations are similar between them (Table 6.6).

TABLE 6.6: Quantification of vascular canal orientation based on segmented SR CT scans of a midshaft region of cortical bone in the long bones of a 1-year-old ostrich (*Struthio camelus*).

Bone	Age	Longitudinal index	Laminar index	Radial index
Femur	Subadult	0.213	0.534	0.0469
Tibiotarsus	Subadult	0.242	0.422	0.0847

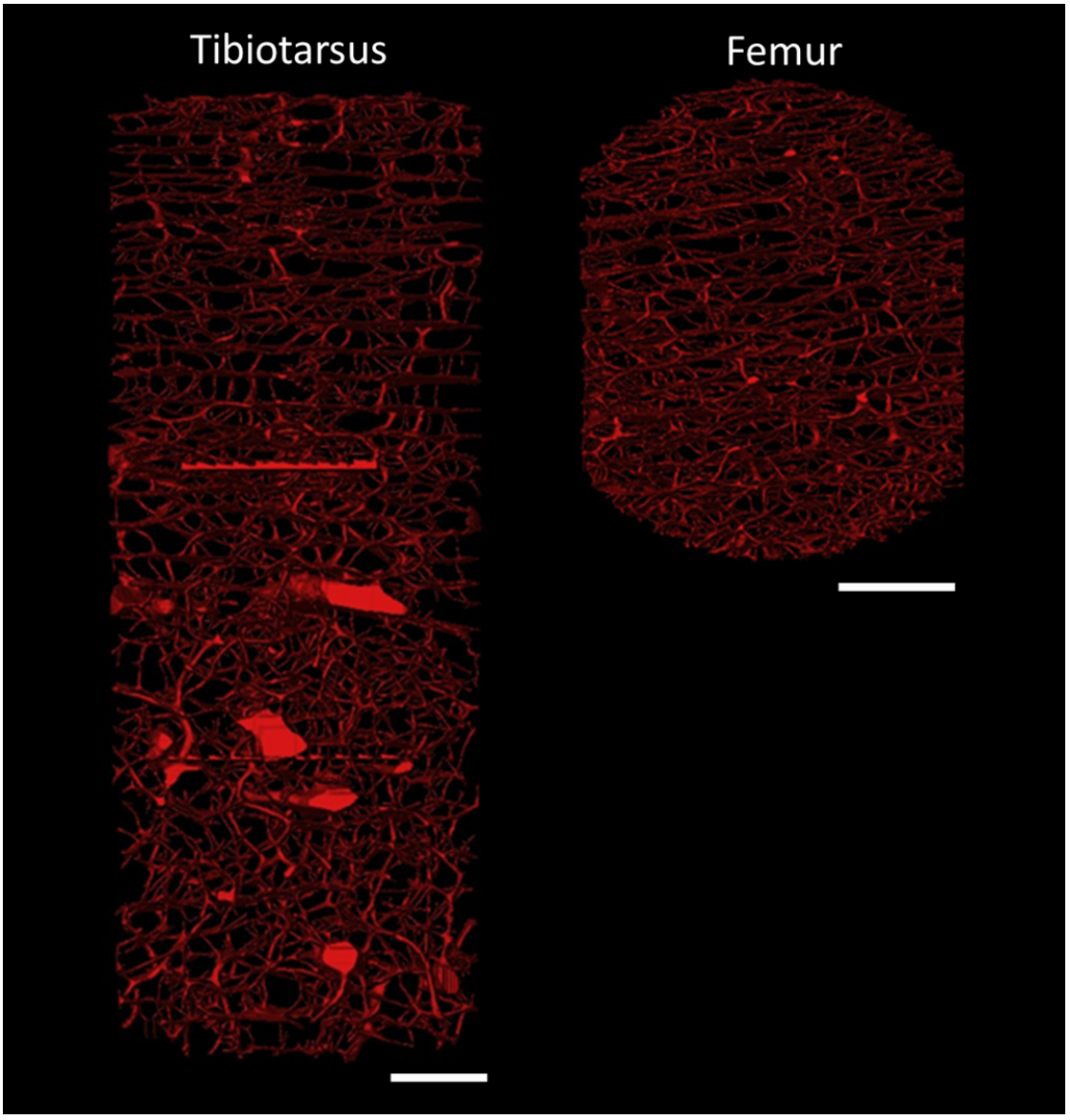

FIGURE 6.12: 3D visualisation of segmented vascular canals from a midshaft region of cortical bone from the tibiotarsus and femur of a 1-year-old ostrich. Transverse view. Scale bars 500 μm.

6.3.2.2 Altricial species

Starling

In the starling, the different bones had different vascular organisations. These differences were most apparent in the juveniles due to the thicker canals, but were maintained through to adulthood (Figure 6.13). In the tibiotarsus, canals appeared to run largely longitudinally when viewed in cross-section, especially towards the periosteal surface (Figure 6.9). At the endosteal surface, some canals appeared to run circumferentially or radially. In 3D, the largely longitudinal arrangement of canals was confirmed (Figure 6.13), and similar to the partridge, the canals in this bone were very cylindrical. In the humerus and femur, canals do not run quite as perfectly longitudinally, and were less cylindrical than those in the tibiotarsus, enhancing the appearance of a more laminar organisation. In the femur, the canal network had a woven appearance. In the humerus, the canals in the juvenile were thicker and appeared more similar to the femur than to the tibiotarsus.

In the femur, the canal orientation in the juvenile appeared quite different in different regions of the bone. In some areas, canals appeared circumferential, while in others they ran radially. In the adult, the canals mostly appeared longitudinal, though some oblique canals were present. More canals appeared circumferential, though a majority were still longitudinal.

In the subadult, the network topology appeared similar to the juvenile, though the canals were much narrower. In the adult, very few canals were present, and in a narrower region compared with the subadult, indicating remodelling of primary bone and deposition of avascular bone on the periosteal and endosteal surfaces.

TABLE 6.7: Quantification of vascular canal orientation based on segmented SR CT scans of a midshaft region of cortical bone in the long bones of starlings (*Sturnus vulgaris*) at different age stages.

Bone	Age	Longitudinal index	Laminar index	Radial index
Femur	Adult	0.274	0.245	0.157
Tibiotarsus	Adult	0.496	0.175	0.105
Humerus	Adult	0.400	0.220	0.125
Femur	Subadult	0.296	0.212	0.146
Tibiotarsus	Subadult	0.606	0.158	0.0600
Humerus	Subadult	0.0884	0.202	0.224
Femur	Juvenile	0.296	0.274	0.0858
Tibiotarsus	Juvenile	0.497	0.130	0.126
Humerus	Juvenile	0.334	0.239	0.134

Rock dove

In the rock dove, only the femur and tibiotarsus were imaged. Canal orientation appeared less biased in the dove compared with the starling, but the tibiotarsus still had more longitudinal canals than the femur (Table 6.8). The femur in the rock dove, like in the starling, had canals with a woven appearance when viewed from the periosteal surface (Figure **??**).

6.4 Discussion

The preliminary results in this chapter support and add to the findings from Chapter 5.

FIGURE 6.13: 3D visualisation of segmented vascular canals from a midshaft region of cortical bone from long bones in juvenile, subadult and adult starlings (*Sturnus vulgaris*). For each visualisation, (Left to right) transverse view, view through the cut edge of the cortex, and view from the periosteal surface.

TABLE 6.8: Quantification of vascular canal orientation based on segmented SR CT scans of a midshaft region of cortical bone in the long bones of rock doves (*Columba livia*) at different age stages.

Bone	Age	Longitudinal index	Laminar index	Radial index
Femur	Adult	0.436	0.201	0.141
Tibiotarsus	Adult	0.559	0.0750	0.150
Femur	Juvenile	0.635	0.0662	0.0872
Tibiotarsus	Juvenile	0.635	0.053	0.114

In terms of bone porosity, the results here confirm that BV/TV can be used to distinguish adult, subadult and juvenile birds. In all cases, except for the rock dove which appeared to be very close to fledging and therefore could almost be considered subadult, the juvenile BV/TV was below 0.95, subadult 0.95-98, and adult 0.98-99. While consistent, these values are very close together, and therefore the subadult-adult distinction should be used with caution, in conjunction with other observations such as the development of an OCL [160]. However, it has the potential to add a layer of argument to the identification of a developmental stage. Interestingly, even after fledging, the BV/TV in the starling remained lower than in the adult. Therefore it is possible to distinguish first year birds from older ones on this basis.

However, it is clear that different bones can mature at different times, as found in previous studies [164] though this is more true of the duck than any of the species studied in this chapter. This means that in fossils, it is critical to study both an upper and lower limb bone, in order to gain a better understanding of the age of the animal as a whole [164]. If only one bone can be studied, then the lower limb should be prioritised, as this may give a better indication of whole animal maturity than the upper limb, whose development may be delayed or disproportionate.

The comparisons between the precocial and altricial species are interesting in terms of growth patterns. In the precocial species, the cortex grew rapidly in thickness, with minimal resorption until much later. Therefore, subadult bone is thicker than adult. In the altricial species, the subadult bone was thinner than the adult. This supports the findings in the Californian gull, where extra material was found to be added to lower limb bones compared with the upper limb bones to strengthen the bone where required [166]. In the altricial species, protection within the nest and relatively sedentary developmental conditions mean that the extra thickening found in juvenile precocial birds is not required. Additionally, this makes the duck humerus more comparable to the altricial development than its precocial legs, confirming the duck as an interesting dual-development model species [164].

Secondary remodelling is an important component of measured bone microstructure. It is known that avian bone responds very rapidly to loading, resulting in very rapid bone remodelling (at least twice as fast as in humans [179]. From these scans, it is difficult to distinguish primary and secondary bone in most cases, since the orientation of the collagen fibres and the presence or absence of cement lines are not visible, though employing phase contrast imaging may help to reveal these structures [23]. The different regions in the ostrich are particularly clear, but the endosteal resorption that occurs in all the species also influences the structures we see. In the smaller altricial species this is particularly important as little primary bone is left once the endosteal regions have been resorbed. Given that growth slows as an animal reaches full size, it is likely that none of the bone tissue deposited early in

development (representing exceptionally rapid growth) is present in any of the study birds, as the nestlings studied for both the rock dove and starling were close to full size.

The canal orientation indices were somewhat variable, demonstrating the need for larger sample numbers and the need for care with interpretations from single fossils. However, there were consistent patterns across the species. In all cases, the longitudinal index was higher in the tibiotarsus than the other bones, confirming results from the duck and pheasant, and supporting published results [21]. Even in species with much smaller body mass (starling) this holds true. Additionally, differences in canal organisation were greater between different bones within an individual than between species. However, there was no clear difference in canal orientations between the femur and tibiotarsus of the ostrich.

In addition to the differences in orientation of the canals, the different bones also have different shapes of canal, which enhances the appearance of the structures in 2D. For example, the humerus tends to have more flattened canals, while the tibiotarsus has more rounded canals. In 2D sections, this made the canals in the humerus appear more laminar than they really are, which reiterates the findings from Chapter 4: that 2D methods cannot accurately capture 3D orientations or disentangle shape from orientation. The variation in shape may be due to differences in deposition rate, though with the exception of the duck the species studied have fairly isometric growth. Alternatively, this variation may be to do with reducing stress concentrations around the cavities, and optimising fibre layup [163], which will have different optimal arrangements according to the primary stresses in the bones [21].

6.4.1 Limitations and future work

This study is very preliminary, using a small number of samples to begin to understand the variation in bone microstructure in extant birds. To fully understand the variation, far more samples, from more species should be studied. The fact that there is variation between species and between different bones highlights the need for further study in extant birds, if we are to accurately extrapolate to fossils.

Further developmental studies should be a priority, including those looking at primary bone deposition in younger altricial birds. Ideally, these would involve fluorescent labelling to understand the rate of deposition at different stages, as carried out by [2, 15].

Finally, the ability to distinguish definitively between primary deposition and secondary remodelling is critical to the interpretation of bone microstructure. Therefore future work should focus on applying phase contrast approaches to identify osteons and incremental lines such as cement lines [23].

6.5 Conclusions

This chapter has begun to discuss the variability in bone deposition and microstructure between different extant avian species and different bones. It has confirmed the relationship between BV/TV and canal diameter and developmental age across multiple species, but also identified the caveat that BV/TV is also influenced by partial Haversian remodelling and therefore the adult/subadult identification should also take into account the presence of the OCL.

In precocial species, additional bone material thickens and strengthens otherwise weak material, while in altricial species relative cortical thickness is low in the juveniles. Therefore, cortical thickness in juvenile bone could be used in fossils to interpret bone usage, and whether the bird was precocial or altricial.

In all species, except the ostrich, the canals appear to have the most longitudinal orientation in the tibiotarsus, and a more laminar organisation in the humerus and femur. Canal orientation should be measured in 3D, given that canal shape is variable between bones. It is important to be able to distinguish shape from orientation to understand how the bone is deposited under different conditions.

However, there is a substantial body of work to be done before we can fully understand the relationships between bone deposition and microstructure and biological traits in birds, including studying more species using larger sample numbers and at different developmental stages, labelling bone deposition to understand growth rates, and biomechanical experiments.

Nonetheless, this chapter provides some additional information from across a range of extant birds that adds to the results from Chapter 5, helping us to better interpret the microstructure of fossil bone.

Chapter 7

Application to extinct birds and future challenges

7.1 Introduction

Studying the bone histology of extant birds is an important prerequisite to understanding the histology of extinct birds. However, it is also important to demonstrate that the techniques applied to the understanding of recent bone can also be applied to fossil bone, and that interpretations of the biology of an extinct bird can therefore be made. This chapter takes techniques used and developed in modern material and applies it to a range of subfossil and fossil samples. The application and limitations of the techniques are discussed, and the limits of current lab-based micro-computed tomographic (μCT) scanning are tested. The tissue architecture on a microscopic scale is then described and interpreted, aiming to better understand the developmental age and biology of the fossil specimens.

7.1.1 Part 1: Fossilisation and imaging fossils

7.1.1.1 Fossilisation alters the chemical make-up of animal remains

Although studying material from extant bird species can help with interpretation of fossil birds, recent and fossil bone are not necessarily directly comparable, because the fossilisation process can change the specimen, both structurally and chemically. In order to test the applicability of the high-resolution, quantitative 3D analysis methods described in previous chapters of this thesis to fossil material, preliminary studies were carried out using a selection of specimens from extinct birds, allowing a test of the methods used in modern birds in fossil material.

Bone is a composite material which includes a mineral phase (hydroxyapatite) and an organic phase (mostly collagen) [162]. In previous chapters of this thesis, recent samples of bone from extant species of bird were studied. The samples were either harvested from recently deceased birds and chemically fixed, or preserved by removal of soft tissue and drying. In both cases, both collagen and mineral are still present. In the present chapter, the specimens comprise specimens from recently extinct species (around 5000 years old), and fossil material from the

Pleistocene and Eocene. The younger specimens are not truly fossilised, as, like other specimens from similar locations and ages, they are likely to contain much of their original chemical makeup, even including proteins such as collagen [188], and DNA [11, 189]). This preservation is due to their relatively young age, and a good preservational environment. Due to the preservation of these specimens, it is expected that they will be comparable in terms of imaging to the modern samples imaged previously.

However, the older specimens are fossilised and are no longer bone. Fossilisation of animal remains occurs when remains are buried under layers of sediment, eventually becoming part of a sedimentary rock. Preservation can occur when, for example, an animal falls to the bottom of a lake and is buried in an anoxic environment[190]. The organic components of an animal break down first, usually only leaving mineralised parts such as teeth and bone. Even the mineralised parts of bone are unlikely to remain composed of the same minerals as were present originally. Bioapatite, the form of apatite in bone, is unstable, meaning it is easily replaced by other minerals. A recent experimental study found that even over short timescales, bioapatite was replaced by a more stable form of apatite, enriched with fluorine [28]. Therefore, gradually, hydroxyapatite is leached and replaced by other mineral crystals. The alignment of the crystals replacing the original minerals can follow the alignment of the original hydroxyapatite crystals, resulting in exceptionally well-preserved structures down to the ultrastructural level [27, 191].

Although ostecyte lacunae and even collagen fibre orientation can be preserved with high fidelity [27], the structure fossilised may not always accurately represent the original structure due to diagenesis (the effects of the physical, chemical, and biological environment on, for example, a bone) [190]. Diagenetic change can alter the appearance and chemical makeup of the bone, through bacterial or fungal invasion, plants, animal disturbance, erosion and weathering. Before fossilisation, bacterial damage can occur on the bone surface, but can also follow the vascular supply, resulting in damage specifically around vascular canals [9], as seen in Figure 7.1. Diagenetic change in bone microstructure is important to consider in analysing fossil bone, particularly in quantitative analysis of fossil bone, since it may change the porosity of the material, and the shape and size of intracortical pores. Therefore, while automated analyses can be applied to recent bone, as demonstrated in the previous two chapters, the preservation of fossil bone and how this affects the appearance of intracortical pores should be assessed before assuming that quantitative results accurately reflect biological truth.

7.1.1.2 X-ray CT applied to palaeobiology

X-ray micro-computed tomography (μCT) is becoming increasingly widespread within palaeobiology, and is now a more-or-less standard tool [115]. It has the potential to provide information not possible to achieve using conventional histological techniques, in theory without damaging the sample, making it an attractive technique in a field where samples are irreplaceable. However, imaging fossils using μCT can be challenging.

Fossils are found embedded in a sedimentary rock matrix, and while they can be prepared in such a way that the bones are separated from the matrix [192], this may be undesirable since it removes positional information about the bones and can lead to damage of the specimen. Here, X-ray imaging becomes very useful in virtually separating the bone from its matrix and studying

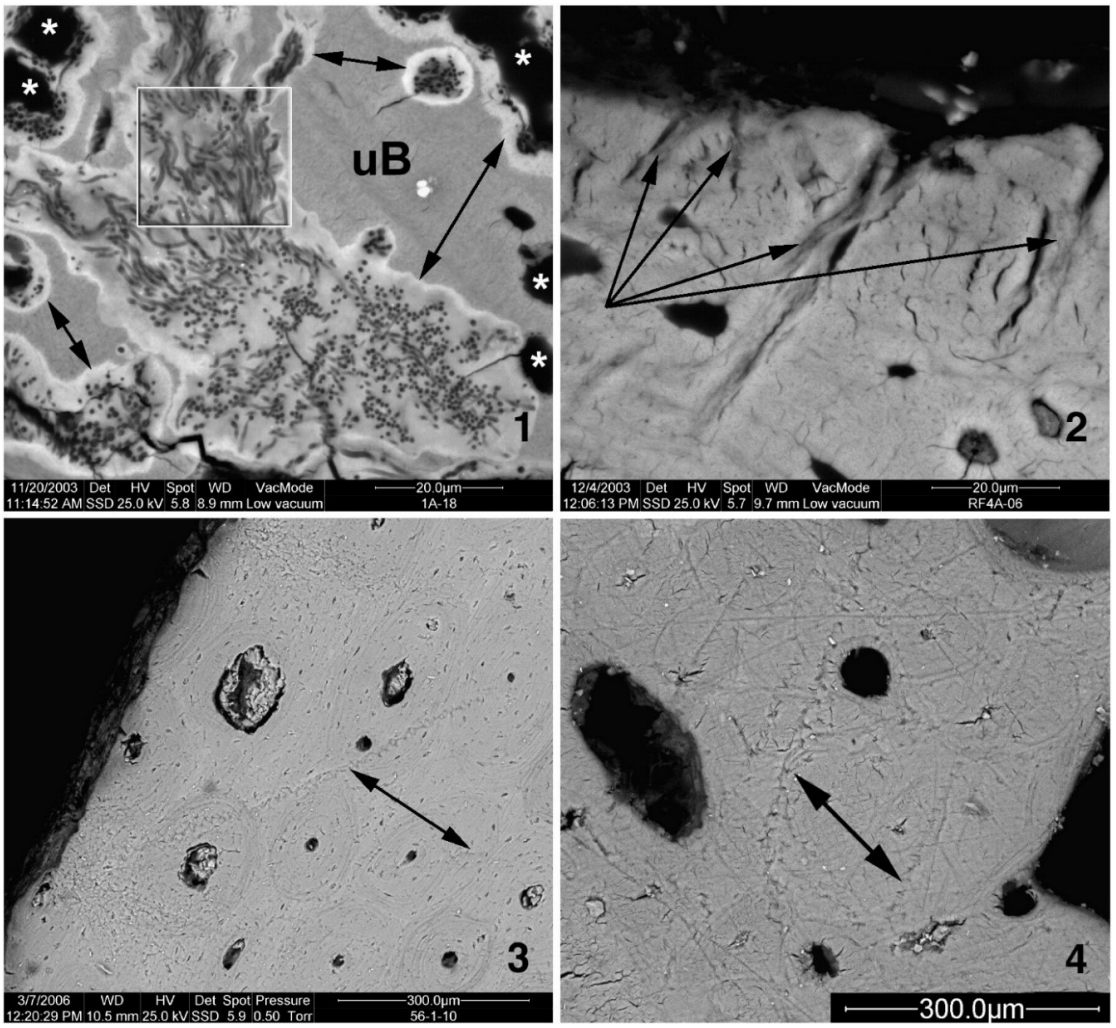

FIGURE 7.1: Bacterial diagenesis in the early stages (within a few years after death) of degradation of bone. SEM images show bacterial colonies and damage to bone. Some regions in very damaged bone are unaffected (uB), while others suffer, and have hypermineralized regions around colonies (very bright regions). Dark patches are where bone has been broken down, in some cases leading to widening of vascular canals within osteons. Black arrows point to tracks assigned to fungi, known as 'Wedl tunnelling' [8]. Figure reproduced from [9].

the internal detail without damaging the specimen. However, in larger samples, X-ray transmission becomes problematic. X-ray attenuation follows an exponential relationship with sample thickness (Beer-Lambert law) [193].

$I = I_0 exp(-\mu p x)$

Where I_0 is the initial X-ray beam energy, I is the final X-ray beam energy, $\mu$is the mass absorption coefficient, p is the density of the material, and x is the thickness of the sample.

Therefore increased sample sizes lead to exponentially increased X-ray attenuation. However, not all X-rays are equal in terms of imaging. X-rays interact with matter in different ways depending on their energy. In the energy ranges used for geological samples, two main interaction types need to be considered: photoelectric absorption and Compton scattering. During photoelectric absorption, the total energy of an X-ray photon is transferred to an inner electron, resulting in the electron being ejected. During Compton scattering, the photon interacts with an outer electron. The electron is ejected but only part of the energy of the

photon is lost, and it is deflected in a different direction. At lower energies, photoelectric absorption is the main cause of X-ray attenuation, and at higher energies the Compton effect is important. Photoelectric absorption is proportional to Z^{4-5} (Z is the atomic number of an atom), but Compton scattering is proportional to Z. Therefore, low-energy (soft) X-rays are more sensitive to materials with different chemical compositions than higher-energy ones and therefore lower energies result in better image contrast.

In CT imaging, there is therefore a trade-off to be made between image contrast (increased when energies are lower) and transmission (energy must be high enough for sufficient signal to reach the detector). With larger samples, higher X-ray energies may be required for penetration, which in turn reduces the contrast that can be achieved.

As in photographing a scene at night, an image can sometimes be improved by increasing exposure time but if transmission is very low this will result in a noisy image. The other alternative is to increase the flux, but in a lab-based μCT system flux is greatly limited. Systems using a synchrotron X-ray system therefore have an advantage here – they produce X-rays in a different way to lab-based systems, which means their flux can be orders of magnitude higher than lab-based X-ray sources. Therefore, due to the much greater flux, lower energies can be used with a better signal-to-noise ratio and, additionally, scan times are much shorter.

An additional advantage of synchrotron systems over lab-based systems is that the high flux in synchrotron systems allows for sufficient filtration that the beam is monochromatic (including a narrow range of X-ray energies). Lab-based μCT systems use polychromatic sources (a broad spectrum of different energies). Lower-energy (softer) X-rays are attentuated more than harder X-rays, so more high-energy X-rays will penetrate a sample than low-energy X-rays. However, (standard) CT reconstruction algorithms assume a monochromatic X-ray beam, and therefore beam hardening artefacts can occur, particularly in large, dense, samples. The problem of very dense materials can be addressed to some extent in lab-based systems using appropriate filtering to pre-harden the beam, and/or applying beam hardening corrections *post hoc* to imaging, or selecting a higher (monochromatic) X-ray energy in monochromatic synchrotron scans. This will increase transmission and reduce beam-hardening artefacts, though will reduce image contrast. Some very attenuating materials such as metals, or crystals of sulfide can cause artefacts which, at worst, obscure features in rest of the fossil [193].

A final important consideration to take into account when using CT for histological imaging is spatial resolution. The higher the resolution, the smaller the available field of view, so there is always a tradeoff between sample size and resolution. For studying osteocyte lacunae, with typical dimensions in the order of 10 μm, this may mean a field of view only a few millimetres in diameter [24]. CT imaging is considered as an imaging technique that is non-destructive [169], which is one of its main strengths in palaeontology. Although it is possible to image a small region of a larger object, the best possible images will be from samples which fit entirely within the field of view, which may involve destructively sampling the specimen.

Many fossil birds are preserved in flattened slabs, with the bones crushed into a single plane [194] due to compression from sediments above them during fossilisation. While this can make for an attractive display preparation, such as the iconic *Archaeopteryx*) specimens (Figure 7.2), it makes CT imaging difficult. Although the front-to-back thickness might only be a centimetre or two, the longer edges are much larger and it is this dimension that becomes the limiting factor for CT imaging of dense materials such as fossilised bones. When the flattened slab is

parallel to the X-ray beam, X-rays may be completely attenuated while there might be an acceptable transmission for other rotation angles of the sample, but this is variable with rotation, making it difficult to attain optimal or at least acceptable CT imaging conditions [195].

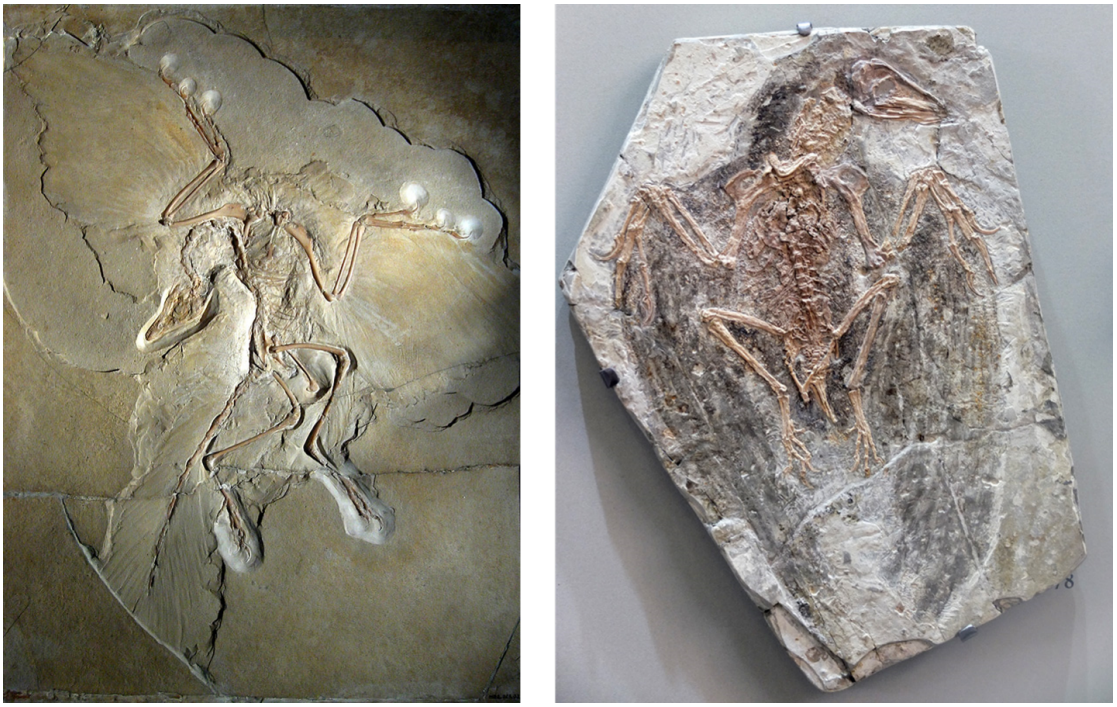

FIGURE 7.2: Typical flattened fossil birds (A) The Berlin specimen of *Archaeopteryx lithographica* (H. Raab.), (B) *Confuciusornis sanctus*, Manchester museum, image by Stu Pond.

Using synchrotron sources, it is possible to obtain high-quality histological information using CT, especially phase-contrast methods, as achieved in a fossil specimen of a perinate enantiornithine [25] (enantiornithines are a group of Mesozoic avialans). However, a goal for the development of these techniques would be to achieve histological-level resolutions in large, flattened samples, both in synchrotron and lab-based systems, since this would increase the accessibility of 3D histological techniques.

7.1.2 Part 2: Interpreting the biology of extinct birds

In addition to technological challenges, this chapter aims to address the biological interpretation of 3D histological results in extinct taxa. As discussed in previous chapters, the aim of histological study in palaeobiology is to uncover details about the depositional history of the bone tissue in question, which relates to the rate of growth [2, 15, 18], mechanical loading [21], phylogeny, and age. Thus studying bone microstructure can provide an estimate of the biology and life history of an animal [96]. Understanding these aspects of the biology of an extinct animal is important for helping us to understand the behaviour [149], life history, ecology, taxonomy [51] and evolution of extinct species.

In this chapter, the methods detailed in previous chapters were applied to samples from four different extinct birds. The selection of species included in this study was opportunistic, using samples with destructive sampling permission. The aim was to test whether their 3D bone

microstructure is similar to the extant species previously studied, and to try to interpret their biology based on data from previous chapters.

7.1.2.1 Elephant birds from Madagascar

The largest and most recent extinct birds studied here are samples from two species of elephant bird, or Aepyornid, from the Pleistocene/Holocene of Madagascar, one a species of *Aepyornis*, another a sample from *Mullerornis modestus* (5597 $\pm$ 40 years BP). The Aepyornids were the largest birds, some reaching 650kg in mass [182]. Of the two elephant bird genera included here, *Aepyornis* is the larger, with very robust limb bones, while *Mullerornis* is smaller with slightly more gracile bones. They had strong, conical beaks, possibly for breaking hard fruits or digging for roots, and had long lifespans, inferred from lines of arrested growth in histological sections [196]. These birds must have been an imposing sight, and it is possible that they are the origin of the Rokh legend in Arabic fairy tales [196]. This indicates the recency of their extinction, likely through human activity such as egg harvesting, and climate change, as well as recently described evidence of butchery [188].

Elephant bird samples, due to their relatively recent age (Holocene or Pleistocene [188]), are classified as subfossil rather than fossil. They retain much of the original chemical makeup of recent bone, and can preserve organic molecules such as proteins and DNA, allowing DNA sequencing and therefore accurate phylogenetic analysis [11, 189, 197].

The palaeognath phylogeny has recently undergone substantial changes due to new DNA evidence, one study using bone-derived DNA [189, 197], another using eggshell-derived DNA [11]. Both recent genetic studies have recreated the same topologies, with the elephant birds emerging as sister group to the kiwi (Figure 7.3).

Until recently, two genera were described, but a recent morphological study has re-examined the elephant birds and designated a third genus (*Vorombe*) and reduced the number of species from eight to four [182]. The systematics of this group has been much debated [196], with limited histological work carried out and therefore limited understanding of growth and development. It has been suggested that some of the morphological variation seen in the bones of these birds could be due to age, local environmental effects, sexual dimorphism, and equally that some morphological variation might be as yet undetected [196]. Although Hansford and Turvey's recent study [182] was exhaustive in terms of specimens, histology and age were not investigated and it is therefore unknown whether apparent characters could be age-related. Therefore, with further studies into the development and genetics of elephant birds could yield a greater or smaller number of species. Understanding their bone histology could help with understanding the biology and taxonomy of these enigmatic birds.

A number of histological descriptions have been published for ratites including elephant birds [70, 180, 196]. The bones of *Aepyornis* have been described as having a highly vascularized, fibrolamellar bone structure with primary osteons running in a laminar fashion, with some regions and some bones undergoing anything from minimal to complete Haversian remodelling [196]. LAGs have been identified, similar to modern palaeognaths including kiwis [156] and ostriches [70], though they are somewhat indistinct [196]. In some specimens, avascular inner and outer circumferential layers are present [196]. Therefore some individuals studied have been interpreted as adult while others were still growing [196].

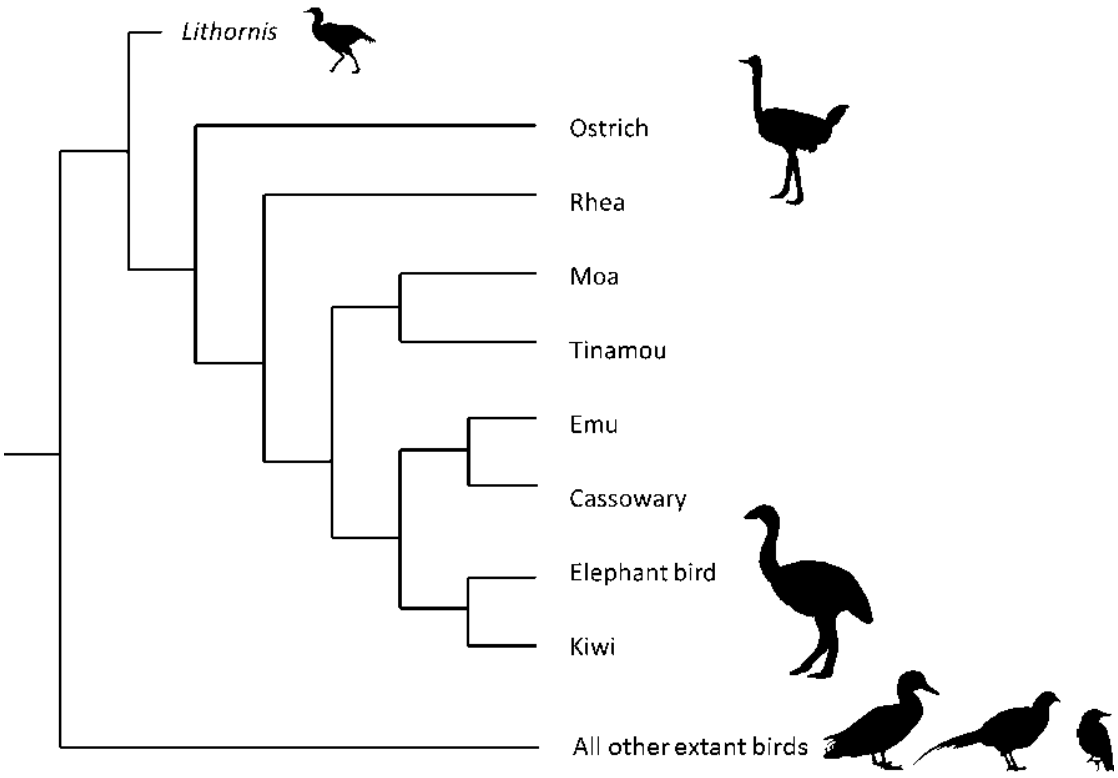

FIGURE 7.3: Phylogenetic relationships within the palaeognaths, following [10, 11]. Palaeognaths are the sister group to all other extant birds. The placement of *Lithornis* is uncertain, but is here placed as sister to all other palaeognaths, following [11]. Elephant birds are placed as sister group to the kiwi.

The samples studied in this chapter are of unknown developmental age, and species that have not yet been studied histologically, and hence this is a new description. Additionally, no studies have yet looked at the 3D microstructure of elephant bird bone.

7.1.2.2 A European palaeognath

The oldest bird specimen studied here is an individual attributed to the genus *Lithornis*, a group of chicken-sized, flighted palaeognaths found in Eocene formations across Europe [198, 199]. This individual was found in the London Clay formation, Eocene, on the Isle of Sheppey, United Kingdom. Houde [200] described species within the *Lithornis* genus as capable of good sustained flight, with sensitive bills possibly for foraging for seeds, insects and berries. The phylogenetic placement of the genus is uncertain, some placing it as sister to the tinamous [198], the other group of flying ratites, and others placing it as sister group to all palaeognaths [11]. Given the recent changes in palaeognath phylogeny, its placement remains uncertain, but here it is placed as sister to all palaeognaths, following [11].

A single histological section from a *Lithornis* tibiotarsus was published by Houde in 1986 [200]. Houde described the osteons in the sample as running longitudinally in the tibiotarsus, like tinamous and neognaths but not other ratites. Other histological descriptions not available for comparison, and therefore again this is a new study for *Lithornis*.

7.1.2.3 An unidentified bird from Florida

The final bird sample included in this study was a tarsometatarsus from an unidentified, approximately chicken-sized, bird found in Pleistocene deposits in Dixie County, Florida. The Pleistocene deposits of Florida contain a large diversity of terrestrial mammals, including megafauna such as mastadons, and the avifauna has been known to include a wide range of species such as ducks, loons, herons (water birds), as well as owls, woodpeckers, hawks, osprey, wild turkey, cardinals, and passenger pigeons [201], many of which are still extant. This specimen is unidentified but would have fitted within the described fauna, and therefore is not a ratite, but a more derived bird.

In this chapter, the same imaging techniques applied to recent bone samples in previous chapters within this thesis were applied to samples from extinct birds. Initially, small samples (a few millimetres) were scanned using SR CT to obtain the best contrast and most appropriate resolution (able to segment both vascular canals and osteocyte lacunae). The scans from these samples were then compared with results from previous chapters in this thesis in order to make interpretations about developmental age, and some aspects of the biology, for the specimens studied.

In addition, a difficult (large, flat) specimen was imaged using a lab-based CT system to assess how far away from the goal of completely non-destructive, widely accessible histological-level CT imaging current technology is. The aim was to establish how much information could be gained from this approach using the full 360 scan. For this experiment, rather than borrowing a fossil bird from a museum, a less valuable, more readily available sample was chosen, of approximately similar dimensions and material to a fossil bird. The chosen sample is a specimen of an echinoderm, *Pleurocystites*. This specimen is not a vertebrate, but, given the sample dimensions, should provide the same technological challenge as a similar bird fossil. Although echinoderms have a completely different body plan to vertebrates (Figure 7.4A), they contain calcified structures (stereom), with features at a similar scale to bone microstructure (Figure 7.4), though calcium carbonate rather than phosphate [12]. The microstructure varies between different body regions (Figure 7.4B-D) and should be detectable at similar spatial resolutions to bone microstructure.

- Hypothesis: The imaging techniques applied to recent material in previous chapters can be applied to fossil specimens to interpret the biology of extinct birds
- Objectives: To apply the same imaging and analysis techniques developed in previous chapters to some extinct species (*Aepyornis*, *Mullerornis*, *Lithornis*, and an unidentified Pleistocene bird from Florida). Specific aims:
    1. To apply high-resolution SR CT imaging techniques to small fossil samples
    2. To test the limits of current lab-based CT techniques for imaging microstructural detail in a large, flat, fossil sample
    3. To interpret the biology of a range of extinct birds

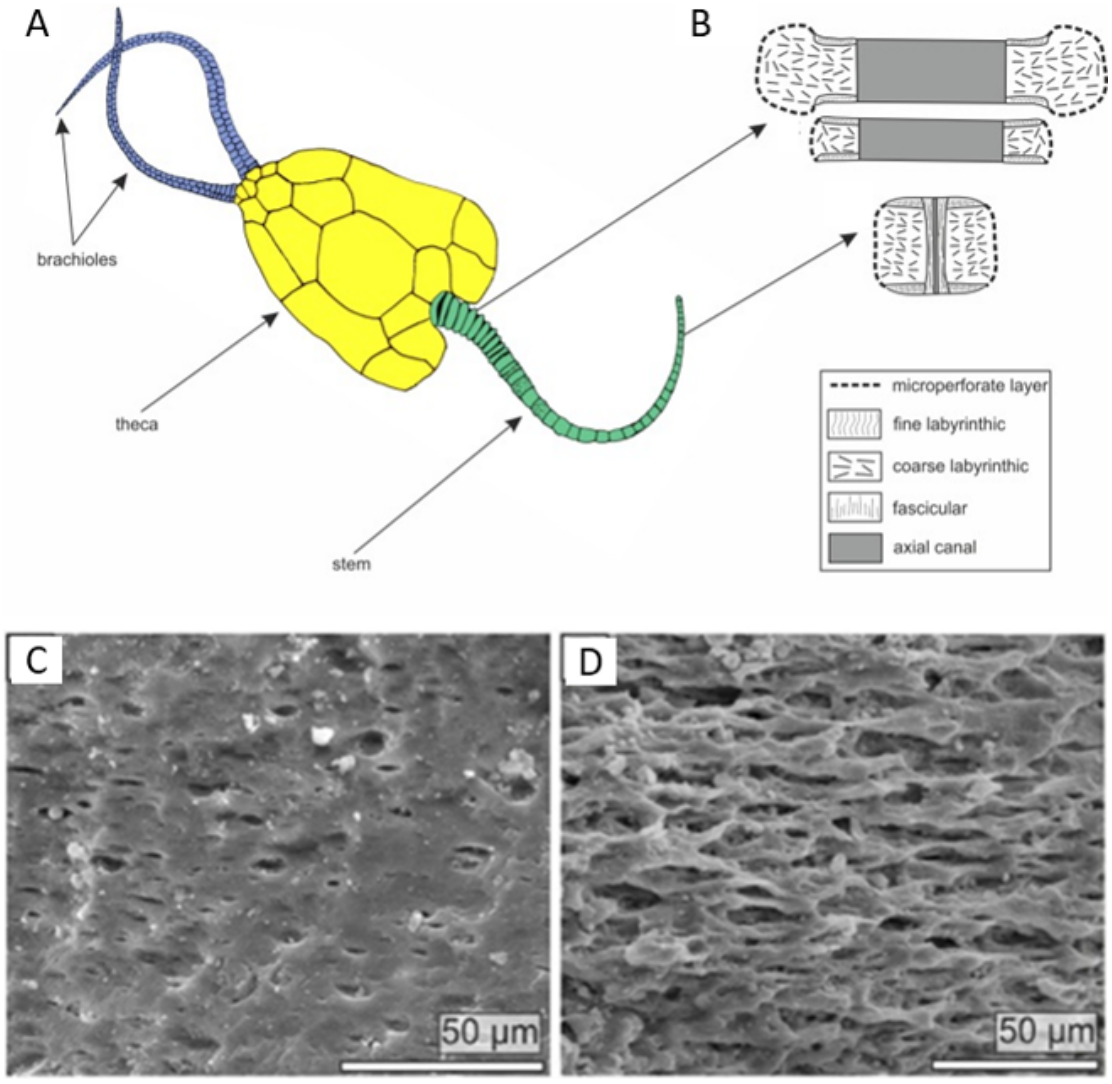

FIGURE 7.4: Stereom microstructure in the fossil echinoderm *Pleurocytstites*, seen under SEM. (A) Body plan of *Pleurocystites*, including a pair of brachioles, a theca, and a stem (B) diagram showing regions containing different microstructures within the stem of the animal (C-D) SEM images showing stereom microstructure at different regions within the stem (C) microperforate layer near surface of stem (D) fascicular stereom near lumen of distal stem. Figure adapted from [12].

7.2 Methods

7.2.1 Materials

Elephant bird samples were kindly provided by James Hansford, samples taken as part of another project. *Aepyornis* (122.9 44 Oslo) and *Mullerornis* (MAD 6768 Paris). Both samples were taken from the midshaft of the tibiotarsus.

The *Lithornis* sample was kindly loaned from the private collection of Marc Jobling.

An unidentified bird tarsometatarsus (Unidentified), from the Pleistocene, Dixie County, Florida, and a specimen of *Pleurocystites*, an Ordovician echinoderm were loaned from the private collection of Neil Gostling, University of Southampton.

7.2.2 Sample preparation

Samples of *Aepyornis*, *Mullerornis*, *Lithornis*, and Unidentified were cut in order to obtain the best contrast and spatial resolution possible. Where possible, samples were cut to approximately 2 mm square, in order to fit within the field of view at the spatial resolution chosen, though some samples were slightly larger. For the elephant bird samples, cuts were made using a slow-speed saw, and to enable imaging across the whole cortex, matchstick-shaped samples of the required diameter were cut across the cortex (Figure 7.5).

Samples were cut from the exposed, broken ends of the humerus and tibiotarsus for *Lithornis* using a handheld rotary tool with a diamond edged blade to minimise damage to the rest of the fossil (Figure 7.6). Similar samples were cut from the broken, exposed end of the Unidentified using a slow-speed saw (Figure 7.7).

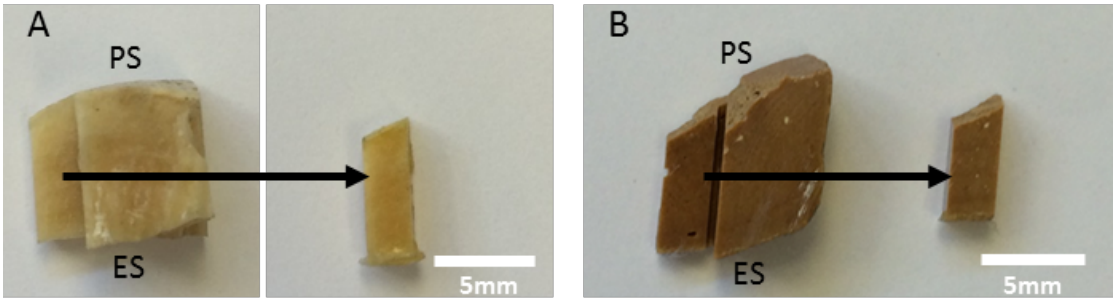

FIGURE 7.5: Sample preparation for elephant bird samples. (A) (Left) Section of *Aepyornis* cortical bone provided by James Hansford, (Right) matchstick-shaped sample cut across the cortex for SR CT imaging (B) (Left) Section of *Mullerornis* cortical bone provided by James Hansford (Right) matchstick-shaped sample cut across the cortex for SR CT imaging. PS periosteal surface, ES endosteal surface.

No preparation was undertaken for the *Pleurocystites* fossil.

7.2.3 Sample mounting

Prepared samples were glued to aluminium SEM stubs to minimise movement and reduce the risk of losing the samples. Elephant bird samples were mounted upright to enable several scans

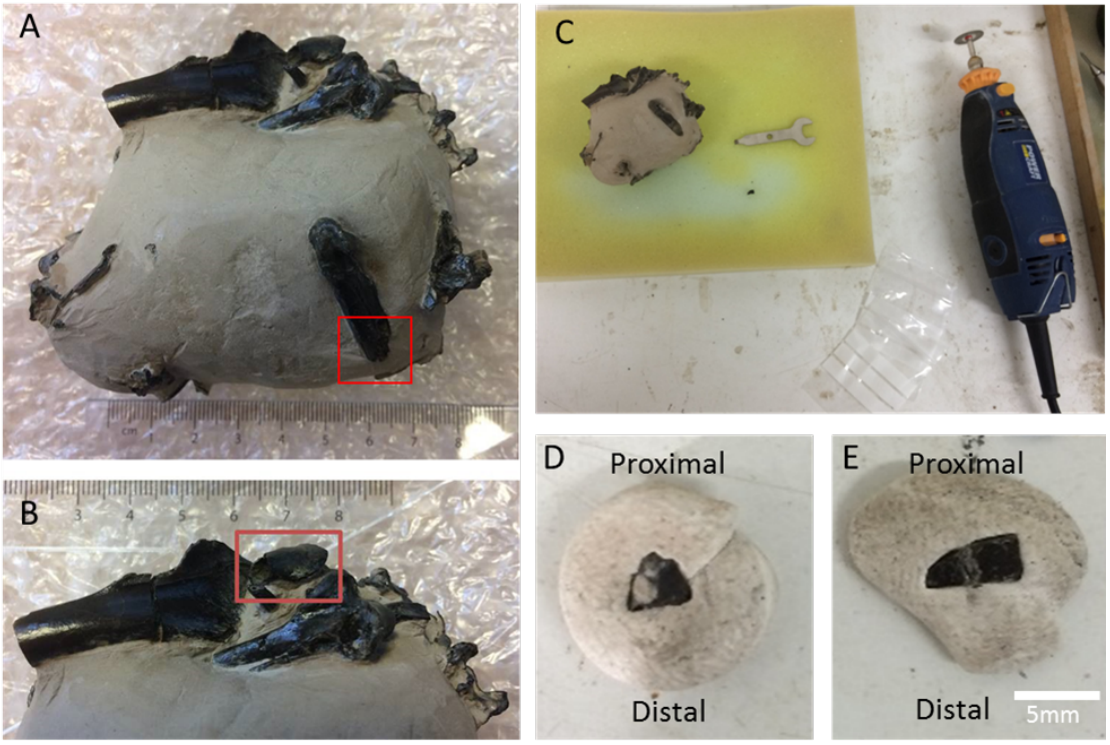

FIGURE 7.6: Sample preparation for *Lithornis*. (A and B) Specimen in London Clay. Red boxes indicate the humerus and tibiotarsus. (C) Removal of small pieces from the ends of bones using a rotary cutting tool. (D) Humerus sample. (E) Tibiotarsus samples.

FIGURE 7.7: Unidentified bird tarsometatarsus. (A) Posterior view. (B) Anterior view. (C) Proximal part of fossil after removal of sample, reflective surfaces are cut surfaces. (D) Scanned sample.

at different heights in y while remaining within the field of view. *Lithornis* and Unidentified were mounted in the same orientation as the earlier studies in modern species, so that

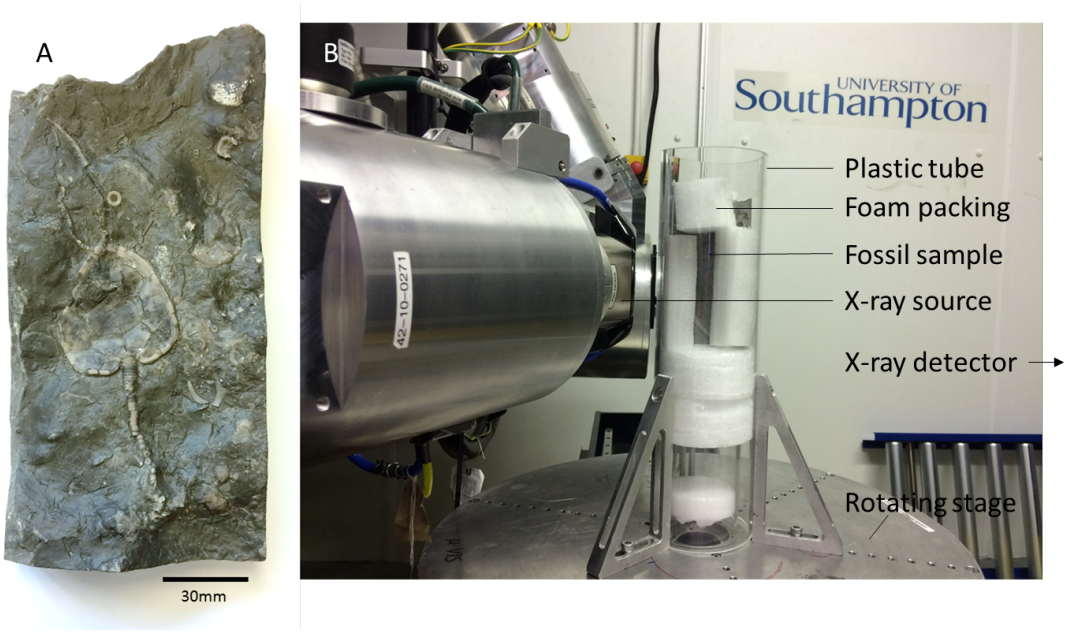

FIGURE 7.8: Scan setup for imaging the microstructure of a small region in a fossil specimen of *Pleurocystites*(A) Pleurocystites fossil specimen. (B) Upright sample mounting inside a plastic tube packed with foam, in a bespoke hutch CT scanner (Nikon Metrology, Tring, Hertfordshire, UK) at μ-VIS X-ray Imaging Centre, University of Southampton, UK.

reconstructed slices showed transverse sections.

7.2.4 Scan setup

Aepyornis, *Mullerornis*, *Lithornis*, and unidentified tarsometatarsus samples were imaged at the I13-2 beamline at Diamond Light Source, Harwell, UK. Scan setup was as follows: 0.8 μm voxel size, pink beam, pco edge 5.5 camera, 4x optical objective. 20 mm propagation distance (sample to detector). 0.16s exposure time per projection. 4001 projections over a range of 180 °rotation. In addition, a 0.7 mm steel filter was used to pre-harden the pink beam.

For scans at multiple heights, the sample was moved 0.5 mm in vertical direction (parallel to the rotation axis).

The echinoderm fossil was scanned using a bespoke hutch μCT scanner (Nikon Metrology, Tring, Hertfordshire, UK) at μ-VIS X-ray Imaging Centre, University of Southampton, UK (Figure 7.8). Energy selected was 200kV, exposure was 708 ms, 8 frames per projection were collected over 360°rotation.

7.2.5 Image processing

For the elephant bird samples, up to six scans were required to cover the whole bone cortex. However, in order to compare these scans to the other samples, a similar image across the entire cortex in a transverse section was required. Therefore the scans were combined by finding matching slices in two scans and discarding duplicate regions. This was straightforward as movement between the scans occurred only in the vertical direction and not in the horizontal directions. However, the resulting composite scan was very large and as a result analysis was

computationally heavy. Therefore, the data volume was reduced by increasing the final voxel size in these scans by averaging 4x in each direction. The final voxel size was therefore 3.6 μm. The merged scans were resliced to match the orientations of all other scans (providing a stack of anatomically transverse sections).

All other scans were binned 2x in each direction, so that results were more directly comparable with modern samples in previous chapters.

The *Lithornis* samples included a region of (highly attenuating) matrix. This region was drawn around and removed manually in Fiji, allowing the segmentation workflow used in previous chapters to work as normal. Similarly, a region of diagenesis in Unidentified was masked off so it did not affect quantification of the image data.

Additionally, manual thresholds were chosen for each sample, as no single threshold or algorithm accurately defined the vascular canals and osteocyte lacunae. Thresholds were selected to give the best (subjective) representation of the structures of interest.

7.2.6 Data analysis

Segmented scans were analysed using methods discussed in Chapter 4. Bone volume fraction (BV/TV), canal diameter, osteocyte lacunar volume, and osteocyte lacunar number density were measured using the Particle Analysis tools in BoneJ [125], a plugin for ImageJ designed for measuring bone. The Fiji distribution of ImageJ was used [123].

Cortical thickness was measured using Particle Analysis tool in BoneJ. A cortical mask was produced by filling pores within the cortical bone and the thickness of the mask was measured. Relative thickness was defined as the thickness of the cortex as a proportion of the diameter of the bone.

Canal orientation was measured using the implementation of Pratt's 2017 method [14] detailed in Chapter 4. Segmented canal networks were thinned to single pixel lines (skeletonised) using the Skeletonize 2D/3D tool within BoneJ, and the network analysed using the Analyze Skeleton tool within the same plugin. The branch points of the skeleton were used to define individual canals as straight segments and the orientation of each segment calculated as a radial angle and a longitudinal angle using a custom Python script. These two angles were then used to calculate a radial index, a laminar index, and a longitudinal index, describing the proportion of canals in the network with those specific orientations. The indices were weighted by canal length to reduce the undue influence of short canal segments.

3D visualisations were generated in Avizo.

7.3 Results

7.3.1 Part 1: High-resolution imaging of fossil material

In the subfossil elephant bird scans, contrast and spatial resolution was sufficient to visualise vascular canals clearly, though the increased voxel size meant that osteocyte lacunae were not so clearly visible and too small to segment reliably (Figure 7.9). In terms of contrast and

resolution, the images are almost indistinguishable from the ostrich scans from Chapter 6. Some surface damage was clear on the periosteal surface of the bone for both specimens, and a crack was visible in the *Aepyornis* scan (Figure 7.9 B, inset), but otherwise the samples were very well preserved.

For Unidentified, similarly good preservation was present through much of the sample (Figure 7.9 C). The periosteal surface had undergone structural diagenesis and therefore the outer layers of the bone were not present (Figure 7.9 C, inset). In addition, where this diagenesis had occurred, small regions of more attenuating mineral were present, further reducing the region that can be studied and causing small streaking artefacts in the surrounding region of bone (Figure 7.9 C, inset). The sample was anisometric (it was a section of cortical bone and therefore relatively flattened), and ring artefacts are present perpendicular to the long edge of the sample, possibly due to insufficient transmission when the sample was at an angle where the X-rays passed through the longest distance. However, in general, the scan provided resolution and contrast comparable to those found in modern bone in the previous chapters of this thesis, enabling automated segmentation and analysis once the diagenetic region was manually removed.

The scans of both *Lithornis* samples demonstrated that microstructural detail had been preserved in this fossil, too, with both vascular canals and osteocyte lacunae visible (Figure 7.9 D, humerus shown here). Both *Lithornis* samples had endosteal deposition of a highly attenuating material (Figure 7.9 E). In the *Lithornis* samples, the scan artefacts appeared worse than in Unidentified (Figure 7.9 C (Unidentified) and F (*Lithornis*)). This is likely due to the matrix layer which was highly attenuating and therefore made X-ray transmission difficult.

The avian fossil scans were all optimised for high-resolution, high-contrast CT imaging, using destructive sampling techniques to minimise the sample size. However, it was also important to be able to test whether the same techniques could work in a larger, more challenging fossil sample, and whether a lab-based, more accessible scan set up could be used. Therefore a much larger, flattened test sample was scanned in a lab-based CT system.

The large, flat *Pleurocystites* fossil proved difficult to image (Figure 7.10). During setup, balancing the need for transmission through the thickest parts of the sample and preventing saturation of regions outside the sample was not entirely possible. The resulting scan was noisy, and different regions had similar grey values. Some fine details, such as cracks, were visible, and the overall morphology of the fossil was clear, but little to no detail was visible within the fossil itself.

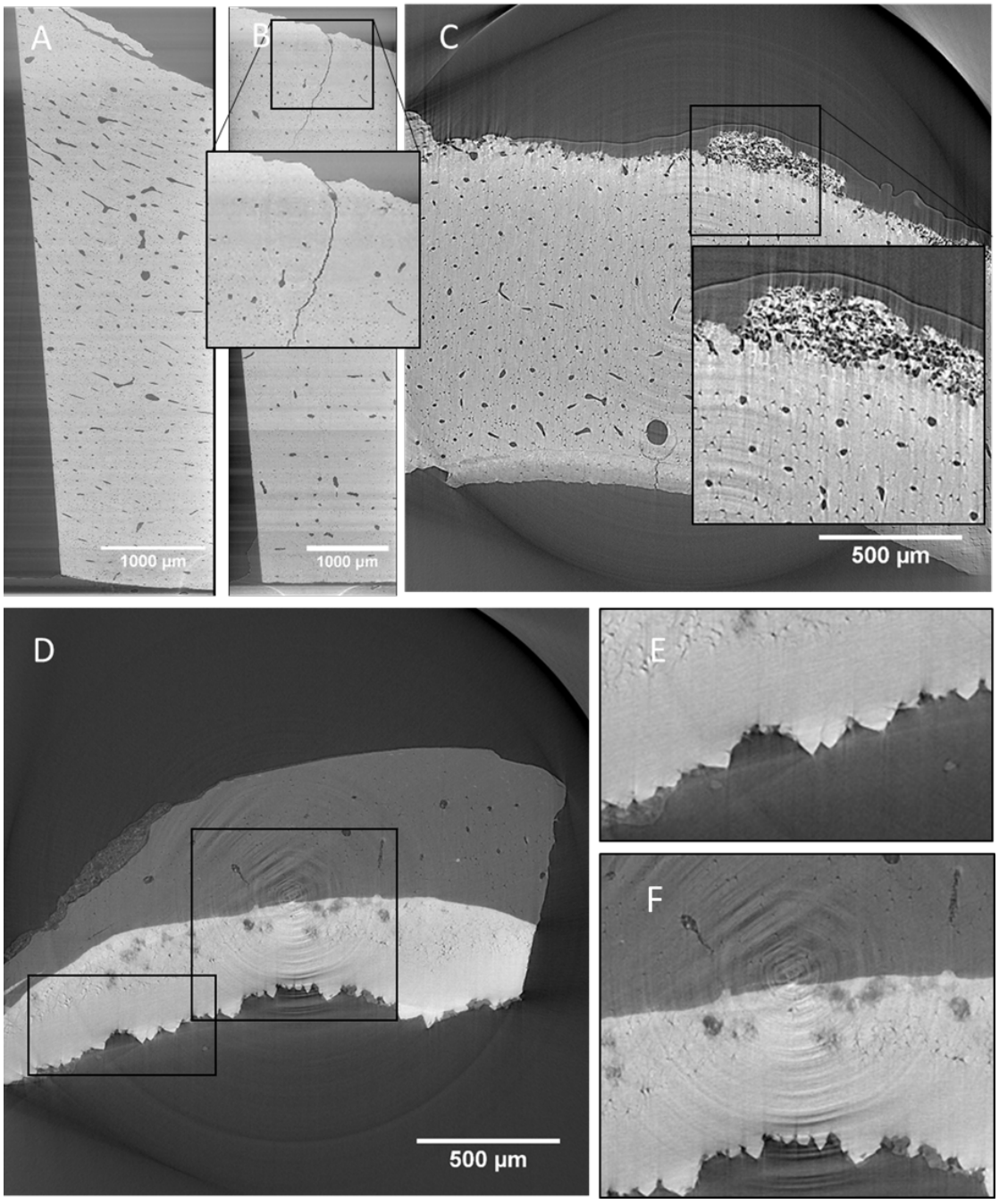

FIGURE 7.9: Summary images for SR CT scans of bone samples from a range of extinct birds (single CT slice, transverse sections). (A) *Mullerornis* tibiotarsus. Voxel size 3.2 μm (B) *Aepyronis* tibiotarsus, voxel size 3.2 μm. Inset shows damage at the bone surface and a crack running across the cortex. (C) Tarsometatarsus from an unidentified Pleistocene bird (Unidentified), voxel size 1.6 μm. Inset shows structural change (diagenesis) at the periosteal surface, highly attenuating inclusions (bright white patches), and resultant streaking artefacts. (D) *Lithornis* humerus, voxel size 1.6 μm. Dark grey, upper region is bone, light grey, lower region is a highly-attenuating deposit on the endosteal surface (E) magnified region of D showing attenuating deposite, (F) magnified region of D showing ring artefacts.

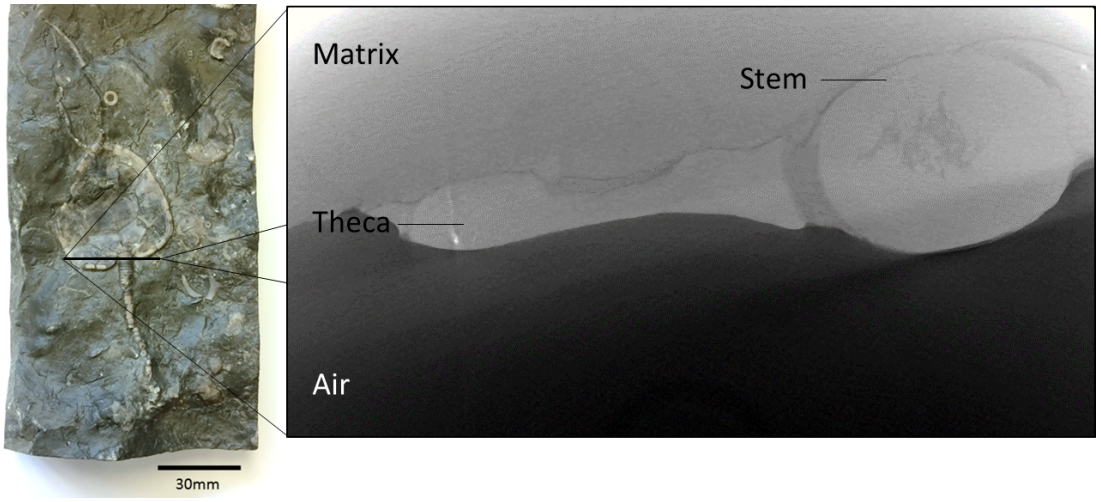

FIGURE 7.10: Section from μCT scan of *Pleurocystites*. Overall shape of the fossil specimen, and different body sections, are visible and could be segmented, but microstructure is not visible due to noise.

7.3.2 Part 2: interpreting the age and biology of extinct birds

7.3.2.1 Subfossil specimens of *Aepyornis* and *Mullerornis*

Mullerornis

The cortex was 7 mm thick. The samples were provided without context and therefore orientation has been assumed from the shape of the samples and position of cut surfaces. For *Mullerornis*, the shape of the sample made this difficult, and it is known that the endosteal surface can be undulating.

Based on a single transverse slice (Figure 7.11A), the cortex was densely vascularized, with a large number of fairly narrow canals. Near the periosteal surface, the primary osteons were laminar in organisation (Figure 7.11A 1). Towards the endosteal surface, the canals appeared more longitudinal.

However, in 3D (Figure 7.11B), it appeared that this structure was more consistent than thought from the 2D slice (Figure 7.11A). The vascular networks showed repeating patterns, with a small number of larger, rounder, radial canals connecting layers of flattened, reticular networks. It seems likely that the layers of flattened networks are primary bone, but some of the less regular, larger canals may be secondary remodelling.

The two regions are similar to those seen in the young ostrich bone scanned in Chapter 6, suggesting growth in the periosteal region and remodelling in the endosteal region. However, the organisation of the remodelled region is quite different to that in the ostrich, where canals appeared disordered. Here, the endosteal region, if anything, was more highly structured than the periosteal, with continuous radial canals connecting layers of laminar networks.

The osteocyte lacunae appeared largest furthest from the canals, suggesting the presence of woven bone in these regions.

The bone volume fraction (BV/TV) for this sample was 0.966, and the mean canal diameter was 25.9 μm (Table 7.1). For the canal orientations, the longitudinal index was measured as 0.288, the laminar index as 0.348, and the radial index as 0.0494.

Aepyornis

The *Aepyornis* cortex was 8 mm thick. The sample (Figure 7.12 A) appeared less densely vascularised and the canals appear narrower than those in the *Mullerornis* sample. Fewer canals appeared to run around the circumference of the bone, though some appeared to run radially. The bone tissue was more consistent in structure across the cortex, except for the endosteal and periosteal regions which appeared less densely vascularised than the rest of the cortex. From the 2D section (Figure 7.12 A), it was difficult to discern a pattern within the vascular organisation, except that it appeared that most of the vascular canals run longitudinally. However, the 3D visualisation (Figure 7.12B) showed a clearly regular and repeating pattern of vasculature, similar to that seen in the endosteal region of the *Mullerornis* sample (Figure 7.11). Concentric layers of flattened canals interspersed with avascular regions were connected by larger, almost radial canals.

At the periosteal surface, a region of reduced vascularisation (the outer circumferential layer, or OCL) was present. An uneven bone surface suggested some bone surface could have been eroded.

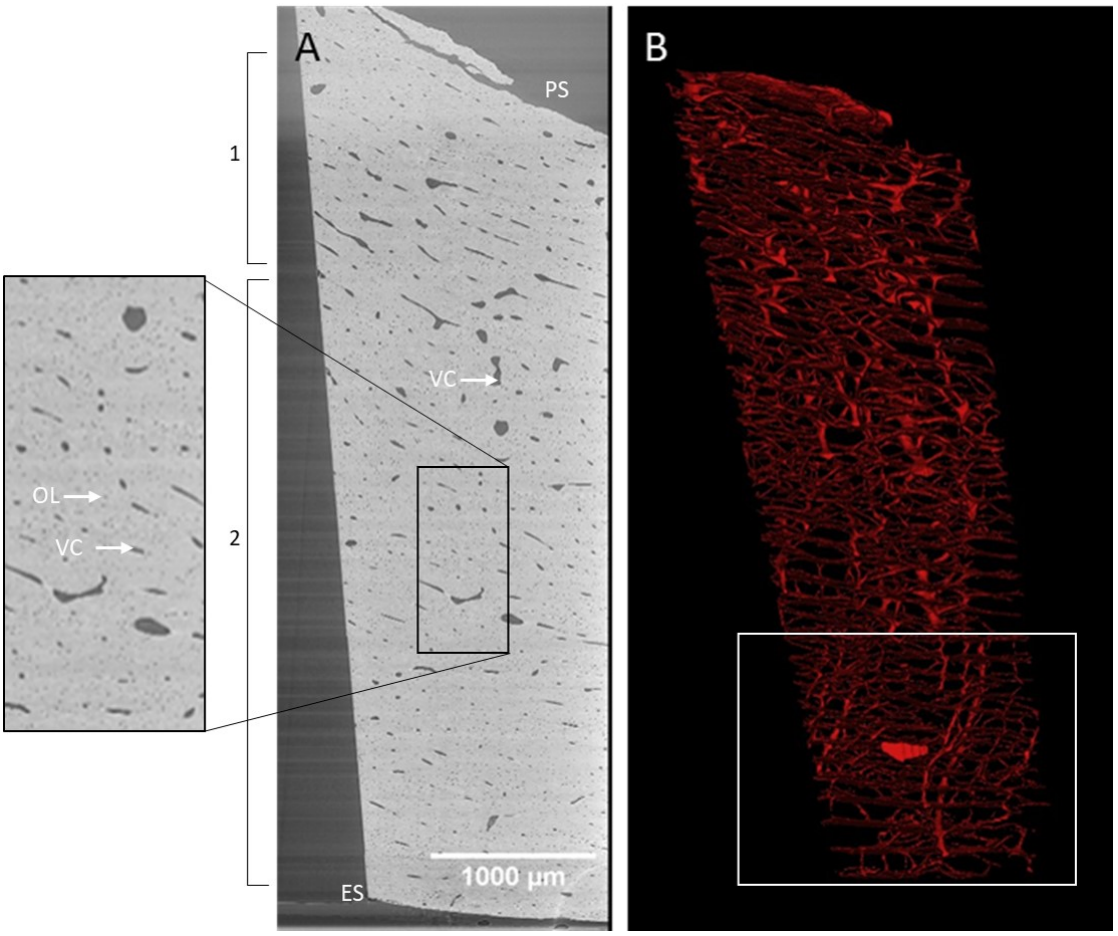

FIGURE 7.11: SR CT images of cortical bone from the midshaft of a tibiotarsus from a specimen of *Mullerornis medius*. Images collected at I13-2 beamline at Diamond Light Source, Harwell, UK. Voxel size 3.2 μm. (A) Transverse section across the cortex, showing vascular canals with apparent laminar organisation near the periosteal surface, and longitudinal organisation nearer the endosteal surface. Black box shows location of magnified region (left). PS periosteal surface, ES endosteal surface, VC vascular canal, OL osteocyte lacunae. 1 Region of vascular canals that appear laminar. 2 Region where vascular canals appear more longitudinal. (B) Vascular canals from the same sample segmented and rendered in 3D using Avizo. White box shows region of different vascular organisation from the rest of the cortex.

In both elephant bird samples, like in the modern bone samples, differences in mineral density were apparent, though subtle. Visually, it appeared that regions around the canals, corresponding to osteons, are darker in colour and therefore less dense than the narrow interosteonal regions. These regions also corresponded to changes in osteocyte lacunae orientation; within the darker regions the osteocyte lacunae were organised concentrically around the canals while in the interosteonal regions they appeared random.

BV/TV for this sample was 0.981, and the mean canal diameter was 40.0 (Table μm 7.1). For the canal orientations, the longitudinal index was measured as 0.301, the laminar index as 0.244, and the radial index as 0.145.

7.3.2.2 *Lithornis*

Tibiotarsus

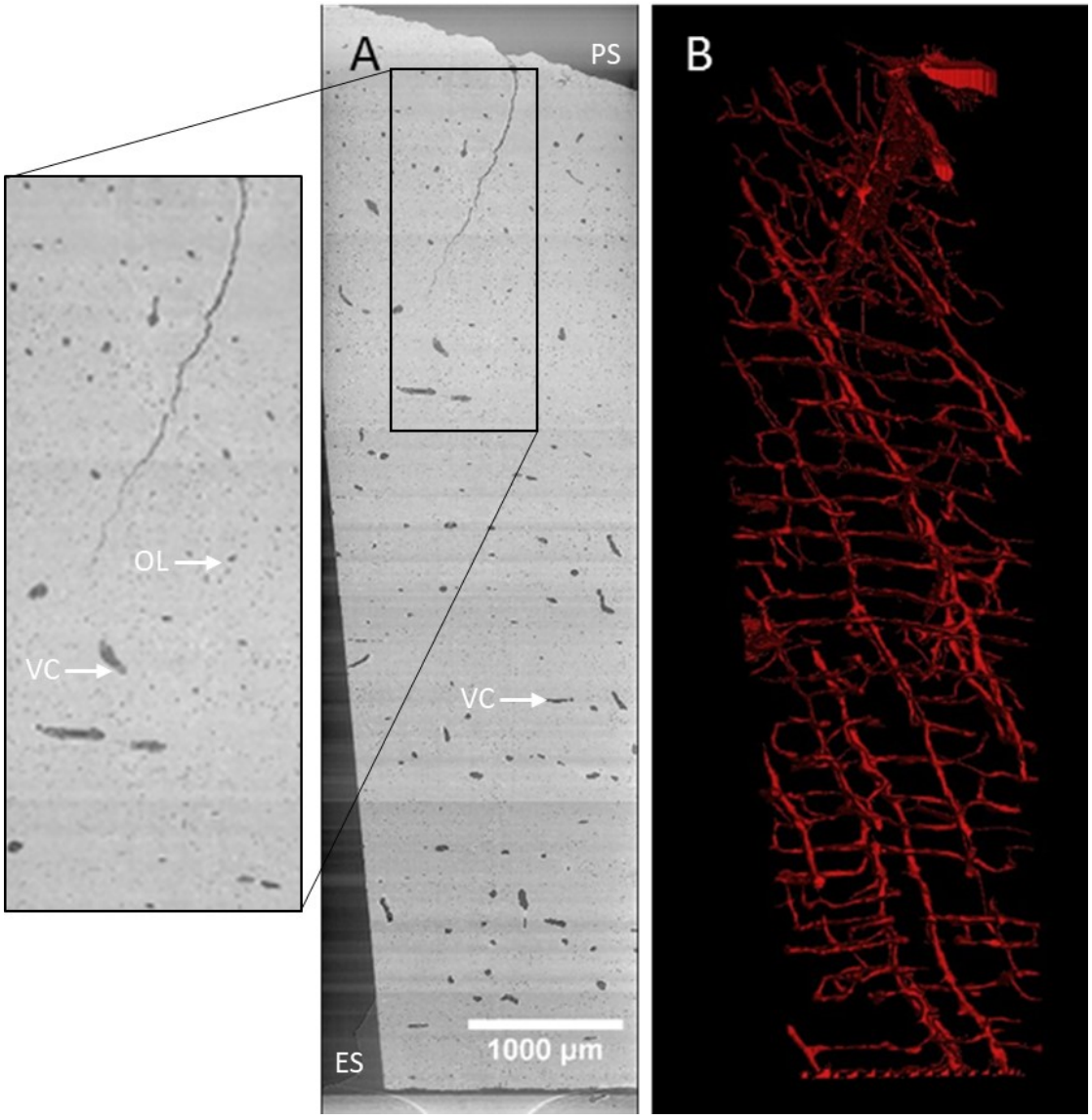

FIGURE 7.12: SR CT images of cortical bone from the midshaft of a tibiotarsus from a specimen of *Aepyornis*. Images collected at I13-2 beamline at Diamond Light Source, Harwell, UK. Voxel size 3.2 μm. (A) Transverse section across the cortex. Black box shows location of magnified region (left). PS periosteal surface, ES endosteal surface, VC vascular canal, OL osteocyte lacunae. (B) Vascular canals from the same sample segmented and rendered in 3D using Avizo.

TABLE 7.1: Quantitative results for extinct birds

Species	BV/TV	Canal diameter (μm)	Longitudinal index	Laminar index	Radial index
Mullerornis	0.966	25.939	0.288	0.348	0.0494
Aepyornis	0.981	40.003	0.301	0.244	0.145
Ostrich	0.964	61.539	0.242	0.422	0.0847
Lithornis (tibiotarsus)	0.994	9.147	0.347	0.483	0.0429
Unidentified	0.978	19.064	0.432	0.147	0.181

The cortex was well-vascularised, and canals appeared narrow (Figure 7.13). The canal network, in cross-section (Figure 7.13A), appeared to be dominated by longitudinal canals, as described by Houde (1986) [200], though, as with Houde's published sample, laminar and

oblique canals are also present. Thin periosteal and endosteal regions were almost avascular, but did contain osteocyte lacunae. Assessment of the osteocyte lacunae was difficult due to the preservation and imaging artefacts discussed above. Relatively few osteocyte lacunae were visible compared to in other samples visualised in this thesis.

3D visualisation (Figure 7.13B) showed that the main portion of the cortex was in fact highly vascularised, and the OCL and endosteal layer contained a number of radial canals leaving the periosteum and entering the medullary cavity, which was not visible in the 2D section.

Due to ring artefacts, osteocyte lacunae could not be reliably segmented and therefore were not visualised in this sample.

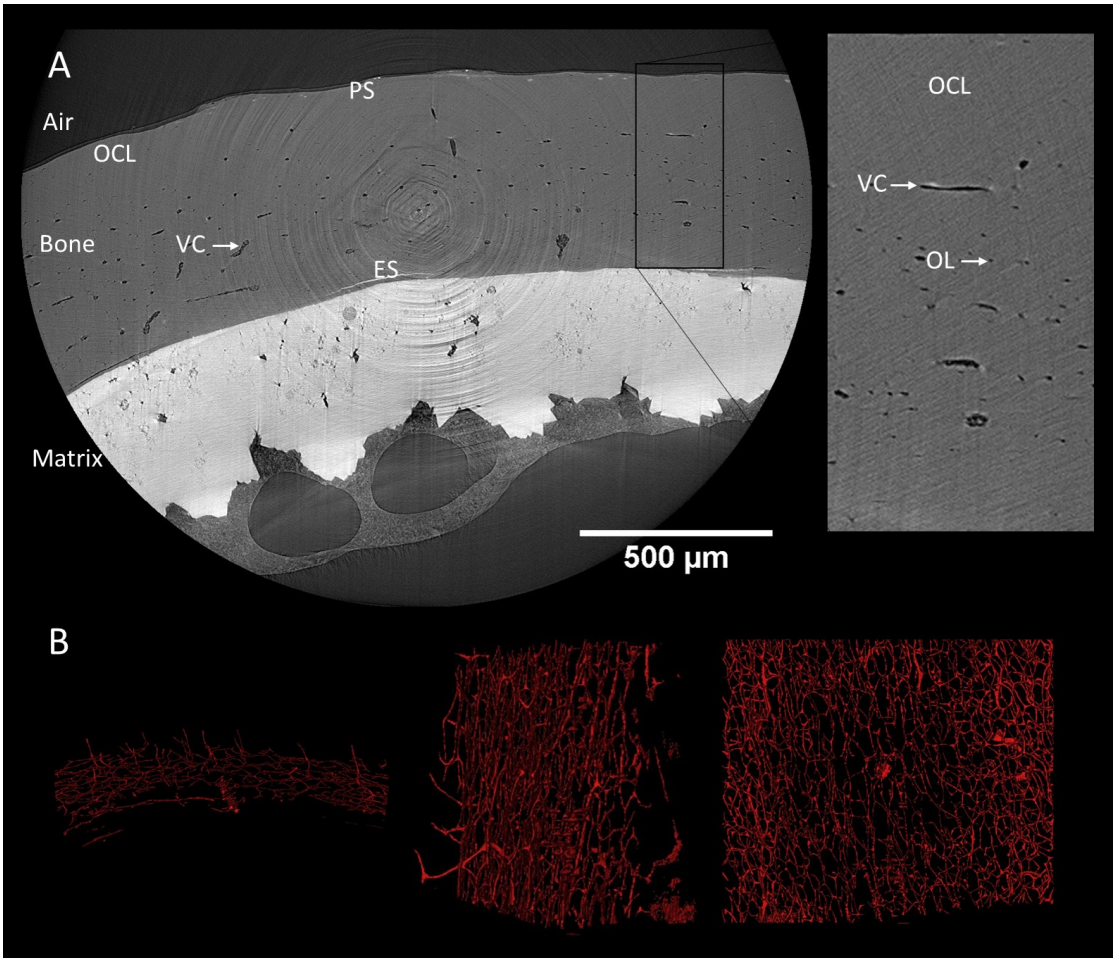

FIGURE 7.13: SR CT scan of a midshaft region of cortical bone from the tibiotarsus of a specimen of *Lithornis*, an Eocene bird. Data collected at I13-2 beamline at Diamond Light Source, Harwell, UK. Voxel size 1.6 μm. (A) Single transverse CT slice, showing well-preserved bone tissue and more highly attenuating matrix (lighter grey region). Black box indicates location of magnified region (right). ES endosteal surface, PS periosteal surface, VC vascular canal, OCL outer circumferential layer, OL osteocyte lacunae. (B) Vascular canals segmented and visualised in 3D in Avizo. Orientations (left to right) transverse, side view of sample, periosteal view of sample.

Humerus

The cortex (Figure 7.14) was less densely vascularised than the modern bone samples studied in previous chapters, but osteocyte lacunar arrangement (layered circumferentially around

canals) demonstrated that the bone was osteonal, possibly fibrolamellar. The canals were narrow, but appeared somewhat variable in diameter.

An inner circumferential layer containing osteocyte lacunae but few to no canals was present, and clearly differentiated from its adjacent bone tissue by osteocyte lacunar organisation. In the endosteal layer, the osteocyte lacunae were oriented around the circumference of the medullary cavity, while elsewhere they followed osteonal organisation (layered circumferentially around canals). Similarly, an outer circumferential layer with osteocyte lacunae but not canals is clearly visible.

Most canals appeared in cross section to run longitudinally, though some appeared radial or reticular. In 3D, the enlarged canals were enlarged only at one end of the sample, and rapidly narrowed (Figure 7.14 B).

Based on 3D visualisations showing osteocyte lacunae coloured by their volume, osteocyte lacunae were smallest near the endosteal surface and in the OCL, and larger in the central portion of the cortex (Figure 7.14 C).

7.3.2.3 Unidentified tarsometatarsus

The bone cortex was highly vascularised (Figure 7.15), with many apparently longitudinal canals (based on a 2D section (Figure 7.15 A)). In the inner 1/3 of the cortex, more canals appear to be oblique or reticular. A much larger canal was present near the endosteal surface.

A clear endosteal layer was present, which from a 2D section would be interpreted as avascular. In 3D (Figure 7.15 B), it was clear that a number of canals pass through this layer into the medullary cavity. In the endosteal layer, osteocyte lacunae were circumferentially arranged. Slight diagenesis and cracking at the endosteal border in this case made the layer more clearly visible. Diagenetic change meant that the OCL, if present, was missing.

Osteocyte lacunae were arranged circumferentially around the vascular canals, indicating osteonal structures. Osteocyte lacunae were mostly present in the regions between supposed osteons, with relatively few very close to the canals. Those that were close to the canals were more flattened in appearance than those further from the canals, and smaller in volume (Figure 7.15 C).

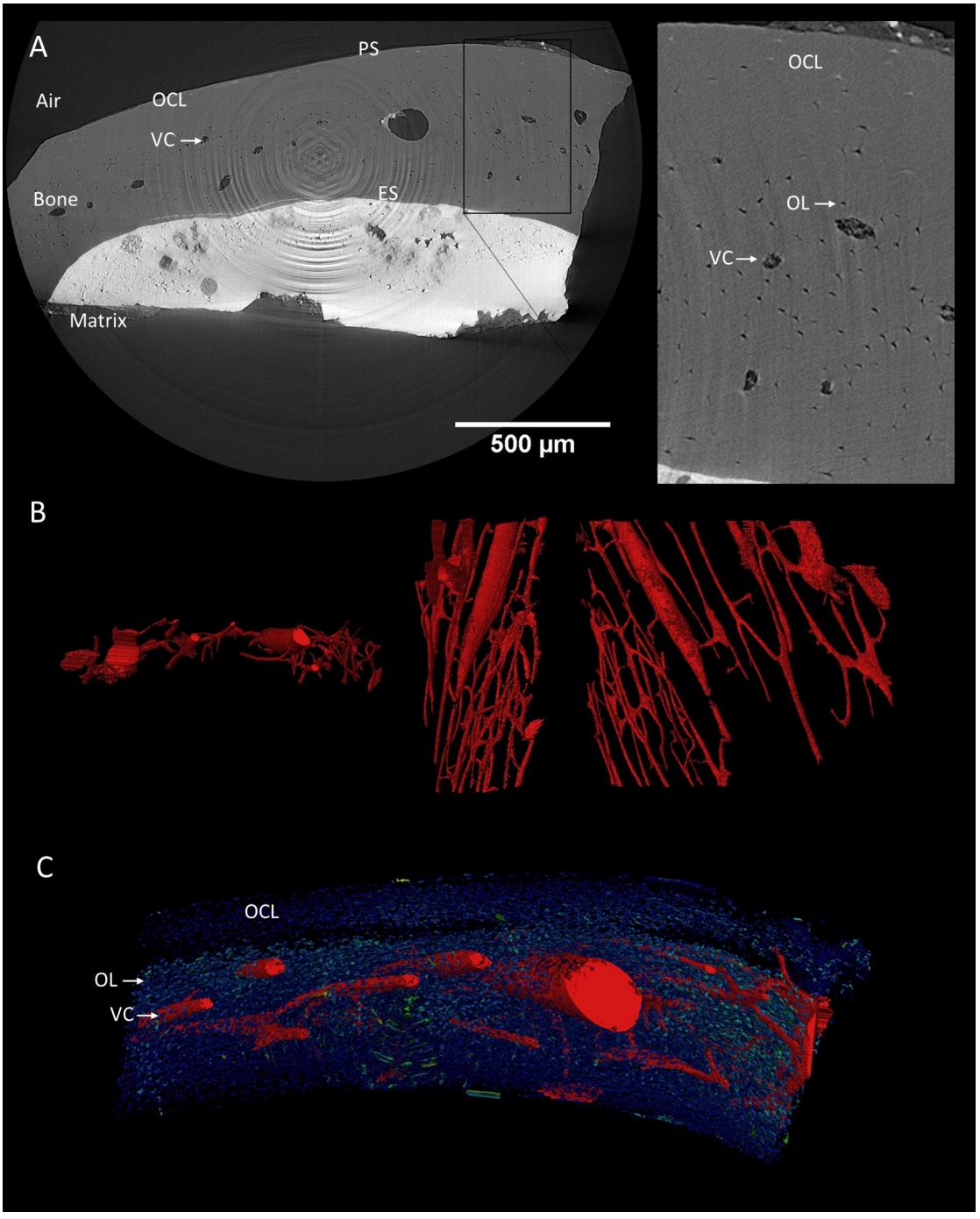

FIGURE 7.14: SR CT scan of a region of cortical bone near proximal end of the diaphysis from the humerus of a specimen of *Lithornis*, an Eocene bird. Data collected at I13-2 beamline at Diamond Light Source, Harwell, UK. Voxel size 1.6 μm. (A) Single transverse CT slice, showing well-preserved bone tissue and more highly attenuating matrix (lighter grey region). Black box indicates location of magnified region (right). ES endosteal surface, PS periosteal surface, VC vascular canal, OCL outer circumferential layer, OL osteocyte lacunae. (B) Vascular canals segmented and visualised in 3D in Avizo. Orientations (left to right) transverse, side view of sample, periosteal view of sample. (C) 3D rendering of vascuar canals (red) and osteocyte lacunae (blue to green). Osteocyte lacunar colour represents its volume (dark blue is smallest, green is larger).

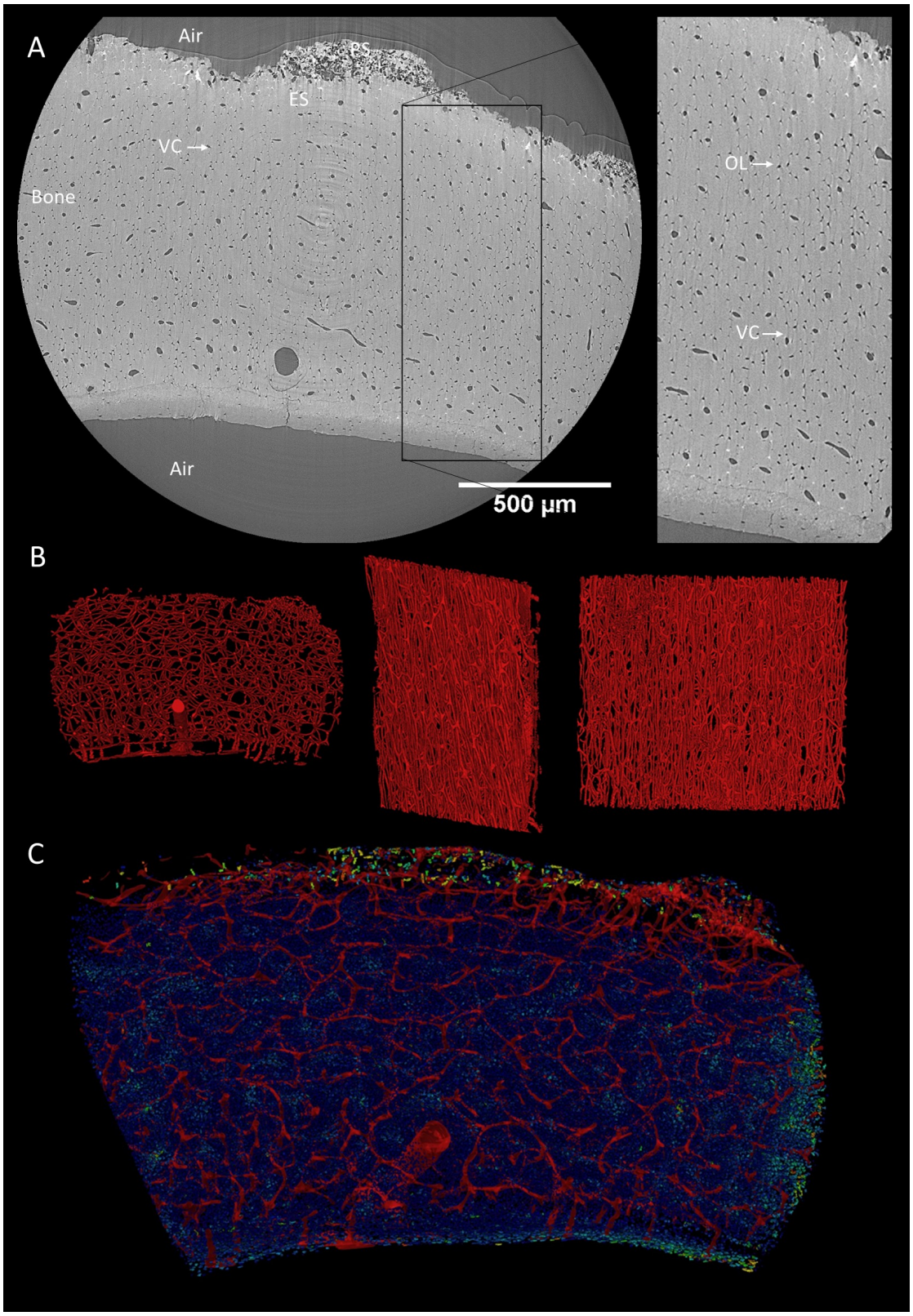

FIGURE 7.15: SR CT scan of a midshaft region of cortical bone from the tibiotarsus of a specimen of *Lithornis*, an Eocene bird. Data collected at I13-2 beamline at Diamond Light Source, Harwell, UK. Voxel size 1.6 μm. (A) Single transverse CT slice, showing well-preserved bone tissue and more highly attenuating matrix (lighter grey region). Black box indicates location of magnified region (right). ES endosteal surface, PS periosteal surface, VC vascular canal, OCL outer circumferential layer, OL osteocyte lacunae. (B) Vascular canals segmented and visualised in 3D in Avizo. Orientations (left to right) transverse, side view of sample, periosteal view of sample. (C) 3D rendering of vascuar canals (red) and osteocyte lacunae (blue to green). Osteocyte lacunar colour represents its volume (dark blue is smallest, green is larger). Osteocyte lacunae are smaller closer to the vascular canals.

7.4 Discussion

7.4.1 Part 1: High-resolution imaging of fossil material

The four extinct bird specimens scanned in this chapter were cut down to just a few millimetres in order to minimise sample sizes and therefore enable the best possible spatial resolutions, signal-to-noise ratio, and image contrast. The elephant bird and Unidentified scans were comparable to modern material and both canals and osteocyte lacunae were resolved. The vascular canals were segmented and analysed with little alteration from the image processing workflow developed in Chapter 2 of this thesis in both samples, so SR CT was demonstrated to be an appropriate technique for visualising the microstructure of the bones of these extinct birds. This finding adds to a growing body of work using SR CT to visualise microstructure in fossil material [25, 140].

The Unidentified sample was damaged at the periosteal surface, which meant that the damaged portion of the bone cortex could not be analysed. Imperfect preservation in fossils is potentially problematic for automated image processing and analysis, since pores within damaged regions would be included as vascular canals or osteocyte lacunae despite not being biological structures at all. Therefore, manual intervention may be required in order to remove damaged regions from the analysis. Manual selection introduces an element of subjectivity to the analysis, since the user must decide which regions can and cannot be analysed. However, once the well-preserved bone region was isolated, it was found that the automated image segmentation and analysis workflow used in previous chapters could be applied to the fossil bone. Therefore, as long as some of the bone is well-preserved, this region can be selected manually and then analysed automatically. In addition, it is worth noting that the 3D and non-destructive nature of SR CT means that it is possible to rescan a slightly different region if this region is better preserved. This would not be possible using conventional histological techniques, where further destructive sections would need to be made, and therefore 3D imaging may provide a means of obtaining more information from samples even when the sample is not consistently preserved throughout.

Although synchrotron-based CT systems are able to generate microstructural datasets from bone, in small samples as shown in the present chapter, and in larger samples [25], the lab-based experiment carried out here demonstrates the ambitious aim of being able to analyse bone histology from in-matrix fossils in more accessible lab-based systems cannot yet be met. For the echinoderm scan carried out here, getting sufficient transmission through the longest edge of the fossil while maintaining a reasonable signal-to-noise ratio proved difficult, and it was not possible to achieve a voxel size as small as used in other histological scans. The resulting image had poor signal-to-noise ratio and relatively large voxels therefore microstructural details could not be resolved. However, the degree of microstructural preservation within this fossil is unknown since the specimen has not been sectioned for histology. *Pleurocystites* fossils have been known to preserve porous microstructural detail in a similar size range to bone microstructure [12] (Figure 7.4), which, if preserved in this specimen, should be visible given sufficient resolution and contrast. For this fossil, it is not clear whether the lack of microstructural detail was due to the noisy image, insufficient resolution, or lack of preservation. Either way, further study is required to optimise high-resolution, lab-based imaging of large, dense, flattened fossil samples.

For small fossil bone samples, SR CT can provide microstructural datasets comparable to those obtained from modern bone samples, and other groups have worked on imaging larger fossils in synchrotron-based systems with success [25]. Based on SR CT datasets, microstructural features including vascular canals and osteocyte lacunae can be resolved and segmented, allowing quantitative assessment of traits such as canal orientation, BV/TV, and canal diameter. However, based on the lab-based scans carried out here, it is not yet possible to image bone microstructure in a larger fossil specimen, in a lab-based system, so further work is required to optimise setup for this type of sample.

7.4.2 Part 2: interpreting the age and biology of extinct birds

7.4.2.1 Subfossil specimens of *Aepyornis* and *Mullerornis*

3D microstructural data from the elephant bird samples begins to provide information about the developmental age of the individuals from which the samples were taken. The comparison of these birds with smaller birds is complicated by their body mass (orders of magnitude greater than most other birds), and their relatively long periods of growth. Unlike in most extant birds, where growth occurs within a single year, elephant birds, and other ratites such as ostriches and kiwis, undergo protracted growth over several years, as evidenced by the presence of LAGs in these species [156, 196]. Here, results are compared between the elephant bird samples and the ostrich samples from Chapter 6, which are the closest extant species to the elephant birds in terms of phylogeny and body mass.

Both elephant bird samples were similar in microstructure structure to the ostrich samples visualised in Chapter 6: their vascular canals formed repeating units of laminar canal networks connected by a smaller number of radial canals (plexiform bone [196]). In both the ostrich and the *Mullerornis* samples, there were differences in the organisation of the vascular canal network at different positions across the bone cortex. In the *Aepyornis* sample, the structure was more homogeneous, and displayed an architecture that more closely resembled that of the endosteal region in the *Mullerornis* sample than it did the periosteal region of the same sample.

The similarity between the *Mullerornis* and the ostrich sample could be age-related. The ostrich sample studied in the previous chapter of this thesis was from an ostrich that was approximately one year of age. At this age, an ostrich has reached close to adult size [202], but has not yet reached full maturity. The bone structure observed in the periosteal region of the cortex in both species resembles the primary plexiform bone previously described in *Aepyornis* bone from conventional histology [196]. The bone in the endosteal region more closely resembles secondary, remodelled bone as seen in some of the other samples of *Aepyornis* from the same paper. In the μCT scans carried out here, it is not possible to see cement lines, which are indicative of resorption and bone redeposition and would help to differentiate primary and secondary osteons. However, the overall structure of the endosteal region of the ostrich and *Mullerornis*, and the whole cortex of the *Aepyornis* sample also presented in this chapter, more closely resemble secondary, Haversian bone than they do primary bone.

In addition, a layer of less densely vascularised bone was observed on the periosteal surface. The less densely vascularised bone is interpreted as an OCL, which is a layer of lamellar bone deposited slowly after the animal has reached full size [160]. This layer was absent from the

Mullerornis sample and the ostrich samples, though in the case of the *Mullerornis* it is possible that this layer was present originally and was lost through surface damage to the sample.

The combination of vascular organisation and absence of an OCL suggests that the *Mullerornis* sample was from an individual that was yet to reach maturity, and may still have been actively growing as it had not yet formed an OCL. Unlike in the smaller birds, even when the bone was not fully mature, significant remodelling had already taken place, but this was also the case in the ostrich. The *Mullerornis* specimen is therefore interpreted as being subadult. This interpretation is supported by the BV/TV value of 0.97, which is consistent with subadult birds across the species studied.

The *Aepyornis* sample, on the other hand, has undergone almost complete remodelling, similar to some of the specimens described by de Ricqlès *et al.* [196], and is therefore interpreted to be skeletally adult, and possibly old. Its BV/TV value is higher than that of *Mullerornis*, but lower than some adult birds of other species. However, this value may be influenced by the small number of enlarged canals, similar to those seen in the ostrich tibiotarsus. Given the very small differences in BV/TV between the different age stages (at least between subadult and older individuals), caution must be applied in the interpretation of these values. This is especially true when preservation or secondary remodelling may alter structures.

It is also worth noting that the protracted growth of ratites may mean that interpretations of their age and biology based on smaller birds such as ducks might not be accurate. Ratites, unlike most other extant birds, take several years to reach maturity [156, 203, 204], and therefore their bone growth and remodelling may follow different constraints. Therefore, further work is required to characterise the microstructural development of extant ratites, such as ostriches, emus, rheas, kiwis and tinamous. It is important to study both the large flightless birds and the smaller birds, especially tinamous since these are the only flighted birds in this group. Therefore, studying their bone development will help to disentangle the effects of phylogeny, body mass, and loading on age-related microstructural changes in cortical bone.

If the *Mullerornis* specimen studied here is indeed a subadult individual, this finding could have implications for its use in taxonomies such as the recent reclassification of elephant birds carried out by Hansford and Turvey [182]. A subadult animal may still be growing, and therefore bone metrics used for defining the species may still change as the animal grows [150]. The recent redescriptions have substantially altered the taxonomy of elephant birds [182], but further work including histological descriptions could provide further insight into intraspecific variation and potentially further reclassification if some individuals were found to be immature. On the other hand, the apparent maturity of the *Aepyornis* sample supports the use of this specimen for taxonomic purposes.

7.4.2.2 *Lithornis*

The *Lithornis* bone samples were interpreted to be from an adult individual. The vascular canals were narrow, the BV/TV value high (0.994), and clearly defined OCL was present, indicating residual growth after the animal had reached full size [160].

The vascular canal organisation in the tibiotarsus was similar to the sampled described by Houde [200], with a predominance of apparently longitudinal canals, as seen in the similarly sized extant birds described in chapters 5 and 6. However, quantitatively, the canal orientations

in the *Lithornis* tibiotarsus were more consistent with the canal orientations measured in the ostrich than the smaller non-ratites measured in previous chapters of this thesis. The longitudinal index measured in the *Lithornis* tibiotarsus is relatively low compared with the average duck or pheasant value, and the laminar index is high, in a similar range to the ostrich. This may represent a phylogenetic signal in the organisation of the canals, since *Lithornis* and ostriches are both ratites. However, given only a single sample has been scanned, and there was substantial variation in the modern birds in previous chapters, further samples should be investigated to test this hypothesis.

The humerus sample is more difficult to assess since the sample was taken from the proximal end of the diaphysis rather than the midshaft, since the midshaft was not preserved. The vascular canal organisation appeared different in the humerus compared with the tibiotarsus, and compared with the humerus of extant species studied in previous chapters: a smaller number of canals were present, and some of these had much larger diameters than found in any other adult specimens. It is possible that this difference is due to sampling location: the articular ends of bones have different microstructures compared with the midshaft, and the epiphyses are filled with trabecular bone, unlike the diaphysis [162]. This question highlights the need for further studies on modern birds looking at different bone regions, given not all regions in all samples will necessarily be preserved in a fossil, as found with this specimen. Alternatively, the widened canals in the humerus of the *Lithornis* sample could relate to secondary remodelling, as new secondary osteons first remove old bone tissue before depositing new, and can form a cone-shaped structure (cutting cone) similar to that observed for the larger canals in the sample presented here [205] before these regions are later infilled. Alternatively, it could be that these regions have undergone bacterial degradation and have widened as a result (Figure 7.1). Further study of different bone regions, as well as bone remodelling in birds is required to interpret microstructure in different bone regions and secondary bone.

The discrepancy between the vascular organisation in *Lithornis* compared with similarly sized birds studied in earlier chapters of this thesis is worth investigating further, to test the presence of phylogenetic signals in bone histology more generally, as this could influence interpretations of developmental age as well as biology. Legendre *et al.* [70] found a phylogenetic signal in several histological measurements in palaeognaths, but used 2D sections, which have been demonstrated to misrepresent vascular canal orientation [18] and only single ages for each species. A good extant comparative species for *Lithornis* would be the kiwi, or a tinamou, since both are smaller ratites, though the practicality of obtaining growth series for these species may preclude this study. If *in vivo* techniques could be used, this would make developmental studies more feasible, such as Beale's lifetime radiographic study of a single kiwi chick [203, 204]. However, SR CT is not applicable to living animals, and *in vivo* scans can not yet reach the required spatial resolutions (for example the Skyscan *In vivo* scanner can obtain images with voxel sizes of 9 μm, which is not small enough for microstructural detail).

Nevertheless, the BV/TV values, largely narrow vascular canals, and presence of an OCL strongly indicate that this sample was from an adult individual, and therefore this specimen could safely be used in phylogenetic analysis.

7.4.2.3 Unidentified tarsometatarsus

The Unidentified tarsometatarsus sample was highly vascularized, with a predominance of longitudinal canals, similar to the extant bird tibiotarsi measured in previous chapters of this thesis. Unfortunately the periosteal bone layer is missing, precluding the identification of an OCL that would suggest a slowing of growth.

The bone cannot be directly compared to the extant specimens scanned, since it is a tarsometatarsus rather than tibiotarsus, but in birds the tibiotarsus and tarsometatarsus are both long bones of the leg, both held relatively vertically (compared with the femur). Therefore, of the three long bones studied previously in this thesis, the tarsometatarsus is likely to be most similar to the tibiotarsus. This is supported by the canal orientation in the tarsometatarsus, which is predominantly longitudinal, comparable to a tibiotarsus in the other species studied.

The BV/TV result (0.978) was comparable to a subadult individual, based on comparison with extant species from previous chapters of this thesis, and the vascular canal diameter was relatively large. The missing periosteal region means that the presence or absence of an OCL cannot be confirmed. Therefore, this specimen is cautiously interpreted as a subadult individual. However, the tarsometatarsus has not been investigated before in this thesis, so it is unknown whether the same values apply to this bone.

7.4.3 Limitations and future work

This study was a preliminary investigation into the application of quantitative, 3D methods for measuring bone microstructure, and an initial attempt at interpreting the developmental age of some specimens from extinct birds based on these methods. As such, the study had a number of important limitations, and future work should aim to address some of these limitations.

One limitation of this study is that the specimens studied at the synchrotrons were sampled destructively and the ability to image larger specimens at these facilities was not investigated. The sample imaged in the lab-based μCT system was of unknown preservational quality and therefore it was not possible to distinguish a lack of visible microstructure due to image quality from lack of structure due to poor preservation. Future work should also remove small samples from a fossil to either scan using SR CT or section histologically, to verify the presence of microstructural detail prior to attempting a more challenging scan setup. Alternatively, a more theoretical approach could be taken, using manufactured 'model' fossil specimens, made from a material of similar X-ray attenuation to rock, but with the inclusion of microstructural features of differing, known sizes (phantoms [122]). This approach would allow imaging setup to be studied in a more systematic way, and the applications and limitations defined more precisely.

The limitations of the CT approach taken here are that key information such as the presence or absence of cement lines, which indicate regions of bone resorption and redeposition, LAGs and collagen organisation are not visible. These important pieces of information would help to confirm the identity of primary and secondary bone, and identify whether the birds were more than a year old. This infomation could either be obtained by sectioning the samples and imaging them using cross-polarized light microscopy [22], or by adding phase contrast to the CT imaging [23, 140]. This has been used, for example, to visualise osteonal structure [23], as well as interpretation of age in years in *Acanthostega* (a stem tetrapod) using LAGs [140].

Given uncertainties about interpretation of the tarsometatarsus, further study is required to characterise intraskeletal variability. In the previous chapters of this thesis, it has been observed that bone microstructure can differ substantially between different bones in an individual, and previous studies have found similar results [2, 15, 164, 206]. Even within a single bone, bone microstructure has been found to vary significantly [172], so a thorough understanding of potential variability is required.

7.5 Conclusions

The experiments carried out in this chapter have demonstrated that exactly the same SR CT and automated quantitative analysis techniques can be applied to both recent and fossil bone when samples of a few mm are cut from a specimen. However, diagenesis can cause problems for automated segmentation and analysis and therefore manual intervention may be required in order to select only non-damaged bone regions. Previous chapters of this thesis have demonstrated that 3D imaging provides additional information unavailable from 2D sections, as well as being less destructive, but the samples studied in this section were still sampled destructively. Technology is improving to the point where in the future, and in some cases now, virtual histological approaches can be truly non-destructive.

SR CT and quantitative analysis can be used to better understand the biology, development, and microanatomy of exinct birds, though further studies should include phase contrast imaging to study ultrastructural variation. Additionally, more studies in modern birds will be required, including studying different bone regions, and more species, in order to fully understand the relationships between biology and age-related changes in bone microstructure.

Chapter 8

Overall Discussion

This project aimed to use high-resolution, minimally-destructive, three-dimensional imaging (synchrotron-based computed tomography) to improve current understanding of age-related changes in bone microstructure in birds, for the purpose of better understanding the biology and taxonomy of extinct birds.

It used several different approaches to determine the best methods for quantifying bone microporosity, carry out preliminary studies testing how bone microstructure changes with age, life history, and body mass in modern birds, and proof-of-concept scans and analysis in fossils.

In this chapter, the main findings, implications, and limitations of the results chapters, as discussed within those chapters, are summarised.

8.1 Review of main findings

8.1.1 Quantifying intracortical bone porosity: an appraisal of 2D and 3D methodologies in the domestic duck (*Anas platyrhynchos*)

Interpretations about age and biological traits from bone histology are usually based on the microporosity within the cortex of the long bones. This includes osteocyte lacunae and vascular canals. The orientation of vascular canals, along with their density, and the shape, size, and number density of osteocyte lacunae have been used to interpret the developmental age, growth rate [15, 18], and bone loading [21] in fossil animals, usually based on 2D sections. However, quantitative estimates of 3D structural traits such as canal orientation have been shown recently to be inaccurate when based on 2D sections [14, 18, 23]. Current palaeobiological research is moving increasingly towards non-destructive 3D imaging [14, 18, 24, 108, 115], but the majority of histology is still carried out using traditional 2D techniques [70, 196, 207]. Therefore, at this stage, it was important to compare traditional 2D section-based methods with 3D volume-based methods, in order to confirm whether 3D methods are really necessary or whether 2D sections can be used to estimate histological traits.

Quantitative methods for measuring canal orientation, osteocyte lacunae aspect ratio and volume, osteocyte lacunar number density, and bone volume fraction based on 2D virtual

sections and 3D volumes were compared. Recent studies have found that measuring canal orientation using 2D sections can underestimate measurements of longitudinal canals and overestimate measurements of laminar canals [18], potentially leading to very different conclusions regarding overall canal orientation and therefore inaccurate interpretations of growth rate or loading. In this project, this observation was tested further, and supported by a combination of simulated and real CT datasets.

The results from this study demonstrated that true 3D measurements are essential for measuring histological traits such as canal orientation, and osteocyte lacunar aspect ratio and volume. This has strong implications for histological practice since the majority of histology is still carried out using 2D sections [70], and canal orientation, and osteocyte lacunar properties are amongst the traits most frequently described and used to interpret growth rate [2, 15, 70], bone loading [21], and developmental age. Given a move towards quantitative rather than qualitative research within fossil bone histology [14, 16, 109], and the increasing use and availability of 3D imaging and analytical techniques, now is the time to transfer histological study to a truly 3D approach.

Further application of 3D imaging and quantitative analysis of bone microporosity could provide entirely new insights into the development of bone, and interpretations of fossils, and could change our ideas about *e.g.* how canal orientation relates to bone loading. However, given that 3D results are not necessarily comparable to 2D results, it will also be necessary to carry out a substantial body of work in extant species, in order to provide a comparative dataset from which to interpret fossils. For this, work is at a very early stage, even in 2D, so rather than continue to gather data in 2D, future studies should endeavour to use 3D approaches where possible.

8.1.2 Testing how bone microstructure changes throughout development in two modern birds

Based on the findings from the previous section, it is clear that work needs to be done in applying 3D techniques to the study of bone. In addition, current understanding of how bone microstructure changes with age in birds, and how this is influenced by factors such as bone growth rate and loading, is limited. If we are to accurately estimate developmental age in fossil birds, it is crucial to fully understand the relationships between these factors in modern birds before trying to interpret fossils.

In this study, two model species were used to characterise age-related changes in modern bird bone microstructure, with the aim of assisting estimation of developmental age. The two species used were the domestic duck *Anas platyrhynchos* and pheasant *Phasianus colchis*. These two species have similar body masses, are both fairly basal birds (branched from the avian phylogenetic tree early), and are both precocial (actively walk and find food from very soon after hatching). Therefore, in the overall context of modern birds, they are fairly similar. However, they have two important differences. Firstly, the duck has been selected for more rapid growth than the pheasant. Secondly, in the pheasant, flight occurs fairly early in development, but in the duck flight is delayed until the bird reaches almost full size [26]. Therefore, the two species differ in their overall rate of growth, and in the growth and loading

of their wing bones at different stages in development [164], allowing a preliminary test of how applicable observations made in one modern species are to another, similar species.

It was found that the same developmental process apply to those described previously and characterised in 2D in several bird species [2, 15], and in 3D in the mouse [129]. In both the duck and the pheasant, bone began as a very porous, foam-like structure, which grew, remaining highly porous for as long as rapid growth occurred. Later, the pores narrowed as layers of bone were deposited on the internal surfaces of the pores, leaving a network of narrow vascular canals in the adult. During growth, the cortical thickness and vascular canal diameter initially increased, up to around 3 weeks of age then decreased. BV/TV followed the opposite pattern: initially decreasing then increasing. Osteocyte lacunar number density also initially increased then decreased.

In the pheasant, all three bones scaled isometrically, and followed the same temporal pattern of changes in bone microstructure. However, in the duck, growth of the humerus was delayed relative to growth of the leg bones, meaning that it grew more rapidly when it did grow to catch up. Unlike the other bones, the relative cortical thickness in the duck humerus remained consistent throughout growth. It also reached its lowest BV/TV later than in the other bones, still being very porous at 6 weeks of age.

Between the two species, the duck grew more rapidly than the pheasant, resulting in greater bone porosity and wider vascular canals in the juveniles, supporting previous findings in the literature that have related bone porosity to growth rate [19]. This makes it challenging to use absolute values of porosity or canal diameter to estimate maturity, since values will differ between species.

It was also found that in the humerus in the duck, the proportion of laminar canals increased with age within the juvenile age stages, though further study is required to test this relationship further and whether it applies to other species.

In this chapter, it was therefore concluded that a combination of BV/TV, vascular canal diameter, osteocyte lacunar volume and number density, as well as qualitative observations could be used to estimate developmental age in these species. However, further work is required to fully characterise the development in these two species given that the sample sizes were small and substantial variability was observed between juvenile birds. In addition, the leg bones are a more consistent source of data since the development of the wing differed between the two similar species studied.

8.1.3 A preliminary investigation into interspecific variability in bone development across extant birds.

Following the results from the study in duck and pheasant, the next step was to investigate how applicable the findings were across a range of extant birds with different life histories (precocial *vs.* altricial) and body masses. Studying full growth series for multiple species was not within the scope of this project, but two to three age stages were investigated for a further precocial species (partridge, *Alectoris rufa*), and two altricial species rock dove, *Columba livia* and starling *Sturnus vulgaris*. In addition, an extreme example of body mass was included: samples from the

ostrich (*Struthio camelus*), the largest extant bird, in order to text how different it is possible for bone microstructure to be in extant birds.

It was found that BV/TV were consistently different and could be used to distinguish adult, subadult, and juvenile birds in all species studied where samples were available at these stages. It was concluded that a BV/TV value below 0.95 likely indicated a juvenile specimen, a value between 0.95 and 0.98 a subadult specimen, and a value 0.98 and above an adult specimen.

However, these values are very close together, especially for the subadult and adult specimens, so further observations such as the presence of an outer circumferential layer are also useful for identifying adult bone. Nonetheless, the case study in the starling demonstrated that a first-year bird could be distinguished from an older bird based on BV/TV and canal diameter, even when the bones appeared very similar externally.

8.1.4 Application to extinct birds and future challenges

The final step in this project was to test the applicability of the methods used in extant birds to extinct ones. First, the imaging setup used in the previous sections, using small bone sections and SR CT, was applied to a selection of subfossil and fossil avian samples.

It was found that the same structures observed in the recent bone samples (vascular canals and osteocyte lacunae) were clearly visible and fairly straightforward to segment in the fossil samples. However, there were some challenging features such as dense regions causing artefacts which obscured some regions of the bone cortex, as found in previous studies [193], and cracks running through the samples. Therefore, it was necessary to manually intervene to some extent with the segmentation of these fossil samples, unlike with the modern bone samples. Nonetheless, with a small amount of manual intervention, segmentation and automated quantitative analysis could be applied to the fossil samples, enabling a quantitative approach to be taken. Published virtual histology demonstrates that similarly high-resolution images can be obtained from larger samples without damaging them, using SR CT [25], though this was not tested in this project.

However, when a case study was attempted using a large, flat specimen, aiming to image microstructural features without damaging the specimen, in a lab-based system, results were less convincing. The scan was noisy and very little microstructural detail could be resolved. Therefore, lab-based setups are further away from being able to visualise histological level detail in large samples, but work is being undertaken to improve visualisation of objects with these aspect ratios [116, 195], so this may be an avenue for the future.

Based on results from the modern birds studied in the previous sections, BV/TV and canal diameter was used to estimate developmental age in the fossil specimens. It was concluded that none were likely to be juvenile, but that some specimens might be subadult (Unidentified and *Mullerornis*), which would have implications for using these specimens in phylogenies and identifying them correctly.

8.2 Limitations and future work

This thesis has a number of limitations and the results highlight the need for further work in several areas.

In terms of the methodological tests carried out in the first part of this thesis, the simulated datasets used were highly simplified. Vascular canals do not exist as separate, straight cylindrical shapes in real bone; they are curved and part of a wider vascular network. Therefore, the simplified shapes used are not completely representative of real vascular canals. Given that the method for estimating 3D orientation based on 2D cross-sections was found to be inaccurate even in these highly simplified systems, it is safe to assume that the method would also not work in real datasets. The simulations may not have been sufficiently complex to truly test the 3D methodology, and therefore it may be that neither method is accurate in real datasets. More complex simulations could be used to test the accuracy of the 3D orientation method, using branch points and curves. However, the method was visually checked at every stage: the skeletonisation was shown to represent the real canal network accurately, and the branch points visualised to confirm they were in the correct locations. Therefore, the method should be accurate. It is not a perfect representation of the curves of the canal network, however, because it takes only the end branch points and does not take into account any bends in the canals, unlike the original method published by Pratt et al. [14]. On the other hand, this simplified method was faster to run and provides the primary orientations of each canal.

For the measurements of osteocyte lacunae, it was not possible to compare volume estimates between 2D and 3D methods in real datasets due to the voxel size chosen in the scans. These scans were carried out for the purpose of the other chapters, where it was important to have a slightly larger sample volume, and prioritised imaging the vascular canals over being able to calculate osteocyte lacunar shape and volume. However, further experiments should be done to compare the methods directly in samples imaged at less than 1 μm voxel size, given that the 2D method was shown to be potentially effective in certain scenarios (cells longitudinally arranged, two perpendicular sections).

Both chapters looking at modern birds were limited somewhat by small sample sizes. In the duck and the pheasant, more specimens were available at some ages than others, due to opportunistic sampling, and for the same reason the cause of death was unknown for these samples. Therefore, these samples may not have been healthy individuals before their deaths and may not perfectly represent typical growth. However, this method of sampling meant that no animals needed to be killed for this project, reducing ethical concerns which could arise with culling animals for research into fossil biology. In addition, the birds used were all raised together, under the same conditions, and for this reason are likely to be less variable in their growth than wild birds. Given the variability seen within the juvenile individuals, future work should look at expanding the sample sizes used, including more individuals at the very young and subadult age stages to gain a fuller picture of the development of these model species.

For the other species studied, further work would ideally look at more age stages, and further samples, to compare development between the precocial and altricial species, and test further whether there are consistent measures of developmental age, particularly amongst juvenile age stages.

Generally far more work is needed to characterise age-related changes in bone development in birds, across the phylogenetic tree and between species with different body masses, life histories and locomotor behaviours, using the 3D quantitative techniques which this project begins to bring together. In addition, before extrapolating to fossils, it may also be useful to carry out further studies in, for example, crocodiles, in order to understand the evolutionary origins of differences in bone microstructure.

In order to develop a method for estimating developmental age from quantitative analysis of bone microstructure, a thorough understanding of all these factors is required, and potentially further quantification including variation in bone microstructure across the bone cortex, which may provide information about depositional history. Once this information is known, it would be possible to feed the data into a model which could be used to automatically detect developmental age, along with measures of biology such as growth rate, similar to developed by [208]. This has potential to be an exceptionally valuable tool in palaeobiology, especially if based in non-destructive imaging techniques which could be applied to a much wider range of fossil birds. However, a great deal more work is required before this model can be developed.

Further work is also required in developing high-resolution imaging in large, flat (typical fossil) samples to remove the need for destructive sampling. Although this is already possible in synchrotron systems [25], developing methods for lab-based μCT systems would enable more researchers to apply the techniques since lab-based systems are more widely available.

8.3 Conclusions

Palaeobiological and histological research is moving towards 3D imaging for good reason: 2D sectioning is destructive, time consuming, and, as confirmed by the first part of thesis, quantitative measurements based on 2D sections can be inaccurate to the point of being meaningless. In this study, *in silico* simulated vascular canals and osteocyte lacunae demonstrated that histological measurements that rely on modelling features using idealised 3D geometries cannot be used accurately in real datasets since these are too dependent on strict geometric assumptions. In real datasets, shape-based measurements produced totally different results based on 2D and 3D methods, and therefore it is inadvisable to measure the shape or orientation of vascular canals or osteocyte lacunae using 2D sections. For these measurements, 3D measurements must be used, and at appropriate spatial resolutions. Some measurements, such as BV/TV and osteocyte lacunae number density, can be carried out using 2D sections, but could equally well be done using 3D imaging which is preferable because it is less destructive and can include a bigger sample volume.

In the duck and the pheasant, bone microstructure changed through development, supporting current understanding of bone growth and how structure relates to age. There were differences in the timings and magnitudes of changes in microstructural features, such as BV/TV between the two species, relating to their differences in growth rate (ducks growing earlier and more quickly than pheasants), but the sequence of changes was the same for the two species. Although in the pheasant, all three bones grew at a similar rate, and therefore were at similar stages of maturity within an individual, in the duck the humerus grew later than the lower limb bones, relating to delayed flight in this species. Therefore, when estimating developmental age it is important to select the bone of interest carefully, and use a lower limb rather than upper

limb bone. However, if there is a difference in maturity between the upper and lower limb bones, this can provide insight into the behaviour of the animal at this stage (walking but not flying).

When the duck and pheasant data were taken together with the data from a range of precocial and altricial species, it was found that in all species studied, juvenile, subadult, and adult species could be distinguished by their values of BV/TV, and further information could be added using measured of vascular canal diameter. Further work may reveal more changes within juvenile age stages, including changes in canal orientation, so more studies are required using more samples, and a more systematic study with more species.

It was also demonstrated that, using a synchrotron-based CT system, high-resolution 3D datasets comparable to modern bone samples can be obtained from fossils, and preliminary estimates of developmental age can be made. It is not yet possible to obtain histological-level detail in a large, flattened fossil in a lab-based CT system, so further work is needed to ensure that this approach is truly non-destructive as well as more widely accessible.

To conclude, the work presented in this thesis has demonstrated the necessity of applying true 3D quantitative methods for characterising the microstructure of cortical bone. It has begun to characterise age-related changes in bone microstructure in extant birds. Developmental similarities between species, which might allow age assessment to be applicable across all extant birds and possibly fossils, and differences, which need further investigation, have been highlighted. The studies carried out in extant species here are preliminary and cannot in themselves be used to develop a reliable age-estimation method for fossils. However, they do provide signposts for the direction of future work which could supplement the findings presented here and be used to develop interpretation methods in the future.

Finally, the 3D quantification methods applied to modern bone material were also successfully applied to fossil material, demonstrating proof-of-concept, though also demonstrating the current limitations of CT scanning for large samples. The preliminary observations from modern material were used to tentatively age four species of extinct bird, demonstrating the potential for more accurate measures and interpretation in the future.

Bibliography

[1] M. S. Y. Lee, A. Cau, D. Naish, and G. J. Dyke. Morphological clocks in paleontology, and a Mid-Cretaceous origin of crown Aves. *Systematic Biology*, 63(3):442–449, 2014.

[2] E De Margerie, J-P Robin, D Verrier, J Cubo, R Groscolas, and J Castanet. Assessing a relationship between bone microstructure and growth rate: a fluorescent labelling study in the king penguin chick (Aptenodytes patagonicus). *Journal of Experimental Biology*, 207(5):869–879, 2004.

[3] L. F. Bonewald. The amazing osteocyte. *Journal of Bone and Mineral Research*, 26(2):229–238, 2011.

[4] P.M. Goggin, K.C. Zygalakis, R.O.C. Oreffo, and P. Schneider. High-resolution 3D imaging of osteocytes and computational modelling in mechanobiology: insights on bone development, ageing, health and disease. *European Cells and Material Journal*, 31:32, 2016.

[5] Q. M. Qu, H. Blom, S. Sanchez, and P. Ahlberg. Three-dimensional virtual histology of silurian osteostracan scales revealed by synchrotron radiation microtomography. *Journal of Morphology*, 276(8):873–888, 2015.

[6] M. de Boef and H. C. E. Larsson. Bone microstructure: quantifying bone vascular orientation. *Canadian Journal of Zoology-Revue Canadienne De Zoologie*, 85(1):63–70, 2007.

[7] R. O. Prum, J. S. Berv, A. Dornburg, D. J. Field, J. P. Townsend, E. M. Lemmon, and A. R. Lemmon. A comprehensive phylogeny of birds (Aves) using targeted next-generation DNA sequencing. *Nature*, 526(7574):569, 2015.

[8] C. J. Hackett. Microscopical focal destruction (tunnels) in exhumed human bones. *Medicine, Science and the Law*, 21(4):243–265, 1981.

[9] Y. Fernández-Jalvo, P. Andrews, D. Pesquero, C. Smith, D. Marín-Monfort, B. Sánchez, E. M. Geigl, and A. Alonso. Early bone diagenesis in temperate environments: Part I: Surface features and histology. *Palaeogeography, Palaeoclimatology, Palaeoecology*, 288(1-4):62–81, 2010.

[10] J. Mitchell and P. M. Sander. The three-front model: a developmental explanation of long bone diaphyseal histology of Sauropoda. *Biological Journal of the Linnean Society*, 112(4):765–781, 2014.

[11] T. Yonezawa, T. Segawa, H. Mori, P. F. Campos, Y. Hongoh, H. Endo, A. Akiyoshi, N. Kohno, S. Nishida, J. Wu, et al. Phylogenomics and morphology of extinct paleognaths reveal the origin and evolution of the ratites. *Current Biology*, 27(1):68–77, 2017.

[12] P. Gorzelak and S. Zamora. Understanding form and function of the stem in early flattened echinoderms (pleurocystitids) using a microstructural approach. *PeerJ*, 4:e1820, 2016.

[13] P. Schneider, M. Stauber, R. Voide, M. Stampanoni, L. R. Donahue, and R. Muller. Ultrastructural properties in cortical bone vary greatly in two inbred strains of mice as assessed by synchrotron light based micro- and nano-CT. *Journal of Bone and Mineral Research*, 22(10):1557–1570, 2007.

[14] I. V. Pratt and D. M. L. Cooper. A method for measuring the three-dimensional orientation of cortical canals with implications for comparative analysis of bone microstructure in vertebrates. *Micron*, 92:32–38, 2017.

[15] E. de Margerie, J. Cubo, and J. Castanet. Bone typology and growth rate: testing and quantifying 'Amprino's rule' in the mallard (Anas platyrhynchos). *Comptes Rendus Biologies*, 325(3):221–230, 2002.

[16] M. D. D'Emic and R. B. J. Benson. Measurement, variation, and scaling of osteocyte lacunae: a case study in birds. *Bone*, 57(1):300–310, 2013.

[17] K. Stein and E. Prondvai. Rethinking the nature of fibrolamellar bone: an integrative biological revision of sauropod plexiform bone formation. *Biological Reviews*, 89(1):24–47, 2014.

[18] I. V. Pratt, J. D. Johnston, E. Walker, and D. M. L. Cooper. Interpreting the three-dimensional orientation of vascular canals and cross-sectional geometry of cortical bone in birds and bats. *Journal of anatomy*, 232(6):931–942, 2018.

[19] B Williams, D Waddington, DH Murray, and C Farquharson. Bone strength during growth: influence of growth rate on cortical porosity and mineralization. *Calcified Tissue International*, 74(3):236–245, 2004.

[20] C. L. Organ, S. L. Brusatte, and K. Stein. Sauropod dinosaurs evolved moderately sized genomes unrelated to body size. *Proceedings of the Royal Society B-Biological Sciences*, 276(1677):4303–4308, 2009.

[21] E. De Margerie, S. Sanchez, J. Cubo, and J. Castanet. Torsional resistance as a principal component of the structural design of long bones: comparative multivariate evidence in birds. *The Anatomical Record Part A: Discoveries in Molecular, Cellular, and Evolutionary Biology: An Official Publication of the American Association of Anatomists*, 282(1):49–66, 2005.

[22] K. Padian and E. T. Lamm. *Bone histology of fossil tetrapods : advancing methods, analysis, and interpretation*. University of California Press, Berkeley, 2013.

[23] C. Hennig, C. D. L Thomas, J. G. Clement, and D. M. L. Cooper. Does 3D orientation account for variation in osteon morphology assessed by 2D histology? *Journal of anatomy*, 227(4):497–505, 2015.

[24] S. Sanchez, P. E. Ahlberg, K. M. Trinajstic, A. Mirone, and P. Tafforeau. Three-dimensional synchrotron virtual paleohistology: A new insight into the world of fossil bone microstructures. *Microscopy and Microanalysis*, 18(5):1095–1105, 2012.

[25] F. Knoll, L. M. Chiappe, S. Sanchez, R. J. Garwood, N. P. Edwards, R. A. Wogelius, W. I. Sellers, P. L. Manning, F. Ortega, F. J. Serrano, et al. A diminutive perinate European Enantiornithes reveals an asynchronous ossification pattern in early birds. *Nature communications*, 9(1):937, 2018.

[26] L. Montes, E. de Margerie, J. Castanet, A. de Ricqles, and J. Cubo. Relationship between bone growth rate and the thickness of calcified cartilage in the long bones of the Galloanserae (Aves). *Journal of Anatomy*, 206(5):445–452, 2005.

[27] R Pawlicki, A Korbel, and H Kubiak. Cells, collagen fibrils and vessels in dinosaur bone. *Nature*, 211(5049):655, 1966.

[28] S. W. Keenan and A. S. Engel. Early diagenesis and recrystallization of bone. *Geochimica et Cosmochimica Acta*, 196:209–223, 2017.

[29] M. Wang, X. L. Wang, Y. Wang, and Z. H. Zhou. A new basal bird from China with implications for morphological diversity in early birds. *Scientific Reports*, 6, 2016.

[30] M. Wang and Z. Zhou. A new adult specimen of the basalmost ornithuromorph bird Archaeorhynchus spathula (Aves: Ornithuromorpha) and its implications for early avian ontogeny. *Journal of Systematic Palaeontology*, page 18, 2016.

[31] N. Brocklehurst, P. Upchurch, P. D. Mannion, and J. O'Connor. The completeness of the fossil record of Mesozoic Birds: Implications for early avian evolution. *Plos One*, 7(6), 2012.

[32] D. W. E. Hone, G. J. Dyke, M. Haden, and M. J. Benton. Body size evolution in Mesozoic birds. *Journal of Evolutionary Biology*, 21(2):618–624, 2008.

[33] R. Amprino. La structure du tissu osseux envisagée comme expression de differences dans la vitesse de l'accroissement. *Archives de biologie*, 58(4):317–330, 1947.

[34] D. H. Enlow. A comparative histological study of fossil and recent bone tissues, part II. *Texas J. Sci.*, 9:186–214, 1957.

[35] N. Klein and M. Sander. Ontogenetic stages in the long bone histology of sauropod dinosaurs. *Paleobiology*, 34(2):247–263, 2008.

[36] G. M. Erickson. On dinosaur growth. *Annual Review of Earth and Planetary Sciences, Vol 42*, 42:675–+, 2014.

[37] S. L. Brusatte, J. K. O'Connor, and E. D. Jarvis. The origin and diversification of birds. *Current Biology*, 25(19):R888–R898, 2015.

[38] G. M. Erickson, O. W. M. Rauhut, Z. H. Zhou, A. H. Turner, B. D. Inouye, D. Y. Hu, and M. A. Norell. Was dinosaurian physiology inherited by birds? reconciling slow growth in Archaeopteryx. *Plos One*, 4(10), 2009.

[39] X. Xu and D. Pol. Archaeopteryx, paravian phylogenetic analyses, and the use of probability-based methods for palaeontological datasets. *Journal of Systematic Palaeontology*, 12(3):323–334, 2014.

[40] R. E. Ricklefs. Patterns of growth in birds .5. comparative-study of development in the starling, common tern, and japanese quail. *Auk*, 96(1):10–30, 1979.

[41] L. Montes, J. Castanet, and J. Cubo. Relationship between bone growth rate and bone tissue organization in amniotes: first test of Amprino's rule in a phylogenetic context. *Animal Biology*, 60(1):25–41, 2010.

[42] L. M. Chiappe, J. Marugán-Lobón, Z. Zhou, et al. Life history of a basal bird: morphometrics of the Early Cretaceous Confuciusornis. *Biology letters*, 4(6):719–723, 2008.

[43] W. S. Peters and D. S. Peters. Life history, sexual dimorphism and 'ornamental' feathers in the mesozoic bird Confuciusornis sanctus. *Biology Letters*, 5(6):817–820, 2009.

[44] L. M. Chiappe, J. Marugan-Lobon, and A. Chinsamy. Palaeobiology of the Cretaceous bird Confuciusornis: a comment on Peters & Peters (2009). *Biology Letters*, 6(4):529–530, 2010.

[45] W. S. Peters and D. S. Peters. Sexual size dimorphism is the most consistent explanation for the body size spectrum of Confuciusornis sanctus. *Biology Letters*, 6(4):531–532, 2010.

[46] A. Chinsamy, L. M. Chiappe, J. Marugan-Lobon, C. L. Gao, and F. J. Zhang. Gender identification of the Mesozoic bird Confuciusornis sanctus. *Nature Communications*, 4, 2013.

[47] A. J. De Ricqles, K. Padian, J. R. Horner, E. T. Lamm, and N. Myhrvold. Osteohistology of Confuciusornis sanctus (Theropoda : Aves). *Journal of Vertebrate Paleontology*, 23(2):373–386, 2003.

[48] N. C. Smith, K. J. Jespers, and A. M. Wilson. Ontogenetic scaling of locomotor kinetics and kinematics of the ostrich (Struthio camelus). *Journal of Experimental Biology*, 213(8):1347–1355, 2010.

[49] A. M. Heers. From extant to extinct: Locomotor ontogeny and the evolution of avian flight. *Journal of Vertebrate Paleontology*, 32:109–109, 2012.

[50] D. W. Hone, A. A. Farke, and M. J. Wedel. Ontogeny and the fossil record: what, if anything, is an adult dinosaur? *Biol Lett*, 12(2), 2016.

[51] C. L. Gao, L. M. Chiappe, F. J. Zhang, D. L. Pomeroy, C. Z. Shen, A. Chinsamy, and M. O. Walsh. A subadult specimen of the Early Cretaceous bird Sapeornis chaoyangensis and a taxonomic reassessment of sapeornithids. *Journal of Vertebrate Paleontology*, 32(5):1103–1112, 2012.

[52] L. H. Hou, Z. H. Zhou, Y. C. Gu, and H. Zhang. Confuciusornis-sanctus, a new Late Jurassic sauriurine bird from China. *Chinese Science Bulletin*, 40(18):1545–1551, 1995.

[53] N. R. Longrich and D. J. Field. Torosaurus is not Triceratops: ontogeny in chasmosaurine ceratopsids as a case study in dinosaur taxonomy. *PloS one*, 7(2):e32623, 2012.

[54] D. G. Pechak, M. J. Kujawa, and A. I. Caplan. Morphology of bone-development and bone remodeling in embryonic chick limbs. *Bone*, 7(6):459–472, 1986.

[55] W. Van Neer, K. Noyen, B. De Cupere, and I. Beuls. On the use of endosteal layers and medullary bone from domestic fowl in archaeozoological studies. *Journal of Archaeological Science*, 29(2):123–134, 2002.

[56] A. K. Huttenlocker and C.G. Farmer. Bone microvasculature tracks red blood cell size diminution in Triassic mammal and dinosaur forerunners. *Current Biology*, 27(1):48–54, 2017.

[57] E. Prondvai, E. R. Bodor, and A. Osi. Does morphology reflect osteohistology-based ontogeny? a case study of Late Cretaceous pterosaur jaw symphyses from Hungary reveals hidden taxonomic diversity. *Paleobiology*, 40(2):288–321, 2014.

[58] J. Castanet, H. FrancillonVieillot, and R. C. Bruce. Age estimation in desmognathine salamanders assessed by skeletochronology. *Herpetologica*, 52(2):160–171, 1996.

[59] J. Castanet, S. Croci, F. Aujard, M. Perret, J. Cubo, and E. de Margerie. Lines of arrested growth in bone and age estimation in a small primate: Microcebus murinus. *Journal of Zoology*, 263:31–39, 2004.

[60] T. Tutken, H. U. Pfretzschner, T. W. Vennemann, G. Sun, and Y. D. Wang. Paleobiology and skeletochronology of Jurassic dinosaurs: implications from the histology and oxygen isotope compositions of bones. *Palaeogeography Palaeoclimatology Palaeoecology*, 206(3-4):217–238, 2004.

[61] T. R. Hubner. Bone histology in Dysalotosaurus lettowvorbecki (Ornithischia: Iguanodontia) - variation, growth, and implications. *Plos One*, 7(1), 2012.

[62] T. M. Cullen, D. C. Evans, M. J. Ryan, P. J. Currie, and Y. Kobayashi. Osteohistological variation in growth marks and osteocyte lacunar density in a theropod dinosaur (Coelurosauria: Ornithomimidae). *Bmc Evolutionary Biology*, 14, 2014.

[63] O. Cambra-Moo, A. D. Buscalioni, J. Cubo, J. Castanet, M. M. Loth, E. De Margerie, and A. de Ricqles. Histological observations of Enantiornithine bone (Saurischia, Aves) from the Lower Cretaceous of Las Hoyas (Spain). *Comptes Rendus Palevol*, 5(5):685–691, 2006.

[64] J. M. Rensberger and R. N. Martinez. Bone cells in birds show exceptional surface area, a characteristic tracing back to saurischian dinosaurs of the Late Triassic. *Plos One*, 10(5), 2015.

[65] R. C. Nelson and T. A. Bookhout. Counts of periosteal layers invalid for aging Canada geese. *Journal of Wildlife Management*, 44(2):518–521, 1980.

[66] N. I. Klomp and R. W. Furness. A technique which may allow accurate determination of the age of adult birds. *Ibis*, 134(3):245–249, 1992.

[67] J. Drozdowska and W. Meissner. Changes in endosteal cell layer number of long bones are not appropriate for ageing birds: Evidence from Baltic razorbills (Alca torda Linnaeus, 1758). *Zoologischer Anzeiger*, 253(6):493–496, 2014.

[68] J. Castanet, K. C. Rogers, J. Cubo, and J. J. Boisard. Periosteal bone growth rates in extant ratites (ostriche and emu). implications for assessing growth in dinosaurs. *Comptes Rendus De L Academie Des Sciences Serie Iii-Sciences De La Vie-Life Sciences*, 323(6):543–550, 2000.

[69] J. Cubo, J. Baudin, L. Legendre, A. Quilhac, and V. De Buffrenil. Geometric and metabolic constraints on bone vascular supply in diapsids. *Biological Journal of the Linnean Society*, 112(4):668–677, 2014.

[70] L. J. Legendre, E. Bourdon, R. P. Scofield, A. J. D. Tennyson, H. Lamrous, A. de Ricqles, and J. Cubo. Bone histology, phylogeny, and palaeognathous birds (Aves: Palaeognathae). *Biological Journal of the Linnean Society*, 112(4):688–700, 2014.

[71] P. Schneider, R. Voide, M. Stampanoni, L. R. Donahue, and R. Muller. The importance of the intracortical canal network for murine bone mechanics. *Bone*, 53(1):120–128, 2013.

[72] A. A. Felder, C. Phillips, H. Cornish, M. Cooke, J. R. Hutchinson, and M. Doube. Secondary osteons scale allometrically in mammalian humerus and femur. *Royal Society open science*, 4(11):170431, 2017.

[73] S.F. Gilbert. *Osteogenesis: The development of bones.* Sinauer Associates, 2013.

[74] Y. Carter, C. D. L. Thomas, J. G. Clement, A. G. Peele, K. Hannah, and D. M. L. Cooper. Variation in osteocyte lacunar morphology and density in the human femur - a synchrotron radiation micro-CT study. *Bone*, 54(1):179–179, 2013.

[75] J. Klein-Nulend, A. D. Bakker, R. G. Bacabac, A. Vatsa, and S. Weinbaum. Mechanosensation and transduction in osteocytes. *Bone*, 54(2):182–190, 2013.

[76] M. B. Schaffler, W. Y. Cheung, R. Majeska, and O. Kennedy. Osteocytes: master orchestrators of bone. *Calcified tissue international*, 94(1):5–24, 2014.

[77] M. Prideaux, D. M. Findlay, and G. J. Atkins. Osteocytes: the master cells in bone remodelling. *Current opinion in pharmacology*, 28:24–30, 2016.

[78] C. M. Semeins, A. D. Bakker, and J. Klein-Nulend. Isolation of primary avian osteocytes. *Bone Research Protocols, Second Edition*, 816:43–53, 2012.

[79] P. Schneider, M. Meier, R. Wepf, and R. Muller. Towards quantitative 3D imaging of the osteocyte lacuno-canalicular network. *Bone*, 47(5):848–858, 2010.

[80] H. M. Britz, Y. Carter, J. Jokihaara, O. V. Leppanen, T. L. N. Jarvinen, G. Belev, and D. M. L. Cooper. Prolonged unloading in growing rats reduces cortical osteocyte lacunar density and volume in the distal tibia. *Bone*, 51(5):913–919, 2012.

[81] K. S. Mader, P. Schneider, R. Muller, and M. Stampanoni. A quantitative framework for the 3D characterization of the osteocyte lacunar system. *Bone*, 57(1):142–154, 2013.

[82] A. Carriero, M. Doube, M. Vogt, B. Busse, J. Zustin, A. Levchuk, P. Schneider, R. Muller, and S. J. Shefelbine. Altered lacunar and vascular porosity in osteogenesis imperfecta mouse bone as revealed by synchrotron tomography contributes to bone fragility. *Bone*, 61:116–124, 2014.

[83] X. Lai, C. Price, S. Modla, W. R. Thompson, J. Caplan, C. B. Kirn-Safran, and L. Wang. The dependences of osteocyte network on bone compartment, age, and disease. *Bone Res*, 3, 2015.

[84] R. F. M. van Oers, H. Wang, and R. G. Bacabac. Osteocyte shape and mechanical loading. *Current Osteoporosis Reports*, 13(2):61–66, 2015.

[85] R. L. Hunter and A. M. Agnew. Intraskeletal variation in human cortical osteocyte lacunar density: implications for bone quality assessment. *Bone reports*, 5:252–261, 2016.

[86] M. Kerschnitzki, W. Wagermaier, P. Roschger, J. Seto, R. Shahar, G. N. Duda, S. Mundlos, and P. Fratzl. The organization of the osteocyte network mirrors the extracellular matrix orientation in bone. *Journal of Structural Biology*, 173(2):303–311, 2011.

[87] N. Reznikov, R. Shahar, and S. Weiner. Bone hierarchical structure in three dimensions. *Acta Biomaterialia*, 10(9):3815–3826, 2014.

[88] C. M. Riggs, L. E. Lanyon, and A. Boyde. Functional associations between collagen fiber orientation and locomotor strain direction in cortical bone of the equine radius. *Anatomy and Embryology*, 187(3):231–238, 1993.

[89] K. W. H. Stein and J. Werner. Preliminary analysis of osteocyte lacunar density in long bones of tetrapods: All measures are bigger in sauropod dinosaurs. *Plos One*, 8(10), 2013.

[90] F. L. Bach-Gansmo, Jensen M. H. Leemreize H. Weaver, J. C., Stampanoni Mader, K. S., A. M., Brüel, J. S. Thomsen, and H. Birkedal. Osteocyte lacunar properties in rat cortical bone: differences between lamellar and central bone. *Journal of structural biology*, 191(1):59–67, 2015.

[91] A. G. Robling, A. B. Castillo, and C. H. Turner. Biomechanical and molecular regulation of bone remodeling. *Annual Review of Biomedical Engineering*, 8:455–498, 2006.

[92] J. M. Starck and A. Chinsamy. Bone microstructure and developmental plasticity in birds and other dinosaurs. *Journal of Morphology*, 254(3):232–246, 2002.

[93] A. Chinsamy, L. D. Martin, and P. Dodson. Bone microstructure of the diving Hesperornis and the volant Ichthyornis from the Niobrara Chalk of western Kansas. *Cretaceous Research*, 19(2):225–235, 1998.

[94] V. de Buffrenil, A. Houssaye, and W. Bohme. Bone vascular supply in monitor lizards (Squamata : Varanidae): Influence of size, growth, and phylogeny. *Journal of Morphology*, 269(5):533–543, 2008.

[95] A. Dawson, D. C. Deeming, A. C. Dick, and P. J. Sharp. Plasma thyroxine concentrations in farmed ostriches in relation to age, body weight, and growth hormone. *Gen Comp Endocrinol*, 103(3):308–15, 1996.

[96] A. Chinsamy-Turan, J. Marugan-Lobon, and L. Chiappe. Life history of the Early Cretaceous bird Confuciusornis: A histological perspective. *Journal of Vertebrate Paleontology*, 31:88–88, 2011.

[97] J. K. O'Connor, M. Wang, S. Zhou, and Z. H. Zhou. Osteohistology of the Lower Cretaceous Yixian Formation ornithuromorph (Aves) Iteravis huchzermeyeri. *Palaeontologia Electronica*, 18(2), 2015.

[98] J. K. O'Connor, M. Wang, X. T. Zheng, X. Wang, and Z. Zhou. The histology of two female Early Cretaceous birds. *Vertebrata Palasiatica*, 52(1):16, 2014.

[99] H. Hu, J. K. O'Connor, and Z. H. Zhou. A new species of Pengornithidae (Aves: Enantiornithes) from the Lower Cretaceous of China suggests a specialized scansorial habitat previously unknown in early birds. *Plos One*, 10(6), 2015.

[100] A. Chinsamy, L. M. Chiappe, and P. Dodson. Mesozoic avian bone microstructure: Physiological implications. *Paleobiology*, 21(4):561–574, 1995.

[101] A. K. Bell, L. M. Chiappe, G. M. Erickson, S. Suzuki, M. Watabe, R. Barsbold, and K. Tsogtbaatar. Description and ecologic analysis of Hollanda luceria, a Late Cretaceous bird from the Gobi Desert (Mongolia). *Cretaceous Research*, 31(1):16–26, 2010.

[102] E. A. Cadena, D. T. Ksepka, and M. A. Norell. New material of Mongolemys elegans Khosatzky and Mlynarski, 1971 (Testudines: Lindholmemydidae), from the Late Cretaceous of Mongolia with comments on bone histology and phylogeny. *American Museum Novitates*, (3766):1–27, 2013.

[103] T. G. Bromage, H. M. Goldman, S. C. Mcfarlin, A. P. Ochoa, and A. Boyde. Confocal scanning optical microscopy of a 3-million-year-old Australopithecus afarensis femur. *Scanning*, 31(1):1–10, 2009.

[104] E. Lozupone, C. Palumbo, A. Favia, M. Ferretti, S. Palazzini, and F. P. Cantatore. Intermittent compressive load stimulates osteogenesis and improves osteocyte viability in bones cultured "in vitro". *Clinical Rheumatology*, 15(6):563–572, 1996.

[105] C. L. Organ, A. M. Shedlock, A. Meade, M. Pagel, and S. V. Edwards. Origin of avian genome size and structure in non-avian dinosaurs. *Nature*, 446(7132):180, 2007.

[106] Y. Carter, C. D. L. Thomas, J. G. Clement, and D. M. L. Cooper. Femoral osteocyte lacunar density, volume and morphology in women across the lifespan. *Journal of Structural Biology*, 183(3):519–526, 2013.

[107] L. Domenis, S. Squadrone, D. Marchis, and M. C. Abete. Osteocyte lacunae features in different chicken bones. *Biotechnologie Agronomie Societe Et Environnement*, 13:29–32, 2009.

[108] I. V. Pratt and D. M. L. Cooper. The effect of growth rate on the three-dimensional orientation of vascular canals in the cortical bone of broiler chickens. *Journal of anatomy*, 2018.

[109] J. Cubo, N. Le Roy, C. Martinez-Maza, and L. Montes. Paleohistological estimation of bone growth rate in extinct archosaurs. *Paleobiology*, 38(2):335–349, 2012.

[110] M. Rucklin, P. C. J. Donoghue, J. A. Cunningham, F. Marone, and M. Stampanoni. Developmental paleobiology of the vertebrate skeleton. *Journal of Paleontology*, 88(4):676–683, 2014.

[111] M. Georgiadis, M. Guizar-Sicairos, O. Gschwend, P. Hangartner, O. Bunk, R. Muller, and P. Schneider. Ultrastructure organization of human trabeculae assessed by 3D sSAXS and relation to bone microarchitecture. *Plos One*, 11(8), 2016.

[112] S. Annibali, D. Bellavia, L. Ottolenghi, A. Cicconetti, M. P. Cristalli, R. Quaranta, and A. Pilloni. Micro-CT and PET analysis of bone regeneration induced by biodegradable scaffolds as carriers for dental pulp stem cells in a rat model of calvarial "critical size" defect: Preliminary data. *Journal of Biomedical Materials Research Part B-Applied Biomaterials*, 102(4):815–825, 2014.

[113] S. Zamora, I. A. Rahman, and A. B. Smith. Plated Cambrian bilaterians reveal the earliest stages of echinoderm evolution. *Plos One*, 7(6), 2012.

[114] G. Sobral, C. A. Hipsley, and J. Muller. Braincase redescription of Dysalotosaurus lettowvorbecki (Dinosauria, Ornithopoda) based on computed tomography. *Journal of Vertebrate Paleontology*, 32(5):1090–1102, 2012.

[115] R. L. Abel, C. R. Laurini, and M. Richter. A palaeobiologist's guide to 'virtual' micro-CT preparation. *Palaeontologia Electronica*, 15(2), 2012.

[116] M. Zuber, M. Laaß, E. Hamann, S. Kretschmer, N. Hauschke, T. Van De Kamp, T. Baumbach, and T. Koenig. Augmented laminography, a correlative 3D imaging method for revealing the inner structure of compressed fossils. *Scientific reports*, 7:41413, 2017.

[117] H. N. Woodward, E. A. F. Fowler, J. O. Farlow, and J. R. Horner. Maiasaura, a model organism for extinct vertebrate population biology: a large sample statistical assessment of growth dynamics and survivorship. *Paleobiology*, 41(4):503–527, 2015.

[118] J. Marugan-Lobon, L. M. Chiappe, S. A. Ji, Z. H. Zhou, G. L. Chunling, D. Y. Hu, and Q. J. Meng. Quantitative patterns of morphological variation in the appendicular skeleton of the Early Cretaceous bird Confuciusornis. *Journal of Systematic Palaeontology*, 9(1):91–101, 2011.

[119] T. Goldschlager, A. Abdelkader, J. Kerr, I. Boundy, and G. Jenkin. Undecalcified bone preparation for histology, histomorphometry and fluorochrome analysis. *JoVE (Journal of Visualized Experiments)*, (35):e1707–e1707, 2010.

[120] HE Gruber, J Ingram, and EN Hanley Jr. An improved staining method for intervertebral disc tissue. *Biotechnic & histochemistry*, 77(2):81–83, 2002.

[121] C. B. Knudson and W. Knudson. Cartilage proteoglycans. In *Seminars in cell & developmental biology*, volume 12, pages 69–78. Elsevier, 2001.

[122] A. C. Kak and M. Slaney. *Principles of computerized tomographic imaging*. SIAM, 1998.

[123] J. Schindelin, I. Arganda-Carreras, E. Frise, V. Kaynig, M. Longair, T. Pietzsch, S. Preibisch, C. Rueden, S. Saalfeld, B. Schmid, et al. Fiji: an open-source platform for biological-image analysis. *Nature methods*, 9(7):676–682, 2012.

[124] Johannes Schindelin, Curtis T Rueden, Mark C Hiner, and Kevin W Eliceiri. The imagej ecosystem: an open platform for biomedical image analysis. *Molecular reproduction and development*, 82(7-8):518–529, 2015.

[125] M. Doube, M. M. Klosowski, I. Arganda-Carreras, F. P. Cordelieres, R. P. Dougherty, J. S. Jackson, B. Schmid, J. R. Hutchinson, and S. J. Shefelbine. BoneJ free and extensible bone image analysis in imageJ. *Bone*, 47(6):1076–1079, 2010.

[126] A. Chinsamy-Turan and J. Hurum. Bone microstructure and growth patterns of early mammals. *Journal of Vertebrate Paleontology*, 25(3):44a–44a, 2005.

[127] K Padian, A. J. de Ricqlès, and J. R. Horner. Dinosaurian growth rates and bird origins. *Nature*, 412(6845):405, 2001.

[128] J. M. Grady, B. J. Enquist, E. Dettweiler-Robinson, N. A. Wright, and F. A. Smith. Evidence for mesothermy in dinosaurs. *Science*, 344(6189):1268–1272, 2014.

[129] E. L. Bortel, G. N. Duda, S. Mundlos, B. M. Willie, P. Fratzl, and P. Zaslansky. Long bone maturation is driven by pore closing: A quantitative tomography investigation of structural formation in young C57BL/6 mice. *Acta biomaterialia*, 22:92–102, 2015.

[130] A. De Ricqles. Recherches paléohistologiques sur les os longs des tétrapodes VII. - sur la classification, la signification fonctionnelle et l'histoire des tissus oseux des tétrapodes. première partie, structures. *Annales de paléontologie.*, 61:78, 1975.

[131] A. H. Lee and E. L. R. Simons. Wing bone laminarity is not an adaptation for torsional resistance in bats. *PeerJ*, 3:e823, 2015.

[132] E. L. R. Simons and P. M. O'connor. Bone laminarity in the avian forelimb skeleton and its relationship to flight mode: testing functional interpretations. *The Anatomical Record: Advances in Integrative Anatomy and Evolutionary Biology*, 295(3):386–396, 2012.

[133] C. A. Marelli and E. L. R. Simons. Microstructure and cross-sectional shape of limb bones in great horned owls and red-tailed hawks: how do these features relate to differences in flight and hunting behavior? *PloS one*, 9(8):e106094, 2014.

[134] D.M.L. Cooper, B. Erickson, A.G. Peele, K. Hannah, C.D.L. Thomas, and J.G. Clement. Visualization of 3D osteon morphology by synchrotron radiation micro-CT. *Journal of anatomy*, 219(4):481–489, 2011.

[135] MC Tan, NL Chin, YA Yusof, and J Abdullah. Novel 2D and 3D imaging of internal aerated structure of ultrasonically treated foams and cakes using X-ray tomography and X-ray microtomography. *Journal of Food Engineering*, 183:9–15, 2016.

[136] A. S. Iyer-Pascuzzi, O. Symonova, Y. Mileyko, Y. Hao, H. Belcher, J. Harer, J. S. Weitz, and P. N. Benfey. Imaging and analysis platform for automatic phenotyping and trait ranking of plant root systems. *Plant physiology*, 152(3):1148–1157, 2010.

[137] A. Chinsamy. Assessing the biology of fossil vertebrates through bone histology. 1997.

[138] JT Haug, C Haug, A Maas, SR Fayers, NH Trewin, and D Waloszek. Simple 3D images from fossil and recent micromaterial using light microscopy. *Journal of Microscopy*, 233(1):93–101, 2009.

[139] K. Mader. *High-throughput, synchrotron based tomographic microscopy tools for the quantitative characterization of complex structures: A bone and foam study*. PhD thesis, ETH Zurich, 2013.

[140] S. Sanchez, P. Tafforeau, J. A. Clack, and P. E. Ahlberg. Life history of the stem tetrapod acanthostega revealed by synchrotron microtomography. *Nature*, 537(7620):408, 2016.

[141] J. Newton. An overview of the UK duck industry. Report, 2012. Sustainable Food and Farming Group.

[142] CH Li and Peter Kwong-Shun Tam. An iterative algorithm for minimum cross entropy thresholding. *Pattern Recognition Letters*, 19(8):771–776, 1998.

[143] L. J. Legendre, L. Segalen, and J. Cubo. Evidence for high bone growth rate in Euparkeria obtained using a new paleohistological inference model for the humerus. *Journal of Vertebrate Paleontology*, 33(6):1343–1350, 2013.

[144] A. Odgaard, K. Andersen, F. Melsen, and H. J. G. Gundersen. A direct method for fast three-dimensional serial reconstruction. *Journal of microscopy*, 159(3):335–342, 1990.

[145] D. Cooper, A. Turinsky, C. Sensen, and B. Hallgrimsson. Effect of voxel size on 3d micro-CT analysis of cortical bone porosity. *Calcified tissue international*, 80(3):211–219, 2007.

[146] P. Casale, N. Conte, D. Freggi, C. Cioni, and R. Argano. Age and growth determination by skeletochronology in loggerhead sea turtles (Caretta caretta) from the Mediterranean Sea. *Scientia Marina*, 75(1):197–203, 2011.

[147] L. Avens, L. R. Goshe, M. Pajuelo, K. A. Bjorndal, B. D. MacDonald, G. E. Lemons, A. B. Bolten, and J. A. Seminoff. Complementary skeletochronology and stable isotope analyses offer new insight into juvenile loggerhead sea turtle oceanic stage duration and growth dynamics. *Marine Ecology Progress Series*, 491:235–+, 2013.

[148] K. Ento and M. Matsui. Estimation of age structure by skeletochronology of a population of Hynobius nebulosus in a breeding season (Amphibia, Urodela). *Zoological Science*, 19(2):241–247, 2002.

[149] L. N. Cooper, A. H. Lee, M. L. Taper, and J. R. Horner. Relative growth rates of predator and prey dinosaurs reflect effects of predation. *Proceedings of the Royal Society B-Biological Sciences*, 275(1651):2609–2615, 2008.

[150] J. R. Horner and M. B. Goodwin. Major cranial changes during Triceratops ontogeny. *Proceedings of the Royal Society B-Biological Sciences*, 273(1602):2757–2761, 2006.

[151] J. B. Scannella and J. R. Horner. Torosaurus Marsh, 1891, is Triceratops Marsh, 1889 (Ceratopsidae: Chasmosaurinae): synonymy through ontogeny. *Journal of Vertebrate Paleontology*, 30(4):1157–1168, 2010.

[152] L. Maiorino, A. A. Farke, T. Kotsakis, and P. Piras. Is Torosaurus Triceratops? geometric morphometric evidence of Late Maastrichtian ceratopsid dinosaurs. *Plos One*, 8(11), 2013.

[153] B. N. Andia, P. K. Dixit, S. Behera, G. Mishra, and H. N. Behera. Assessment of age and growth in common tree frog, Polypedates maculatus Gray by skeletochronology. *Proceedings of the National Academy of Sciences India Section B-Biological Sciences*, 80:221–229, 2010.

[154] R. C. Bruce and J. Castanets. Application of skeletochronology in aging larvae of the salamanders Gyrinophilus porphyriticus and Pseudotriton ruber. *Journal of Herpetology*, 40(1):85–90, 2006.

[155] K. A. Bjorndal, A. B. Bolten, R. A. Bennett, E. R. Jacobson, Valesk and J. J. Wronski, T. J., and P. J. Eliazar. Age and growth in sea turtles: Limitations of skeletochronology for demographic studies. *Copeia*, (1):23–30, 1998.

[156] E. Bourdon, J. Castanet, A. de Ricqles, P. Scofield, A. Tennyson, H. Lamrous, and J. Cubo. Bone growth marks reveal protracted growth in New Zealand kiwi (Aves, Apterygidae). *Biology Letters*, 5(5):639–642, 2009.

[157] A. de Ricqles, O. Mateus, M. T. Antunes, and P. Taquet. Histomorphogenesis of embryos of Upper Jurassic theropods from Lourinha (Portugal). *Comptes Rendus De L Academie Des Sciences Serie Ii Fascicule a-Sciences De La Terre Et Des Planetes*, 332(10):647–656, 2001.

[158] G. Marotti. Static and dynamic osteogenesis. *Ital J Anat Embryol*, 115(1-2):123–6, 2010.

[159] D.M.L. Cooper, C.E. Kawalilak, K. Harrison, B.D. Johnston, and J.D. Johnston. Cortical bone porosity: what is it, why is it important, and how can we detect it? *Current osteoporosis reports*, 14(5):187–198, 2016.

[160] F. Ponton, A. Elzanowski, J. Castanet, A. Chinsamy, E. de Margerie, A. de Ricqles, and J. Cubo. Variation of the outer circumferential layer in the limb bones of birds. *Acta Ornithologica*, 39(2):137–140, 2004.

[161] E. De Margerie. Laminar bone as an adaptation to torsional loads in flapping flight. *Journal of Anatomy*, 201(6):521–526, 2002.

[162] J. D. Currey. *Bones: structure and mechanics*. Princeton university press, 2006.

[163] J.D. Currey. The many adaptations of bone. *Journal of biomechanics*, 36(10):1487–1495, 2003.

[164] E. Prondvai, P. Godefroit, D. Adriaens, and D. Y. Hu. Intraskeletal histovariability, allometric growth patterns, and their functional implications in bird-like dinosaurs. *Scientific reports*, 8(1):258, 2018.

[165] T. R. Dial and D. R. Carrier. Precocial hindlimbs and altricial forelimbs: partitioning ontogenetic strategies in Mallard ducks (Anas platyrhynchos). *Journal of Experimental Biology*, pages jeb–057380, 2012.

[166] D. Carrier and L. R. Leon. Skeletal growth and function in the California gull (Larus californicus). *Journal of Zoology*, 222(3):375–389, 1990.

[167] N. Harcourt-Brown. Development of the skeleton and feathers of dusky parrots (Pionus fuscus) in relation to their behaviour. *Veterinary Record*, 154(2):42–48, 2004.

[168] C. G. Dacke, S. Arkle, D. J. Cook, I. M. Wormstone, S. Jones, M. Zaidi, and Z. A. Bascal. Medullary bone and avian calcium regulation. *Journal of Experimental Biology*, 184:63–88, 1993.

[169] A. J. Curtin, A. A. Macdowell, E. G. Schaible, and V. L. Roth. Noninvasive histological comparison of bone growth patterns among fossil and extant neonatal elephantids using synchrotron radiation X-ray microtomography. *Journal of Vertebrate Paleontology*, 32(4):939–955, 2012.

[170] AA Biewener and KP Dial. In vivo strain in the humerus of pigeons (Columba livia) during flight. *Journal of Morphology*, 225(1):61–75, 1995.

[171] Alexander V Badyaev. Growing apart: an ontogenetic perspective on the evolution of sexual size dimorphism. *Trends in Ecology & Evolution*, 17(8):369–378, 2002.

[172] J. Nunez, A. Goring, D. Gomez-Nicola, B. Javaheri, A.A. Pitsillides, P. Thurner, P. Schneider, C. Clarkin, et al. Regional diversity in the murine cortical vascular network is revealed by synchrotron X-ray tomography and is amplified with age. *European cells & materials*, 35:281–299, 2018.

[173] R. E. Ricklefs. Patterns of growth in birds .2. growth-rate and mode of development. *Ibis*, 115(2):177–201, 1973.

[174] J Matthias Starck and Robert E Ricklefs. Patterns of development: the altricial-precocial spectrum. *Oxford Ornithology Series*, 8:3–30, 1998.

[175] JM Starck. Evolution of avian ontogenies. In *Current ornithology*, pages 275–366. Springer, 1993.

[176] J. M. Starck. Quantitative design of the skeleton in bird hatchlings: does tissue compartmentalization limit posthatching growth rates? *Journal of Morphology*, 222(2):113–131, 1994.

[177] A. Chinsamy and A. Elzanowski. Bone histology: evolution of growth pattern in birds. *Nature*, 412(6845):402, 2001.

[178] A. Mayya, P. Praveen, A. Banerjee, and R. Rajesh. Splitting fracture in bovine bone using a porosity-based spring network model. *Journal of The Royal Society Interface*, 13(124):20160809, 2016.

[179] T. Clinton and L.E. Lanyon. Regulation of bone formation by applied dynamic loads. *J Bone Joint Surg Am*, 66:397–402, 1984.

[180] S. T. Turvey, O. R. Green, and R. N. Holdaway. Cortical growth marks reveal extended juvenile development in New Zealand moa. *Nature*, 435(7044):940–943, 2005.

[181] T. M. Blackburn and K. J. Gaston. The distribution of body sizes of the world's bird species. *Oikos*, pages 127–130, 1994.

[182] J. P. Hansford and S. T. Turvey. Unexpected diversity within the extinct elephant birds (Aves: Aepyornithidae) and a new identity for the world's largest bird. *Open Science*, 5(9):181295, 2018.

[183] A. M. Zahm, M. A. Bucaro, P. S. Ayyaswamy, V. Srinivas, I. M. Shapiro, C. S. Adams, and K. Mukundakrishnan. Numerical modeling of oxygen distributions in cortical and cancellous bone: oxygen availability governs osteonal and trabecular dimensions. *American Journal of Physiology-Cell Physiology*, 299(5):C922–C929, 2010.

[184] S Mishra. Biomechanical aspects of bone microstructure in vertebrates: potential approach to palaeontological investigations. *Journal of biosciences*, 34(5):799–809, 2009.

[185] CF Thompson and JEC Flux. Body mass, composition, and survival of nestling and fledgling starlings (Sturnus vulgaris) at Belmont, New Zealand. *New Zealand journal of ecology*, pages 41–47, 1991.

[186] R. G. Cooper. Growth in the ostrich (Struthio camelus var. domesticus). *Animal Science Journal*, 76(1):1–4, 2005.

[187] J. Adams and B. J. Revell. Ostrich farming:–a review and feasibility study of opportunities in the EU. *Website address: http://www. mluri. sari. ac. uk/livestocksystems/feasibility/ostrich. htm*, 2003.

[188] J. Hansford, P.C. Wright, A Rasoamiaramanana, V. R. Pérez, L. R. Godfrey, D. Errickson, T. Thompson, and S. T. Turvey. Early Holocene human presence in Madagascar evidenced by exploitation of avian megafauna. *Science Advances*, 4(9):eaat6925, 2018.

[189] K. J. Mitchell, B. Llamas, J. Soubrier, N. J. Rawlence, T. H. Worthy, J. Wood, M. S. Y. Lee, and A. Cooper. Ancient DNA reveals elephant birds and kiwi are sister taxa and clarifies ratite bird evolution. *Science*, 344(6186):898–900, 2014.

[190] S. M. Holland. The non-uniformity of fossil preservation. *Phil. Trans. R. Soc. B*, 371(1699):20150130, 2016.

[191] J. M. Rensberger and M. Watabe. Fine structure of bone in dinosaurs, birds and mammals. *Nature*, 406(6796):619–622, 2000.

[192] A. Davidson. Preparation of a fossil dinosaur. *Objects Specialty Group Postprints*, 10:49e61, 2004.

[193] R. A. Ketcham and W. D. Carlson. Acquisition, optimization and interpretation of X-ray computed tomographic imagery: applications to the geosciences. *Computers & Geosciences*, 27(4):381–400, 2001.

[194] Y. Wang, M. Wang, J. K. O'connor, X. Wang, X. Zheng, and X. Zhang. A new Jehol enantiornithine bird with three-dimensional preservation and ovarian follicles. *Journal of Vertebrate Paleontology*, 36(2):e1054496, 2016.

[195] A. Houssaye. Advances in vertebrate palaeohistology: recent progress, discoveries, and new approaches. *Biological Journal of the Linnean Society*, 112(4):645–648, 2014.

[196] A. De Ricqles, E. Bourdon, and L. Legendre. Preliminary assessment of bone histology in the extinct elephant bird Aepyornis (Aves, Palaeognathae) from Madagascar. *Comptes Rendus Palevol*, 2015.

[197] A. Grealy, M. Phillips, G. Miller, M. T. P. Gilbert, J. M. Rouillard, D. Lambert, M. Bunce, and J. Haile. Eggshell palaeogenomics: Palaeognath evolutionary history revealed through ancient nuclear and mitochondrial DNA from Madagascan elephant bird (Aepyornis sp.) eggshell. *Molecular phylogenetics and evolution*, 109:151–163, 2017.

[198] L. Leonard and M. Dyke, G. J.and Van Tuinen. A new specimen of the fossil palaeognath Lithornis from the Lower Eocene of Denmark. *American Museum Novitates*, pages 1–11, 2005.

[199] G. Mayr. First substantial Middle Eocene record of the Lithornithidae (Aves): A postcranial skeleton from Messel (Germany). In *Annales de paléontologie*, volume 94, pages 29–37. Elsevier, 2008.

[200] P. Houde. Ostrich ancestors found in the Northern Hemisphere suggest new hypothesis of ratite origins. *Nature*, 324(6097):563, 1986.

[201] G. E. Woolfenden. A pleistocene avifauna from Rock Spring, Florida. *The Wilson Bulletin*, 71(2):183–187, 1959.

[202] S. B. Ramos, S. L. Caetano, R. P. Savegnago, B. N. Nunes, A. A. Ramos, and D. P. Munari. Growth curves for ostriches (Struthio camelus) in a Brazilian population. *Poult Sci*, 92(1):277–82, 2013.

[203] G. Beale. A radiological study of the kiwi (Apteryx australis mantelli). *Journal of the Royal Society of New Zealand*, 15(2):187–200, 1985.

[204] G. Beale. The maturation of the skeleton of a kiwi (Apteryx australis mantetti)-a ten year radiological study. *Journal of the Royal Society of New Zealand*, 21(2):219–220, 1991.

[205] R. Marsell and T. A. Einhorn. The biology of fracture healing. *Injury*, 42(6):551–555, 2011.

[206] H. N. Woodward, J. R. Horner, and J. O. Farlow. Quantification of intraskeletal histovariability in Alligator mississippiensis and implications for vertebrate osteohistology. *Peerj*, 2, 2014.

[207] D Angst, A Chinsamy, L Steel, and JP Hume. Bone histology sheds new light on the ecology of the dodo (Raphus cucullatus, Aves, Columbiformes). *Scientific reports*, 7(1):7993, 2017.

[208] J. Cubo, P. Legendre, A. De Ricqlès, L. Montes, E. De Margerie, J. Castanet, and Y. Desdevises. Phylogenetic, functional, and structural components of variation in bone growth rate of amniotes. *Evolution & Development*, 10(2):217–227, 2008.